universität wien

MASTERARBEIT / MASTER'S THESIS

Titel der Masterarbeit / Title of the Master's Thesis

„Hydro-geomorphic changes of the Salza River near Gusswerk, Styria"

verfasst von / submitted by

Jakob Pamminger BSc

angestrebter akademischer Grad / in partial fulfilment of the requirements for the degree of

Master of Science (MSc)

Wien, 2021 / Vienna 2021

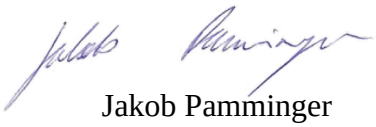
Studienkennzahl lt. Studienblatt / degree programme code as it appears on the student record sheet:	A 066 855
Studienrichtung lt. Studienblatt / degree programme as it appears on the student record sheet:	Masterstudium Geographie
Betreut von / Supervisor:	Mag. Dr. Ronald Pöppl, BA

Eidesstattliche Erklärung

Hiermit versichere ich,

- dass die ich die vorliegende Masterarbeit selbstständig verfasst, andere als die angegebenen Quellen und Hilfsmittel nicht benutzt und mich auch sonst keiner unerlaubter Hilfe bedient habe,
- dass ich dieses Masterarbeitsthema bisher weder im In- noch im Ausland in irgendeiner Form als Prüfungsarbeit vorgelegt habe
- und dass diese Arbeit mit der vom Begutachter beurteilten Arbeit vollständig übereinstimmt.

Wien, am 04.11.2021



Jakob Pamminger

Acknowledgements

First of all, I hereby would like to thank the Austrian Federal Forests (Österreichische Bundesforste) namely DI Andreas Haas and Dr. Monika Kanzian as well as my supervisor at the Department of Geography and Regional Research (University of Vienna) Mag. Dr. Ronald E. Pöppl, BA. for providing the main idea and designated study area of the Salza River used in this thesis. Further specific thanks go to the Austrian Federal Forests for sponsoring the travel and field work expenses as well as providing the digital elevation model used throughout this thesis and a coarse mapping done previously by a student which was addressed and compared with the mapping done in this thesis.

I would like to thank Erich Fischer from the Federal Ministry of Agriculture, Regions and Tourism (Bundesministerium für Landwirtschaft, Regionen und Tourismus/Sektion I – Wasserwirtschaft/Abteilung I/3 – Wasserhaushalt) for providing the discharge data from the gauging station in Gusswerk. Further thanks go to GIS-Styria/Comission of the Styrian government (Amt der Steiermärkischen Landesregierung/Abteilung 17 Landes- und Regionalentwicklung/Referat Statistik und Geoinformation) for providing the orthophotos. Also, I would like to thank the Austrian State Archives (Österreichisches Staatsarchiv) for allowing me the use of the historic maps in my thesis.

I would also like to thank Alexey Pasumansky from Agisoft LLC for helping solve some technical difficulties with the software Agisoft Metashape.

I further want to thank Markus Meller, Marco van Burik and Johannes Earl Schaffer for proofreading my final thesis version.

Lastly, I would like to greatly thank my parents for supporting me as well as enabling me the opportunity to be the first in the family to attend and complete a university degree.

Table of Contents

Table of Contents i

List of figures iv

List of tables x

List of abbreviations xiii

Abstract xiv

Zusammenfassung (Abstract in German) xv

1. Introduction 1

2. Research questions and hypotheses 2

3. Study area 4

3.1 General 4

3.2 Hot spot between river km 58.7 - 58.8 7

4. State-of-the-art of hydro-geomorphic changes 8

4.1 Reconstruction of past hydro-geomorphic changes using historic maps and orthophotos 8

4.2 Mapping of in and out-of-channel river features 9

4.3 Monitoring present hydro-geomorphic river changes 10

4.4 Modelling future hydro-geomorphic river changes 13

5. Data and Methods 17

5.1 Reconstruction of past hydro-geomorphic changes of the Salza River 17

5.1.1 Data 17

5.1.2 Methods 19

5.2 Mapping of in and out-of-channel geomorphic units 20

5.2.1 Data 20

5.2.2 Methods 21

5.3 Monitoring of the erosion hotspot 26

5.3.1 Data 26

5.3.2 Methods 26

5.4 Modelling of future hydro-geomorphic changes of the Salza River 41

5.4.1 Data 41

5.4.2 Methods 42
6. Results 58
6.1 Reconstruction of past hydro-geomorphic changes of the Salza River 58
6.1.1 Historical maps of the study area dating 1678 - 1887 58
6.1.2 orthophotos of the study area dating 2004 - 2017 65
6.1.3 Sinuosity index of the study area 82
6.1.4 Hotspot Sinuosity index and cross section 88
6.2 Mapping of in and out-of-channel geomorphic units 91
6.2.1 First map: Mapping of fluvial margins 91
6.2.2 Second map: Mapping of Tier 2 geomorphic units 96
6.2.3 Third map: Mapping of Tier 3 geomorphic units 103
6.2.4 Comparison with ÖBf mapping 111
6.3 Monitoring of the erosion hotspot 113
6.3.1 Erosion Pin Version 1 113
6.3.2 Erosion Pin Version 2 115
6.3.3 Photogrammetric analysis 116
6.4 Modelling of future hydro-geomorphic changes of the Salza River 122
6.4.1 Granulometric analysis 122
6.4.2 Modelling 128
7. Discussion 143
7.1 Reconstruction of past hydro-geomorphic changes of the Salza River 143
7.2 Mapping of in and out-of-channel geomorphic units 146
7.3 Monitoring of the erosion hotspot 154
7.4 Modelling of future hydro-geomorphic changes of the Salza River 160
7.5 Research questions and hypotheses 168
8. Conclusion 174
9. Outlook and Perspectives 176
10. Bibliography 177
11. Appendix 183

List of figures

Figure 1: Cause and effect of the removal of riparian vegetation. 3
Figure 2: Location of the Salza River study area (red line) in Austria in relation to its overriding larger rivers (adapted Basemap: basemap.at [1]) 4
Figure 3: Location of the Salza River study area (red line) on the Salza River (adapted Basemap: basemap.at [1]). 4
Figure 4: Closeup of the Salza River study area (red line) (adapted Basemap: basemap.at [1]). 5
Figure 5: Hourly mean discharge data of the gauging station Gusswerk from 01.01.1976 to 31.12.2018. 6
Figure 6: On the left: orthophoto (2011 - 2013) of the hotspot before the flooding event (SteiermarkGIS [4]). On the right: orthophoto (2013 - 2015) of the hotspot after the flooding event (SteiermarkGIS [4]) 7
Figure 7: Mapping methods for in and out of channel river features. 9
Figure 8: Appropriate time scales for techniques to measure bank erosion and stream migration (LAWLER 1992: 784). 11
Figure 9: Installed devices to monitor bank stability (HABERSACK et al. 2012: 414). 13
Figure 10: Schematic view of different model types for simulating river systems. (a) Landscape evolution; (b) reach-scale cellular automaton; (c) reach-scale CFD; (d) alluvial stratigraphy; (e) meandering. (Adapted from Van De Wiel et al.). (COULTHARD et al. 2012: 2125) 14
Figure 11: Schematic drawing of the sinuosity index as described by SCHUMM 1963. 19
Figure 12: Base map for mapping the Salza River study area. 22
Figure 13: Annotated base map for mapping the Salza River study area. 22
Figure 14: Flow chart of identifying a fluvial margin (WHEATON 2015: 274). 23
Figure 15: Flow chart of identifying a structural element (WHEATON 2015: 277). 24
Figure 16: Flow chart of identifying a geomorphic unit (WHEATON 2015: 280) 25
Figure 17: A column of erosion pins marked in red (Lawler 1992: 803). 27
Figure 18: Bank erosion hotpot at river km 58.7 - 58.8 of the Salza River study area. 27
Figure 19: Set up of erosion pins version 1 at the erosion hotpot at river km 58.7 - 58.8 of the Salza River study area. 28
Figure 20: Measurement of erosion pins version 1 at the erosion hotpot at river km 58.7 - 58.8 of the Salza River study area. 28
Figure 21: Instalment of erosion pins version 1 at the erosion hotpot at river km 58.7 - 58.8 of the Salza River study area. 29
Figure 22: Set up of erosion pins version 2 at the erosion hotpot at river km 58.7 - 58.8 of the Salza River study area. 30

Figure 23: Close up of the setup of erosion pins version 2 at the erosion hotpot at river km 58.7 - 58.8 of the Salza River study area. 30
Figure 24: Measurement of erosion pins version 2 at the erosion hotpot at river km 58.7 - 58.8 of the Salza River study area. 31
Figure 25: Capturing scenarios for a photogrammetric analysis (AGISOFT METASHAPE: 6). 32
Figure 26: Camera position and capturing direction at the erosion hotspot of the Salza River study area. 33
Figure 27: Tripod positioning for image capturing of the erosion hotspot of the Salza River study area. 33
Figure 28: Before and after images of mowed grass of the collapsed bank at the erosion hotspot of the Salza River study area. Top images, orographic lowest location at the erosion hotspot facing upstream. Bottom images, middle location at the erosion hotspot facing upstream. 34
Figure 29: Main steps of image processing with Agisoft Metashape, Adapted (AGISOFT METASHAPE: 12) 35
Figure 30: Before (left) and after (right) image of an applied mask via Agisoft Metashape. 36
Figure 31: Align photos window (left) and Optimize camera alignment window (right) in Agisoft Metashape 36
Figure 32: Build dense cloud window in Agisoft Metashape. 37
Figure 33: Compiled sparse cloud after the “Align Photos” step (left) and compiled dense cloud after the “Build Dense Cloud” step (right) in Agisoft Metashape. 37
Figure 34: Open Ascii File window in Cloud Compare. 38
Figure 35: Cloud registration tool in Cloud Compare. 38
Figure 36: Before and after the automatic cloud registration tool in Cloud Compare. 39
Figure 37: M3C2 distance plugin window in Cloud Compare 39
Figure 38: 2.5D Volume calculation in Cloud Compare. 40
Figure 39: Set up of a Line-count-analysis in the study area of the Salza River between river km 60.1 and 60.2 43
Figure 40: B-axis of a stone on the left (FEHR 1987: 1105) and b-axis measurement of stones on the right in the field. 44
Figure 41: FEHR’S form to notate and analyse a Line-count-analysis in the field (FEHR 1987: 1107). 44
Figure 42: Before and after image of a Line-count-analysis in the Salza River study area. 45
Figure 43: Assessment of which Fuller curve best fits with the mean Line-count-analysis of the Salza River study area. 46
Figure 44: FEHR'S Form to translate a Line-count-analysis of the top layer into a Volume weighted analysis of the lower grain sizes and estimate of fine sediment via Fuller (FEHR 1987: 1108). 46

Figure 45: Lowering of bottle into the river for suspended sediment collection between river km 61.9 and 62 (left) and two 1.5l bottles filled with suspended sediments in the Salza River study area (right). 47
Figure 46: Deposited suspended solids (left), drained suspended solids (middle) and dried suspended solids (right). 47
Figure 47: Save Raster Layer as... window in QGIS to reduce the DEM resolution, see red box. 49
Figure 48: Raster calculator window in QGIS to decrease the DEM height by 10m, see red box..... 50
Figure 49: Rasterize window in QGIS (left), Merge window in QGIS (right)..... 50
Figure 50: Merging of the DEM -10m altitude file (top left) with the confining margin line shapefile (top right) to create the final Bedrock data file (bottom) used in the modelling of the Salza River study area. Map excerpt located between river km 54.1 and 58.2. 51
Figure 51: Original max discharge 1976 - 2018 of the Salza River study area. 52
Figure 52: Max discharge scenarios used for the modelling of the Salza River study area. 53
Figure 53: Open sediment tab in CAESAR-Lisflood. 55
Figure 54: Discharge input location (left) and Cell Properties window (right) in CAESAR-Lisflood. 56
Figure 55: Final window when starting a CAESAR-Lisflood modelling. 57
Figure 56: Map excerpt of the Salza River study area, taken from the Vischer map 1678. Source: https://upload.wikimedia.org/wikipedia/commons/0/0b/Steiermark_Vischer_1678.jpg 58
Figure 57: Map excerpt of the Salza River study area, taken from the Josephinische Land survey 1784 - 1785. Source: Mapire [7]. 59
Figure 58: Map excerpt of the Salza River study area, taken from the Franziszeische Land survey 1809 - 1818. Source: Mapire [7]. 60
Figure 59: Map excerpt of the Salza River study area, taken from the Franziszeische cadastre 1817 - 1861. Source: Mapire [7]..... 61
Figure 60: Map excerpt of the Salza River study area, taken from the updated Franziszeische Land survey 1821 - 1836. Source: Mapire [7]..... 62
Figure 61: Map excerpt of the Salza River study area, taken from the Francisco-Josephinische Land survey 1869 - 1887, with changes marked in red. Source: Mapire [7]..... 63
Figure 62: Visual changes A and B in the Franziszeische Land survey 1821 - 1836 (left) and Francisco-Josephinische Land survey 1869 - 1887 (right)..... 64
Figure 63: Visual changes C of the hotspot in the Franziszeische Land survey 1821 - 1836 (left) and Francisco-Josephinische Land survey 1869 - 1887 (right)..... 64
Figure 64: orthophoto of the Salza River study area taken on 02.09.2004. Source: GIS-Styria, with changes marked in red. 65
Figure 65: Visual changes A, B and C in the Francisco-Josephinische Land survey 1869 - 1887 (left) and the 2004 orthophoto (right)..... 66

Figure 66: Visual changes D in the Francisco-Josephinische Land survey 1869 - 1887 (left) and the 2004 orthophoto (right). 66
Figure 67: Visual changes E in the Francisco-Josephinische Land survey 1869 - 1887 (left) and the 2004 orthophoto (right). 66
Figure 68: Visual changes F in the Francisco-Josephinische Land survey 1869 - 1887 (left) and the 2004 orthophoto (right). 67
Figure 69: Visual changes G in the Francisco-Josephinische Land survey 1869 - 1887 (left) and the 2004 orthophoto (right). 67
Figure 70: orthophoto of the Salza River study area taken on 27.07.2009. Source: GIS-Styria, with changes marked in red. 68
Figure 71: Visual changes A in the 2004 orthophoto (left) and the 2009 orthophoto (right). 68
Figure 72: Visual changes B in the 2004 orthophoto (left) and the 2009 orthophoto (right). 69
Figure 73: Visual changes C in the 2004 orthophoto (left) and the 2009 orthophoto (right). 69
Figure 74: Visual changes D and E in the 2004 orthophoto (left) and the 2009 orthophoto (right). 69
Figure 75: Visual changes F in the 2004 orthophoto (left) and the 2009 orthophoto (right). 70
Figure 76: orthophoto of the Salza River study area taken on 30.05.2011. Source: GIS-Styria, with changes marked in red. 71
Figure 77: Visual changes A in the 2009 orthophoto (left) and the 2011 orthophoto (right). 72
Figure 78: Visual changes B and C in the 2009 orthophoto (left) and the 2011 orthophoto (right). 72
Figure 79: Visual changes D in the 2009 orthophoto (left) and the 2011 orthophoto (right). 72
Figure 80: Visual changes E in the 2009 orthophoto (left) and the 2011 orthophoto (right). 73
Figure 81: orthophoto of the Salza River study area taken on 10.06.2014. Source: GIS-Styria, with changes marked in red. 74
Figure 82: Visual changes A in the 2011 orthophoto (left) and the 2014 orthophoto (right). 74
Figure 83: Visual changes B and C in the 2011 orthophoto (left) and the 2014 orthophoto (right). 75
Figure 84: Visual changes D in the 2011 orthophoto (left) and the 2014 orthophoto (right). 75
Figure 85: Visual changes E in the 2011 orthophoto (left) and the 2014 orthophoto (right). 76
Figure 86: orthophoto of the Salza River study area taken on 08.09.2017. Source: GIS-Styria, with changes marked in red. 77
Figure 87: Visual changes A in the 2014 orthophoto (left) and the 2017 orthophoto (right). 78
Figure 88: Additional visual changes A in the 2014 orthophoto (left) and the 2017 orthophoto (right). 78
Figure 89: Visual changes B in the 2014 orthophoto (left) and the 2017 orthophoto (right). 78
Figure 90: Visual changes C in the 2014 orthophoto (left) and the 2017 orthophoto (right). 79
Figure 91: Visual changes D in the 2014 orthophoto (left) and the 2017 orthophoto (right). 79
Figure 92: Visual changes E in the 2014 orthophoto (left) and the 2017 orthophoto (right). 80

Figure 93: Visual changes F in the 2014 orthophoto (left) and the 2017 orthophoto (right). 80
Figure 94: Visual changes G in the 2014 orthophoto (left) and the 2017 orthophoto (right)..... 81
Figure 95: Visual changes H in the 2014 orthophoto (left) and the 2017 orthophoto (right)..... 81
Figure 96: Overlapping the thalwegs of the three historic maps of the Salza River study area. 84
Figure 97: Overlapping the thalwegs of the most recent historic map with the oldest orthophoto of the Salza River study area. 86
Figure 98: Overlapping the thalwegs of the orthophotos of the Salza River study area. 87
Figure 99: Overlapping the thalwegs of the orthophotos of the erosion hotspot in the Salza River study area. 89
Figure 100: Changes of the erosion hotspot in all orthophotos of the Salza River study area. 90
Figure 101: Mapped fluvial margins for the whole Salza River study area. 92
Figure 102: Bar chart visualizing the results from Table 17 of the length of river and confining margin of the Salza River study area. 93
Figure 103: Top: Mapped fluvial margins of the upper unconfined Salza River, Middle: Mapped fluvial margins of the lower unconfined Salza River and Bottom: Mapped fluvial margins of the confined Salza River. 95
Figure 104: Mapped Tier 2 geomorphic units for the whole Salza River study area. 96
Figure 105: Mapped Tier 2 geomorphic units for the Salza River between river km 59.5 and 62.85. . 98
Figure 106: Mapped Tier 2 geomorphic units for the Salza River between river km 56 and 59. 99
Figure 107: Mapped Tier 2 geomorphic units for the Salza River between river km 54.1 and 55.6. . 100
Figure 108: Area coverage of Tier 2 geomorphic units in the total, confined and unconfined Salza River study area. 101
Figure 109: Mapped Tier 3 geomorphic units for the whole Salza River study area. 103
Figure 110: Mapped Tier 3 geomorphic units for the Salza River between river km 60 and 62.85. .. 105
Figure 111: Mapped Tier 3 geomorphic units for the Salza River between river km 56 and 59. 106
Figure 112: Mapped Tier 3 geomorphic units for the Salza River between river km 54.1 and 55.6. . 107
Figure 113: Area coverage of Tier 3 geomorphic units in the total, confined and unconfined Salza River study area. 110
Figure 114: ÖBf mapping extent of all shapefiles for the Salza River study area. 111
Figure 115: ÖBf mapping extent of all polygon and point shapefiles for the Salza River study area. 112
Figure 116: Set up of erosion pin method 1 at the erosion hotspot in the Salza River study area. 113
Figure 117: Extracted erosion pins at the erosion hotspot..... 114
Figure 118: View of the erosion hotspot after the erosion pin extraction in the Salza River study area. 115
Figure 119: Set up of erosion pin method 2 at the erosion hotspot in the Salza River study area. 115
Figure 120: Comparison of any 2D changes (in metres) from cloud #1 to cloud #2. 117

Figure 121: Comparison of any 2D changes (in metres) from cloud #2 to cloud #3. 118
Figure 122: Comparison of any 2D changes (in metres) from cloud #3 to cloud #4. 118
Figure 123: Comparison of any 2D changes (in metres) from cloud #4 to cloud #5. 119
Figure 124: Comparison of any 2D changes (in metres) from cloud #1 to cloud #5. 119
Figure 125: 2.5D cloud comparison of clouds #1, #2, #3, #4 and #5 of the erosion hotspot. 120
Figure 126: 2.5D cloud comparison of cloud #5 with #1 of the erosion hotspot. 121
Figure 127: Location of line count analyses and suspended sediment pickup in the Salza River study area. 122
Figure 128: Close up of the four completed line-count analyses in the Salza River study area. 123
Figure 129: Computed results of the four line-count analyses of the Salza River study area with a mean of all four. 124
Figure 130: Mean line count analysis with the picked Fuller curve. 125
Figure 131: Approximated grain size distribution for the Salza River study area. 125
Figure 132: Condensed approximated grain size distribution for the Salza River study area. 126
Figure 133: Sediment parameters in CAESA-Lisflood. 128
Figure 134: Overlapping the thalweg of the 2011 DEM and pre-modelled 2018 DEM of the Salza River study area. 133
Figure 135: Overlapping the thalweg of the pre-modelled 2018 DEM as well as all four 2050 DEMs for the four different discharge scenarios of the Salza River study area. 134
Figure 136: Change in the cross sections of the four detected potential changes in the four modelled 2050 DEMs compared to the pre modelled 2018 DEM. 135
Figure 137: Elevation profile of thalwegs from the original 2011 DEM, the pre modelled 2018 DEM and the 2050 DEMs for all four discharge scenarios. 136
Figure 138: Max discharge scenarios used for the modelling of the Salza River study area. 137
Figure 139: Erosion and accumulation volumes for the discharge scenario 1 for the timeframe 2019 - 2050. 138
Figure 140: Erosion and accumulation volumes for the discharge scenario 2 for the timeframe 2019 - 2050. 139
Figure 141: Erosion and accumulation volumes for the discharge scenario 3 for the timeframe 2019 - 2050. 140
Figure 142: Erosion and accumulation volumes for the discharge scenario 4 for the timeframe 2019 - 2050. 140
Figure 143: Total erosion and accumulation volumes for all four discharge scenarios for the timeframe 2019 - 2050 141
Figure 144: D50 grainsizes for the four different discharge scenarios for the timeframe 2019 - 2050. 142

Figure 145: Linear trendlines for the D50 grainsizes for the four different discharge scenarios for the timeframe 2019 - 2050. 142
Figure 146: Contrasting assemblages of tiers 2 and 3 in-channel geomorphic units across the three example sites (WHEATON et al. 2015: 291)..... 150
Figure 147: Area coverage of Tier 2 geomorphic units in the total, confined and unconfined Salza River study area..... 151
Figure 148: Left: 2017 orthophoto of compound bar between river 58.7 - 58.8, Right: Compound point bar with bar platform, ridges and chute channel (BRIERLEY et al. 2005: 97). 152
Figure 149: Area coverage of Tier 3 geomorphic units in the total, confined and unconfined Salza River study area..... 153
Figure 150: Slumped bank material (HOOKE 1979: 54)..... 154
Figure 151: Bank morphology and coded targets as Ground Control Points (KOEHL et al. 2020: 65), edited. 158
Figure 152: Schematic bank erosion phases (DURÓ et al. 2018: 935). 158
Figure 153: Computed results of the four line-count analyses of the Salza River study area with a mean of all four. 161
Figure 154: Overlapping the thalwegs of the pre-modelled 2018 DEM as well as all four 2050 DEMs for the four different discharge scenarios of the Salza River study area. 164
Figure 155: Total erosion and accumulation volumes for all four discharge scenarios for the timeframe 2019 - 2050..... 166
Figure 156: Linear trendlines for the D50 Grain size for the four different discharge scenarios for the timeframe 2019 - 2050. 167
Figure 157: Cause and effect of the removal of riparian vegetation. 173
Figure 158: Normal distribution of the 2D changes (in metres) from cloud #1 to cloud #2. 186
Figure 159: Normal distribution of the 2D changes (in metres) from cloud #2 to cloud #3. 187
Figure 160: Normal distribution of the 2D changes (in metres) from cloud #3 to cloud #4. 187
Figure 161: Normal distribution of the 2D changes (in metres) from cloud #4 to cloud #5. 188
Figure 162: Normal distribution of the 2D changes (in metres) from cloud #1 to cloud #5. 188

List of tables

Table 1: Available historical maps of the Salza River study area. 18
Table 2: Available orthophotos of the Salza River study area. 18
Table 3: Images taken throughout the field work of the Salza River study area. 20
Table 4: Available DEM of the Salza River study area. 21
Table 5: Photogrammetric image taking at the hotspot of the Salza River study area. 26
Table 6: Number of M3C2/Compute 2.5D Volume calculations in Cloud Compare of the created point clouds. 40
Table 7: Line-count-analysis of the riverbed of the Salza River study area. 41
Table 8: Suspended sediment samples taken of the Salza River study area. 41
Table 9: Available hourly discharge data of the gauging station Gusswerk of the Salza River study area. 42
Table 10: Available DEM of the Salza River study area. 42
Table 11: Statistical data for the original discharge 1976 - 2018 (left) and number of flooding events of HQ1, HQ5 and HQ10 for the adapted original discharge 1976 - 2018 (right). 52
Table 12: Statistical data for the four discharge scenarios for 2019 - 2050. 54
Table 13: Number of flooding events of HQ1, HQ5 and HQ10 for the four discharge scenarios for 2019 - 2050 54
Table 14: Changes in Riverbed displacement at the erosion hotspot in the Salza River study area. 89
Table 15: Number of mappings of the Salza River study area. 91
Table 16: Length of valley- and valley bottom margin and overlap in % of both of the Salza River study area 93
Table 17: Length of river margin and confining margin as well as overlap in % of both of the Salza River study area. 93
Table 18: Area coverage for the Tier 2 geomorphic units for the total, confined and unconfined Salza River study area. 101
Table 19: Length of river margin and riparian vegetation as well as overlap in % of the total, confined and unconfined Salza River study area. 102
Table 20: Total recorded in-stream structural elements of the total, confined and unconfined Salza River study area. 102
Table 21: Area coverage for the Tier 3 geomorphic units for the total, confined and unconfined Salza River study area. 109
Table 22: Erosion pin versions used at the hotspot of the Salza River study area. 113
Table 23: Measurements for the first erosion pin method on the 06.05.2017. 114
Table 24: Measurements for the second erosion pin method. 116
Table 25: Computed point clouds of the erosion hotspot in the Salza River study area. 116

Table 26: 2.5D volume changes and additional metrics of the computed point clouds of the erosion hotspot in the Salza River study area. 121
Table 27: Rock statistics for the compiled digitalized line-count analyses (LCA) of the Salza River study area..... 124
Table 28: Values for the approximated grain size distribution for the Salza River study area. 126
Table 29: Values for the condensed approximated grain size distribution for the Salza River study area. 127
Table 30: Results for the approximated suspended grain size distribution for the Salza River study area. 127
Table 31: Final Parameters used in CAEASR-Lisflood for the modelling of the Salza River study area. 130
Table 32: Year of change for the four main sections marked in Figure 135. 134
Table 33: Mean erosion and accumulation rate for the time frame 2019 - 2050 for all four discharge scenarios. 138
Table 34: Years with lower/higher erosion/accumulation rate than the 1_2050m mean erosion rate for all four discharge scenarios. 138
Table 35: Volume changes and additional metrics of the computed point clouds of the erosion hotspot in the Salza River study area. 160
Table 36: Year of change for the four main sections marked in Figure 135. 165
Table 37: Statistical data for the four discharge scenarios for 2019 - 2050. 167
Table 38: Measured distances (unconfined, confined and total) of the Salza River study area of the historic maps. 183
Table 39: Measured lengths (unconfined, confined and total) of the Salza River study area of the historic maps. 183
Table 40: Sinuosity index for the unconfined valley of the historic maps of the Salza River study area. 183
Table 41: Sinuosity index for the confined valley of the historic maps of the Salza River study area. 183
Table 42: Sinuosity index for the whole Salza River study area of the historic maps. 184
Table 43: Measured distances (unconfined, confined and total) of the Salza River study area of the orthophotos. 184
Table 44: Measured lengths (unconfined, confined and total) of the Salza River study area of the orthophotos. 184
Table 45: Sinuosity index for the unconfined valley of the orthophotos of the Salza River study area. 184
Table 46: Sinuosity index for the confined valley of the orthophotos of the Salza River study area. 185

Table 47: Sinuosity index for the whole Salza River study area of the orthophotos. 185
Table 48: Measured distance of the erosion hotspot of all orthophotos in the Salza River study area. 185
Table 49: Measured lengths of the erosion hotspot of all orthophotos in the Salza River study area. 185
Table 50: Sinuosity index for the erosion hotspot of all orthophotos in the Salza River study area... 186
Table 51: Measured distances (unconfined, confined and total) of the Salza River study area of initial DEM, pre-modelled year 2018 and modelled year 2050 for the five different discharge scenarios... 189
Table 52: Measured lengths (unconfined, confined and total) of the Salza River study area of initial DEM, pre-modelled year 2018 and modelled year 2050 for the five different discharge scenarios... 189
Table 53: Sinuosity index for the unconfined valley of the Salza River study area of initial DEM, pre-modelled year 2018 and modelled year 2050 for the five different discharge scenarios. 189
Table 54: Sinuosity index for the confined valley of the Salza River study area of initial DEM, pre-modelled year 2018 and modelled year 2050 for the five different discharge scenarios. 190
Table 55: Sinuosity index for the whole Salza River study area of initial DEM, pre-modelled year 2018 and modelled year 2050 for the five different discharge scenarios. 190

List of abbreviations

ALS	=	Airborne laser scanning
BMLRT	=	Bundesministerium für Landwirtschaft, Regionen und Tourismus
CFD	=	Computational fluid dynamics
D50	=	Median diameter at 50% of the particle size distribution
DEM	=	Digital elevation model
DoD	=	DEM of Difference
dp	=	Decimal places
EDM	=	Electronic distance measurement
ero/acc	=	Erosion and accumulation
GCP	=	Ground Control Points
GIS	=	Geographic information system
GPS	=	Global positioning system
HQ1,5,10	=	Values representing the probability of a 1-, 5- or 10-year flooding event
LCA	=	Line count analyses
LEM	=	Landscape evolution model
LiDAR	=	Light detection and radar
M3C2	=	Multiscale model-to-model cloud comparison
ÖBf	=	Österreichische Bundesforste
PEEP	=	Photoelectronic erosion pins
SfM	=	Structure from Motion
UAV	=	Unmanned aerial vehicle

Abstract

Fluvial geomorphology seeks to examine and comprehend how rivers form and evolve. Locating past, mapping and monitoring present as well as modelling future hydro-geomorphic changes within a river are the core elements of this study. The following master's thesis has attempted to study these elements in an 8.75 km reach of the Salza River near Gusswerk in Styria, Austria. Historic maps as well as modern orthophotos were analysed descriptively as well as numerically via using a sinuosity index to locate bank erosion hotspots between 2004 and 2017. Mapping the in and out-of-channel fluvial landforms of the study area using a framework developed by WHEATON et al. 2015 has shown, that the most common in-channel river shapes are in descending order transition zones, planar, concave and convex shapes. Monitoring the largest hotspot using erosion pins has shown a mean change of the whole bank of -1.63 cm from 15.06.2017 - 11.07.2017. Applying a photogrammetric analysis using a Gauss normal distribution to the same hotspot for the timeframe 06.05.2017 - 11.06.2018 has shown a mean change of roughly -2 m for the whole bank while a 2.5D volume change analysis for the same timeframe has shown an eroded volume of -319 m^3. Potential future changes with four different discharge scenarios using the software CAESAR-Lisflood has shown four potential hot areas for a lateral shift of 20 m to 130 m. The results obtained offer a very detailed insight into the past, present and future hydro-geomorphic changes of the study area and present a solid basis for further technical measures and studies.

Zusammenfassung (Abstract in German)

Die Fluvialgeomorphologie untersucht und versucht zu verstehen, wie sich Flüsse bilden und entwickeln. Dabei bilden die Lokalisierung vergangener, die Kartierung und das Monitoring aktueller sowie die Modellierung zukünftiger fluvial morphologischen Veränderungen die zentralen Elemente dieses Teilgebiets. Die folgende Masterarbeit hat versucht diese Elemente an einem 8,75 km langen Flussabschnittes des Salza Flusses im Raum Gusswerk, Österreich anzuwenden. Historische Karten sowie moderne Orthophotos wurden dabei deskriptiv sowie auch numerisch analysiert mithilfe der Verwendung des Sinuosität-Index, um Ufererosion Hotspots zwischen 2004 und 2017 zu verorten. Eine Kartierung der fluvialen Oberflächenformen innerhalb und außerhalb des Flusses unter Verwendung eines Rahmenkonzeptes entwickelt von WHEATON et al. 2015 zeigte, dass die häufigsten Flussformen im Fluss in absteigender Reihenfolge: Übergangs-, Ebene-, Konkave- und Konvexe Bereiche sind. Das Monitoring der größten Ufererosion mittels Erosion-Pins zeigte einen veränderten Mittelwert entlang des gesamten Ufers von -1,63 cm zwischen 15.06.2017 - 11.07.2017. Die Anwendung einer photogrammetrischen Analyse mittels einer Gauß Normalverteilung desselben Erosion Hotspots für den Zeitraum 06.05.2017 - 11.06.2018 zeigte eine mittlere Veränderung von etwa -2 m für das gesamte Ufer, während eine 2,5D Analyse der Volumenveränderung für den gleichen Zeitraum ein erodiertes Volumen von -319 m³ zeigte. Die potenziellen zukünftigen Veränderungen mittels vier verschiedenen Abflussszenarien unter der Verwendung der Software CAESAR-Lisflood zeigte, vier potenziell gefährdete Bereiche für eine laterale Verlagerung von 20 m bis 130 m. Die erlangten Ergebnisse zeigen einen sehr detaillierten Einblick in die Vergangenheit, Gegenwart und Zukunft aller fluvialgeomorphologischen Veränderungen im Untersuchungsgebiet und bieten eine solide Basis für weitere technische Maßnahmen und Forschung.

1. Introduction

The main idea and designated study area of the Salza River for the following master's thesis arose as part of a cooperation between the Austrian Federal Forests (Österreichische Bundesforste) under the supervision of DI Andreas Haas and Dr. Monika Kanzian and the Department of Geography and Regional Research (University of Vienna) under the supervision of Mag. Dr. Ronald E. Pöppl, BA. The detailed and final thesis concept has its focus on the hydro-geomorphic changes within the study area and is described in concise manner.

The study area, a roughly 9 km long and mainly meandering stretch of the Salza River (between river km 54.1 - 62.85) in the area of the town Gusswerk in Styria, Austria, was subject to several hydro-geomorphic changes in the past. One specific bank erosion hotspot was located after a flooding event in 2014 which initiated the demand to monitor the hotspot, as well as gave the stimulus for this master thesis.

The need to study this hotspot as well as other hydro-geomorphic changes in the study area and also river systems in Austria in general, can be seen by examining the scientific predictions regarding the effects of climate change on European rivers. Directly quoting a passage by (WETHERALD et al. 2002: ACL7-14) *"By the middle of the 21st century, runoff from many European rivers increases by more than 20%"*. Another study by (BLÖSCHL et al.2019: 2) found a 0-5% increase in the "*Change in mean annual flood discharge per decade"* from 1960 - 2010 for central and western Austria. Climate change could therefore accelerate hydro-geomorphic changes making their study even more relevant today.

The objective of this thesis is therefore to try and locate, map and quantify past and current hydro-geomorphic changes within the study area. Furthermore, to assess the potential future hydro-geomorphic changes in the study area, the geomorphological/landscape evolution model "CAESAR-Lisflood" developed by COULTHARD et al. 2013 will be used to model, estimate and quantify future scenarios for the years 2019 - 2050 using four different discharge scenarios.

2. Research questions and hypotheses

The central research question of this thesis reads as follows:
"Which hotspots of hydro-geomorphic changes exist within the river course of the Salza River (between river km 54.1 - 62.85) in the area of Gusswerk, Styria and what is the expected future development of the river course?"

My hypothesis regarding the central research question reads as follows:
I expect to find hotspots of hydro-geomorphic changes in the study area in the form of bank erosion in the river bends with more developed curvature especially in areas without riparian vegetation. Furthermore, I hypothesize, when modelling with a high discharge scenario for the years 2019 - 2050 that the selected hotspots will cut-off the river and alter its existing riverbed by the year 2050.

Besides the main question, there are several sub-questions.
These are the following:

a. *"How fast is the rate of bank erosion at the hotspots?"*
b. *"Which changes of the riverbed are to be expected?"*
c. *"How do cross sections of the riverbed alongside the hotspots change?"*
d. *"What impact do flood events have on the future river course development?"*
e. *"Which role does the riparian vegetation have on the bank stability?"*

My hypotheses regarding the sub-questions will be addressed in the same order and read as following:

a. The rate of bank erosion will mostly be affected by large flooding events, which will heavily incise into the banks. With a high discharge scenario, I predict bank erosion rates of around 1 m per year. In addition, an absence of heavy floods will reduce and mitigate the bank erosion rate.
b. The riverbed of the Salza River study area will alter laterally in areas with heavy bank erosion and possibly cut-off the existing river. Additionally, the riverbed will incise in areas of restricted lateral movement.

c. The cross sections of the majority of the riverbed will remain unchanged. However, in areas of increased bank erosion, the cross sections of the riverbed will widen.
d. Flood events of a high magnitude alter the river. I think that the max discharge will have the highest effect based on the erosion hotspot which occurred after a flooding event in 2014. A discharge scenario with only the discharge from the year 2014 will most likely cause the most impact on the river course.
e. The riparian vegetation is natures natural bank protection. Where there is a removal of riparian vegetation, for example after a large flooding event, there will be an increased bank erosion rate as shown in the graphic below.

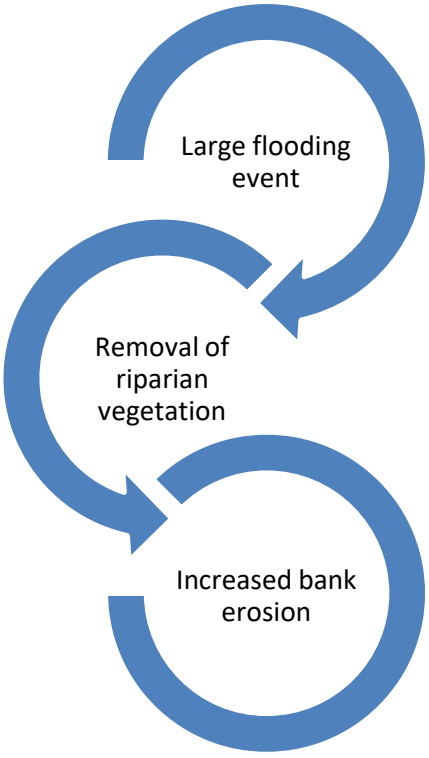


Figure 1: Cause and effect of the removal of riparian vegetation.

All research questions as well as stated hypotheses will be answered with the acquired results in chapter *7.5 Research questions and hypotheses*.

3. Study area

3.1 General

The study area (red line in Figure 2), lies along the Salza River (turquoise line in Figure 2), a mostly wild flowing alpine river in the Eastern Alps in Austria which mainly runs through the state of Styria. The Salza River is a tributary of the Enns River (light blue line in Figure 2) which itself debouches into the Danube River drainage basin, (dark blue line in Figure 2) and thus belongs to the second largest drainage basin in Europe. The green rectangle will be zoomed into in Figure 3.

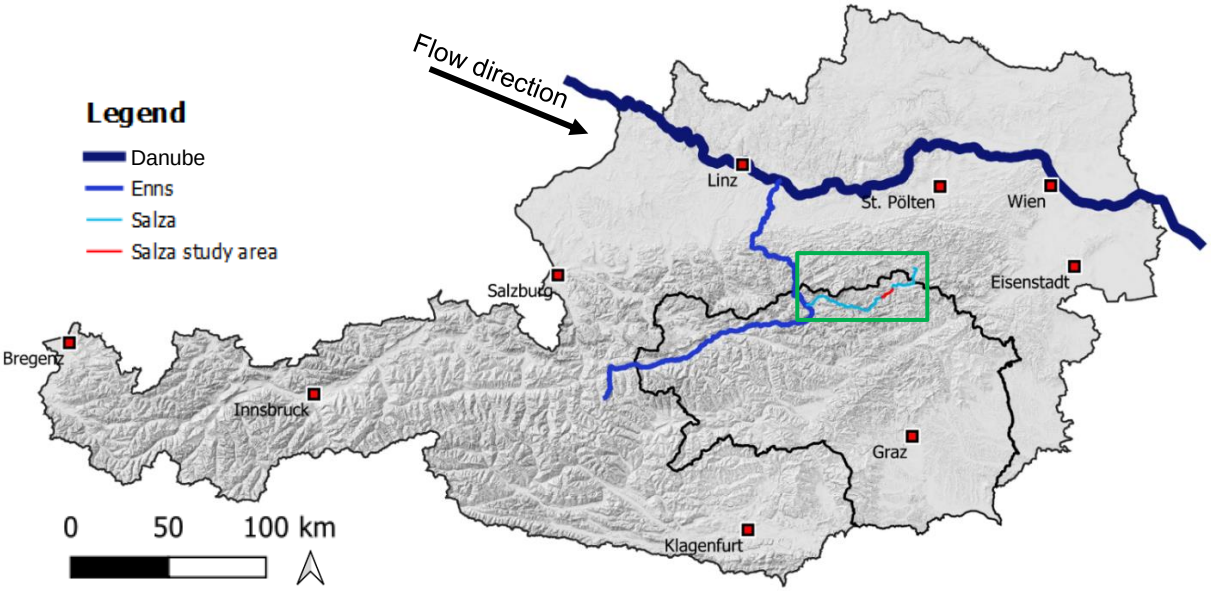


Figure 2: Location of the Salza River study area (red line) in Austria in relation to its overriding larger rivers (adapted Basemap: basemap.at [1]).

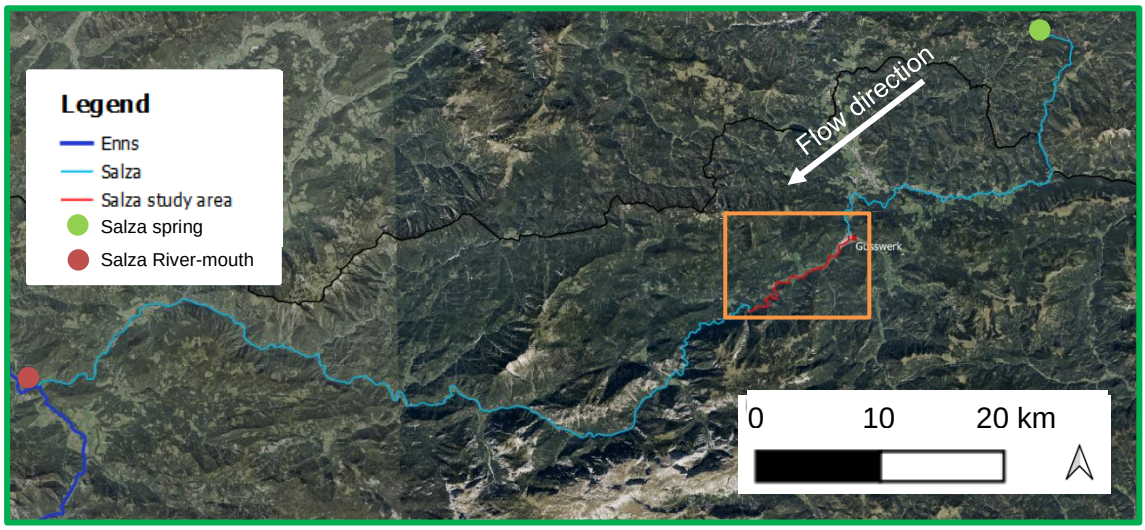


Figure 3: Location of the Salza River study area (red line) on the Salza River (adapted Basemap: basemap.at [1]).

The Salza River's spring is located in Lower Austria near Ulreichsberg at around 1137 m above sea level (green dot in Figure 3, Coordinate Location : 47.83679, 15.44471 [2]) and has its river-mouth in Styria at Großreifling at an altitude of around 464 m where it flows into the Enns River (red dot in Figure 3, Coordinate location : 47.67071, 14.72738 [2]). In total the Salza River has a watershed of 868.30 km² (BMLRT 2011: 39), stretches over 90 km (own calculation in QGIS) through mountainous landscape whilst having an elevation difference of around 673 m. The orange rectangle containing the Salza River study area will be zoomed into in Figure 4.

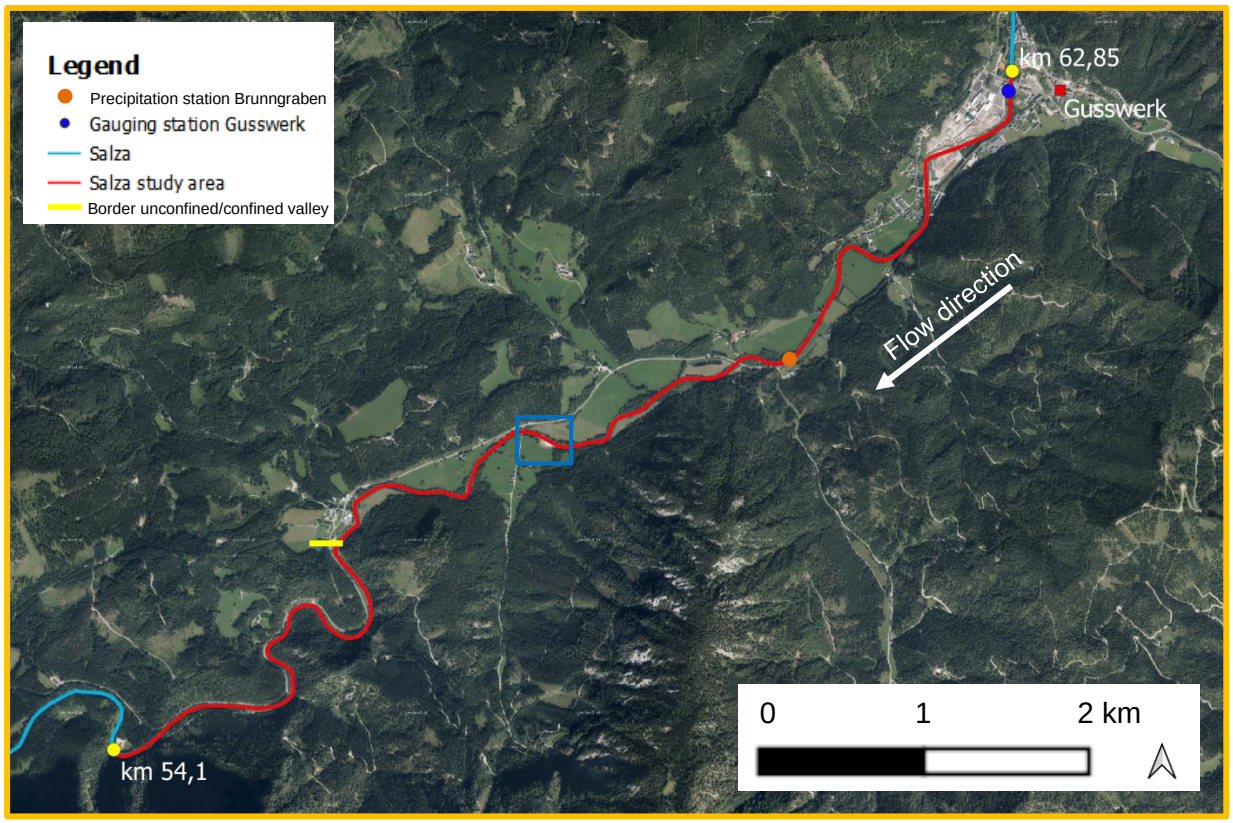


Figure 4: Closeup of the Salza River study area (red line) (adapted Basemap: basemap.at [1]).

Figure 4 shows an overview of the Salza River study area (red line). It reaches from the top right yellow point at river km 62.85 with an altitude of 736 m [2], near the town of Gusswerk, to the bottom left yellow point at river km 54.1 with an altitude of 712 m [2]. This reach of the Salza River study area is exactly 8.75 km long with an elevation difference of around 24 m [2].

From the orthophoto we can deduct that the river flows in a largely unconfined valley bed which turns into a confined bed further downstream at around the location of the yellow marking, see in Figure 4. The changeover, positioned at the river km 57, separates the two

segments of the river into a longer unconfined 5.85 km reach and a shorter confined 2.9 km reach, which will be used in the thesis to contrast the results for the two segments.

The gauging station Gusswerk (blue dot in Figure 4), on which all hydrological discharge data will be based on for the modelling, lies at river km 62.75 at an altitude of 735.5 m. It measures a watershed of 280 km² and has an average annual discharge of 7.29 m³/s [3]. The station records the water level since 01.01.1961 and discharge data since 01.01.1965 [3]. However hourly discharge data, which is needed for the modelling, is only available from 01.01.1976 onwards. In Figure 5 we see the discharge curve for the Gusswerk gauging station showing the hourly mean discharge from 01.01.1976 - 31.12.2018. The HQ1, HQ 5 and HQ10, which are the values representing the probability of a 1-, 5- or 10-year flooding event for the gauging station, are 50 m³/s, 100 m³/s and 126 m³/s and are marked in the Figure below. The peak discharge ever recorded was 284 m³/s on the 08.07.1997 and the lowest discharge recorded was 0.15 m³/s on 21.02.1978.

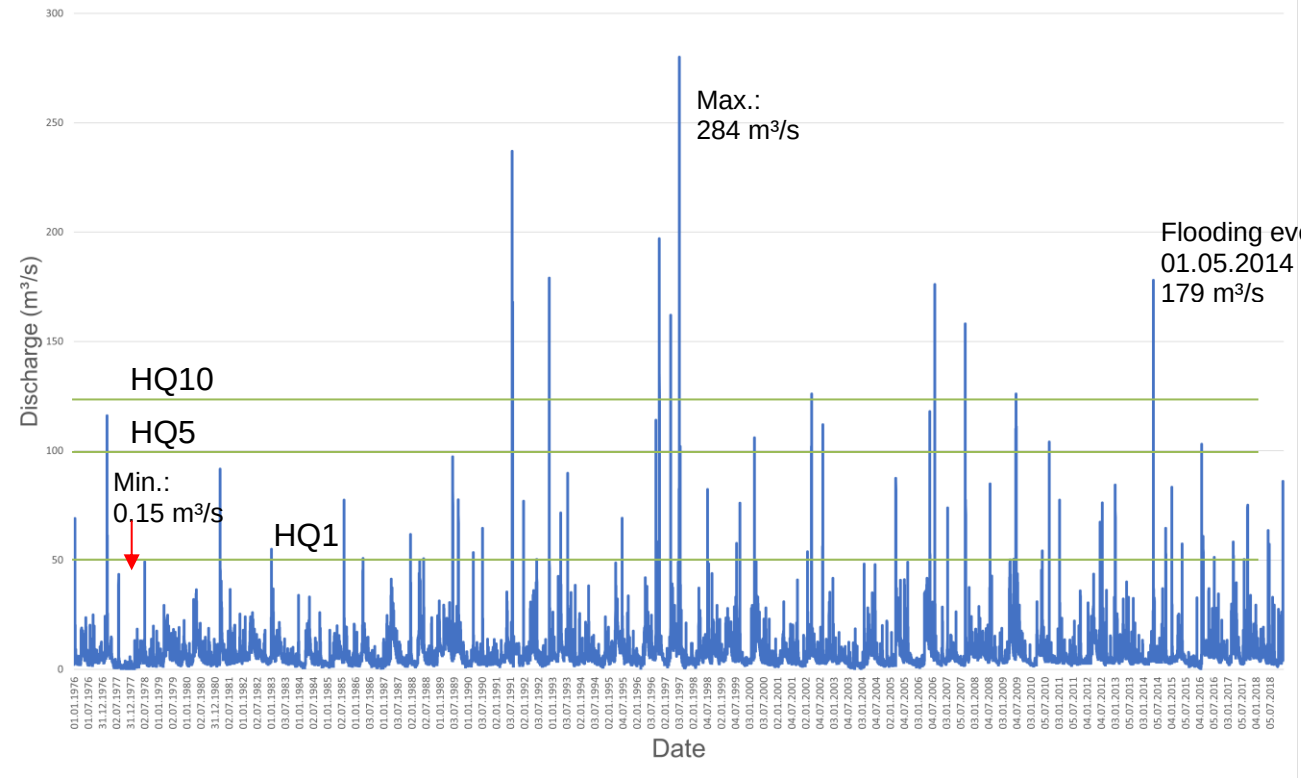


Figure 5: Hourly mean discharge data of the gauging station Gusswerk from 01.01.1976 to 31.12.2018.

In addition, there is a precipitation station (orange dot in Figure 4) within the study area which lies at an altitude of 710 m at Brunngraben, recording rainfall data since 01.01.1945 with a mean annual precipitation of 1333.9 mm (WAKONIGG 2010: 66). The blue rectangle in Figure 4 will be zoomed into in Figure 6.

3.2 Hot spot between river km 58.7 - 58.8

As mentioned in the introduction, the basis for the following thesis was a prominent bank erosion which occurred after a major flooding event on the 01.05.2014. It had a recorded peak discharge of 179 m^3/s being the 4^{th} largest discharge event recorded since 1965, see Figure 5. The before and after orthophotos of the erosion hotspot can be seen below in Figure 6. On the left showing the hotspot before and on the right after the flooding event with the resulting bank erosion. As seen on the images the riparian vegetation at the hotspot on the left bank is gone in the right image and the river has noticeably changed its course and threatens to erode more bank material. Furthermore, a large compound bar has formed on the opposite side of the bank.

The monitoring of this hotspot will indicate whether further movement of the bank exists throughout the field work. In addition, during the modelling of the study area for the timeframe 2019 - 2050, it will be interesting to find out how unstable or stable this site is.



Figure 6: On the left: orthophoto (2011 - 2013) of the hotspot before the flooding event (SteiermarkGIS [4]). On the right: orthophoto (2013 - 2015) of the hotspot after the flooding event (SteiermarkGIS [4]).

4. State-of-the-art of hydro-geomorphic changes

Since the beginning of time rivers have been affected by hydro-geomorphic changes in various forms. Only with the onset of humankind, settling on easily accessible river floodplains and terraces, have the hydro-geomorphic changes become a risk. Since then, humans have aspired to tame the rivers in various sorts to use them without being negatively affected by their hydro-geomorphic changes.

In recent times the threat of hydro-geomorphic changes on humans has gained importance due to a detectable increase in the globally averaged, annual mean surface temperature anomaly between 1850 from 0°C and 2020 to 0.8°C which goes hand in hand with an increase in precipitation and river discharge in some areas (WETHERALD et al. 2002: ACL7-6). Following the trend *"by the middle of the 21st century, runoff from many European rivers increases by more than 20%"* (WETHERALD et al. 2002: ACL7-14). The Danube in particular, showed a change of +20.7% in a simulated runoff by 2050 (WETHERALD et al. 2002: ACL7-9). Another study by (BLÖSCHL et al.2019: 2) observed regional trends of river flood discharges in Europe (1960–2010) in Figure 1 in the article and found a 0-5% increase in the "*Change in mean annual flood discharge per decade"* for central and western Austria, in which the study area of the Salza River is located.

The importance to reconstruct past hydro-geomorphic changes, map and monitor present, as well as model possible future scenarios for hydro-geomorphic changes has therefore never been greater. The following four subchapters give an insight into current state-of-the-art methods available.

4.1 Reconstruction of past hydro-geomorphic changes using historic maps and orthophotos

When trying to reconstruct past hydro-geomorphic changes the only viable option is via remote sensing. Historic maps offer the only source for evaluating historic changes of a river and depending on their mapping accuracy, they can be georeferenced for further analysis. Whereas more recent changes in hydro-geomorphic features are best found through modern georeferenced orthophotos which are ideally in colour. The state-of-the-art is hereby confined to the available database and both historic maps as well as orthophotos were used in this thesis. The techniques used to reconstruct changes in the available historic maps and

orthophotos were either in a descriptive analysis such as implemented by ZLINSZKY et al. 2013 and FUCHS et al. 2015 or via a numerical analysis with the use of a sinuosity index used by KALANTAR et al. 2020 as well as in the following selected state-of-the-art articles: (GARCÍA et al. 2019), (KAR et al. 2020) and (MOMIN et al. 2020).

4.2 Mapping of in and out-of-channel river features

The first question to answer before planning a mapping is, at what scale does one want to map? In field mapping provides the greatest detail at the current state of the art when it comes to assessing in-channel river features within the river margin. However, if only out-of-channel river features, besides the river margin want to be assessed then off-site mapping via remote sensing provides sufficient detail, see Figure 7. However, in field mapping can provide further detail for out-of-channel mapping. Combining the best of both worlds, using in field and off-site mapping together provides the best overall result.

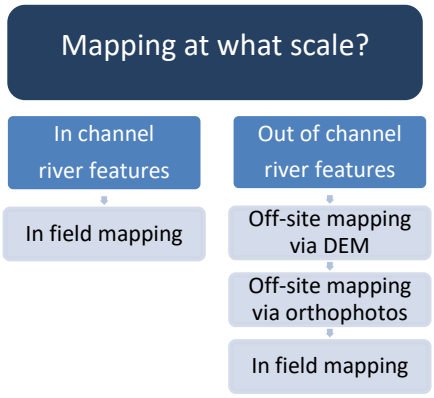


Figure 7: Mapping methods for in and out of channel river features.

While the only restriction when mapping in field is the Mapper himself, when mapping off-site via remote sensing, the Mapper is dependent on the current state-of-the-art remote sensing data available as well as its resolution. Currently there are 2 main categories of remote sensing data available for mapping purposes. On the one side, there are DEMs (digital elevation models) which *"are a gridded digital representation of terrain, with each pixel value corresponding to a height above a datum"* (HAWKER et al. 2018: 1). These are obtained via ALS (airborne laser scanning) through an aircraft or more recently also through an unmanned aerial vehicle (UAV). And on the other side are orthophotos, which are georeferenced images and "*are characterized by having a uniform scale and showing objects in their true geographical locations."* (HABIB 2007: 25). These are obtained via satellite images or aerial images through aircrafts or more recently also through unmanned aerial vehicles as well. The available resolution for both DEMs and orthophotos nowadays is often at or below 1m x 1m, however *"Imagery collected from a UAV typically has a resolution in the order of a few centimetres"* (PULITI et al. 2019: 1).

After deciding on the mapping extent, next a method to map the hydro-geomorphic features must be chosen. While there have been several books describing different fluvial features in the past, they lacked a structured mapping framework. There have been frameworks available mapping the main in stream river features such as *riffles, runs, pools and glides* as described as of page 155 in HARMAN et al. 2012 but which overall lacked in hydro-geomorphic detail.

Using existing fluvial landforms, Gary Brierley and Kirstie Fryirs have developed and extended an unprecedented river mapping framework called River Styles framework accessible via https://riverstyles.com/ (last opened: on 02.11.2021). *"Applications of the River Styles framework generate a coherent package of geomorphic information, providing a physical template for river rehabilitation activities."* (BRIERLY et al. 2005: Back cover). Based on BRIERLEY and FRYIRS books *Geomorphology and River Management* from 2005 and *Geomorphic Analysis of River Systems* from 2015, WHEATON et al. in corporation with BRIERLEY and FRYIRS published the paper *Geomorphic mapping and taxonomy of fluvial landforms*, using the framework which *"provides a rigorous and repeatable approach to identification of topographically defined features of riverscapes"* (WHEATON et al. 2015: 1). WHEATON'S et al. described unique and complete framework is therefore the current state-of-the-art for mapping in and out of stream hydro-geomorphic units and was thus used in this thesis while in field and off-site mapping.

4.3 Monitoring present hydro-geomorphic river changes

Monitoring hydro-geomorphic changes over a period of time, provides information to the current rate of change and gives insight on the possible future rate. Specific areas within a river, which are especially prone to changes, are riverbanks. *"Riverbanks are transitional boundaries, or ecotones, between the aquatic and terrestrial ecosystems, and they frequently change under naturally dynamic hydrologic conditions. "* (FLORSHEIM et al. 2008: 519).

Considering the possible increase in river discharge over time as stated in (WETHERALD et al. 2002) and (BLÖSCHL et al. 2019), we can assume that an increase in riverbank erosion will follow. Monitoring existing areas of bank erosion are therefore gaining importance. The significance of monitoring rivers has such a current scientific actuality that the institute for hydraulic engineering and stream research (Institut für Wasserbau, Hydraulik und Fließgewässerforschung (IWA)) at the University of Natural Resources and Life Sciences

Vienna has an ongoing lecture called *"Monitoring in river engineering"* hosted by Marcel G. Liedermann, Mario Klösch, Marlene Haimann and Helmut Habersack, which I have attended in 2016. Below the noteworthy bank erosion related state-of-the-art monitoring methods are presented in a concise manner.

Before deciding on what to monitor, the appropriate time scale for techniques to measure bank erosion must be selected. When measuring bank erosion there are three main appropriate timescales as described by LAWLER 1992 in Figure 8. Long timescale methods such as sedimentological evidence, botanical evidence or historical evidence have a timescale of interest anywhere from 10 to 20.000 years with a resolution of 1 to 100 years. Intermediate timescale methods such as planimetric resurvey and repeated cross profiling have a timescale of interest anywhere from 1 to 50 years with a resolution of 0.08 to 1.3 years. Lastly short timescale methods such as terrestrial photogrammetry, erosion pins or so-called photoelectronic erosion pins, in short PEEP (LAWLER 1992: 797), have a timescale of interest anywhere from 0.5 to 10 years with a resolution of 0.0001 to 0.8 years.

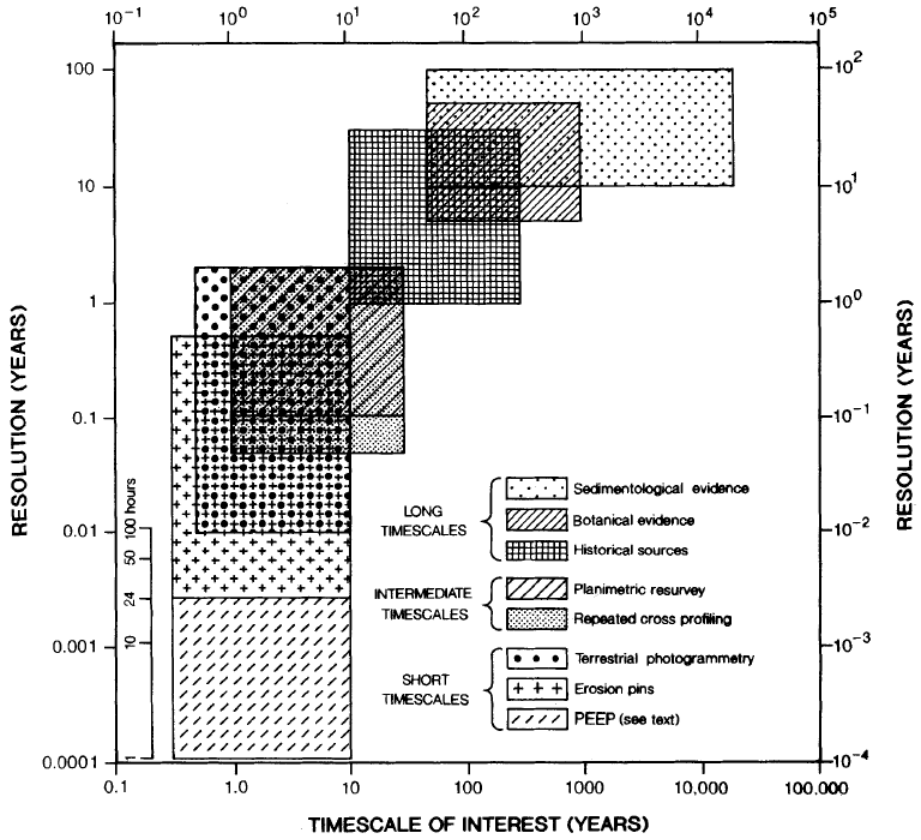


Figure 8: Appropriate time scales for techniques to measure bank erosion and stream migration (LAWLER 1992: 784).

The following monitoring techniques described, fall into the short to intermediate timescale techniques as this timescale falls into the study timeframe available for this thesis and has the most state-of-the-art methods. Besides the already familiar remote sensing via the use of orthophotos and ALS, there is also green LiDAR (light detection and ranging) obtained through aircrafts or more recently also through unmanned aerial vehicles. The green light can penetrate the water surface and record the riverbed.

Another remote sensing monitoring method can be applied by analysing the changes in low water discharge of the gauging stations over time, to see changes in the elevation of the riverbed. The cross sections of the riverbed can be analysed further using a Sonar/GPS probe attached to a boat for larger rivers. The boat is driven or pulled across a river whilst recording the location of the boat, the depth of the riverbed and the time, from which a riverbed cross section can be computed. For smaller rivers, the river profile can be measured through a simple tape and measuring rod.

When wanting to monitor larger bank erosion sites one has the option of measuring only distances via a EDM device (electronic distance measurement) measuring from the base station to the point, described in (LAWLER 1992: 792-796) or through the use of a tacheometer positioned opposite of a bank erosion to also monitor the height.

Monitoring erosion rates of planar gravel banks can be done by applying simple colour markings on the gravel bar and recording when the coloured gravel has been transported downstream. For the monitoring of scours, the insertion of a scour chain can deliver worthwhile information on changes, described in LARONNE et al. 1994.

There are three main methods suitable for the monitoring of volumetric changes, which can also be used in conjunction with each other to provide more thorough data. Erosion pins, described in (LAWLER 1992: 803), provide a simple method to analyse changes in the bank over time. Using terrestrial photogrammetry from captured images or using a terrestrial laser scanner can provide further insight on volumetric bank erosion changes.

A more complex but optimal setup to monitor bank stability was used by HABERSACK et al. 2012. The bank was fitted with Matrix sensors, tensiometers, an ombrometer and a

groundwater pressure probe while simultaneously monitoring the river level and capturing all visual changes through a time lapse camera.

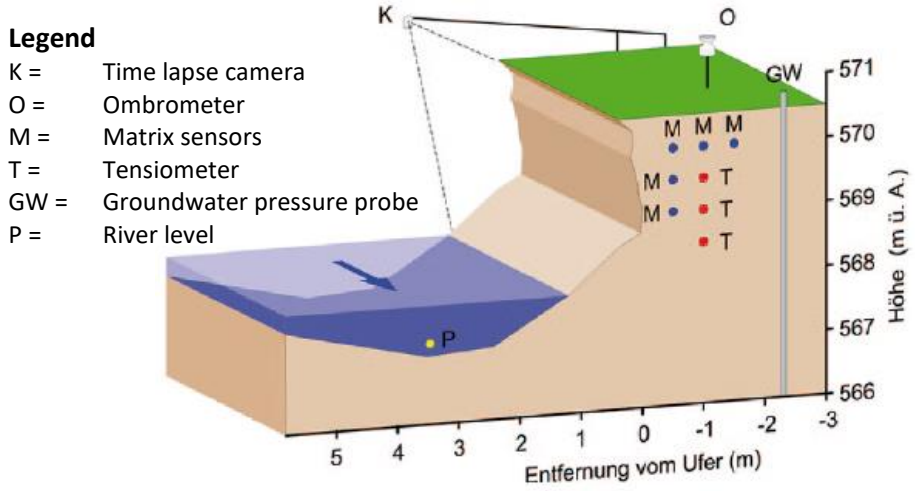


Figure 9: Installed devices to monitor bank stability (HABERSACK et al. 2012: 414).

The easiest and most economic monitoring method to monitor the bank erosion in the study area was the use of erosion pins. In addition, the state-of-the-art method of terrestrial photogrammetry was used to back up the results as well as provide further insight.

4.4 Modelling future hydro-geomorphic river changes

Besides analysing past changes, mapping current hydro-geomorphic features and monitoring current changes, modelling future scenarios of a river using a modelling software is the most innovative and state-of-the-art of all four methods. Nowadays there is a sheer abundance of open and closed source river modelling software available, and the choice simply depends on the underlying research question. In general, we can differentiate between five different model types for simulating river systems as seen in Figure 10.

There are landscape evolution models (LEMs), box (a) in Figure 10 which *"simulate the development of drainage basins by guiding water across a mesh of cells (representing the landscape) according to the steepest slope, and eroding and depositing sediment according to the amount of water in a cell…"* (COULTHARD et al. 2012: 2126). They are best suited for long time scales and over large areas. In addition, *"Given the current state-of-the-art, LEMs, or variants thereof, could provide one of the most appropriate ways for modelling river histories and especially for analysing how river systems interact with their wider environment."* (COULTHARD et al. 2012: 2127)

Next are reach-scale cellular automation models, box (b) in Figure 10. Also *"termed 'reduced complexity models'"* (COULTHARD et al. 2012: 2130), they represent the river with a grid of cells where water is *"routed downstream by allowing water to 'flow' to lower neighbouring cells"* (COULTHARD et al. 2012: 2130). *"Though having proved insightful in investigating how geomorphic processes interact and why certain phenomena occur, they have proved difficult to validate quantitatively and for this reason may be unsuitable for engineering predictions. In this manner, they are at present more akin to experimental physical models than to calibrated flume experiments."* (COULTHARD et al. 2012: 2131)

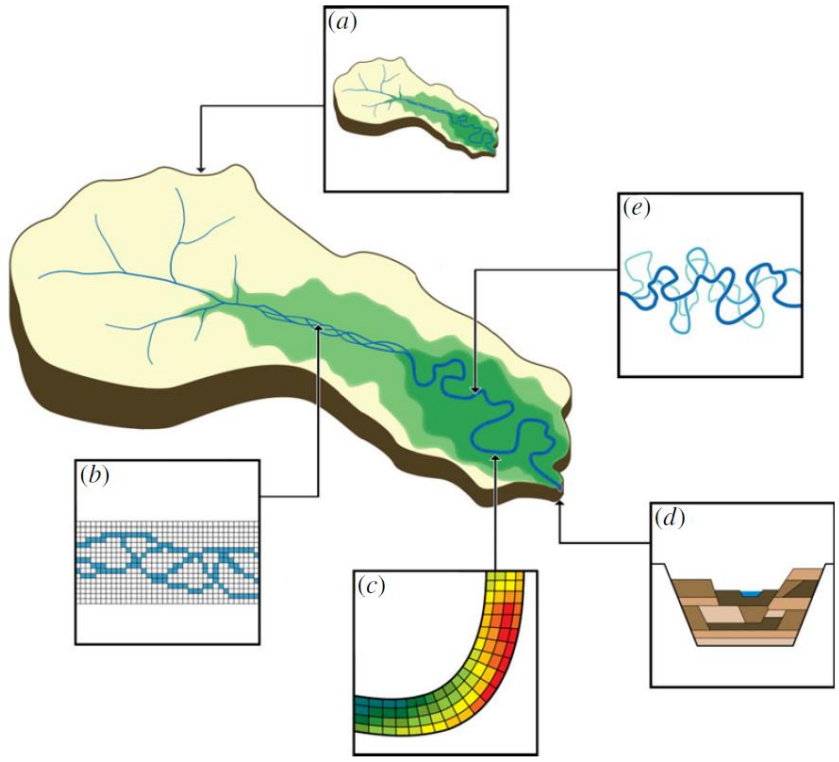


Figure 10: Schematic view of different model types for simulating river systems. (a) Landscape evolution; (b) reach-scale cellular automaton; (c) reach-scale CFD; (d) alluvial stratigraphy; (e) meandering. (Adapted from Van De Wiel et al.). (COULTHARD et al. 2012: 2125)

Next are reach-scale CFD models so called Computational fluid dynamics models as seen in box (c) in Figure 10. *"Applications of CFD models can be broadly divided into two categories: those with sediment transport modelling and those without. The latter rely on the CFD equations alone, and can be used to investigate hydraulic flow properties over an unchanging topography, notably the simulation of flood propagation and inundation extent…"* (COULTHARD et al. 2012: 2134). *"Although useful, these models cannot simulate river evolution, because the morphology of their river never changes."* (COULTHARD et al. 2012: 2134).

Next in box (d) in Figure 10, are alluvial stratigraphy models, which are *"designed to simulate the vertical and horizontal development of basin stratigraphy. These alluvial architecture models have been developed mainly to simulate sub-surface heterogeneity of facies for natural resource exploitation, but they can also be very useful in the context of palaeogeomorphology."* (COULTHARD et al. 2012: 2131) *"Unfortunately, the often highly simplified process representation in stratigraphic models could limit their capacity to investigate such river responses in sufficient detail."* (COULTHARD et al. 2012: 2131).

And lastly are meandering models as seen in box (e) in Figure 10, which *"simulate the development of channel planform in single-thread meandering rivers over time scales typically up to several millennia"* (COULTHARD et al. 2012: 2129). Being mostly used for shorter time scales they have some serious limitations when modelling longer timeframes making them unsuitable for simulating hydro-geomorphic processes (COULTHARD et al. 2012: 2131).

Regarding the main research question in this thesis of trying to analyse possible future hydro-geomorphic changes, LEMs are the best contemplable model type of the five. Within the LEM type however are several models to pick from which again depends on the underlying research question. In the article *Landscape evolution models: a software review* by COULTHARD 2001, five LEMs named SIBERIA, GOLEM, CASCADE, CHILD and CAESAR are described. In *"A short introduction to landscape evolution modelling"* from TUCKER 2010 he complements the five mentioned LEMs by adding DRAINAL, GILBERT, ELIM/MARSSIM, ZSCAPE, EROS, TISC, LAPSUS and APERO/CIDRE to the list of available LEMs published between 1991 and 2005 (TUCKER 2010: 3). The difficulty in picking the right model is therefore exemplified by the number of models available, which have nowadays increased in number. One limitation which must be considered when using a LEM is that they only use a steady flow of discharge (COULTHARD et al. 2013: 1897) and the model CAESAR specifically, which may be the case for all LEMs, *"predict greater sediment yields"* (COULTHARD et al. 2013: 1901).

With these known obstacles in mind when trying to simulate possible future hydro-geomorphic changes for four different discharge scenarios LEMs are unable to use varying discharge data, which is a key varying element for simulating the potential river change in this

thesis. TOM J. COULTHARD et al. 2013 approached this key LEM limitation by designing a new model merging the LISFLOOD-FP 2D hydrodynamic model with the CAESAR landscape evolution model to create the new CAESAR-Lisflood model (COULTHARD et al. 2013: 1897).

Coulthard's et al. conclusion reads as follows:
"The successful integration of LISFLOOD-FP with CAESAR creates a new LEM (CAEAR-Lisflood) that is faster, simpler, and has a stronger physical basis. The increase in computing power and the development of new flow algorithms like LISFLOOD-FP mean it is now possible to model geomorphic and longer term landscape change in a far more realistic and physically based way. This addresses a process limitation in existing LEMs and is a step change leading to the development of a 'second generation' of hydrodynamic LEMs that may lead us to significantly different conclusions about the physical basis of landscape evolution." (COULTHARD et al. 2013: 1905).

Based on Coulthard's et al. findings the merged model CAESAR-Lisflood seems optimal for the use in this thesis as we want to examine how varying discharge scenarios affect the landscape of the study area. Therefore, CAESAR-Lisflood will be used in simulating the possible future hydro-geomorphic changes in the study area between 2019 - 2050 using four different discharge scenarios.

5. Data and Methods

In the subsequent chapter, all the obtained data and applied methods used to compile the results are thoroughly presented and are described in concise manner.

The hydro-geomorphic changes in historic maps as well as more modern orthophotos of the study area will be analysed via remote sensing. The mapping process of the Salza River course as well as recent hydro-geomorphic processes and designation of fish spawn mesohabitats will be made on site and digitalized off-site. The record of any changes of the bank erosion hotspot will be conducted through monitoring via erosion pins and terrestrial photogrammetry on site and analysed off-site. Further, a granulometric analysis of the riverbed will be made on site. Lastly the generation of future scenarios of the hydro-geomorphic changes will be carried out through a geomorphological/landscape evolution model using the modelling software “CAESAR-Lisflood” off-site. This uses data of the river stretch to visualize and quantify areas of future erosion and accumulation within the river reach for the period 2019 - 2050 using four different discharge scenarios.

The data was obtained either through a secondary source or by me in the field. Most methods are based on established techniques however some were modified to work around difficulties, which occurred during the field work.

5.1 Reconstruction of past hydro-geomorphic changes of the Salza River

5.1.1 Data

The data used for reconstructing the past hydro-geomorphic changes in the study area, were both obtained from secondary sources and were selected as the state-of-the-art data for remote sensing past changes are historic maps and orthophotos, as previously described in chapter *4.1 Reconstruction of past hydro-geomorphic changes using historic maps and orthophotos.*. Below the datasets used are thoroughly described.

Historic maps

A total of 6 historical maps were obtained through screenshots from Mapire (https://mapire.eu/de/ last opened: on 02.11.2021), see Table 1. The use of the maps in this thesis was approved by the Austrian State Archives (Österreichisches Staatsarchiv). These were used to compare the historical river course of the Salza River in the study area. None of

the maps obtained were georeferenced.

Table 1: Available historical maps of the Salza River study area.

Map	Survey date	Map name	Scale
#1	1678	Steiermark Vischer map	Ca.1:150,000
#2	1784 - 1785	Josephinische Land survey	1:28,800
#3	1809 - 1818	Franziszeische Land survey	1:28,800
#4	1817 - 1861	Franziszeischer Cadastre	1:2880
#5	1821 - 1836	Steiermark Franziszeische Land survey	1:28,800
#6	1869 - 1887	Francisco-Josephinische Land survey	1:25,000

Orthophotos

Orthophotos were used for supplying worthwhile information of the changes within the study area from 2004 - 2017. These images were ordered by me, after consulting my supervisor Mag. Dr. Ronald Pöppl, BA, through GIS-Styria department A17 Rural and Regional development of the Styrian government (A17 Landes- und Regionalentwicklung, Amt der Steiermärkischen Landesregierung). Five sets of georeferenced orthophotos of the whole study area were obtained ranging in scan flight dates from 2004 to 2017 see Table 2.

In addition to the orthophotos, a satellite image of the erosion hotspot dating from the year 2019 was available on Google Earth.

Table 2: Available orthophotos of the Salza River study area.

Dataset	Scan flight date
orthophoto #1	02.09.2004
orthophoto #2	27.07.2009
orthophoto #3	30.05.2011
orthophoto #4	10.06.2014
orthophoto #5	08.09.2017
Satellite image #1	07.09.2019*

*Only of the hotspot

5.1.2 Methods

The described methods were selected as being the state-of-the-art remote sensing methods to assess past changes as described in the previous chapter *4.1 Reconstruction of past hydro-geomorphic changes using historic maps and orthophotos.* They were selected to aid in answering the central research question as well as the sub-questions *"How fast is the rate of bank erosion at the hotspots?"* and *"How do cross sections of the riverbed alongside the hotspots change?"*. Below the exact methods used are described.

General study area

Firstly, the general study area of the Salza River between river km 54.1 - 62.85 will be analysed descriptively by looking for and highlighting changes in the historic maps dating from 1678 - 1887 as well as in the five sets of orthophotos dating from 2004 - 2017. To make the historic maps comparable, all maps except for the oldest Vischer map due to its unrealistic representation, were georeferenced via the open-source GIS software QGIS (Version 3.10.6-A Coruña). The obtained orthophotos were already georeferenced.

In a second step, the georeferenced maps and orthophotos will be analysed numerically via the Sinuosity Index, see equation to the right, like described by SCHUMM, S.A. (1963).

$$P = \frac{L}{D}$$

P=Sinuosity
L=Length
D=Distance

This index indicates the level of sinuosity (curvature) of a river and is schematically drawn in Figure 11. By dividing the length of a river (measured along the river thalweg), with the distance (measured from start to finish of the river and being a straight line) a value is given. If the value is closer to 1, the river flow is defined as mostly straight. If the value is greater than 1, the river flow is more meandering and therefore sinuous. Moreover, the greater the index, the more sinuous the river flow. The index will be applied for the whole Salza River study area as well as the confined and unconfined segments separately. All measurements were done and extracted via QGIS.

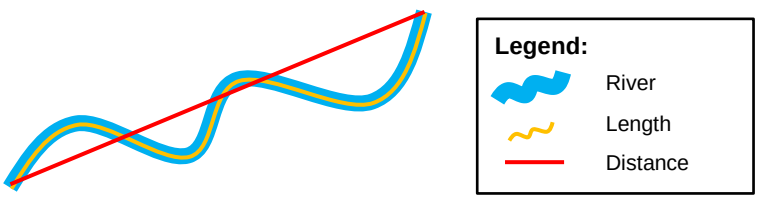


Figure 11: Schematic drawing of the sinuosity index as described by SCHUMM 1963.

Erosion Hotspot

Besides the study area as a whole, the historic maps and orthophotos will also be used to zoom in on the hotspot, from Figure 6, to see how it changed over time. Any changes will again be firstly described and where possible also analysed via applying the Sinuosity index as described in the previous chapter. Additionally, the recent changes in the cross-section of the erosion hotspot will be compared.

5.2 Mapping of in and out-of-channel geomorphic units

5.2.1 Data

In total four different datasets were used during the in-field mapping as well as off-site digitalization. Hereby only the Photos were primary data and the rest from a secondary source. Below the datasets used are thoroughly described.

Photos

Photos were taken by me during the field work in the study area on several occasions between May 2017 and June 2018 see Table 3, supplying images to help with the digitalisation of the mapping process as well as a medium to record what was done in the study area. For taking images, I used the digital camera model Panasonic TZ41 with a 18,1 Megapixel lens and a GPS function in order to have a set of geotagged photos. Additionally, several non-geotagged pictures were taken with a Samsung J5 13 Megapixel smartphone camera.

Table 3: Images taken throughout the field work of the Salza River study area.

Measurement	Date
#1	04.05.2017
#2	05.05.2017
#3	06.05.2017
#4	07.05.2017
#5	15.06.2017
#6	11.07.2017
#7	06.10.2017
#8	11.06.2018
#9	12.06.2018
#10	13.06.2018

Digital elevation model

A high-resolution digital elevation model (DEM) from an Airborne Laser Scanning (ALS) with a scan flight date from 2011 was provided through the ÖBf, via Dr. Monika Kanzian see Table 4. The DEM has a pixel resolution of 1 x 1 m and was very useful during the in-field mapping as well as the off-site digitalization.

Table 4: Available DEM of the Salza River study area.

Dataset	Scan flight date	Pixel resolution
#1	26.08.2011-27.08.2011	1m x 1m

Further GIS data

Finally, the online digital atlas of Styria, accessible through the website of GIS Styria [4] was very helpful in obtaining information of the study area such as the location of river kilometers, the scan flight dates etc.

ÖBf Mapping

DI Andreas Haas and Dr. Monika Kanzian from the ÖBf also provided a fragmentary mapping data file, which a former colleague mapped during a previous fieldwork in the Salza River study area. It contains point shapefiles of noteworthy river objects of two side reaches of the Salza River, area shapefiles of a small part of the Salza River as well as line shapefiles of the Salza River as well as its tributaries.

The coverage of the mapping however is only of a local area of the study area between river km 57.6 and 59 and I will try to embed it into the results later to see if any worthwhile comparison can be made.

5.2.2 Methods

The described method was selected as being the state-of-the-art mapping method to map geomorphic units in a river system as described in the previous chapter *4.2 Mapping of in and out-of-channel river features.* The chosen method helps in answering the central research question as well as the sub-question *"Which role does the riparian vegetation have on the bank stability?"* and gives an overall detailed present insight into the study area. The exact approach which was used is described on the following pages.

Preparatory work

Prior to heading out for the on-site mapping, I prepared a set of base maps. These contained the DEM of the study area from 2011 with the river km marks of the Salza River, see Figure 12. They were obtained from the online digital atlas of GIS-Styria and were screenshot into 11 map segments roughly covering a 1 km stretch of the Salza River. The segments were printed out on A4 and put into clear document wallets.

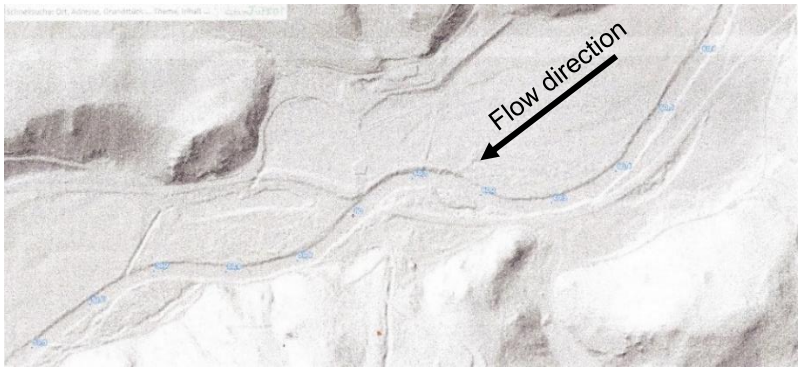


Figure 12: Base map for mapping the Salza River study area.

The mapping itself was done in situ in May of 2017 at each river segment, where the identifiable fluvial margins and geomorphic river features based on WHEATON et al. 2015 were drawn with a waterproof pen on the clear document wallets, see below Figure 13.



Figure 13: Annotated base map for mapping the Salza River study area.

Additionally, georeferenced photos were used for further analysis. A follow up mapping was done in June 2018 to see if any obvious changes happened during the 13 months and finally, all annotated features were digitalized off-site via GIS software QGIS generating three maps of the initial mapping and if necessary, one follow up map marking any changes from May 2017 to June 2018. Additionally, a bar chart will be presented in chapter *6. Results*, showing the area coverage of the mapped polygon features differentiating between the whole study area, the confined and unconfined Salza River study area.

Mapping framework

The paper *Geomorphic mapping and taxonomy of fluvial landforms* by WHEATON et al. 2015 provides an established *"framework for producing a geomorphic map of a riverscape"* (WHEATON 2015: 275) which was used for mapping my study area to construct 3 different maps of the Salza River study area. In it is a flowchart on how to best tackle a mapping of a river study area which consists of 4 four main features and will be described in the following 4 paragraphs.

Firstly, fluvial margins of the Salza River were mapped by following the workflow in Figure 14. The first step is to differentiate between a natural and anthropogenic margin. If it is a natural margin, then the margin is identified and assessed whether the margin is a channel margin, valley margin, valley bottom margin and whether the margin is a confining margin. The confining margin of the river hereby is *"where the channel margin abuts other margins that constrain its ability to adjust laterally"* (WHEATON 2015: 275). If it is an anthropogenic margin, then the margin type is identified and assessed whether the margin is a confining margin. The results of the mapped margins are a set of line shapefiles, which will produce the first map. The line shapefile of the confining margins in particular, will also be needed for the modelling step later.

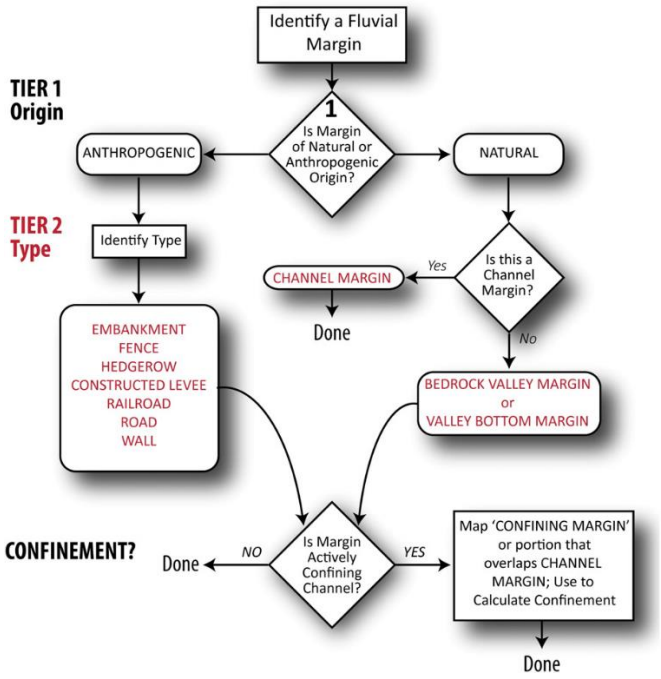


Figure 14: Flow chart of identifying a fluvial margin (WHEATON 2015: 274).

Next, the structural elements of the Salza River were mapped by following the workflow in Figure 15. The structural elements of the river are objects, which are in the flow of the river such as large woody debris or a boulder and can be natural or anthropogenic. The position of the element within the river and its influence on the river flow are the main features, which help in differentiating the type of structural element. The results of the mapped structural elements are a set of point shapefiles.

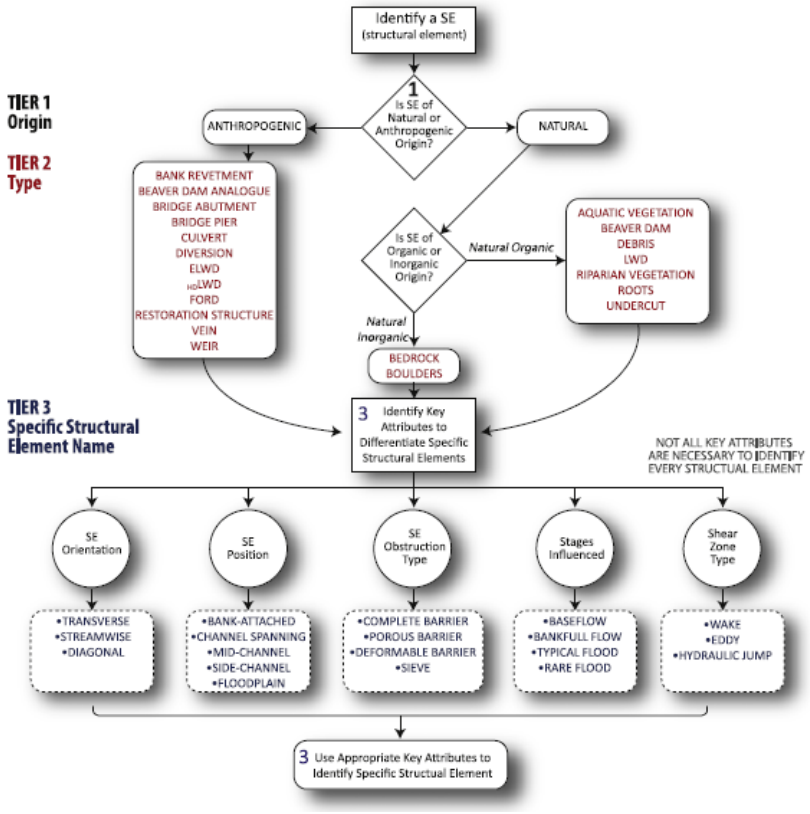


Figure 15: Flow chart of identifying a structural element (WHEATON 2015: 277).

Next, the In- and out-of-channel Tier 2 geomorphic units of the Salza River study area were mapped, following the first two tier steps in the workflow shown in Figure 16. We differentiate the shapes in 3 categories being either concave, convex or planar. All in and out-of-channel shapes are mapped as a polygon shapefile. Combining the results of the In- and out-of-channel Tier 2 units with the prior explained structural elements and confining margins will give us the second map.

Finally, the In- and out-of-channel specific Tier 3 geomorphic units of the Salza River study area were mapped, following the first three tier steps in the workflow shown in Figure 16. The difference in the tier 3 and tier 2 units is simply the greater detail with which the tier 3 units are described, respectively their morphology. For example, two prior mapped concave in-

channel geomorphic units from the tier 2 level can be further identified as a bar forced pool and a plunge pool during the tier 3 identification. Alternatively, two prior mapped convex in-channel geomorphic units from the tier 2 level can be further identified as a forced bar and a forced riffle during the tier 3 identification. All in- and out-of-channel geomorphic units are also mapped as a polygon shapefile. Combining the results of In- and out-of-channel specific hydro-geomorphic elements (tier 3) with the prior explained structural elements and confining margins will give us the final third and most detailed map of the study area. In addition to the three maps, bar charts will be presented showing, among others, the area coverage of the mapped tier 2 and 3 polygon features of the whole Salza River study area, the confined and unconfined segments for comparison. The metric data was obtained by using the Field Calculator in QGIS.

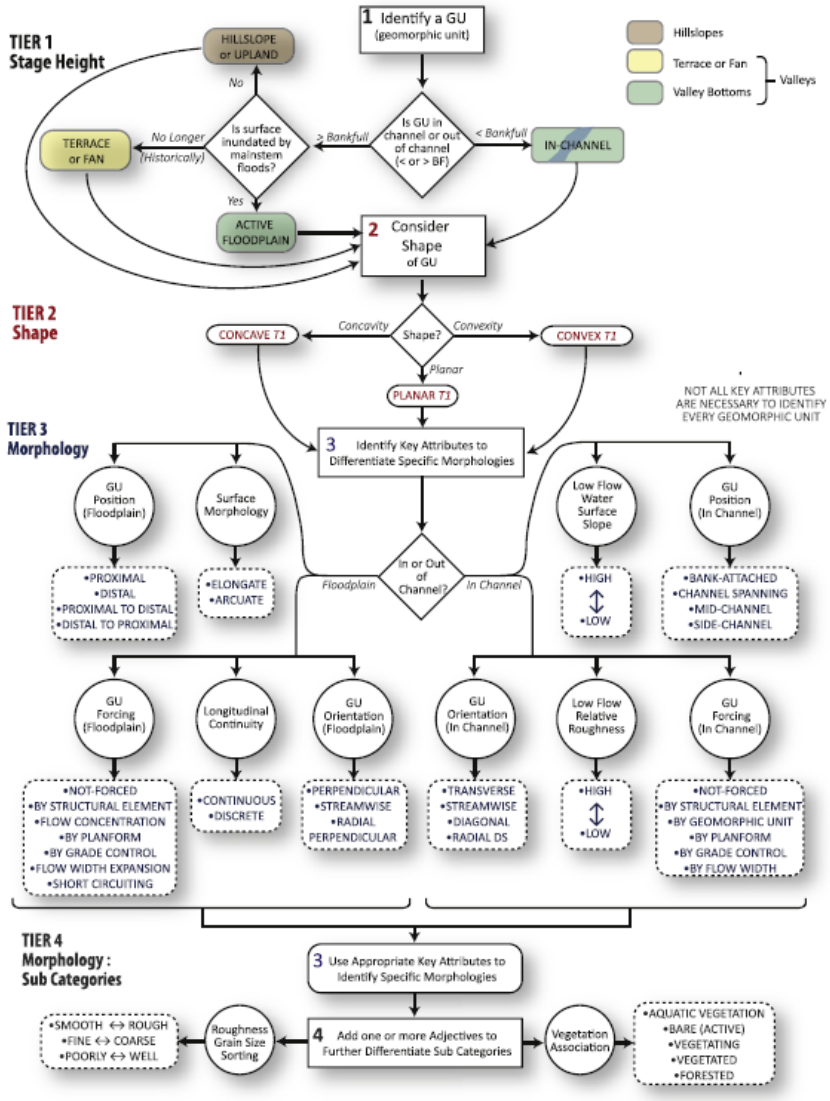


Figure 16: Flow chart of identifying a geomorphic unit (WHEATON 2015: 280).

5.3 Monitoring of the erosion hotspot

5.3.1 Data

For the first monitoring method there was no data used to obtain the results and for the second method the data used were photos taken by me during the field work. Below the data used are thoroughly described.

Photos were taken by me during the field work in the study area on several occasions between May 2017 and June 2018 see Table 5, supplying images to help with the photogrammetric monitoring of the hotspot. For image capturing, I used the digital camera model Panasonic TZ41 (18,1 Megapixel lens) with a GPS function to have a set of geotagged photos.

Table 5: Photogrammetric image taking at the hotspot of the Salza River study area.

Measurement	Date
#1	06.05.2017
#2	15.06.2017
#3	11.07.2017
#4	06.10.2017
#5	11.06.2018

5.3.2 Methods

To monitor the erosion hotspot seen in Figure 6, two different methods were applied. One being an adapted erosion pin method and the second a photogrammetric analysis. Both methods were decided on as being a state-of-the-art technique to monitor changes in a river system as described in chapter *4.3 Monitoring present hydro-geomorphic river changes.* The selected methods aid in answering the sub-question *"How fast is the rate of bank erosion at the hotspots?"* as well as *"Which role does the riparian vegetation have on the bank stability?".* Following, the exact approach used is described.

Erosion pins

To monitor the erosion hotspot, it was decided beforehand to use erosion pins on the bank erosion to assess any changes over time. Erosion pins were meant to be used like shown in Figure 17, where rods are placed horizontally into the bank and their residual protruding length is measured. The further the bank erodes, the further the rods protrude from the bank.

The rate of erosion of the bank can be assessed over the entire height of the bank, by measuring the difference in length of the rods.

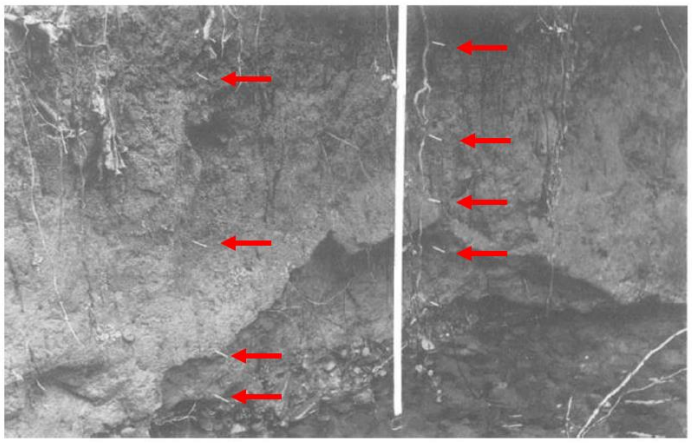


Figure 17: A column of erosion pins marked in red (Lawler 1992: 803).

Version 1

However, upon my first arrival at the hot spot, I noticed that the bank was covered with the previously collapsed bank, see Figure 18, which made it impossible to apply the method as described by LAWLER 1992.



Figure 18: Bank erosion hotpot at river km 58.7 - 58.8 of the Salza River study area.

After some reconsideration in the field, I decided to instead place large main markers (marker 1) on top of the bank and measure the distance from the markers to the edge of the bank, see Figure 20 on the left. The markers were simple plastic pipes, normally used for electrical installation and the top of the markers were spray painted for better visibility. Before installation, I measured the length of the bank with a long measuring tape, see Figure 19 on the right, and placed the marker 1 every 5 metres apart along the 106.5 m long bank and roughly 2 metres away from the edge of the bank.

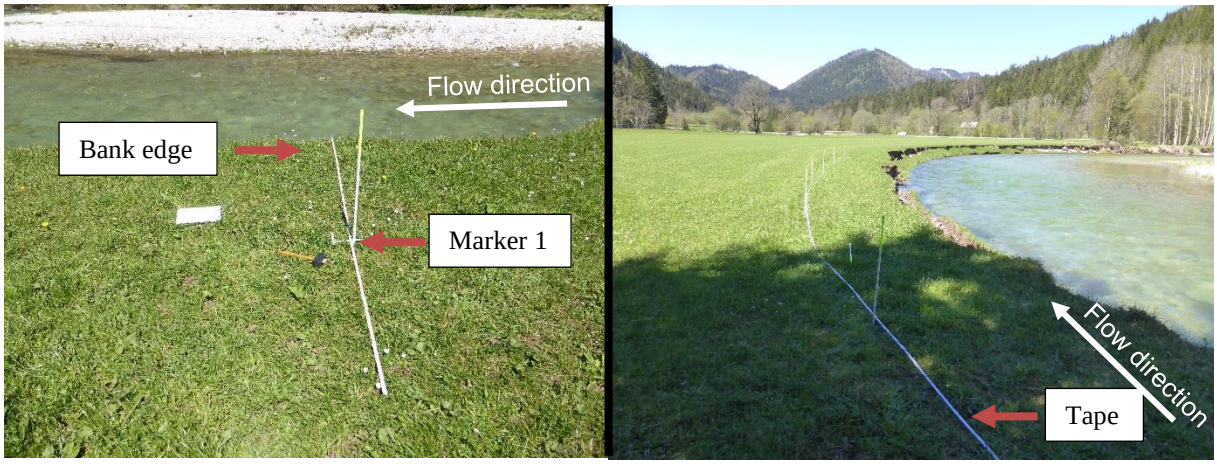


Figure 19: Set up of erosion pins version 1 at the erosion hotpot at river km 58.7 - 58.8 of the Salza River study area.

Next, in order to always measure in the same angle towards the bank edge, I placed an additional marker 2 at ground level between marker 1 and the edge, see Figure 20 on the left. Hereby I used a plastic endcap normally used to close sewer pipes.

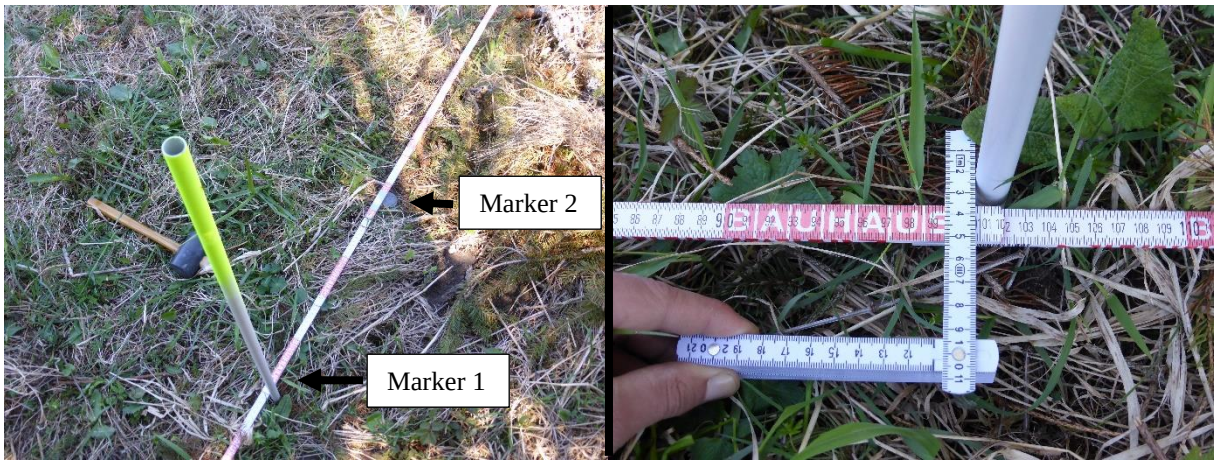


Figure 20: Measurement of erosion pins version 1 at the erosion hotpot at river km 58.7 - 58.8 of the Salza River study area.

After setting up the markers, I measured the distance from the marker 1 to the edge. I taped two 2 m folding meter sticks together and used them to align the two markers, see Figure 20 on the left, and placed a smaller folding meter stick perpendicular to read the distance off the long meter stick see Figure 20 on the right. In total, 23 markers 1 and 23 markers 2 were placed on the bank of the hotspot, see Figure 21.



Figure 21: Instalment of erosion pins version 1 at the erosion hotpot at river km 58.7 - 58.8 of the Salza River study area.

Version 2

A second set of erosion pins were installed on the 15.06.2017. Before instalment, I once again measured the length of the bank roughly 2 m from the edge with a long measuring tape, see Figure 22.



Figure 22: Set up of erosion pins version 2 at the erosion hotpot at river km 58.7 - 58.8 of the Salza River study area.

Next, I cut simple plastic pipes, normally used for electrical installation, into smaller pieces as a new marker 1 which I hammered every 10 metres apart and roughly 2 metres away from the edge into the bank. This time however the markers were hammered in to be level with the ground. Next, in order to always measure in the same angle towards the edge, I placed an additional marker 2 between the marker 1 and the edge at ground level, see Figure 23.



Figure 23: Close up of the setup of erosion pins version 2 at the erosion hotpot at river km 58.7 - 58.8 of the Salza River study area.

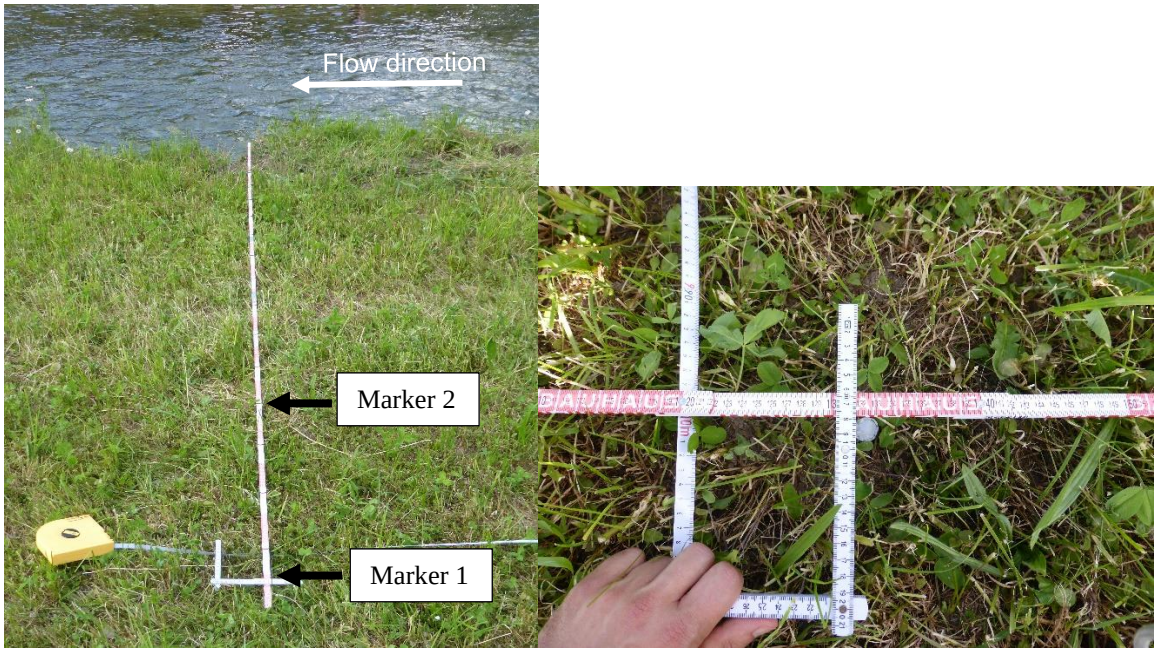


Figure 24: Measurement of erosion pins version 2 at the erosion hotpot at river km 58.7 - 58.8 of the Salza River study area.

After setting up the markers, I measured the distance from the marker 1 to the edge. I taped two 2 m folding meter sticks together and used them to align the two markers, see Figure 24 on the left, and placed a smaller folding meter stick perpendicular to read the distance off the long meter stick see Figure 24 on the right.

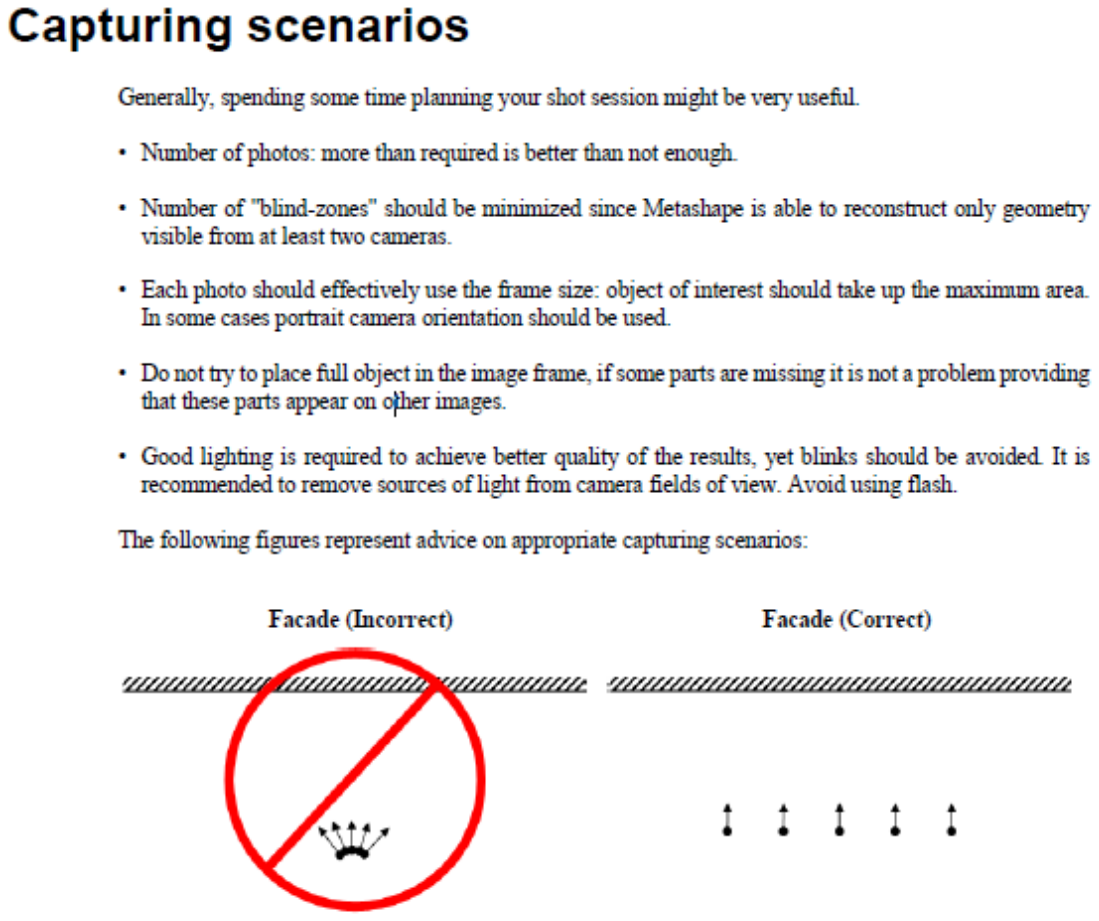
In total 12 markers 1 and 12 markers 2 were placed on the bank of the hotspot. An initial measurement of the distances was taken on the 15.06.2017 and a follow up measurement on the 11.07.2017.

Photogrammetry

The second method used to monitor the hotspot in Figure 6 was a terrestrial, photogrammetric analysis. Photographs were hereby taken of the hotspot at 5 separate timeframes, see Table 5, which were used to construct a point cloud for every separate timeframe. These clouds could then be compared with each other to analyse any changes, which happened in the 13-month timeframe.

Image capturing

First off, to capture the correct images for a successful photogrammetric analysis, several factors had to be considered. In the user manual "Standard Edition, Version 1.6" of the software Agisoft Metashape, which was used to construct the point clouds, there is a guideline on how to capture correct photos. On page 6 we find the following key factors for capturing scenarios as well as how one should and should not capture the images of a facade, see Figure 25.



Capturing scenarios

Generally, spending some time planning your shot session might be very useful.

- Number of photos: more than required is better than not enough.
- Number of "blind-zones" should be minimized since Metashape is able to reconstruct only geometry visible from at least two cameras.
- Each photo should effectively use the frame size: object of interest should take up the maximum area. In some cases portrait camera orientation should be used.
- Do not try to place full object in the image frame, if some parts are missing it is not a problem providing that these parts appear on other images.
- Good lighting is required to achieve better quality of the results, yet blinks should be avoided. It is recommended to remove sources of light from camera fields of view. Avoid using flash.

The following figures represent advice on appropriate capturing scenarios:

Figure 25: Capturing scenarios for a photogrammetric analysis (AGISOFT METASHAPE: 6).

Based on the user manual, I used my Panasonic TZ41 in order to take a heap of geotagged photographs facing the erosion bank from the opposite lying compound bar, at each of the 7 different camera positions, see Figure 26. Taking images from different positions made sure that the photographs overlap, which is necessary to create a point cloud. I used a tripod for my camera to take photographs which are at level with the erosion hotspot, see Figure 27.

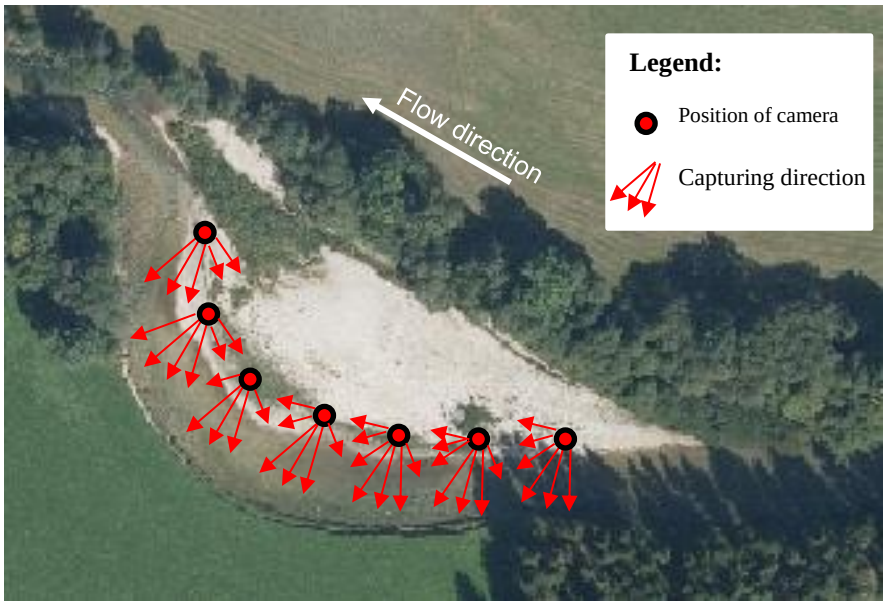


Figure 26: Camera position and capturing direction at the erosion hotspot of the Salza River study area.

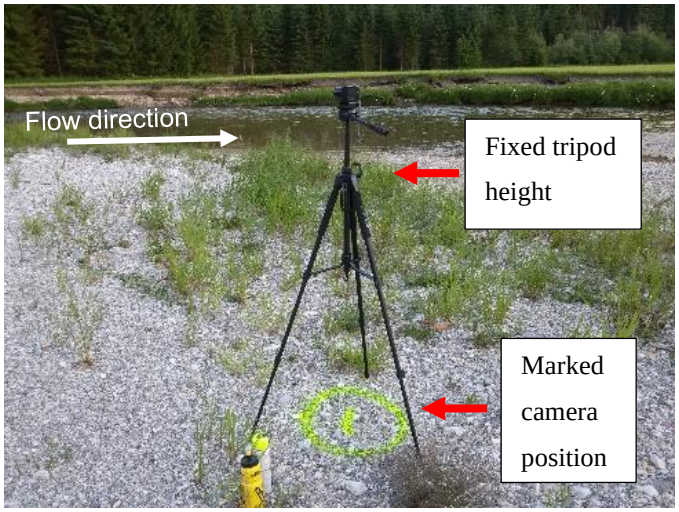


Figure 27: Tripod positioning for image capturing of the erosion hotspot of the Salza River study area.

During my first recording on the 06.05.2017, I additionally spray painted the location of the camera position onto the gravel bank, see Figure 27, however during my consecutive recordings, the paint was washed away during a flooding event, so the ongoing camera positions were estimated, but nonetheless georeferenced via the camera.

Another aspect which had to be considered before taking the images of the erosion bank was to eliminate any “blind zones” as described in the manual in the second line, see Figure 25. In my case, as seen in Figure 28, the blind zone was the bank of the bank erosion, which was visually covered from the capturing direction by grass growing on the collapsed bank. In order to have a clear view of the bank, I had to mow the collapsed bank of the higher grass before starting the image capturing process. In the image below the before and after pictures of the bank show how in the before images the bank was not visible whereas after mowing the bank was visible, which was essential for the image capturing process.

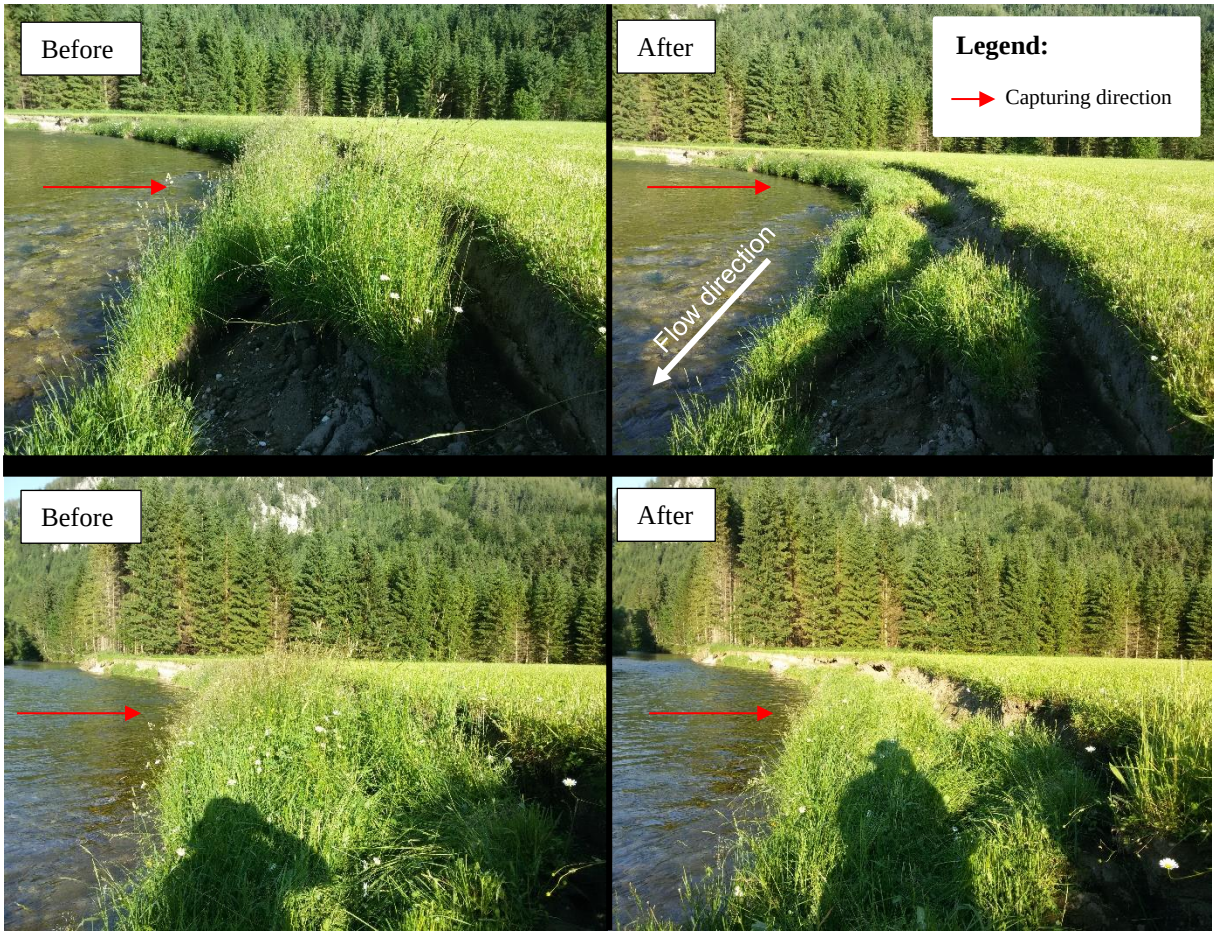


Figure 28: Before and after images of mowed grass of the collapsed bank at the erosion hotspot of the Salza River study area. Top images, orographic lowest location at the erosion hotspot facing upstream. Bottom images, middle location at the erosion hotspot facing upstream.

Lastly, to take images at optimal lighting conditions at the erosion hotspot, all images were taken in the afternoon. In the morning, the sun illuminates the bank unequally and only after around 1 pm was there an even, indirect and identical light exposure so that all images of the bank are at a light, but not bright lighting condition.

Generating point clouds

Next, the images were analysed via the photogrammetric processing software Agisoft Metashape (30-day-trial, Version 1.7.2 pre-release) to generate point clouds. The user manual on page 12 gives a general workflow on how to process the images, see Figure 29.

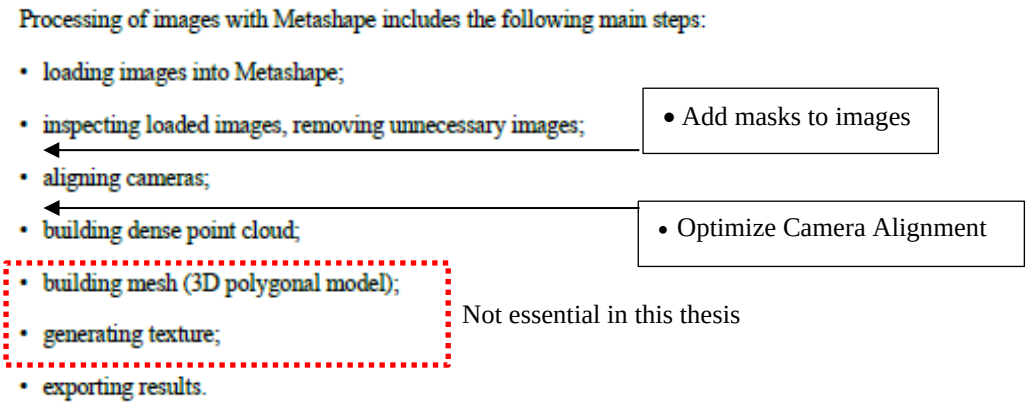


Figure 29: Main steps of image processing with Agisoft Metashape, Adapted (AGISOFT METASHAPE: 12).

For the analysis not all workflow steps were essential, however two additional steps were added. The building mesh and generating texture step in the above image were not used, see red striped rectangle, and the steps "Add masks to images" and "Optimize Camera Alignment" were added.

In the workspace I first created a chunk via the "Add Chunk" for each timeframe and loaded my images for each timeframe into Agisoft Metashape via "Add Photos". I then inspected the images and removed any unnecessary ones, which were too zoomed in, did not overlap with other images, or had poor lighting.

Next, I went through every image of every timeframe and added a mask to every photo. *"Masks are used in Metashape to specify the areas on the photos which can otherwise be confusing to the program or lead to incorrect reconstruction results."* (AGISOFT METASHAPE: 43). The mask itself was applied by selecting the erosion bank with the "Rectangle selection", clicking "Invert selection" and then right mouse click "Add Selection". This mask, masks everything in the image, except for the erosion bank, and is not considered throughout the further computational steps, thus saving computation time. Figure 30, shows the before and after of an applied mask to an image. From here on the steps are always processed for every chunk.



Figure 30: Before (left) and after (right) image of an applied mask via Agisoft Metashape.

I then aligned the images of every chunk via the "Align Photos" with the settings seen on the left in Figure 31. This step locates the camera position of every image as well as looks for overlapping points in all the images in every chunk. The result is a sparse point cloud from Tie Points, as seen on the left in Figure 33.

After photo alignment the images of every chunk were optimized via the "Optimize Camera Alignment" window with the settings seen on the right in Figure 31.

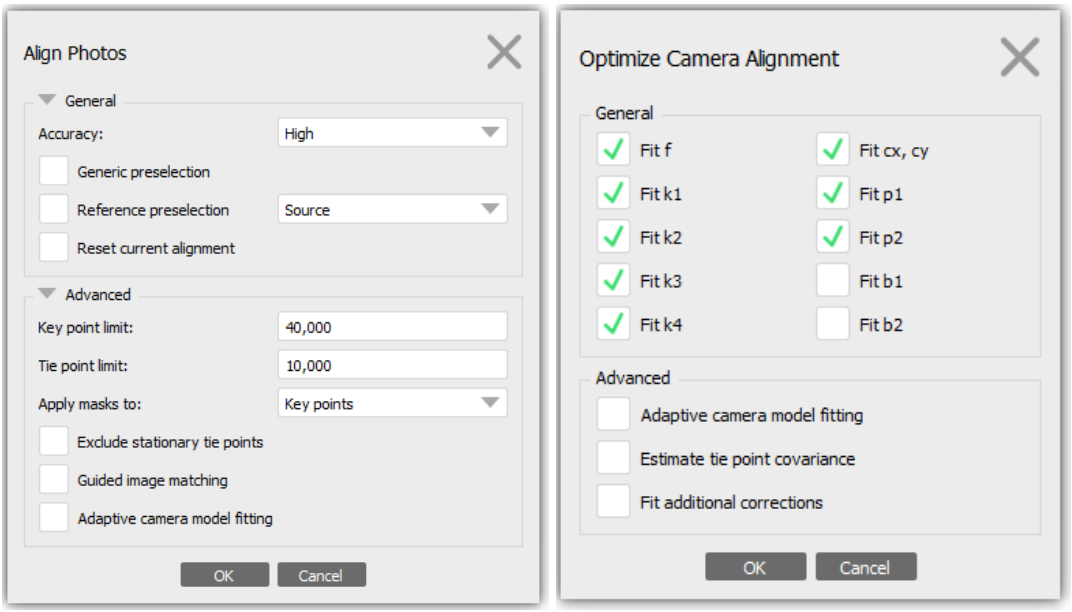


Figure 31: Align photos window (left) and Optimize camera alignment window (right) in Agisoft Metashape.

Finally, the last step was to create a point cloud of every chunk via the "Build Dense Cloud" window with the settings seen in Figure 32.

"*Dense point cloud generation is based on depth maps calculated using dense stereo matching. Depth maps are calculated for the Overlapping image pairs considering their relative*

exterior and interior orientation parameters estimated with bundle adjustment. Multiple pair-wise depth maps generated for each camera are merged together into combined depth map, using excessive information in the Overlapping regions to filter wrong depth measurements." (AGISOFT METASHAPE: 19).

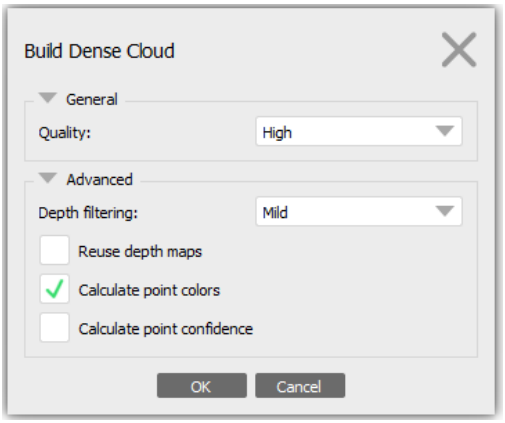


Figure 32: Build dense cloud window in Agisoft Metashape.

The result of a dense cloud can be seen on the right in Figure 33, in comparison with a previously compiled, detail lacking sparse cloud on the left. The general and advanced settings for the dense cloud generation required some trial and error before obtaining a setting with the best visualization of the bank erosion. During the dense cloud generation technical difficulties were discussed with and solved by Alexey Pasumansky, technical specialist at Agisoft LLC. The fitted dense cloud for each chunk could then be exported as a XYZ point cloud in a .txt file. In total, 5 dense clouds from the 5 timeframes in Table 5 were computed.

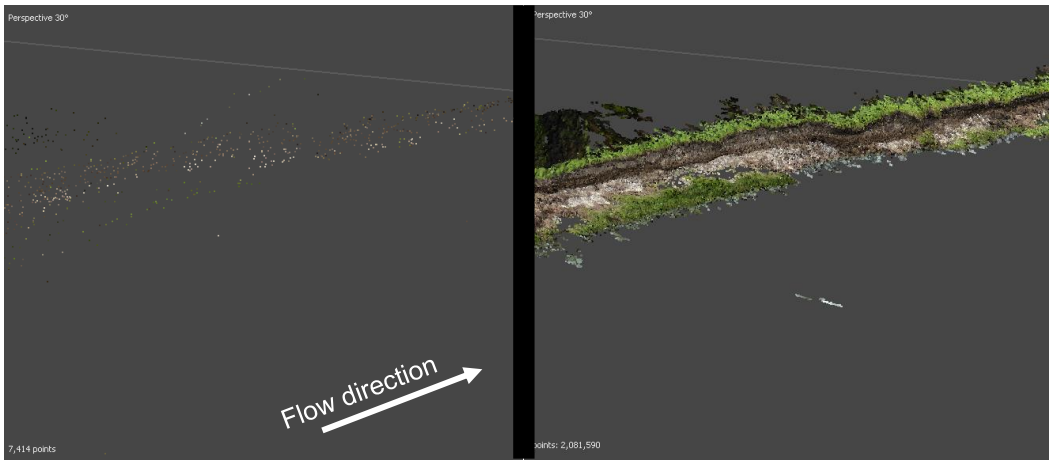


Figure 33: Compiled sparse cloud after the "Align Photos" step (left) and compiled dense cloud after the "Build Dense Cloud" step (right) in Agisoft Metashape.

Analysing point clouds

For analysing the generated dense clouds, the open-source 3D point cloud and mesh processing software Cloud Compare (Version 2.11.3 Anoia) was used. All information was obtained from the online documentation wiki found under (https://www.cloudcompare.org/doc/wiki last opened: on 02.11.2021).

First all 5 clouds were opened via the open function and "apply all" was selected for all clouds confirming the X, Y and Z coordinates as well as other attributes.

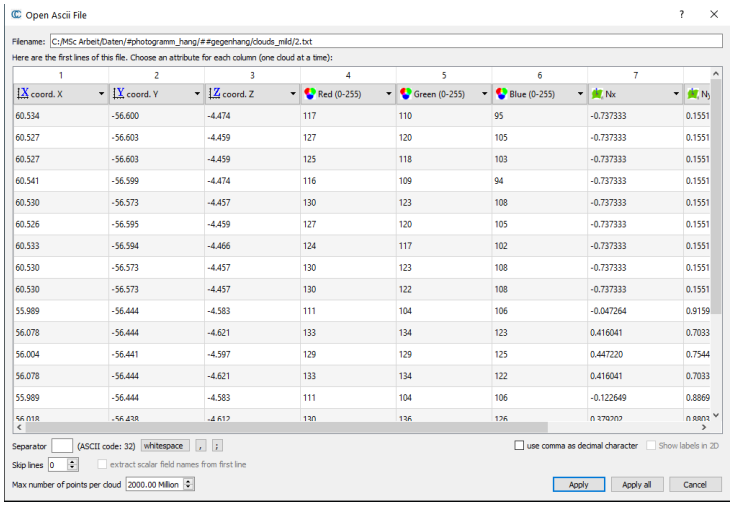


Figure 34: Open Ascii File window in Cloud Compare.

Next the clouds had to be aligned. This was done automatically by using the Tools→Registration→**Fine Registration (ICP) tool**. The point cloud from the first timeframe in Table 5 was used as the reference cloud. Every consecutive cloud was aligned with the previous cloud in four registration steps. In Figure 35 we see the reference cloud in yellow and the to be aligned cloud in red. The before and after alignment can be seen in Figure 36.

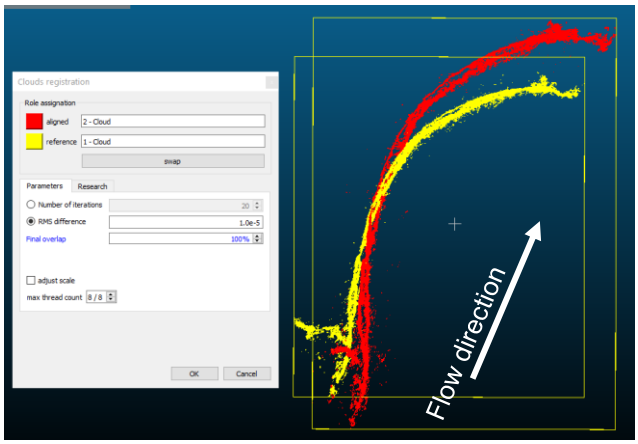


Figure 35: Cloud registration tool in Cloud Compare.

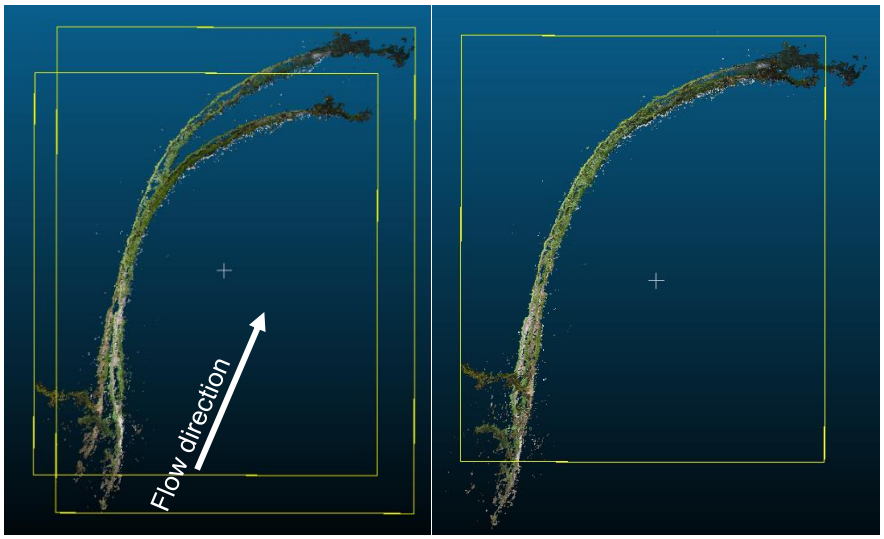


Figure 36: Before and after the automatic cloud registration tool in Cloud Compare.

After alignment, the clouds could be analysed for any 2D differences. Hereby the plugin M3C2 was used which *"…is the unique way to compute signed (and robust) distances directly between two point clouds."* [8]. Two clouds were selected, Plugins→**M3C2 distance** was selected to open the window in Figure 37. "Guess params" was selected and then "OK".

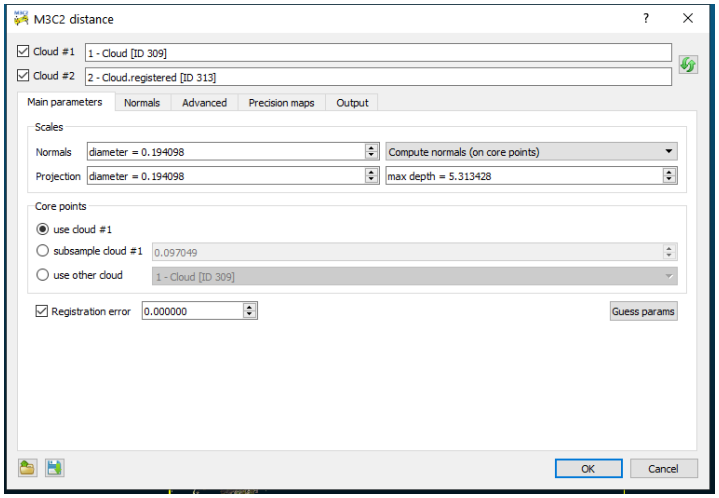


Figure 37: M3C2 distance plugin window in Cloud Compare.

Every cloud was compared with the previous cloud and the cloud from the last recording was also compared the first. In total 5 calculations were made see Table 6.

Table 6: Number of M3C2/Compute 2.5D Volume calculations in Cloud Compare of the created point clouds.

Number	M3C2/Compute 2.5D Volume calculation
#1	Cloud 2 with reference cloud 1
#2	Cloud 3 with reference cloud 2
#3	Cloud 4 with reference cloud 3
#4	Cloud 5 with reference cloud 4
#5	Cloud 5 with reference cloud 1

The results for these calculations are 5 separate output clouds. They display any visual differences (in metres) with a colour scale showing erosion and accumulation points on the reference cloud. Additionally, a histogram of the results will be given per calculation.

And finally, to also have volume metrics of the erosion and accumulation changes from the clouds from Table 6, I applied a volume calculation via Tools→Volume→**Compute 2.5D Volume**. The below Figure 38 displays the window after selecting the two clouds to compare.

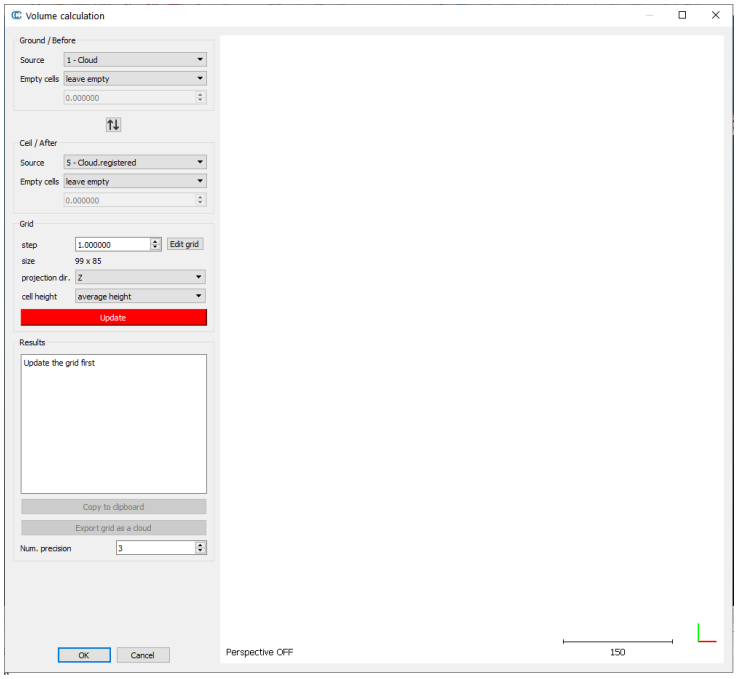


Figure 38: 2.5D Volume calculation in Cloud Compare.

5.4 Modelling of future hydro-geomorphic changes of the Salza River

5.4.1 Data

In order to successfully simulate the future Salza River three essential datasets were needed namely grain size data, hydrological discharge data as well as a digital elevation model. The grain size data was obtained by me in the field and the other two were obtained through secondary sources and are thoroughly described below.

Grain size

The grain size distribution of the riverbed, needed for the modelling step later using CAESAR-Lisflood, was approximated via a method called “Linienzahlanalyse”, briefly translated to Line-count-analysis. 4 datasets were gathered on two separate occasions.

Table 7: Line-count-analysis of the riverbed of the Salza River study area.

Measurement	Date	River location
#1	07.05.2017	Between river km 58.7 and 58.8
#2	07.05.2017	Between river km 60.1 and 60.2
#3	12.06.2018	Between river km 58.7 and 58.8, during low water
#4	12.06.2018	Roughly at river km 56.4, during low water

Finally, during my field work in June of 2018 a heavy rainfall event occurred resulting in an increase in discharge as well as an increase in suspended sediments within the discharge later that evening. A very primitive method was used to collect two suspended sediment samples, see Table 8.

Table 8: Suspended sediment samples taken of the Salza River study area.

Measurement	Date
#1	12.06.2018
#2	12.06.2018

Hydrological data

A large array of hydrological data consisting of discharge, water level and rainfall data was initially obtained in April 2017 through Erich Fischer from the Federal Ministry of Agriculture, Regions and Tourism after consulting my supervisor Mag. Dr. Ronald Pöppl, BA. However, after a reconception of what was going to be modelled, only hourly discharge data from the gauging station Gusswerk was going to be used.

The received discharge data from 2017 dated from 01.01.1976 - 31.12.2014 and lacked recent years. Thus, I recontacted Erich Fischer from the Federal Ministry of Agriculture, Regions and Tourism twice more in 2018 and 2021 to obtain newer datasets ranging from 01.01.2015 - 31.12.2018. The used hourly discharge data can be found below in Table 9. They year 2015 overlapped in datasets #2 and #3.

Table 9: Available hourly discharge data of the gauging station Gusswerk of the Salza River study area.

Dataset	Survey date	Description
#1	01.01.1976 - 31.12.2014	Gusswerk discharge QSUM60
#2	01.01.2015 - 31.12.2015	Gusswerk discharge QSUM60
#3	01.01.2015 - 31.12.2018	Gusswerk discharge QSUM60

Digital elevation model

A high-resolution digital elevation model (DEM) from an Airborne Laser Scanning (ALS) scan flight date in 2011 was provided through the ÖBf, via Dr. Monika Kanzian see Table 4. The DEM has a pixel resolution of 1 x 1 m and was essential for the modelling of the study area.

Table 10: Available DEM of the Salza River study area.

Dataset	Scan flight date	Pixel resolution
#1	26.08.2011 - 27.08.2011	1 x 1 m

5.4.2 Methods

The modelling software CAESAR-Lisflood was selected to be used during the modelling step in this thesis as it presented the best suited state-of-the-art method, see chapter *4.4 Modelling future hydro-geomorphic river changes*, to achieve the goal of modelling the study area for the timeframe 2019 - 2050 with four different discharge scenarios. Further this step aided in answering the central research question as well as the sub-questions *"Which changes of the riverbed are to be expected?", "How do cross sections of the riverbed alongside the hotspots change?" and "What impacts do flood events have on the future river course development?"*. Prior to the final modelling, the grain sizes had to be approximated, the data had to be prepared to fit the format of the software and a parametrization had to be performed. Following, the exact approach used is described.

Riverbed grain size approximation

For the approximation of the grain size of the riverbed, I decided to use the so called "Linienzahlanalyse" briefly translated to Line-count-analysis by FEHR 1987. His paper describes an easy method with which the coarse grain sizes can be gathered by analysing the top layer. Based on the coarse grain size measured in the field, the fine grain sizes can be approximated using a Fuller curve (paraphrased FEHR 1987: 1107). All following steps are based on FEHR'S 1987 article and are briefly described on the following pages.

First, the location of the Line-count-analysis had to be decided on. Fehr describes the ideal location to be in the river channel during low water and the line to be in line with the river flow (paraphrased FEHR 1987: 1106). After a first location was found, a tape measure was used to mark a line alongside the river flow on the bank, see Figure 39.

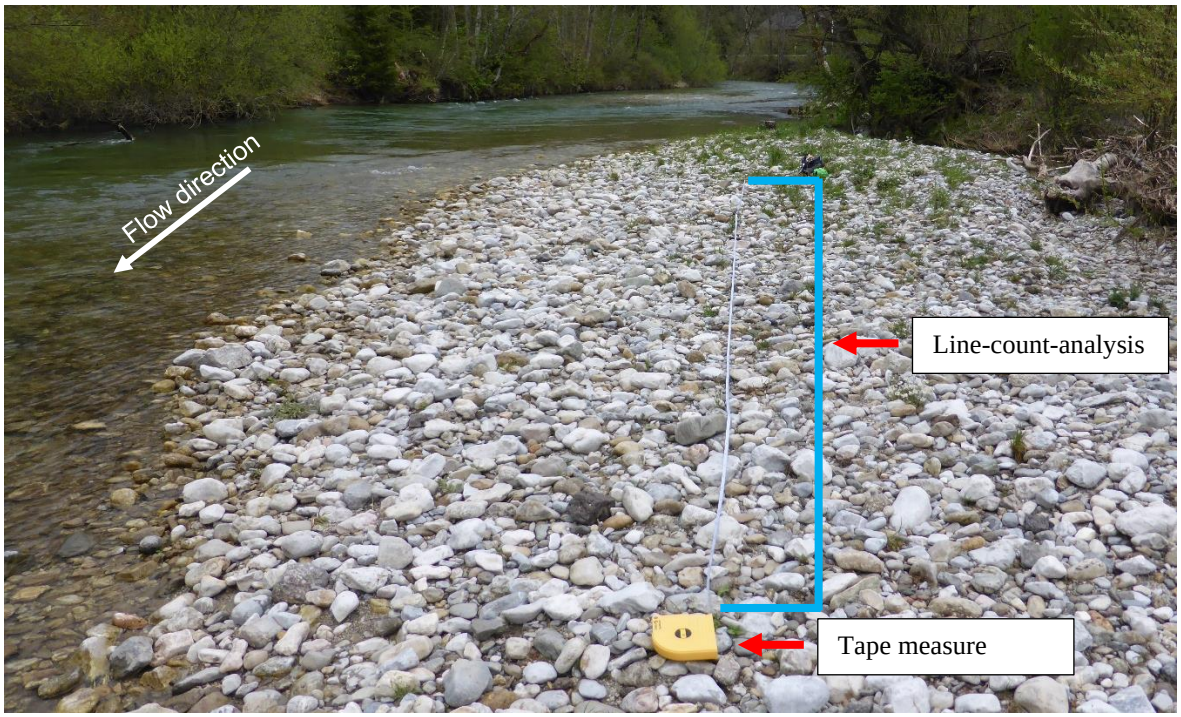


Figure 39: Set up of a Line-count-analysis in the study area of the Salza River between river km 60.1 and 60.2

Next FEHR mentions that a minimum of 150 stones, with a diameter of over 1 - 2 cm, should be counted with at least 30 stones of the mean grain size to make the method valid (paraphrased FEHR 1987: 1106). In order to be on the safe side, I decided on marking a 10 m strip on the riverbed for each line count analysis.

Next the method states, to examine all stones of the top layer under the marking and determine the width at the widest point of each stone also called the b-axis, see Figure 40 on

the left. This was done to all stones for each separate line count analysis via a meter stick see Figure 40 on the right.

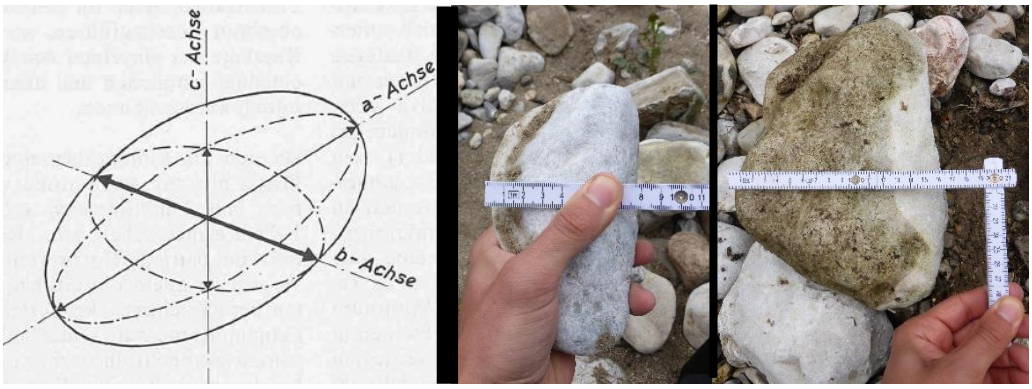
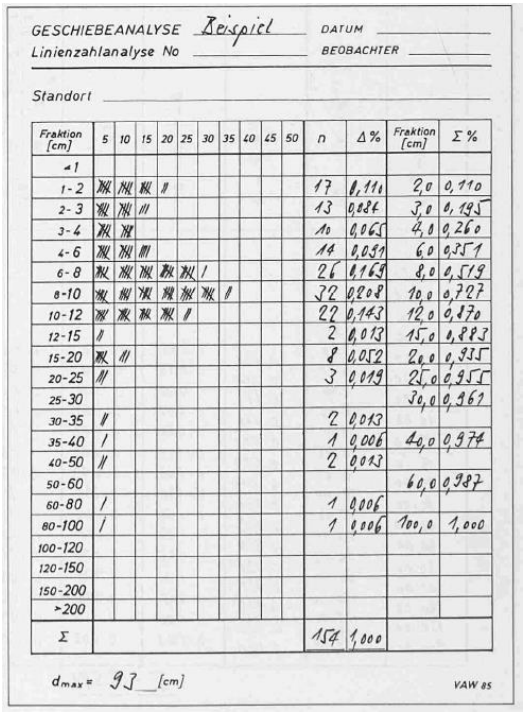


Figure 40: B-axis of a stone on the left (FEHR 1987: 1105) and b-axis measurement of stones on the right in the field.

Recordings of the analysis were done on paper in the field using a blank form like presented in Figure 41. All results were subsequently transferred into Microsoft Excel off-site.



GESCHIEBEANALYSE Beispiel DATUM
Linienzahlanalyse No BEOBACHTER
Standort

Fraktion [cm]	5	10	15	20	25	30	35	40	45	50	n	Δ %	Fraktion [cm]	Σ %
<1														
1-2	𝍸	𝍸	𝍸	//							17	0,111	2,0	0,110
2-3	𝍸	𝍸	///								13	0,084	3,0	0,195
3-4	𝍸	𝍸									10	0,065	4,0	0,260
4-6	𝍸	𝍸	////								14	0,091	6,0	0,351
6-8	𝍸	𝍸	𝍸	𝍸	𝍸	/					26	0,169	8,0	0,519
8-10	𝍸	𝍸	𝍸	𝍸	𝍸	//					32	0,208	10,0	0,727
10-12	𝍸	𝍸	𝍸	𝍸	//						22	0,143	12,0	0,870
12-15	//										2	0,013	15,0	0,883
15-20	𝍸	///									8	0,052	20,0	0,935
20-25	///										3	0,019	25,0	0,955
25-30													30,0	0,961
30-35	//										2	0,013		
35-40	/										1	0,006	40,0	0,974
40-50	//										2	0,013		
50-60													60,0	0,987
60-80	/										1	0,006		
80-100	/										1	0,006	100,0	1,000
100-120														
120-150														
150-200														
>200														
Σ											154	1,000		

d_{max} = 9,7 [cm] VAW 85

Figure 41: FEHR'S form to notate and analyse a Line-count-analysis in the field (FEHR 1987: 1107).

The before and after image of a Line-count-analysis in Figure 42 shows the distinctive line in the top layer left after measuring every top layer stone along the marker. The analysis was performed at four locations in the Salza River study area during two separate timeframes see Table 7.

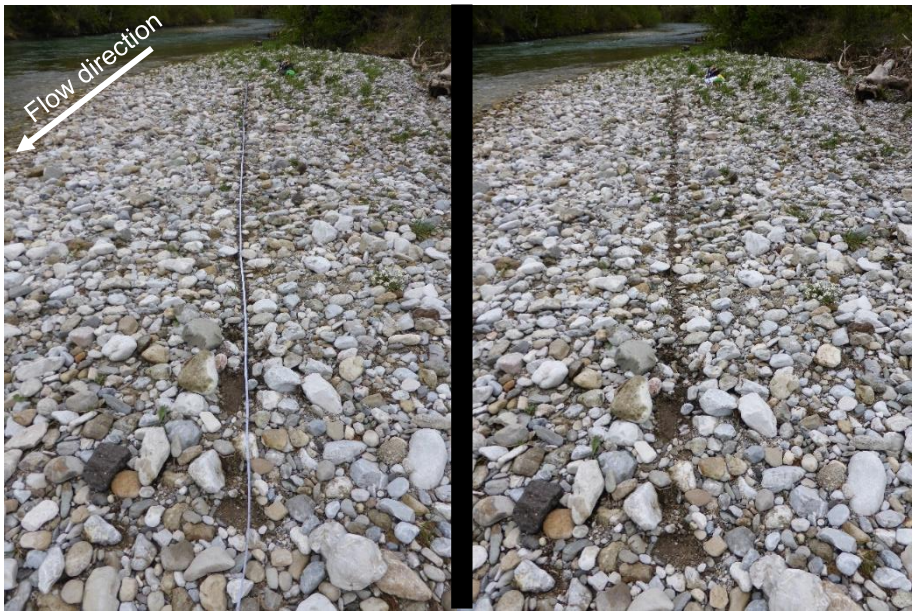


Figure 42: Before and after image of a Line-count-analysis in the Salza River study area.

After obtaining the results a simple grain size distribution was calculated for every analysis in Table 7. Additionally, further metrics were calculated to be sure of having counted a minimum of 150 stones, with at least 30 stones of the mean grain size to make the method valid (paraphrased FEHR 1987: 1106).

Subsequently a mean grain size distribution was calculated from the four single distributions to have a more representative grain size distribution for the whole study area. Now several calculations were needed to transform the Line-count-analysis of the top layer into a representable grain size distribution for both fine and coarse grain sizes. This was done in several steps. First several Fuller curves were created using the below formula.

$$p(d) = \sqrt{\frac{d}{d_{max}}} \text{ where } d = diameter\ of\ specific\ grain\ size \text{ and } d_{max} = diameter\ of \max grain\ size$$

The curves were contrasted with the mean Line-count analysis in Figure 43, where a Fuller curve was selected which fits the distribution of the coarse grain sizes the best (FEHR 1987: 1109), since a Line-count-analysis underestimates the fine grain sizes (FEHR 1987: 1107).

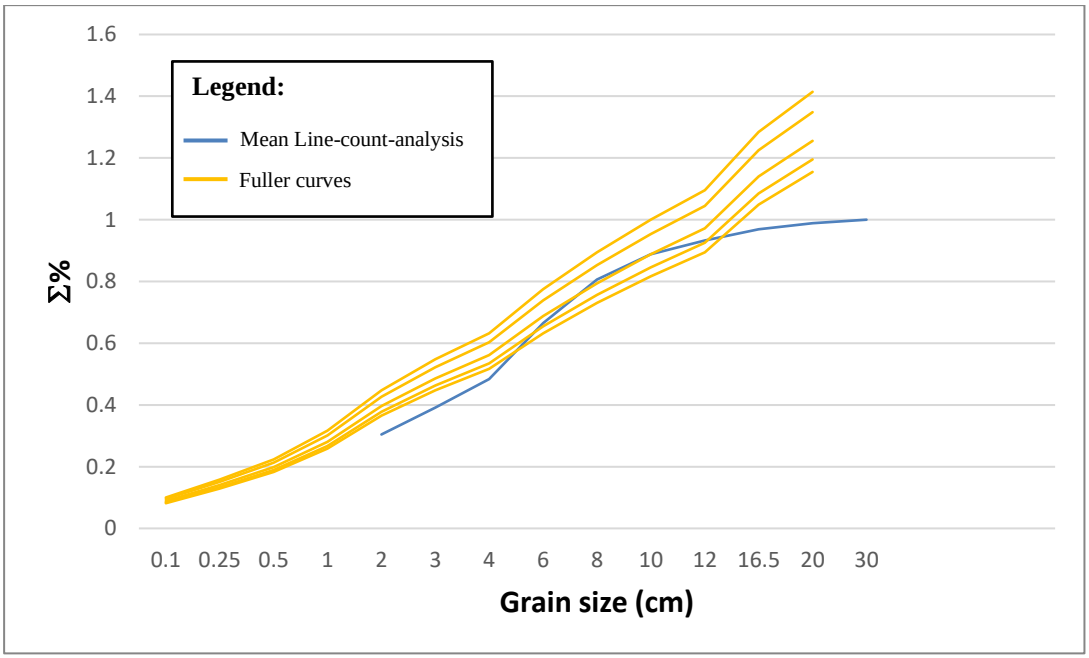
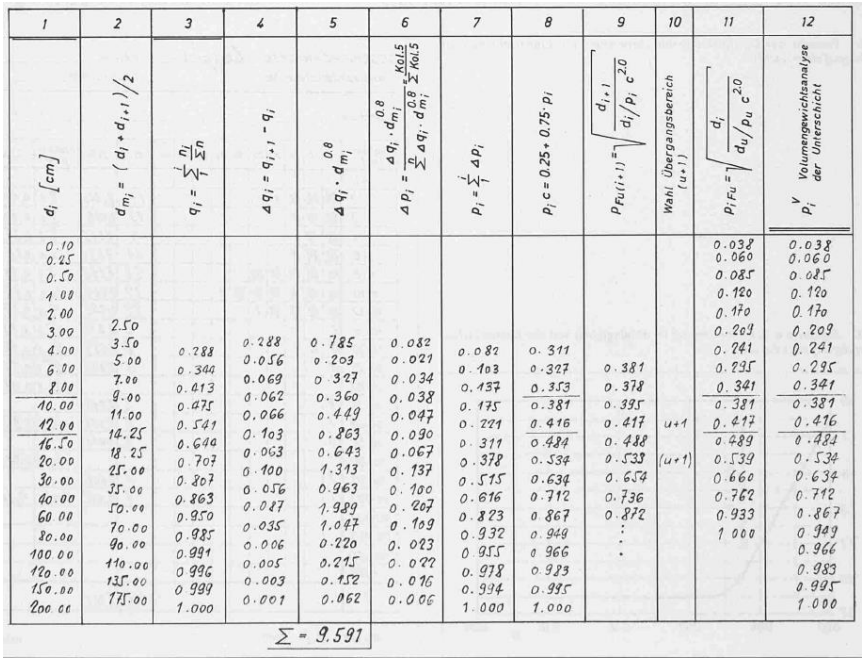


Figure 43: Assessment of which Fuller curve best fits with the mean Line-count-analysis of the Salza River study area.

Finally, the mean Line-count-analysis and the selected Fuller curve were used to calculate an approximated grain size distribution for both smaller and larger grain sizes of the Salza River study area. This was done by following the calculation steps in Figure 44 where the data of the mean Line-count analysis was inputted into column 3 and the data from the selected Fuller curve was inputted into column 11, resulting in a final approximated grain size distribution in column 12.



1	2	3	4	5	6	7	8	9	10	11	12
d_i [cm]	$d_{m_i} = (d_i + d_{i+1})/2$	$q_i = \frac{n_i}{\sum n}$	$\Delta q_i = q_{i+1} - q_i$	$\Delta q_i \cdot d_{m_i}^{0.8}$	$\Delta p_i = \frac{\Delta q_i \cdot d_{m_i}^{0.8}}{\sum \Delta q_i \cdot d_{m_i}^{0.8}} \cdot \frac{\text{Kol.5}}{\sum \text{Kol.5}}$	$p_i = \sum_1^i \Delta p_i$	$p_i\, c = 0.25 + 0.75 \cdot p_i$	$p_{Fu(i+1)} = \sqrt[n]{\frac{d_{i+1}}{d_i / p_i\, c^{2.0}}}$	Wahl Übergangsbereich (u+1)	$p_{i\,Fu} = \sqrt[n]{\frac{d_i}{d_u / p_u\, c^{2.0}}}$	Volumengewichtsanalyse der Unterschicht $\overset{v}{p_i}$
0.10										0.038	0.038
0.25										0.060	0.060
0.50										0.085	0.085
1.00										0.120	0.120
2.00										0.170	0.170
3.00	2.50									0.209	0.209
4.00	3.50	0.288	0.288	0.785	0.082	0.082	0.311			0.241	0.241
6.00	5.00	0.344	0.056	0.203	0.021	0.103	0.327	0.381		0.295	0.295
8.00	7.00	0.413	0.069	0.327	0.034	0.137	0.353	0.378		0.341	0.341
10.00	9.00	0.475	0.062	0.360	0.038	0.175	0.381	0.395		0.381	0.381
12.00	11.00	0.541	0.066	0.449	0.047	0.221	0.416	0.417	u+1	0.417	0.416
16.50	14.25	0.644	0.103	0.863	0.090	0.311	0.484	0.488		0.489	0.483
20.00	18.25	0.707	0.063	0.643	0.067	0.378	0.534	0.533	(u+1)	0.539	0.534
30.00	25.00	0.807	0.100	1.313	0.137	0.515	0.634	0.674		0.660	0.634
40.00	35.00	0.863	0.056	0.963	0.100	0.616	0.712	0.736		0.762	0.712
60.00	50.00	0.950	0.087	1.989	0.207	0.823	0.867	0.872		0.933	0.867
80.00	70.00	0.985	0.035	1.047	0.109	0.932	0.949	⋮		1.000	0.949
100.00	90.00	0.991	0.006	0.220	0.023	0.955	0.966	⋮			0.966
120.00	110.00	0.996	0.005	0.215	0.022	0.978	0.983	⋮			0.983
150.00	135.00	0.999	0.003	0.152	0.016	0.994	0.995	⋮			0.995
200.00	175.00	1.000	0.001	0.062	0.006	1.000	1.000	⋮			1.000
				$\Sigma = 9.591$							

Figure 44: FEHR'S Form to translate a Line-count-analysis of the top layer into a Volume weighted analysis of the lower grain sizes and estimate of fine sediment via Fuller (FEHR 1987: 1108).

Lastly, the calculated grain size distribution, consisting of 14 grain sizes, had to be condensed into 9 grain sizes, since the modelling software CAESAR-Lisflood only takes a maximum of 9 grain sizes. This was done by deleting 5 classes which did not alter the general grain size distribution, which is similar to reducing the resolution of a map. All results of the described methods will be presented in the results section in chapter *6.4.1 Granulometric analysis*.

Suspended grain size approximation

While being in the field, a sudden heavy rainfall event caused an increase in river discharge and a rise in the suspended sediments of the river later that evening. I decided to attempt to capture the suspended sediments with a primitive method, in foresight of possibly being able to use the results for the sediment input during the modelling.

I simply used two 1.5 l bottles attached to a string and lowered the bottles into the river at the bridge, between river km 61.9 and 62 filling both, see Figure 45.



Figure 45: Lowering of bottle into the river for suspended sediment collection between river km 61.9 and 62 (left) and two 1.5l bottles filled with suspended sediments in the Salza River study area (right).

Back home, I waited for the solids to deposit a couple of days later and decanted the clear water see Figure 46 on the left. The remaining solids and water from each bottle were drained into a separate coffee filter. The filters were weighed to 3 dp before and left to air-dry.



Figure 46: Deposited suspended solids (left), drained suspended solids (middle) and dried suspended solids (right).

Finally, I weighed each filter with the dried suspended sediment to obtain a simple concentration value of suspended sediments per 1.5 l bottle.

Modelling

The modelling of the Salza River study area will be done by using the open-source software CAESAR-Lisflood (Version 1.9j) developed by Tom J. Coulthard from the University of Hull, U.K. A very detailed description of the structure and build-up of the software can be obtained from the paper COULTHARD et al. 2013 but for my application a short description will suffice, see below.

"CAESAR-Lisflood is a geomorphological / Landscape evolution model that combines the Lisflood-FP 2D hydrodynamic flow model (BATES et al, 2010) with the CAESAR geomorphic model to simulate erosion and deposition in river catchments and reaches over time scales from hours to 1000's of years." [9]

CAESAR-Lisflood will be used in this thesis in "reach-mode" to model, visualize and quantify areas of future erosion and accumulation within the river flow of the Salza River study area for the years 2019 - 2050 using four different discharge scenarios. Further, changes in the D50 grain size (median diameter at 50% of the particle size distribution) of the surface layer of sediment will be examined, changes in sinuosity of the river reach from 2019 - 2050 and changes in cross sections as well as changes in the elevation profile. All needed steps to acquire the result are described below and all necessary information on CASEAR-Lisflood were gathered via the CASEAR-Lisflood Wiki found on https://sourceforge.net/p/caesar-lisflood/wiki/Home/ (last opened: on 02.11.2021).

Data preparation

Before being able to use CAESAR-Lisflood in its described function the data must be prepared and adapted to fit the input requirements of the software.

The first main input, the DEM from Table 10 which provides the map for the model, must be reduced in pixel resolution to speed up the modelling process. The original resolution was 1 x 1 m and was reduced to 10 x 10 m. This was accomplished by loading the DEM into QGIS, right clicking it, and selecting the "Save Raster Layer as…". In the window, seen in Figure 47, the horizontal and vertical resolution were adapted to 10, a new file name was generated, and the button OK was selected. The output DEM was the DEM data file for all further modelling.

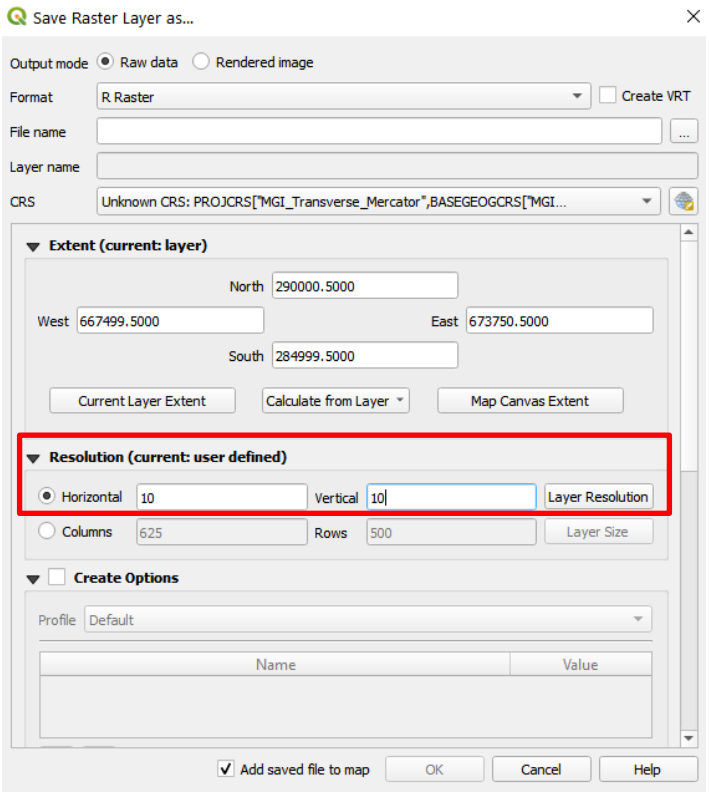


Figure 47: Save Raster Layer as... window in QGIS to reduce the DEM resolution, see red box.

The second input which had to be created, was a Bedrock DEM to incorporate the confining margins obtained during the prior mapping process and described in the second paragraph in chapter 5.2.2 Methods. *"Within CAESAR, bedrock is effectively a layer below which erosion cannot happen (not landslides etc..). This file should be in the same format, and must be the same size as the main DEM loaded."* [9]. To compile the bedrock DEM first the elevation of every pixel in the prior compiled 10 x 10 m DEM was reduced by 10m. This was done using the Raster→**Raster Calculator** in QGIS with the expression *""DEM 10x10m@1"- 10"* see Figure 48. The result was a new DEM where the height of every pixel was reduced by 10m.

Next the confining margins line-vector shapefile had to be converted to a raster by using the Raster→Conversion→**Rasterize** tool, see Figure 49 on the left. Next the Raster Calculator was used again to subtract the rasterized confining margin with the original 10x10m resolution DEM obtaining a Raster file with elevation data. This was done with the expression *""DEM 10x10m@1"- raster confining margin"*. Finally, the DEM with the 10m lower elevation and the Raster file with elevation data were joined using the Raster→Miscellaneous→**Merge** tool, as seen in Figure 49 on the right to obtain the final Bedrock data file.

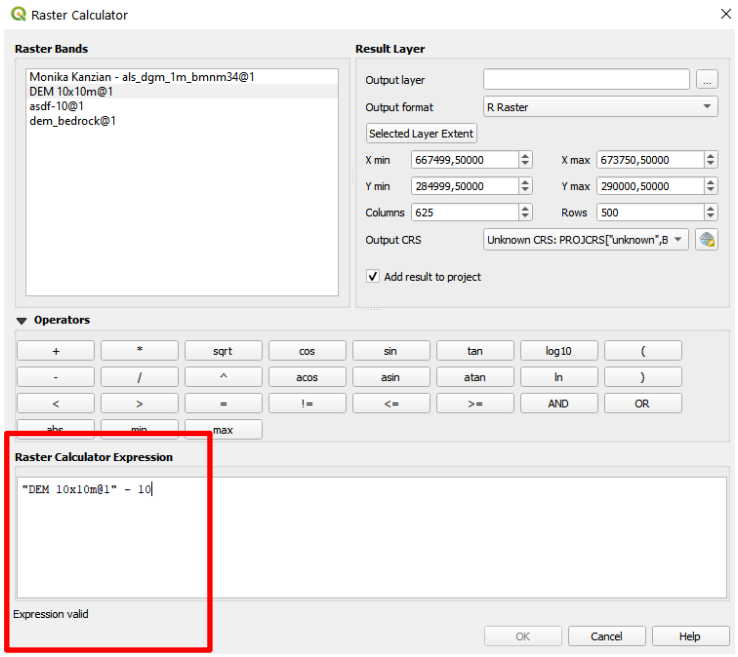


Figure 48: Raster calculator window in QGIS to decrease the DEM height by 10m, see red box.

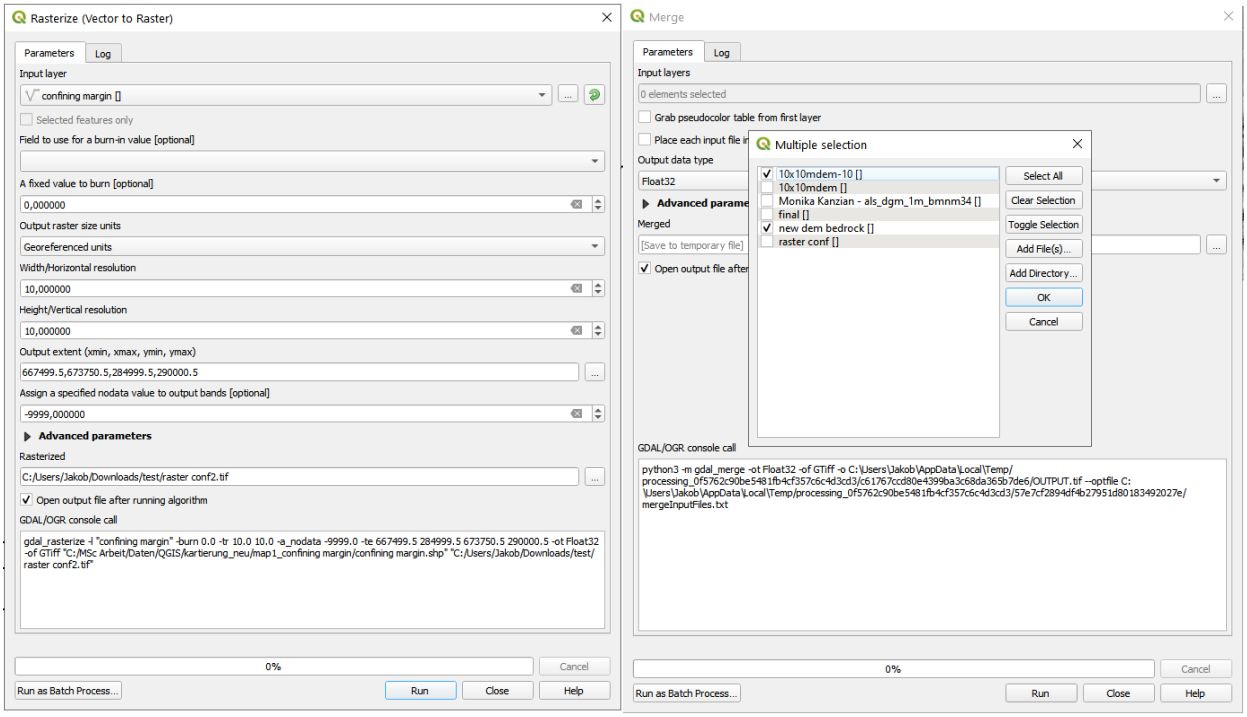


Figure 49: Rasterize window in QGIS (left), Merge window in QGIS (right).

Below in Figure 50 the integration of the confining margin shapefile on the top right with the DEM -10 m altitude file on the top left is displayed. The confining margins stand out visually in the bottom final Bedrock data file and help in making the modelling more realistic by restricting erosion in the DEM where there are confining margins.

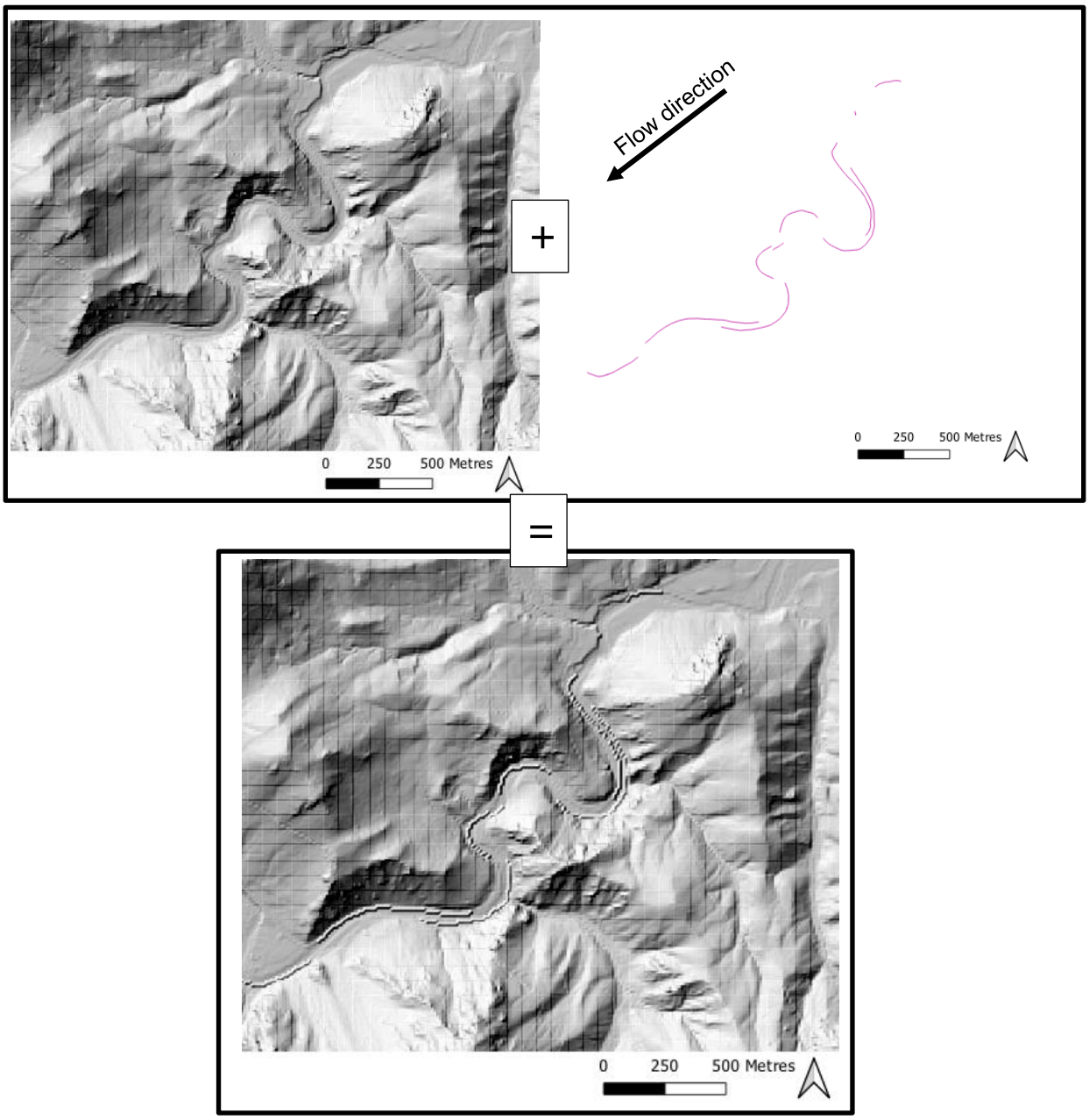


Figure 50: Merging of the DEM -10m altitude file (top left) with the confining margin line shapefile (top right) to create the final Bedrock data file (bottom) used in the modelling of the Salza River study area. Map excerpt located between river km 54.1 and 58.2.

The third input data which had to be prepared was the hydrological discharge data. CAESAR-Lisflood uses hourly discharge data and reads the data for every year in the format on the right from a .txt file. Every row represents one hour where the first number is a consecutive number and the second number being an hourly discharge value in m³/s.

```
0 4.08
1 4.11
2 4.24
3 4.14
…
```

Therefore, the discharge data from Table 9 for the timeframe 01.01.1976 - 31.12.2018 had to be prepared by extracting the hour values per year and saving them in the above format in a .txt file.

As mentioned before, the modelling will be executed using four different discharge scenarios for 2019 - 2050. The four scenarios which were decided on by my supervisor and myself are: 1) similar discharge in 2019 - 2050 compared to 1976 - 2018, 2) more discharge in 2019 - 2050 compared to 1976 - 2018, 3) a lot more discharge in 2019 - 2050 compared to 1976 - 2018 and 4) only discharge from the year 2014, the year in which a flooding event caused the erosion hotpot described in chapter *3.2 Hot spot between river km 58.7* - 58.8.

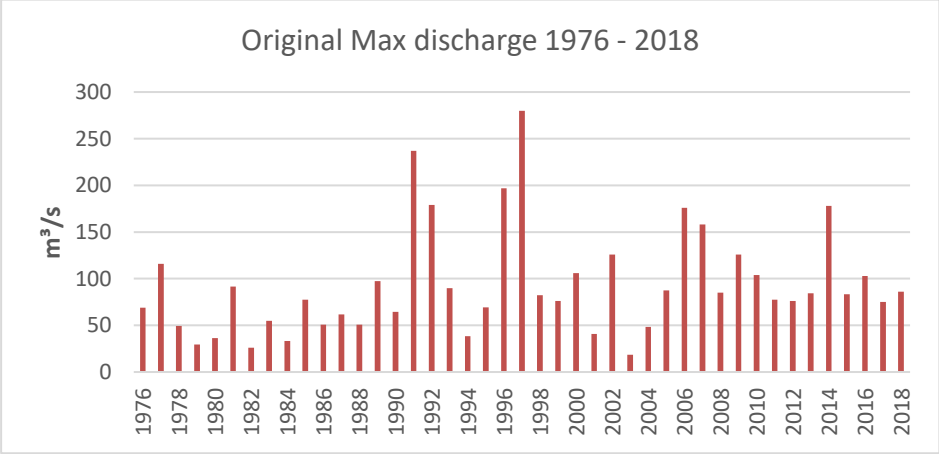


Figure 51: Original max discharge 1976 - 2018 of the Salza River study area.

Table 11: Statistical data for the original discharge 1976 - 2018 (left) and number of flooding events of HQ1, HQ5 and HQ10 for the adapted original discharge 1976 - 2018 (right).

Statistics	Original discharge (m³/s) 1976 - 2018
Mean	7,22
Min	1,51
Max	92,94

HQ events	Original discharge (m³/s) 1976 - 2018
HQ1 (50m³/s)	25
HQ5 (100m³/s)	10
HQ10 (126m³/s)	5

The basis for evaluating the scenarios was made, by examining the discharge data from 1976 - 2018, specifically the max discharge as seen in Figure 51, but also the other statistical values and number of flooding events as listed in Table 11. The goal was to create a set of 32 years (from 2019 - 2050) which best represent each described scenario in the prior paragraph and evidently had the numbers to prove it. Except for the fourth scenario, which only used the discharge data of the year 2014 for every year from 2019 - 2050.

To accomplish this, a hundredfold of 32-year sets were generated using the function **RANDBETWEEN(1976, 2018)** in Microsoft Excel. From the generated sets, only 3 were picked which best fit the description of similar, more and a lot more discharge in 2019 - 2050 compared to 1976 - 2018, see Figure 52. Looking at Table 12, the mean as well as the max increased distinctively for every scenario compared to the original data, however the mean discharge of the 2014 discharge was noticeably lower. Looking at Table 13 the number of HQ1 flooding events are similar, but there is a clear increase in the amount of HQ5 and HQ10 flooding events of the generated scenarios compared to the original data. The generated scenarios will provide all data needed for the hydrological input data into CAESAR-Lisflood.

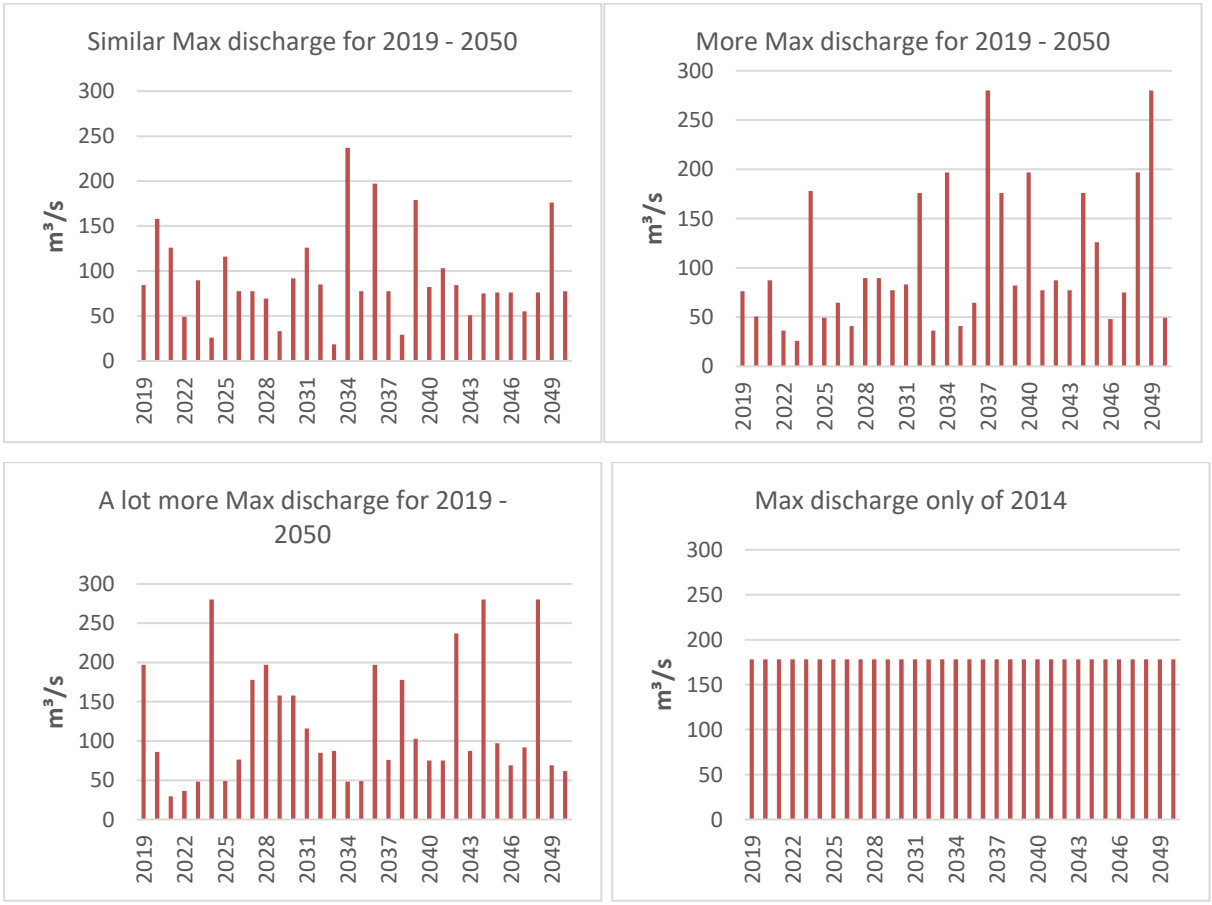


Figure 52: Max discharge scenarios used for the modelling of the Salza River study area.

Table 12: Statistical data for the four discharge scenarios for 2019 - 2050.

Statistics	Similar discharge(m^3/s) for 2019 - 2050	More discharge (m^3/s) for 2019 - 2050	A lot more discharge (m^3/s) for 2019 - 2050	2014 discharge (m^3/s) for 2019 - 2050
Mean	7.25	7.4	7.7	6.05
Min	1.63	1.38	1.35	2.57
Max	237	280	280	179

Table 13: Number of flooding events of HQ1, HQ5 and HQ10 for the four discharge scenarios for 2019 - 2050.

HQ events	Similar discharge(m^3/s) for 2019 - 2050	More discharge (m^3/s) for 2019 - 2050	A lot more discharge (m^3/s) for 2019 - 2050	2014 discharge (m^3/s) for 2019 - 2050
HQ1 (50m^3/s)	27	24	26	32
HQ5 (100m^3/s)	9	10	13	32
HQ10 (126m^3/s)	5	9	11	32

And lastly the approximated grain size distribution from the prior chapter had to be prepared to fit the CAESAR-Lisflood requirements.

Parametrization (pre-modelling)

During the Parametrization, which is a pre-modelling step prior to the final modelling, all available parameters within CAESAR-Lisflood are analysed regarding their applicability for the Salza River study area. The results of this pre-modelling yield the best usable parameter combination for the final modelling. Particular emphasis lies on the sediment parameters in the sediment tab as seen in the red rectangle in Figure 53, since it is important to have a realistic rate of erosion and accumulation, so any future modelling delivers representable results for the outlook of the Salza River study area. Moreover, in order to be able to work with CAESAR-Lisflood, the system language of the PC used must be changed to English.

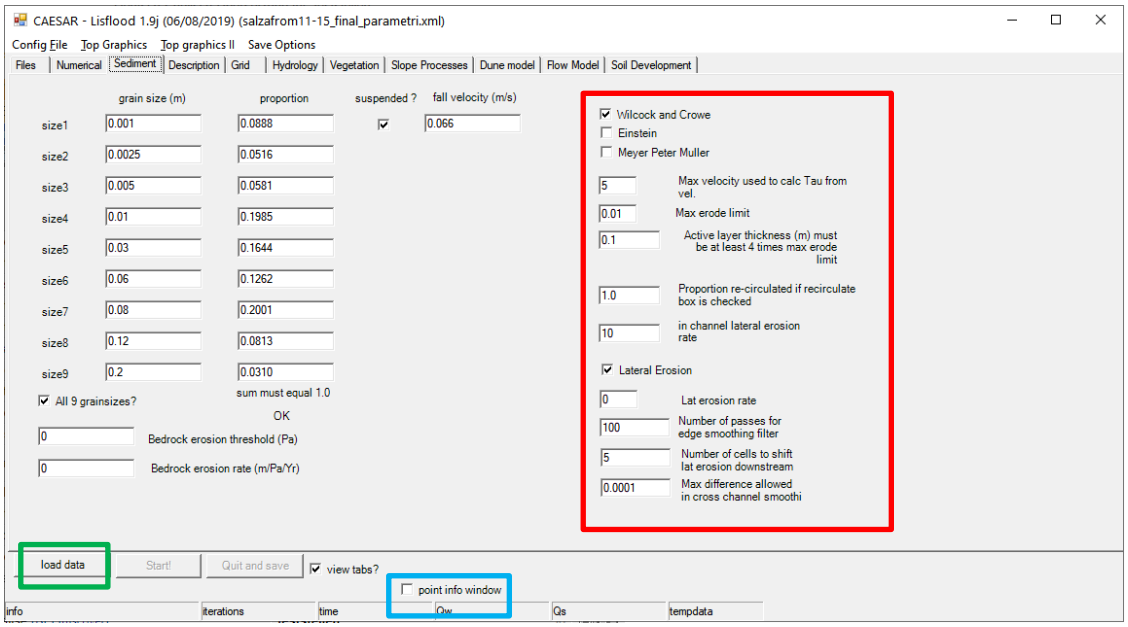


Figure 53: Open sediment tab in CAESAR-Lisflood.

An initial minor inconvenience regarding the scan flight date of the DEM turned out to be quite helpful. The timeframe of the flight date was between the 26.08.2011 and 27.08.2011 see Table 10, while discharge hourly data is available from 01.01.1976 - 31.12.2018. Further the erosion hotspot, described in chapter *3.2 Hot spot between river km 58.7* - 58.8 , formed after a flooding event in May of 2014 and is therefore not yet visible in the DEM recorded in 2011.

In order to assess the optimal parameters, the prepared inputs from chapter *5.4.2 Methods* will be used to pre model the timeframe 27.08.2011 - 31.12.2018. For every relevant parameter, especially all sediment parameters, CAESAR-Lisflood will be run separately. When the output results approximate the optical rate and area of erosion and accumulation in the Salza River study area and depict the erosion hotspot in 2014, this set of parameters will be used for the final modelling.

Final modelling

In the last step, the final modelling uses the prior prepared data from chapter *Data preparation* as well as the final chosen parameters assessed in the preceding chapter *Parametrization (pre-modelling)* to model the timeframe 2019 - 2050 of the Salza River study area using four different discharge scenarios developed in chapter *Data preparation*.

In order to load the data into CAESAR-Lisflood, the data files of the DEM, Bedrock DEM and discharge data of the selected year must be in the same folder as the .exe file of the software in .txt format. The name of the DEM and Bedrock DEM .txt files must be added in the File tab and the discharge .txt file in the Hydrology tab. The sediment data can simply be added by writing the grain size (m) as well as its proportion in the cells in the Sediment tab, see Figure 53 on the left. Now the load data button in the bottom left corner of CAESAR-Lisflood can be pressed, see green rectangle in Figure 53.

One final adaptation must be made, which is deciding on the location of where the discharge data enters in the DEM while modelling. First the DEM must be selected in the top graphics tab to make it visible in CAESAR-Lisflood. Now via selecting the point info box, see blue rectangle in Figure 53, the cell properties window can be opened, see image on the right in Figure 54. When clicking in the DEM the X and Y-coordinates as well as the elevation is displayed in the window. These X and Y values must be added in the Hydrology tab.

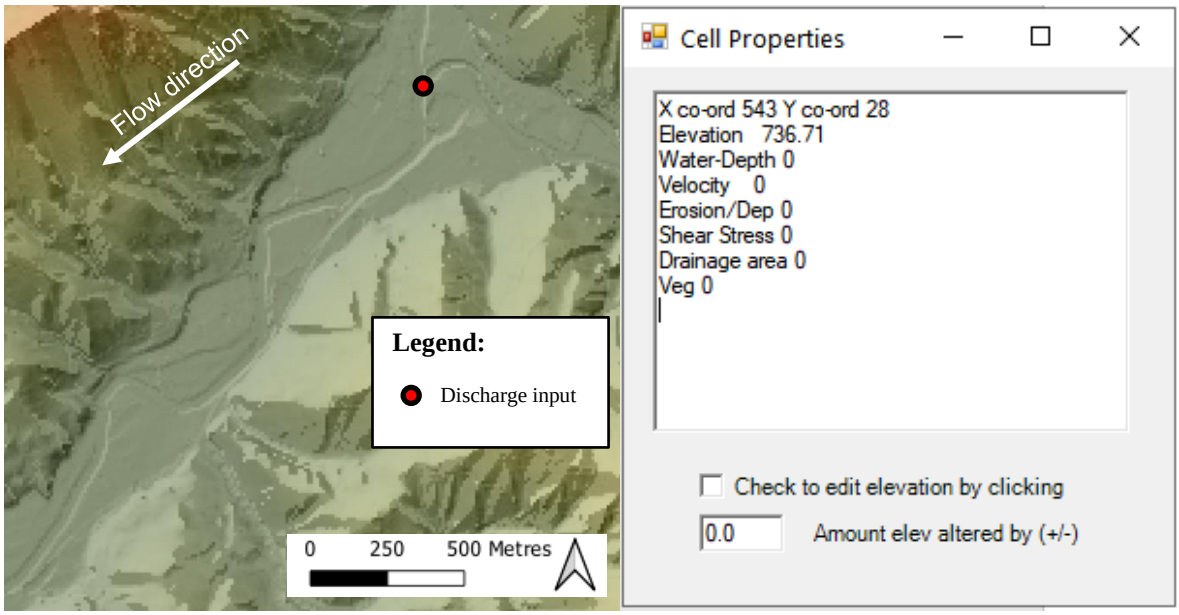


Figure 54: Discharge input location (left) and Cell Properties window (right) in CAESAR-Lisflood.

Finally, the start button can be pressed, see red rectangle in Figure 55, and CAESAR-Lisflood starts modelling for the selected timeframe of one year.

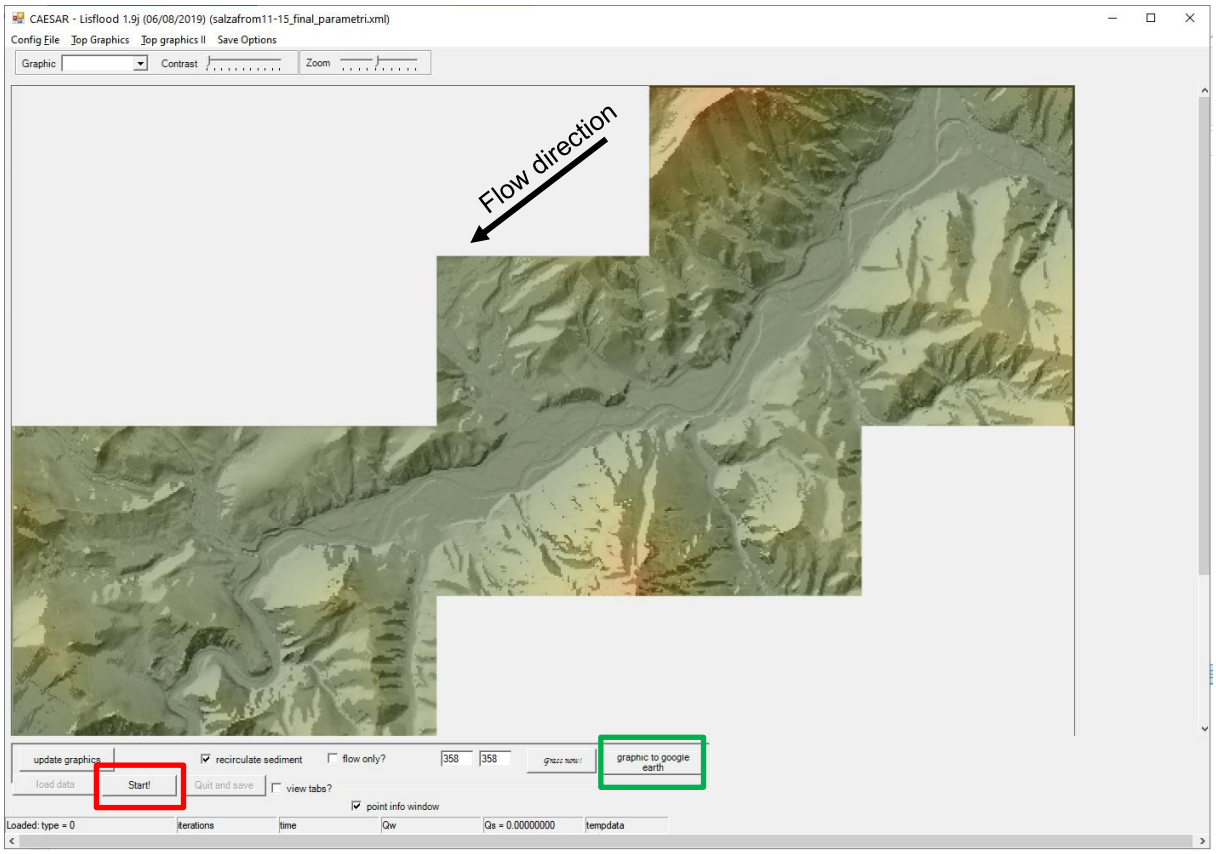


Figure 55: Final window when starting a CAESAR-Lisflood modelling.

After every modelling, CEASAR-Lisflood delivers four outputs in .txt format. These are 1) D50top.txt, the D50 grain of the surface layer of sediment, 2) elev.txt, the new DEM, 3) elevdiff.txt, a DEM of Difference (DoD) of the input and output DEM and 4) grain.txt, the grain size information which is not needed in this thesis modelling. Additionally, screenshots were made via pressing the graphic to google earth button during the modelling, see green rectangle in Figure 55.

The D50 results for every discharge scenario were prepared in Microsoft Excel and will be presented in one diagram with the linear trendlines from every scenario in another diagram. The 2050 DEM results will be used to determine any visual changes which happened during the modelling and will again be analysed numerically via the Sinuosity Index in QGIS. The results from the sinuosity step will also provide data for constructing altitude profiles in QGIS. The DEM of Difference (DoD) results were prepared in Excel and will be presented as a diagram for each induvial scenario as well as overall for every scenario providing numerical results in m^3 of the rate of erosion and accumulation from 2019 - 2050.

6. Results

In the following chapter all results created throughout the thesis will be presented using the data and methods described in the previous chapters.

6.1 Reconstruction of past hydro-geomorphic changes of the Salza River

At first in chapter 6.*1.1*, the historical maps of the whole Salza River study area, listed in Table 1, will be presented and historical changes will be compared using the available old maps. Changes in the available orthophotos, listed in Table 2, will be compared and described in chapter 6.*1.2*. The sinuosity index of the whole Salza River study area will be analysed in chapter 6.*1.3* and finally the sinuosity index of the erosion hotspot as well as any changes in the cross section of the hotspot will be analysed in chapter 6.*1.4*.

6.1.1 Historical maps of the study area dating 1678 - 1887

The oldest available map of the Salza River study area in Styria, is the so called Vischer map, which was drawn by the Austrian cartographer Georg Matthäus Vischer in 1678. In the below Figure 56 a map excerpt of the much larger Vischer map, showing the entire state of Styria scaled ca. 1:150,000, can be seen with the presumed location of the Salza River study area. With the topographical tools in 1678 being relative primitive compared to today's mapping detail, the Salza River in the study area is visualised as one line with 2 curves. The begin of the study area can be pinpointed with certainty to the river km 62.85 as seen in Figure 4, where the tributary of the Salza River, the Aschbach flows into the Salza River. The lower end of the study area being at river km 54.1 can only be assumed. The general lack of detail in the oldest topographical map however does not allow for a more specific comparison with a sinuosity index.

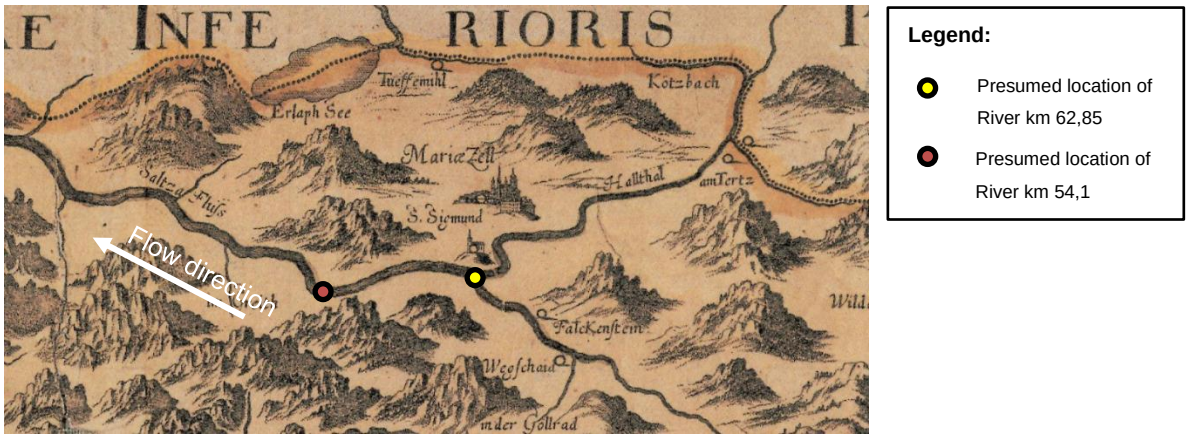


Figure 56: Map excerpt of the Salza River study area, taken from the Vischer map 1678. Source: https://upload.wikimedia.org/wikipedia/commons/0/0b/Steiermark_Vischer_1678.jpg

The second oldest map available of the Salza River study area, recorded between 1784 and 1785, is the “Josephinische Land Aufnahme” also known as the first land survey of Austria. Named after the reigning Holy Roman Emperor Joseph II it was the first and at the time topographically very accurate map with a scale of 1:28,800. Comparing the below map excerpt of the Salza River study area, see Figure 57, with a more modern orthophoto of 2017 in Figure 4, we notice a overlap of the unconfined valley area, however the lower part of the study area was not yet mapped in much detail and is only depicted with a more or less straight line. We can pinpoint the location of river km 62.85 in the study area with certainty but can only presume the location of the river km 54.1 due to lack in mapping precision. The lack of detail also does not allow for a sinuosity index. Overall, the flow of the Salza River itself was also mapped more artistically than topographically accurate.

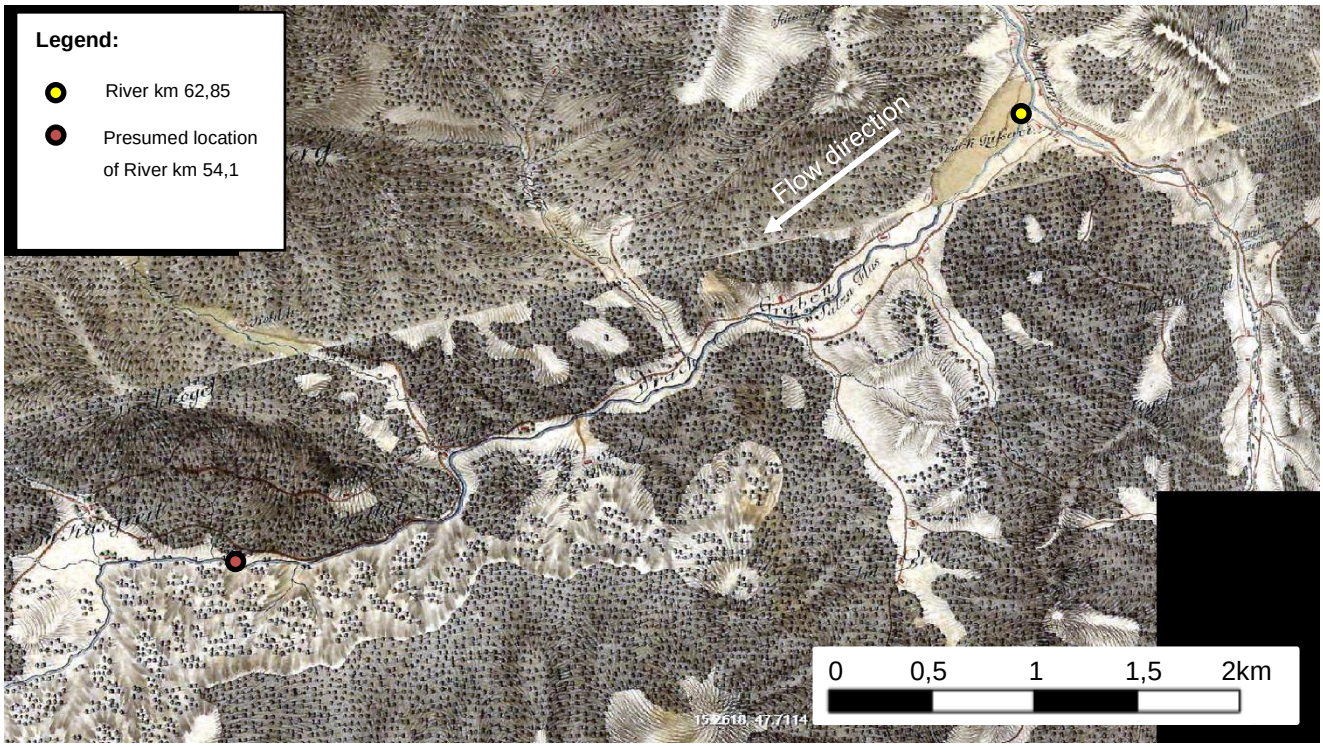


Figure 57: Map excerpt of the Salza River study area, taken from the Josephinische Land survey 1784 - 1785. Source: Mapire [7].

The third map available of the Salza River study area is the "Franziszeische Land Aufnahme" created between 1809 - 1818, also known as the second land survey of Austria. Named after the last reigning Holy Roman Emperor Francis II, it was created with a scale of 1:28,800. Like in the prior map, the below map excerpt of the study area in Figure 58, allows the river km 62.85 to be pinpointed very accurately, however the lower map of the study area was still not very precise, compared to a 2017 orthophoto see Figure 4,. Hence the exact location of river km 54.1 can only be presumed. Due to the lack in detail of the lower half, a sinuosity index would not be suitable for comparison. The position of the Salza River however in the unconfined area of the study area starts to resemble its today flow as can be seen in the 2017 orthophoto see Figure 4. A comparison to the map in Figure 57 however is not very meaningful due to lack in topographical accuracy.

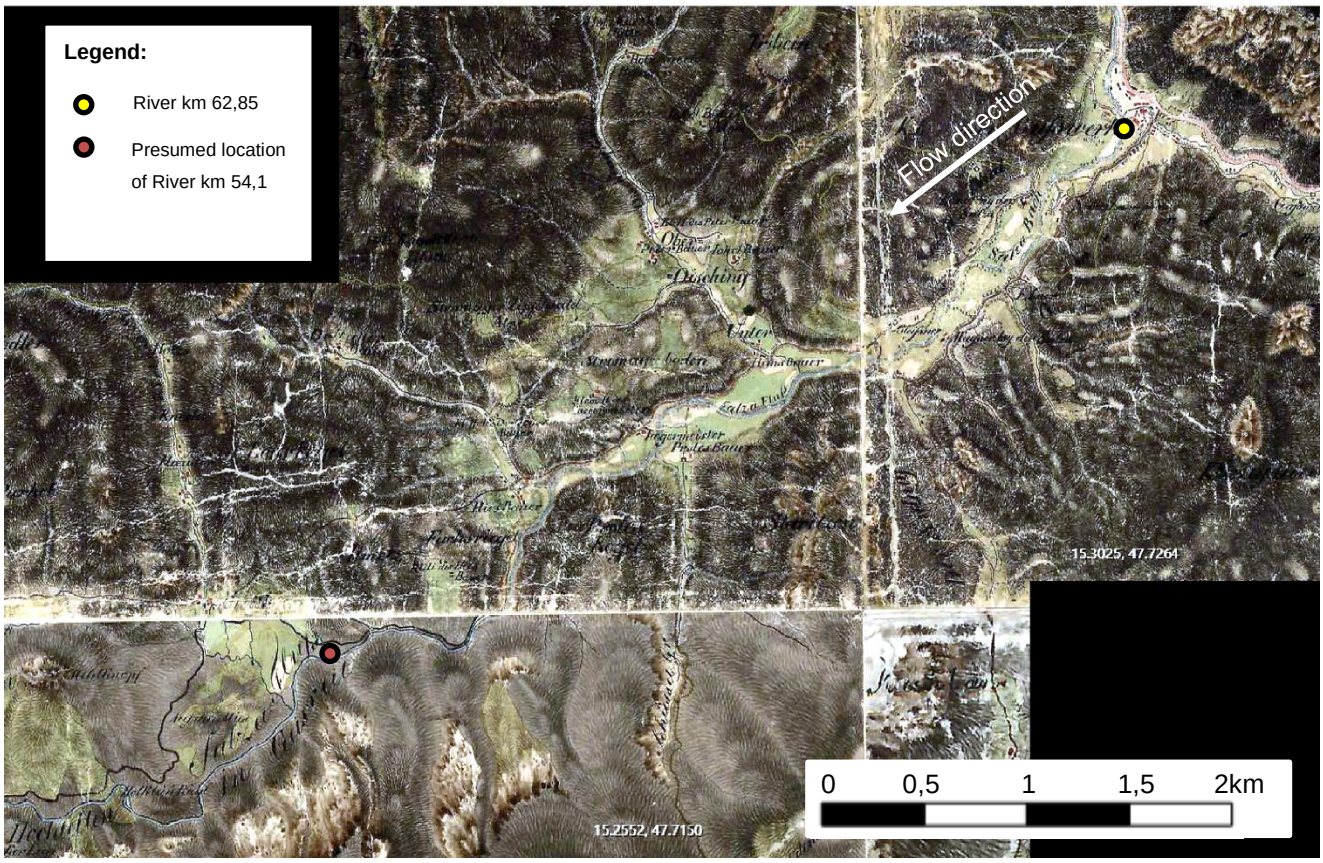


Figure 58: Map excerpt of the Salza River study area, taken from the Franziszeische Land survey 1809 - 1818. Source: Mapire [7].

The following map constructed between 1817 and 1861 shortly after the "Franziszeische Land survey" was the "Franziszeische cadastre" also named after the last reigning Holy Roman Emperor Francis II. Being the first cadastre of Austria containing a precise recording of all land lots it is also the oldest accurate depiction of the study area with a scale of 1:2,880. Comparing the below map excerpt in Figure 59 of the Salza River study area with an orthophoto of 2017, see Figure 4, we can with certainty locate the border of the unconfined and confined Salza River in the study area. Also, the river km 62.85 and 54.1 can be pinpointed. The unconfined valley of the upper part is very accurate and the flow of the Salza River has not changed very drastically compared to today, except for the hotspot where there seems to have been an island, see red box in Figure 59. The lower confined valley of the Salza River seems to be topographically very accurate with one exception. The bend of the river at the river km 54.1 is not as prominent and is probably lacking in detail. Overall, the detail is sufficiently accurate which allows for a comparison in the sinuosity index of the mapping.

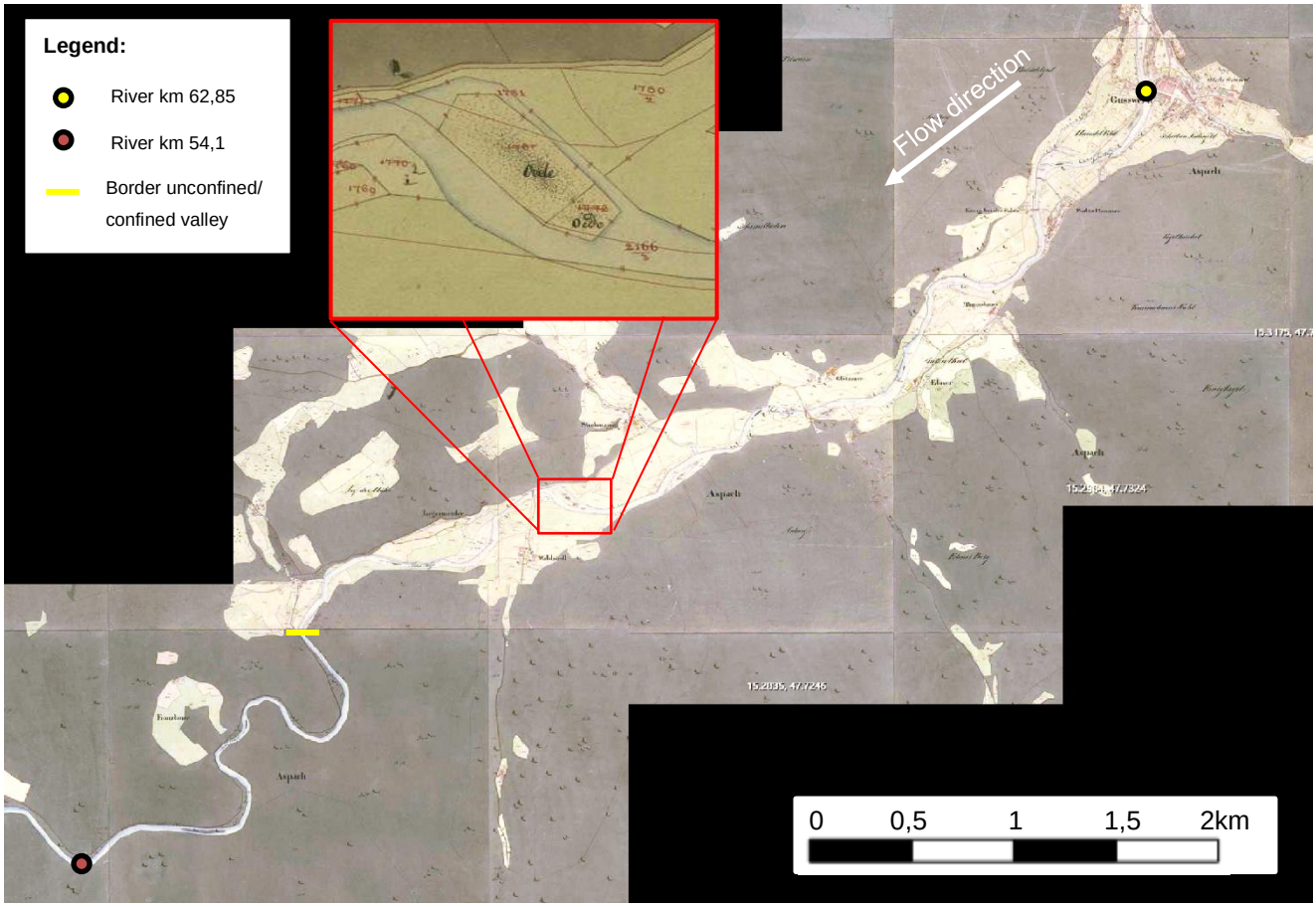


Figure 59: Map excerpt of the Salza River study area, taken from the Franziszeische cadastre 1817 - 1861. Source: Mapire [7].

The next available map of the Salza River study area dates from 1821-1836 and is the updated "Franziszeische Aufnahme" named after the last reigning Holy Roman Emperor Francis II it was also created with a scale of 1:28,800. It is the first topographically accurate mapping of the Salza River study area and is based on the prior Franziszeische cadastre. In the map excerpt below, in Figure 60, one can clearly pinpoint the location of the river km 62.85 and 54.1. Compared with the orthophoto of 2017 in Figure 4, one can also locate the border where the river flow changes from an unconfined to a confined valley. Only very minor changes of the flow of the river in the unconfined valley can be noticed compared with the prior map in Figure 59, mainly since the below map was largely based after the prior map. The flow of the river is depicted with accurate precision, with the same exception as in the last map being the bend at river km 54.1. However, the detail is sufficiently accurate which allows for a comparison in the sinuosity index of the mapping.

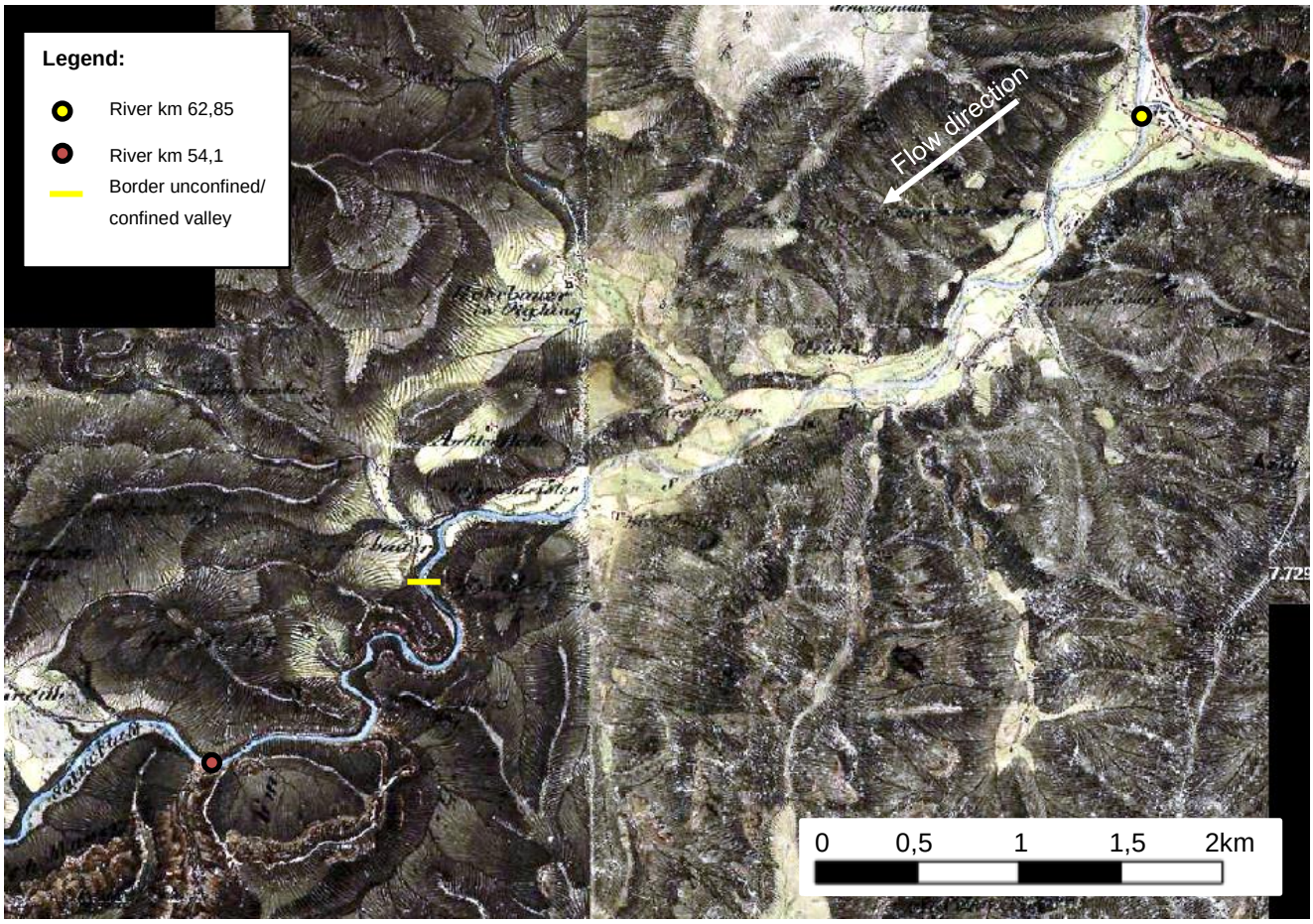


Figure 60: Map excerpt of the Salza River study area, taken from the updated Franziszeische Land survey 1821 - 1836. Source: Mapire [7].

Lastly the youngest of the historic maps available of the Salza River study area is the "Francisco-Josephinische Land Aufnahme" dating back to 1869-1887 and is known as the third land survey of Austria. It was constructed in a scale of 1:25,000 and shows the greatest detail compared to all other historic maps, see below map excerpt in Figure 61. Both River km, enclosing the study area can be pinpointed with certainty as well as the border of the unconfined and confined valley can be clearly seen compared to an orthophoto of 2017, see Figure 4. Its detail also allows for a sinuosity index. Compared with the prior map in Figure 60 we also notice that the Salza River does still flow in nearly the same riverbed with three main exceptions.

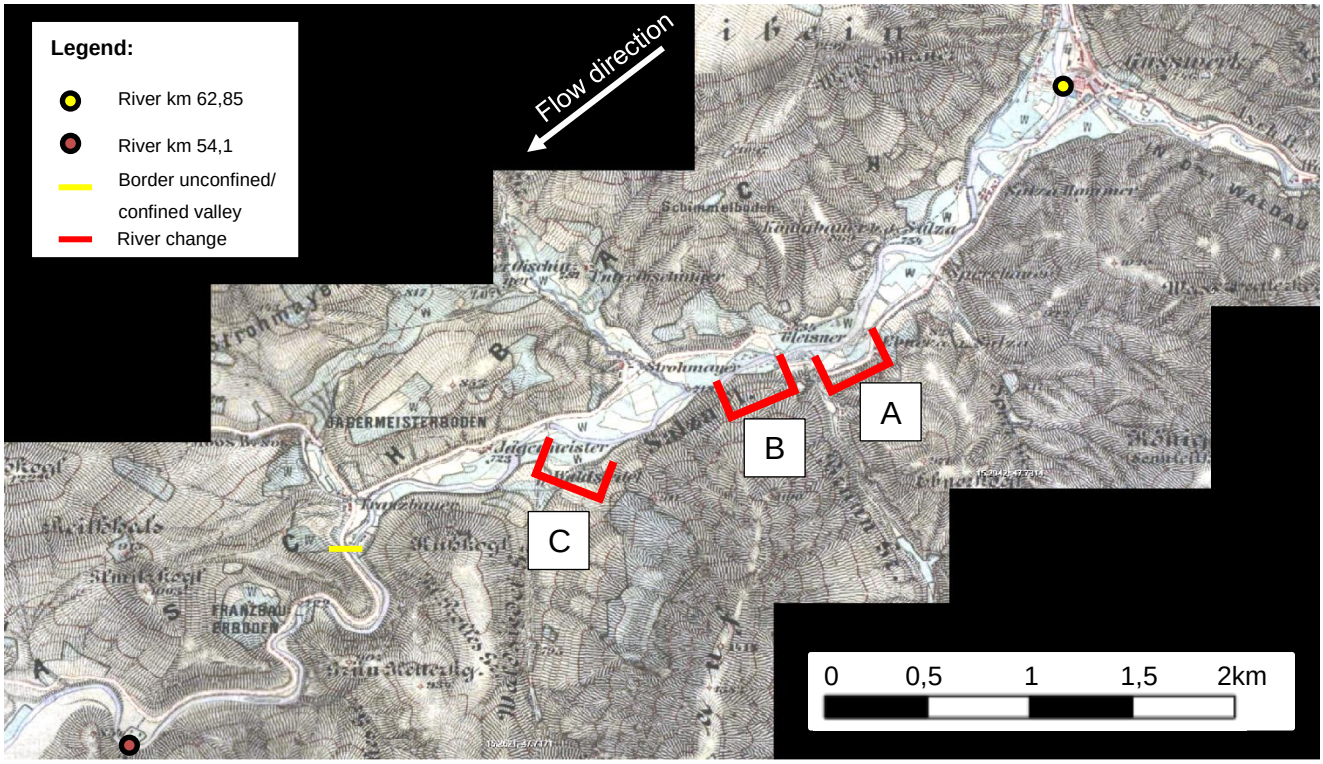


Figure 61: Map excerpt of the Salza River study area, taken from the Francisco-Josephinische Land survey 1869 - 1887, with changes marked in red. Source: Mapire [7].

Marked in red with the letter A in the map above, the river flow seems to have been narrowed and straightened a bit, which can be seen in the zoomed in map excerpt in Figure 62. Also marked in red with the letter B in the map above, a short stretch of the river has been straightened which previously meandered, also visible in Figure 62.



Figure 62: Visual changes A and B in the Franziszeische Land survey 1821 - 1836 (left) and Francisco-Josephinische Land survey 1869 - 1887 (right).

Also, the erosion hotspot at location C in Figure 61, has changed quite a bit see Figure 63. The flow of the river in the "Franziszeische Land Aufnahme" map seems to have split in two channels flowing around a vegetated island as mentioned also in Figure 59. In the "Francisco-Josephinische Land Aufnahme" the island has disappeared, and the river seems to have straightened.



Figure 63: Visual changes C of the hotspot in the Franziszeische Land survey 1821 - 1836 (left) and Francisco-Josephinische Land survey 1869 - 1887 (right).

6.1.2 orthophotos of the study area dating 2004 - 2017

The oldest available orthophoto from GIS-Styria of the Salza River study area was taken on 02.09.2004 see Figure 64. Being an orthophoto and not a drawn map, its detail is flawless, and a sinuosity index will be calculated later. Both river km as well as the border of the unconfined and confined valley can be pinpointed and the riverbed resembles the bed from the most recent orthophoto in 2017, see Figure 4. A comparison to the Francisco-Josephinische land survey from 1869 - 1887 shown in Figure 61 can be made by showing 7 changes of the river course in the unconfined valley. The confined valley has remained the same, however the orthophoto now depicts the bend at river km 54.1 with exact accuracy compared to the Francisco-Josephinische land survey.

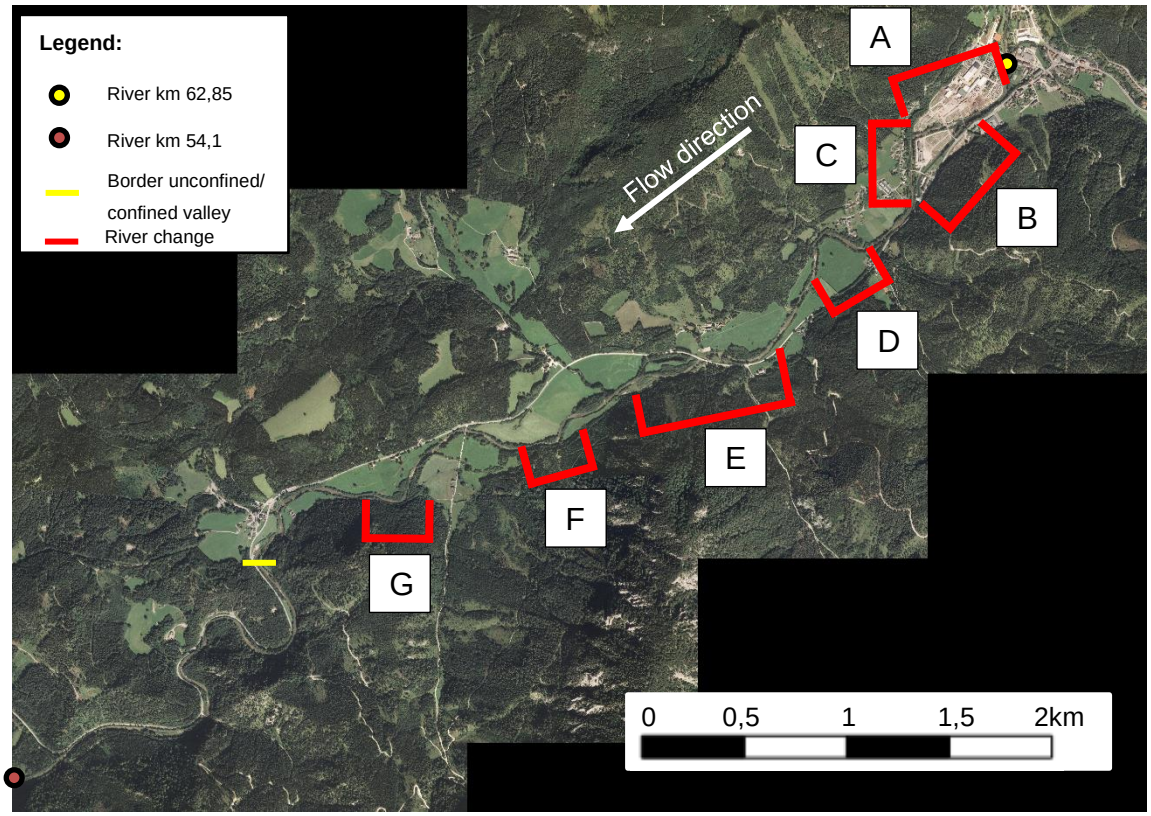


Figure 64: orthophoto of the Salza River study area taken on 02.09.2004. Source: GIS-Styria, with changes marked in red.

Firstly, looking at the visual changes marked A, B and C in the above overview Figure and zoomed into in Figure 65, the stretch marked with A, seems to have been straightened; Presumably due to the weir placed there. Combined with the weir placement, a second channel has been constructed, marked with B in the Figure flowing to a small hydroelectric power station. Also, the stretch marked with C, seems to have been narrowed and straightened.

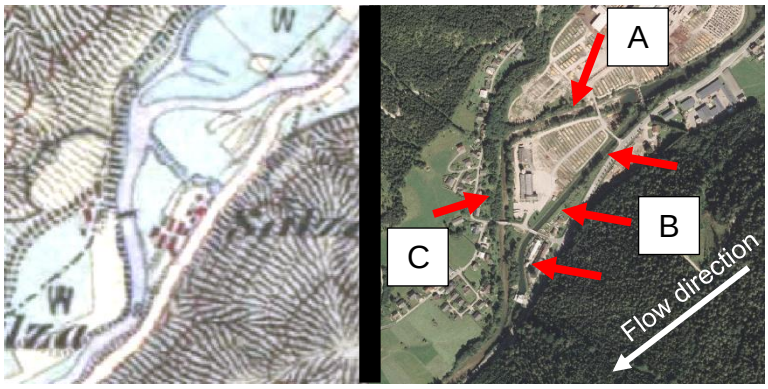


Figure 65: Visual changes A, B and C in the Francisco-Josephinische Land survey 1869 - 1887 (left) and the 2004 orthophoto (right).

Next the meander marked in D in the overview, see zoomed in map/orthophoto in Figure 66, seems to have been cutting into the bank causing the Salza River to increase in sinuosity in this section. Further the riverbed appears to have narrowed.



Figure 66: Visual changes D in the Francisco-Josephinische Land survey 1869 - 1887 (left) and the 2004 orthophoto (right).

The stretch marked with E in the overview, see zoomed in map/orthophoto in Figure 67, which was more or less straight in the Francisco-Josephinische Land survey 1869-1887, now meanders ever so slightly in the 2004 orthophoto.

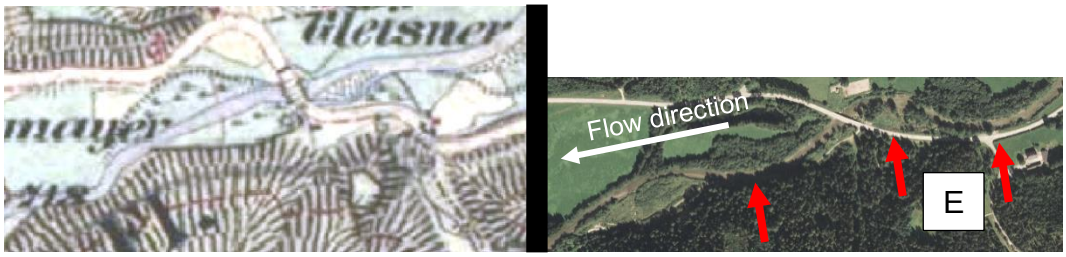


Figure 67: Visual changes E in the Francisco-Josephinische Land survey 1869 - 1887 (left) and the 2004 orthophoto (right).

The two bends marked with F in the overview, see zoomed in map/orthophoto in Figure 68, have increased in sinuosity and eroded the bank. The lower bend has formed a near perfect 90° angle.



Figure 68: Visual changes F in the Francisco-Josephinische Land survey 1869 - 1887 (left) and the 2004 orthophoto (right).

Lastly the bend at G in the overview, see zoomed in map/orthophoto in Figure 69, is also almost at a 90° angle and the stretch above the bend has straightened and eroded the orographic right bank.

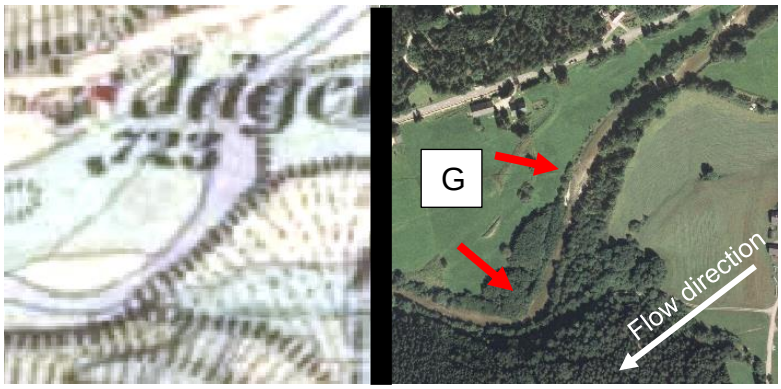


Figure 69: Visual changes G in the Francisco-Josephinische Land survey 1869 - 1887 (left) and the 2004 orthophoto (right).

The second available orthophoto from GIS Styria of the Salza River study area was taken on the 27.07.2009. Both river km as well as the border of the unconfined and confined valley can be pinpointed, and a sinuosity index will be made later. The riverbed seems unchanged at first glance, but a total of 6 minor changes could be determined between the prior orthophoto of 2004 from Figure 64 and the orthophoto of 2009 as seen in Figure 70.

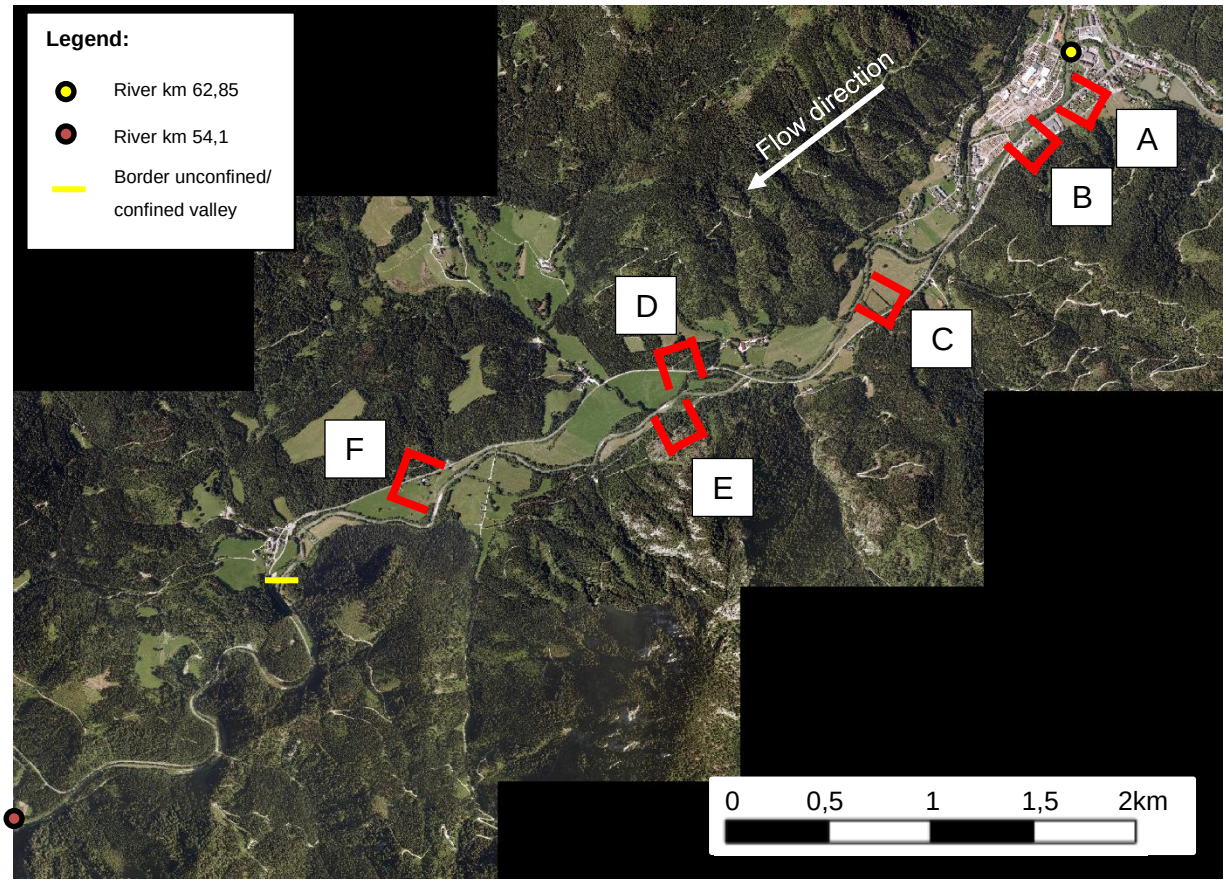


Figure 70: orthophoto of the Salza River study area taken on 27.07.2009. Source: GIS-Styria, with changes marked in red.

At the marked stretch A in the overview and zoomed into in Figure 71, we see on the orographic right side, that riparian vegetation was planted to presumably strengthen the bank.

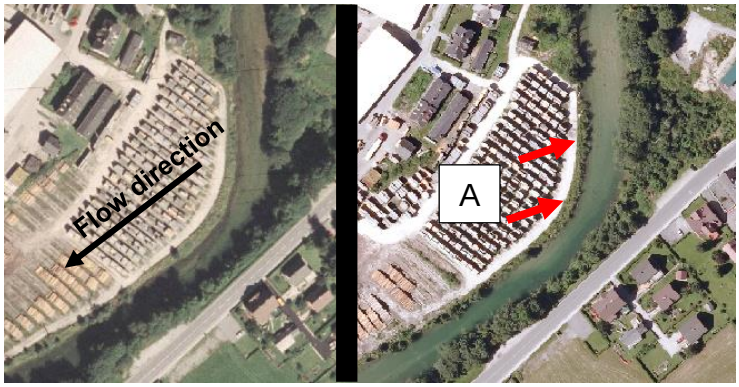


Figure 71: Visual changes A in the 2004 orthophoto (left) and the 2009 orthophoto (right).

In the location B in the overview, a fish ladder was constructed in the year 2006, allowing fish to travel passed the weir, see zoomed in map excerpt below in Figure 72.

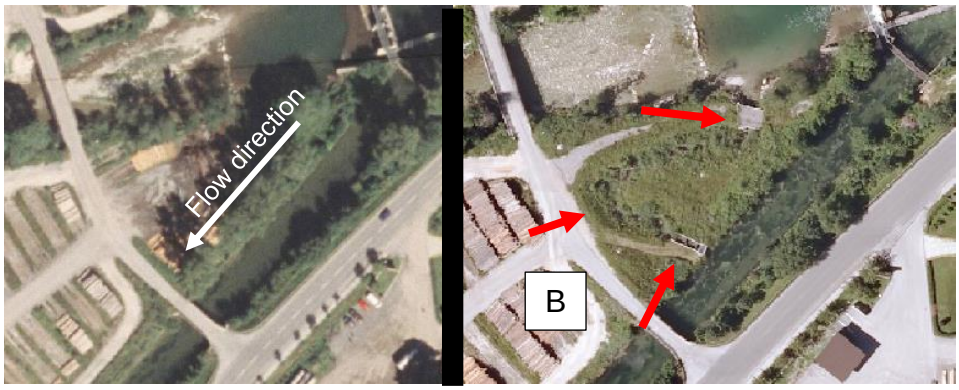


Figure 72: Visual changes B in the 2004 orthophoto (left) and the 2009 orthophoto (right).

In location C in the overview, a small strip of the riparian vegetation was removed on the orographic left side of the Salza River, see below Figure 73.



Figure 73: Visual changes C in the 2004 orthophoto (left) and the 2009 orthophoto (right).

At the location D in the overview, the riparian vegetation was removed at the outflow of a nearby fishpond, see Figure 74. Nearby at the location E, the river widened on the orographic left side caused by a washout where also part of the vegetation was removed.

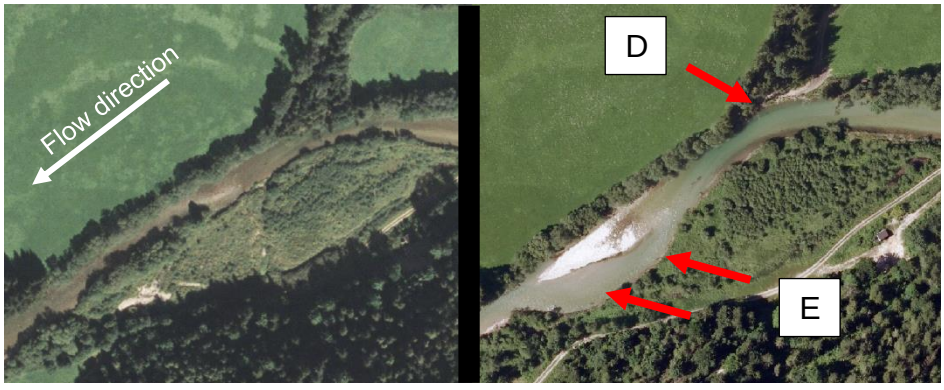


Figure 74: Visual changes D and E in the 2004 orthophoto (left) and the 2009 orthophoto (right).

Lastly at point F, see zoomed in orthophoto in below Figure 75, the riparian vegetation on the orographic right side of the river was removed and the river widened. Also, a small washout seems to have occurred.

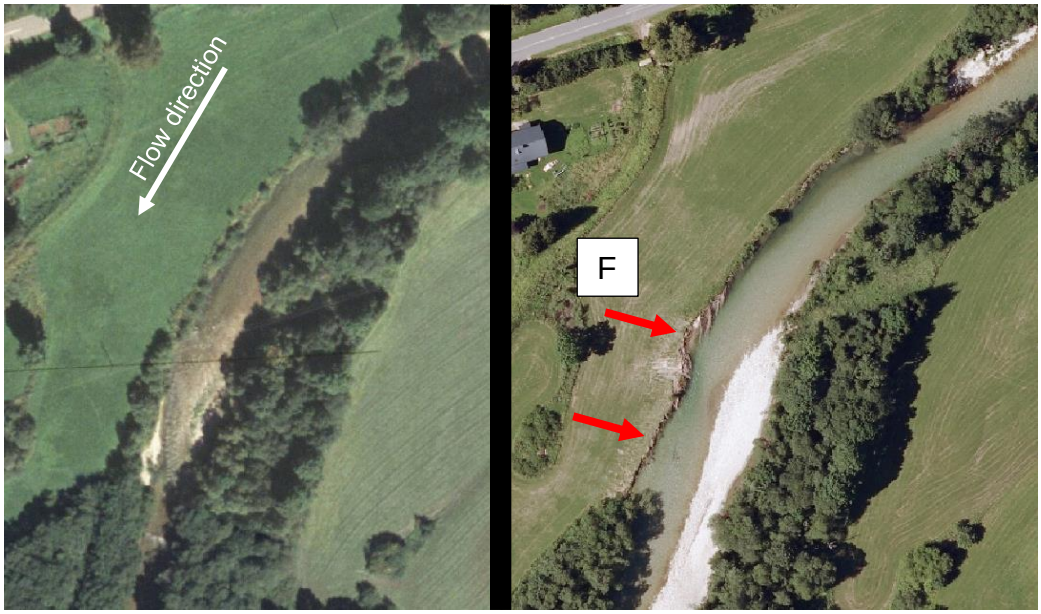


Figure 75: Visual changes F in the 2004 orthophoto (left) and the 2009 orthophoto (right).

It is worthwhile mentioning, that the riparian vegetation has grown quite decently in the 6-year time span alongside the whole Salza River study area. In comparison, the confined valley in the lower part of the study area has once again not changed at all.

The third available orthophoto from GIS Styria of the Salza River study area was taken on the 30.05.2011. Both river km as well as the border of the unconfined and confined valley can be pinpointed, and a sinuosity index will be made later. In total 5 changes were identified from 2009 to 2011 visible in the below overview map in Figure 76.

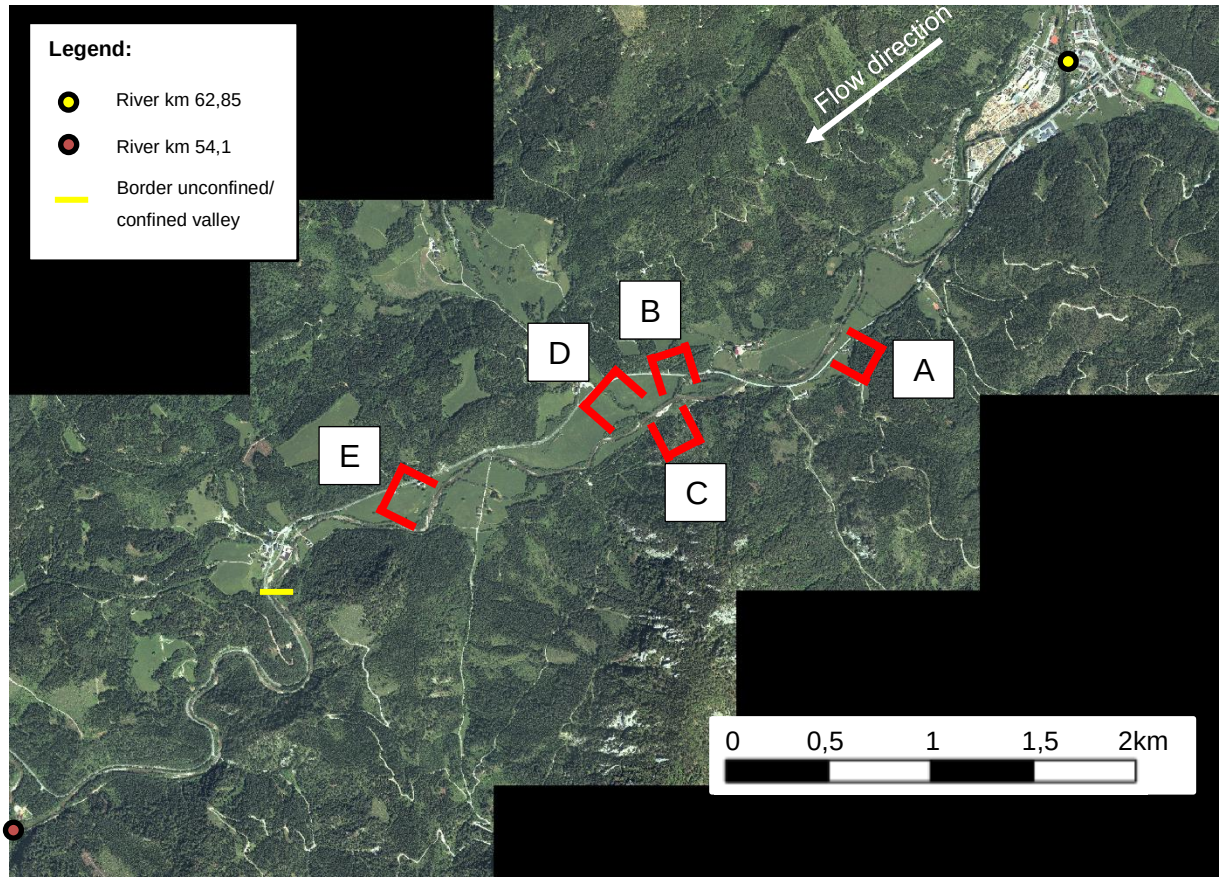


Figure 76: orthophoto of the Salza River study area taken on 30.05.2011. Source: GIS-Styria, with changes marked in red.

In location A in the overview, zoomed into in Figure 77, there appears to have been some kind of intervention to the riverbank on both sides. Possible some kind of input of armour stones to protect the bank because the river width at that section seems to have decreased.



Figure 77: Visual changes A in the 2009 orthophoto (left) and the 2011 orthophoto (right).

In section B in the overview, zoomed into in Figure 78, the vegetation of the outflow of the fish pond seems to have grown back resembling the status in 2004 see Figure 74. The washout at location C in the overview, which was first seen in 2009 see Figure 74, has in 2011 been filled with transported river sediments creating a gravel bar see Figure 78.

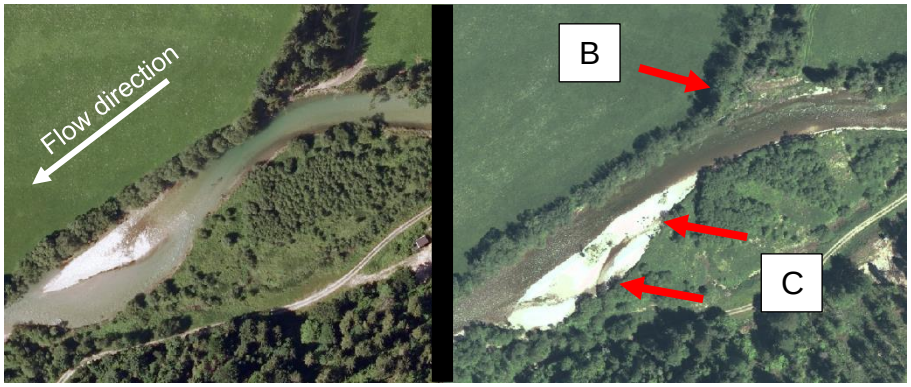


Figure 78: Visual changes B and C in the 2009 orthophoto (left) and the 2011 orthophoto (right).

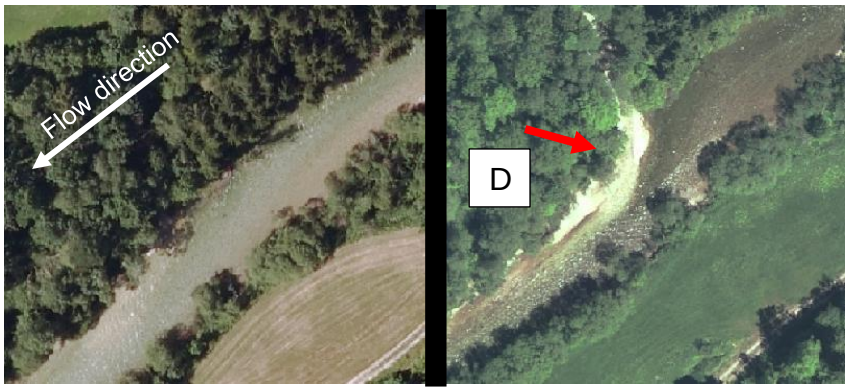


Figure 79: Visual changes D in the 2009 orthophoto (left) and the 2011 orthophoto (right).

At location D in the overview there seems to have been a large sediment input from a tributary river, see zoomed in orthophoto excerpt in Figure 79, which narrowed the stream.

Lastly in location E in the overview, the local washout has been filled and the bank has been stabilised and regrown some riparian vegetation, see zoomed in orthophoto excerpt in Figure 80.

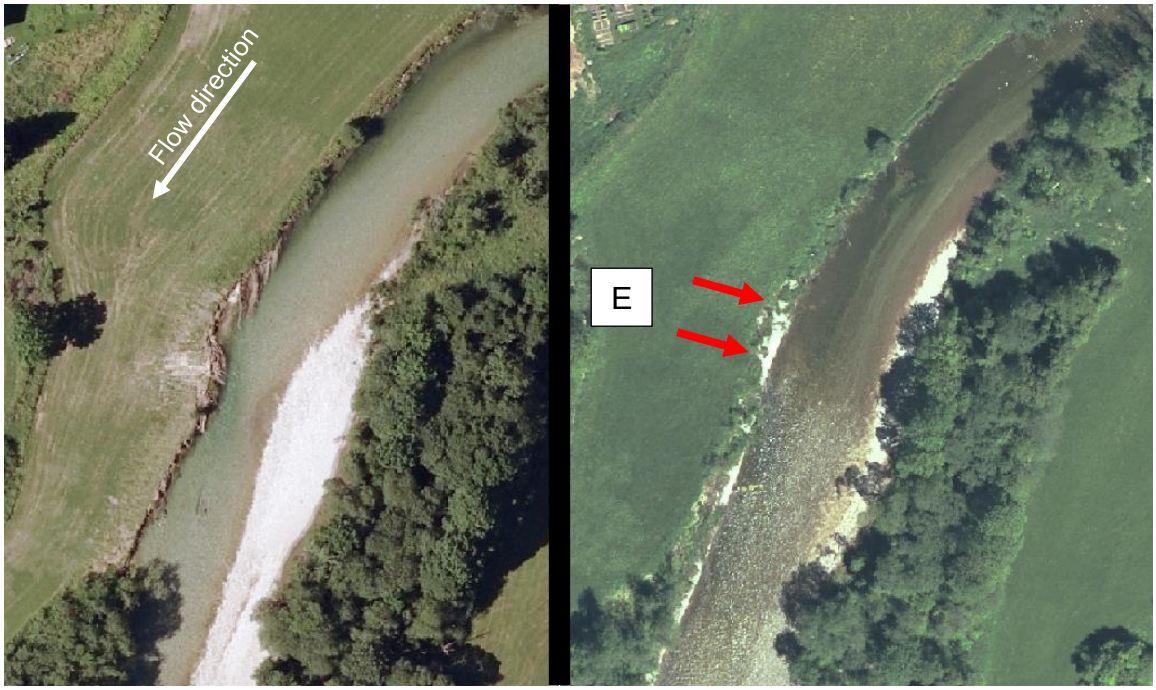


Figure 80: Visual changes E in the 2009 orthophoto (left) and the 2011 orthophoto (right).

The confined valley in the lower part of the study area, has once again in comparison not changed at all in the 2-year timeframe from 07.2009 to 05.2011

The fourth available orthophoto from GIS Styria of the Salza River study area was taken on the 10.06.2014. Both river km as well as the border of the unconfined and confined valley can be pinpointed, and a sinuosity index will be made later. In the below orthophoto, see Figure 81, a total of 5 changes could be found compared to the 2011 orthophoto.

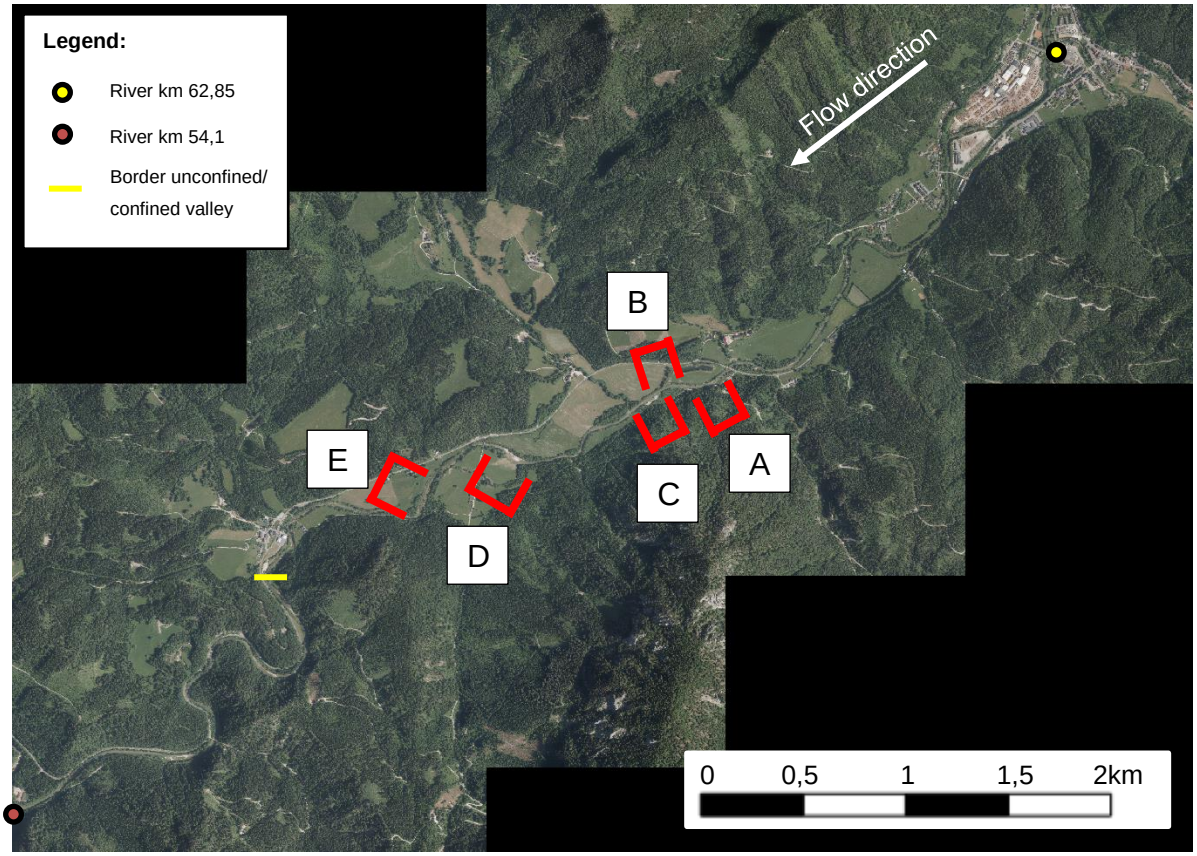


Figure 81: orthophoto of the Salza River study area taken on 10.06.2014. Source: GIS-Styria, with changes marked in red.

In the first location A, zoomed into in Figure 82 a small stretch of the bank on the orographic right side of the river was stripped of its riparian vegetation.



Figure 82: Visual changes A in the 2011 orthophoto (left) and the 2014 orthophoto (right).

At location B in the overview, zoomed into in Figure 83 the outflow of the fishpond has regrown its riparian vegetation on the bank and now nearly looks the same as it did in the orthophoto of 2004 in Figure 74. The gravel bar at location C has started to regrow vegetation showing the ecological succession taking place.

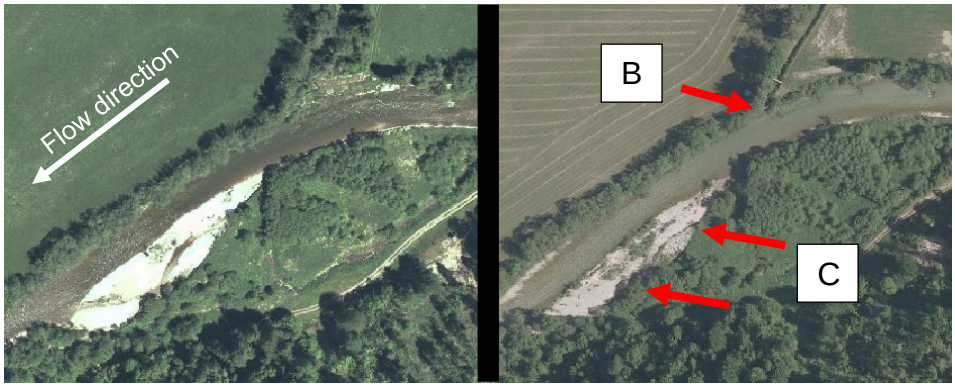


Figure 83: Visual changes B and C in the 2011 orthophoto (left) and the 2014 orthophoto (right).

At location D in the overview, zoomed into in Figure 84, we first see the erosion hotspot between river km 58,9 and 58,6 which was the initial trigger for this thesis. In the zoomed in map in Figure 84 the riparian vegetation on the orographic left riverbank was removed, the river has eroded the bank and formed a compound bar after a flooding event on the 01.05.2014. Further in-depth changes of the hotspot will be assessed in chapter *6.1.4 Hotspot Sinuosity index and cross section.*

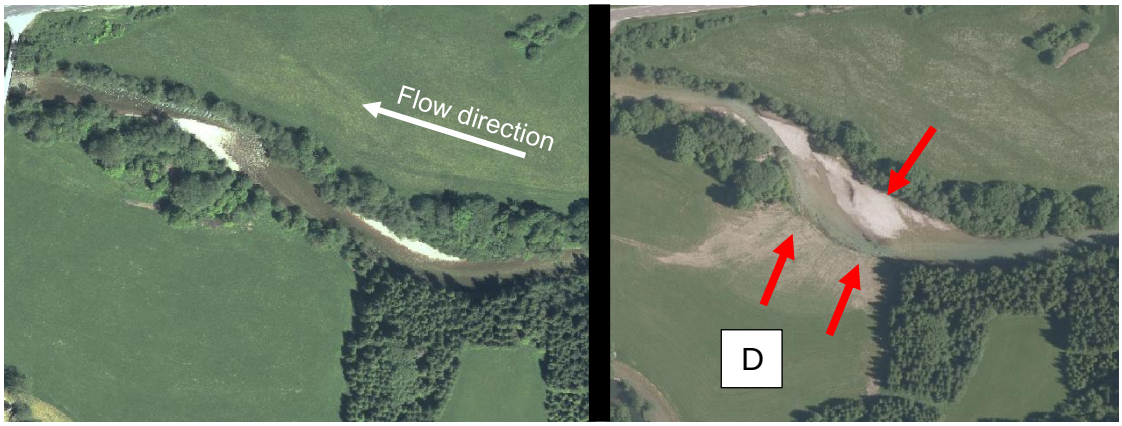


Figure 84: Visual changes D in the 2011 orthophoto (left) and the 2014 orthophoto (right).

And finally, in location E in the overview, zoomed into in below Figure 85, the riparian vegetation on the orographic right riverbank has started to regrow.

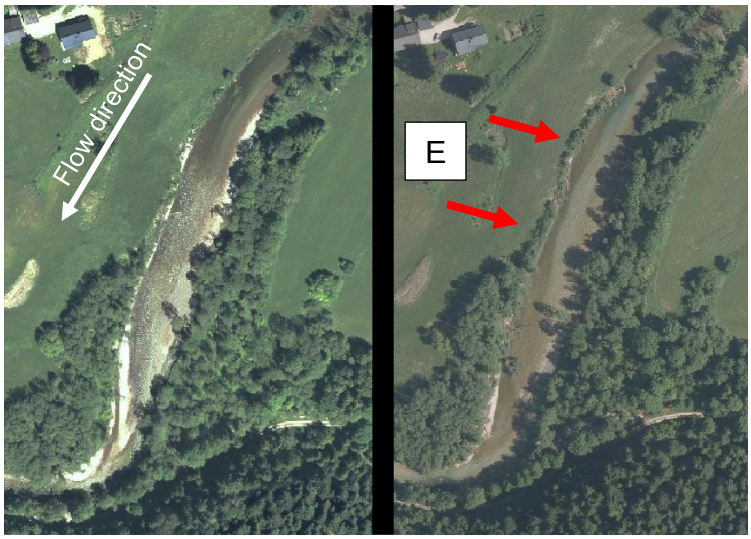


Figure 85: Visual changes E in the 2011 orthophoto (left) and the 2014 orthophoto (right).

The confined valley in the lower part of the study area in the orthophoto of 2014, continues to remain unchanged to the map from 2011.

The final and most recent orthophoto available from GIS Styria of the Salza River study area was taken on the 08.09.2017, see Figure 86. Both river km as well as the border of the unconfined and confined valley can be pinpointed, and a sinuosity index will be made later. A total of 8 major changes could be identified.

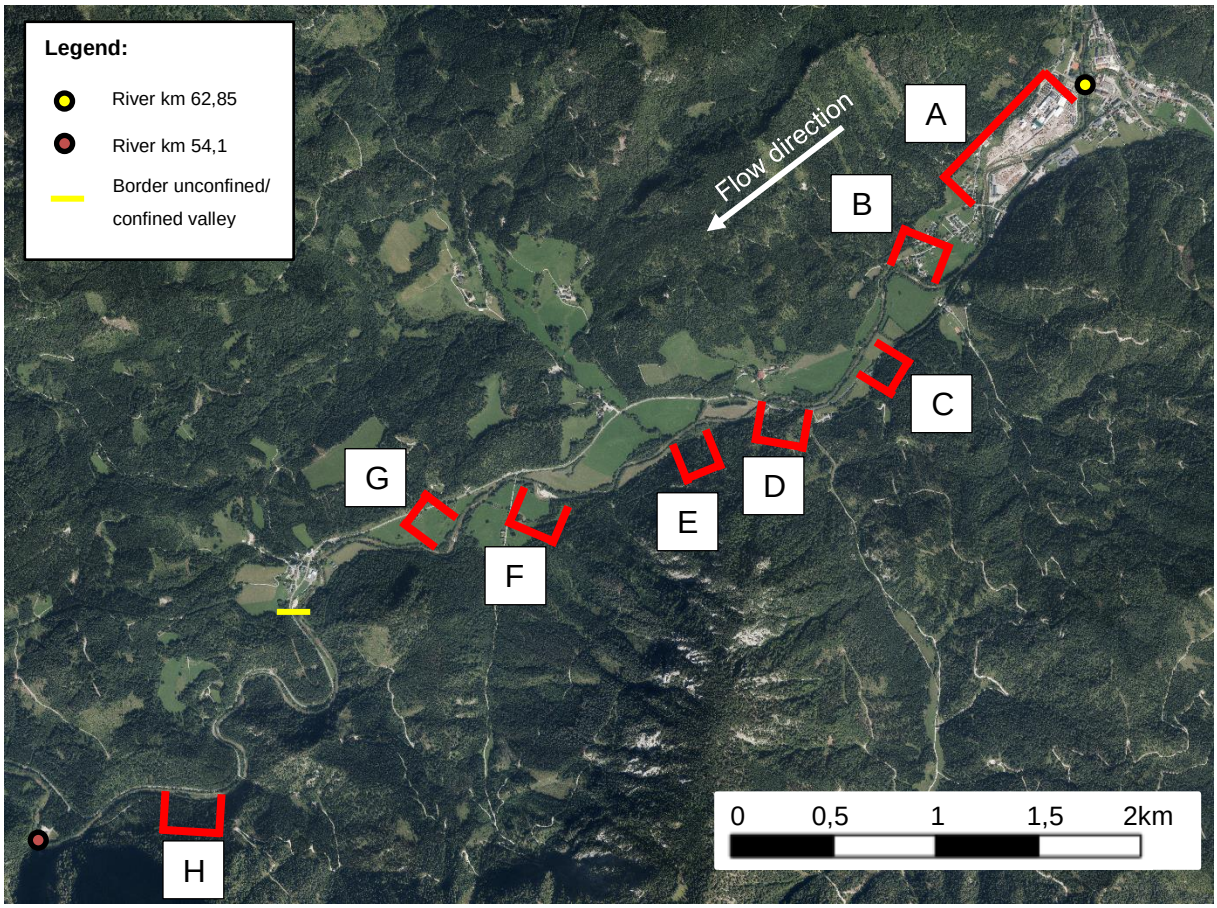


Figure 86: orthophoto of the Salza River study area taken on 08.09.2017. Source: GIS-Styria, with changes marked in red.

The first and largest change in size was the removal of the riparian vegetation on both sides of the riverbank in location A in the overview, coupled with the construction of a levee. In the zoomed in orthophoto excerpt in Figure 87, we see the vegetation removal and erected levee on the orographic right side of the Salza River above the weir. In Figure 88 we can see the changes that happened below the weir. Between both bridges, in Figure 88, the riparian vegetation was removed almost completely on both sides and a levee was erected. It seems that the levee on the right bank reaches until the river bend and on the orographic left bank continues through the bend, covering the bank between the bridges. Additionally, the bank was somewhat solidified with riprap. Presumably, the listed changes were made to protect the resident sawmill against a future flooding event.

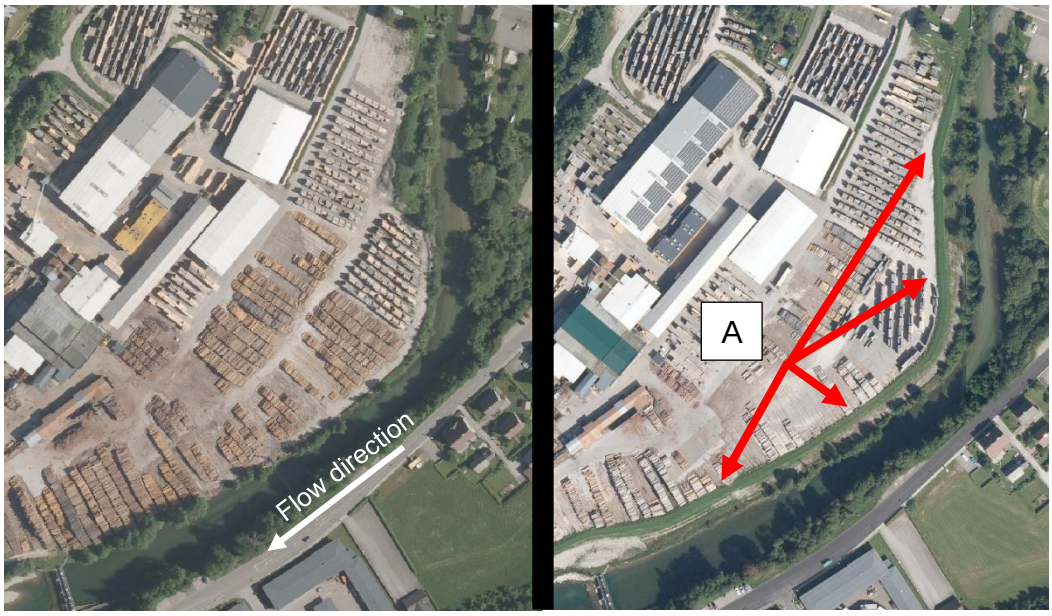


Figure 87: Visual changes A in the 2014 orthophoto (left) and the 2017 orthophoto (right).

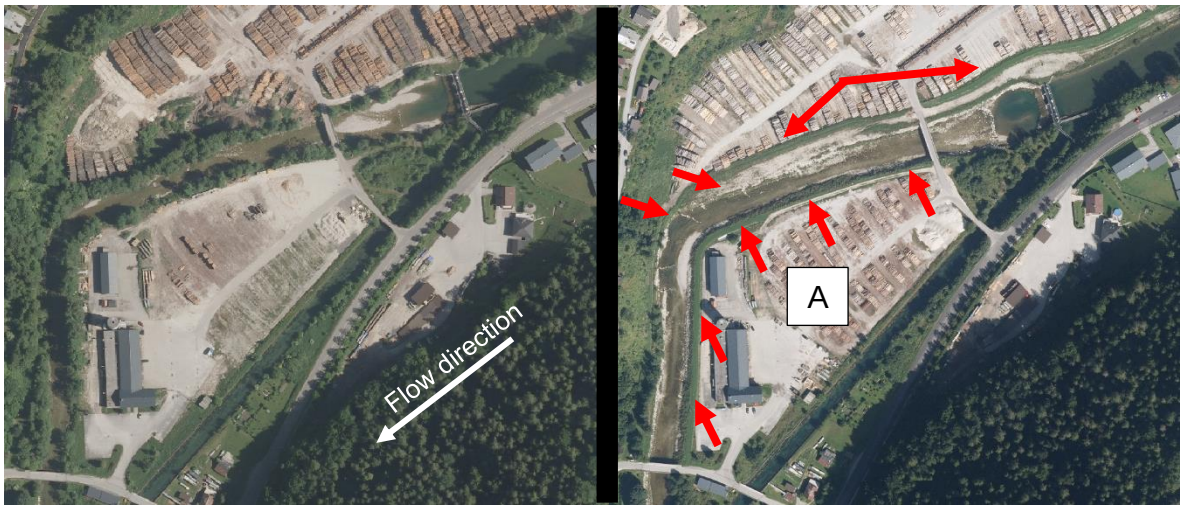


Figure 88: Additional visual changes A in the 2014 orthophoto (left) and the 2017 orthophoto (right).

The next noticeable change downstream is at location B in the overview, zoomed into in Figure 89. A prior point bar from 2014 see left image, has been fully covered through new vegetation and a new island formed further upstream see right image.



Figure 89: Visual changes B in the 2014 orthophoto (left) and the 2017 orthophoto (right).

Next in location C in the overview, zoomed into in Figure 90, we notice that the orographic left bank has been somewhat eroded.



Figure 90: Visual changes C in the 2014 orthophoto (left) and the 2017 orthophoto (right).

In location D in the overview, zoomed into in Figure 91, we can see that the secondary channel of the Salza River has been almost cut off and the vegetation cover has increased drastically.

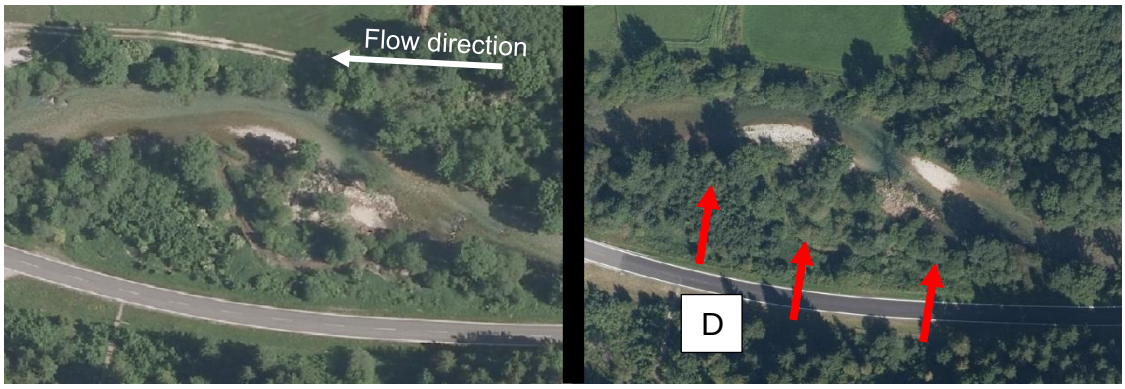


Figure 91: Visual changes D in the 2014 orthophoto (left) and the 2017 orthophoto (right).

The location E in the overview, as seen in the zoomed in orthophoto excerpt in Figure 92, clearly shows ecological succession which restored the riparian vegetation. In the orthophoto of 2017 the gravel bar has more or less vanished. The stretch of the Salza River now resembles the orthophoto from 2004 see Figure 74.



Figure 92: Visual changes E in the 2014 orthophoto (left) and the 2017 orthophoto (right).

At location F in the overview, see zoomed in orthophoto in Figure 93, is the change of the hotspot from 2014 to 2017. We can clearly see a decent increase of the bank erosion, a shift of the riverbed as well as an increase in size of the compound bar. More detailed changes will be presented in chapter *6.1.4 Hotspot Sinuosity index and cross section.*

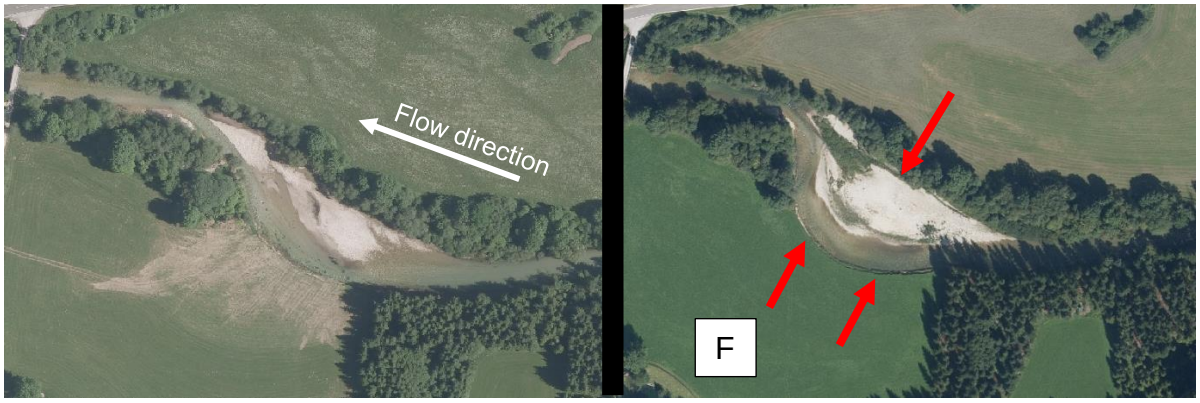


Figure 93: Visual changes F in the 2014 orthophoto (left) and the 2017 orthophoto (right).

Location G in the overview, zoomed into in Figure 94, shows the formation of an instream island splitting the main channel in two. Additionally, the island is already vegetated.

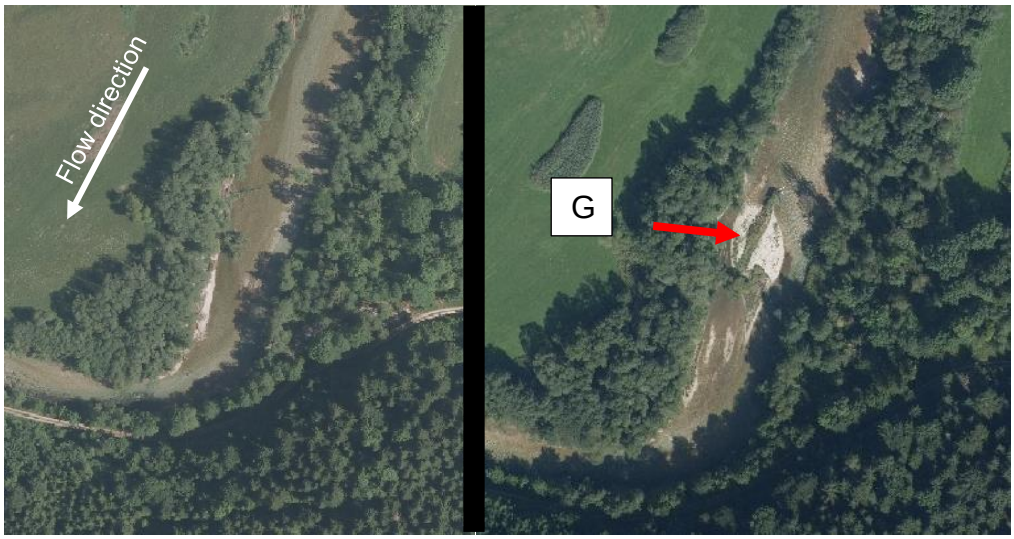


Figure 94: Visual changes G in the 2014 orthophoto (left) and the 2017 orthophoto (right).

Finally in location H in the overview, the island which has more or less remained in the same state in the past orthophotos, has had an increase in vegetation cover from 2014 to 2017.

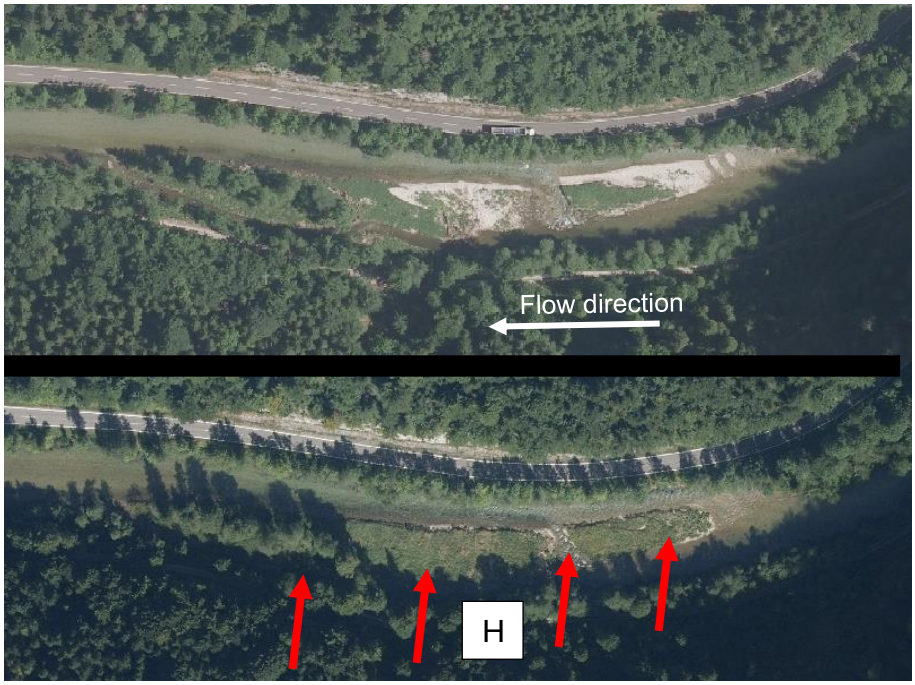


Figure 95: Visual changes H in the 2014 orthophoto (left) and the 2017 orthophoto (right).

Apart from this vegetation increase, the confined valley in the lower part of the study area has once again in comparison to the last map not changed at all. Lastly, the established riparian vegetation has noticeably increased in size and density in the whole Salza River study area from the timeframe 2014 to 2017.

6.1.3 Sinuosity index of the study area

After recording all visual changes of the past historical maps and orthophotos of the Salza River study area in the prior chapter, in this chapter the sinuosity index, as described in chapter *5.1.2 Methods*, of the three most recent historic maps as well as all orthophotos will be compared. The accompanying tables with the measured lengths, distances and indexes can be found in chapter *11. Appendix* and will only be addressed with the table number. A sinuosity index was performed for not only the whole study area, but also individually for the study area lying in the unconfined and confined valley. The point of changeover from the unconfined and confined valley was marked on all maps with a yellow line. Besides the numerical comparison of the index, the thalweg of the historic maps and orthophotos will be overlapped to pinpoint any changes.

Looking at the historical maps first, the different distances of the study area of the three maps obtained via QGIS can be seen in Table 38. The distance hereby is a straight line between two points, more specifically a line between the presumed location of the river km 54.1 and 62.85. Besides the distance of the total study area, the distance values for the unconfined and confined valley are also listed.

Next in Table 39 are the recorded lengths of the Salza River in the historic maps. The length hereby being the line following the river flow or the thalweg between river km 54.1 and 62.85 and was obtained via QGIS. In the table are the values for the total study area, as well as the unconfined and confined valley reaches.

Taking the distances and lengths from the three most recent maps, the sinuosity index was calculated for all parts. Beginning with Table 40, we see the sinuosity index for the unconfined valley which increased slightly from the Franziszeische cadastre to the Franziszeische land survey by 0,0057 and decreased slightly by -0.0197 from the Franziszeische Land survey to the Francisco-Josephinische Land survey. In total there is also a decrease in sinuosity from 1817 - 1861 to 1869 - 1887, indicating that the unconfined valley has ever so slightly straightened. In general, the index for all three indicates only a unincisive meandering of the valley.

Comparing the sinuosity index for the confined valley in Table 41, the index decreased both from the Franziszeische cadastre to the Franziszeische Land survey by -0.0105 and from the Franziszeische Land survey to the Francisco-Josephinische Land survey by -0.0725. Also, from the first to the last map, there was a distinct decrease in sinuosity. The values also show that the index is far greater for the confined valley than the unconfined valley confirming the higher curvature of the confined valley.

In total we can see that the sinuosity index for the whole Salza River, see Table 42, has decreased minutely from the Franziszeische Land survey to the Franziszeische Land survey by -0.0003, although we could say that there is no change at all. There was however a decrease from the Franziszeische Land survey to the Francisco-Josephinische Land survey by -0.0236 and thus also a decrease from the first to last map. Very noticeable in the total sinuosity index, is that although the unconfined and confined indices differ by a lot, the total index is only slightly larger than for the unconfined indices, since the unconfined valley makes up 67% of the whole study area.

Next the lengths, or thalwegs, of the Salza River study area from the three historic maps were overlapped in Figure 96, to pinpoint the differences in the sinuosity indices. First, we can mention that the river course did not change very drastically, however there are three main deviations which stick out. At location A, the Franziszeische cadastre, illustrated in green in the map, the Salza River seems to have flown a bit different, which was not visible when comparing only the maps. Next at location B, the Salza River seemed to have been straightened in the Francisco-Josephinische Land survey as already mentioned in Figure 62. And at location C there used to be an island in the Franziszeische Land survey also stated in Figure 63.

Although all historic maps were georeferenced, we see that while the unconfined valley was already mapped with quite good precision and the three thalwegs overlap quite well, we see a slight discrepancy in thalweg overlap in the lower part of the Salza River study area.

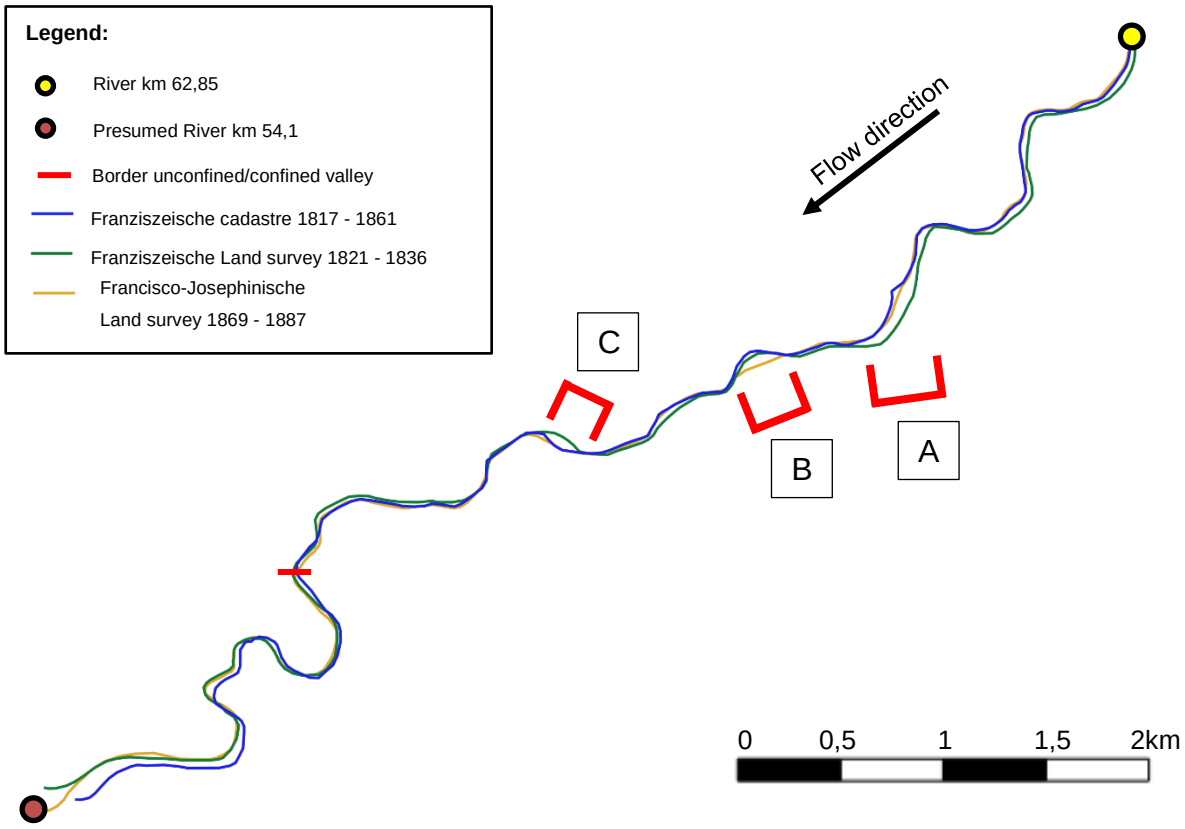


Figure 96: Overlapping the thalwegs of the three historic maps of the Salza River study area.

Next the sinuosity indices of the orthophotos were analysed. In Table 43 are the distances of the total Salza River, the unconfined and confined reach. Since all orthophotos were georeferenced beforehand, the same distance value can be applied for all years.

Next, the lengths for all scan flight dates were measured and can be seen in Table 44 for the total river length, the unconfined and confined reach.

Applying the distances from Table 43 and lengths from Table 44 of the orthophotos, the sinuosity indices were calculated. In Table 45 one can spot a small decrease in the index for the unconfined valley from 2004 to 2009, and since 2009 to 2017 a steady increase of 0.0016, 0.0012 and 0.0059 between each timeframe. From 2014 to 2017 the increase was the largest in comparison. Also, there was a total increase from the oldest to newest orthophoto indicating an increase in curves in the unconfined valley.

The sinuosity indices for the confined valley were obtained and are in Table 46. We see that there was a slight increase in the index from 2004 to 2009 by 0.0011 and a slight decrease from 2009 to 2011 by -0.0152. From 2011 to 2014 there was another increase by 0.0112 and in the last set from 2014 to 2017 there was no change measured. Overall, the index ever so slightly decreased from 2004 to 2017 by -0.0029.

Finally examining the indices for the total Salza River in the study area we could find a decrease in the index from both 2004 to 2009 and 2009 to 2011 by -0.0021 and -0.0027. Opposite to these decreases there has been a steady increase from 2011 to 2014 by 0.0039 and from 2014 to 2017 by 0.0043. But overall, from 2004 to 2014 there is a minuscule decrease.

Next, comparing the newest historic map, the Francisco-Josephinische Land survey from 1869-1887, with the oldest orthophoto from 2004 we can see an increase of the sinuosity index by 0.0363 from 1.3049 to 1.3412 in the 117 - 135-year timeframe. Following in Figure 97 the two thalwegs were overlapped showing the difference of the lengths of both. All visual changes which were marked in Figure 64 can be seen in the Figure 97. The obvious increased meandering of the river in the orthophoto from 2004 compared to Francisco-Josephinische Land survey results in the increase of the calculated sinuosity index. Worthwhile mentioning is that besides the increase in the index, the main flow of the river has not changed drastically and has only moved in a narrow range in the valley.

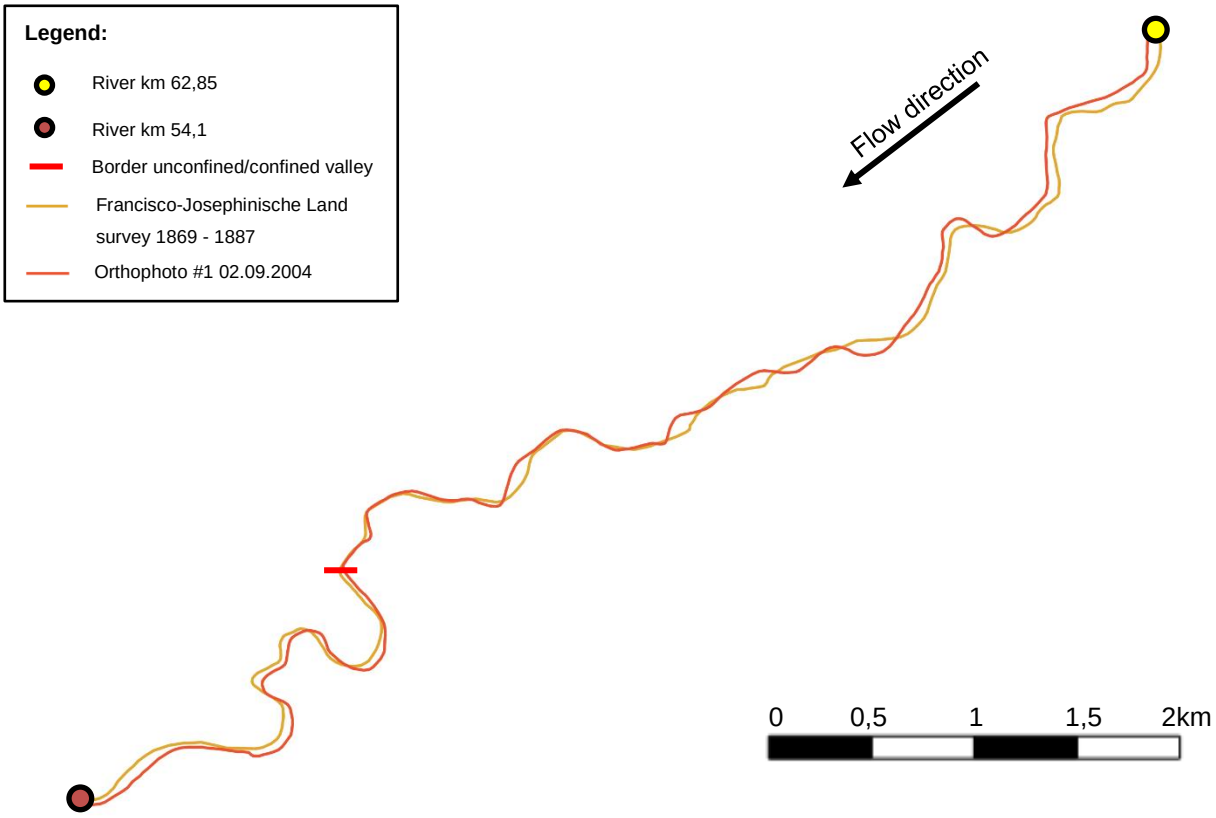


Figure 97: Overlapping the thalwegs of the most recent historic map with the oldest orthophoto of the Salza River study area.

Lastly, all thalwegs of the five orthophotos were compiled and overlapped in Figure 98. The Salza River has, apart from two exceptions not greatly moved outside its riverbed between the 13 years from 2004 to 2017. Location A in the Figure was one occasion from 2004 to 2009 where the river dug into the orographic left bank at river km 59.6 as described in Figure 74. And the location B in the below Figure is the hotspot between river km 58.7 and 58.8 which has been the most active area in the entire Salza River study area as described in Figure 84 and Figure 93.

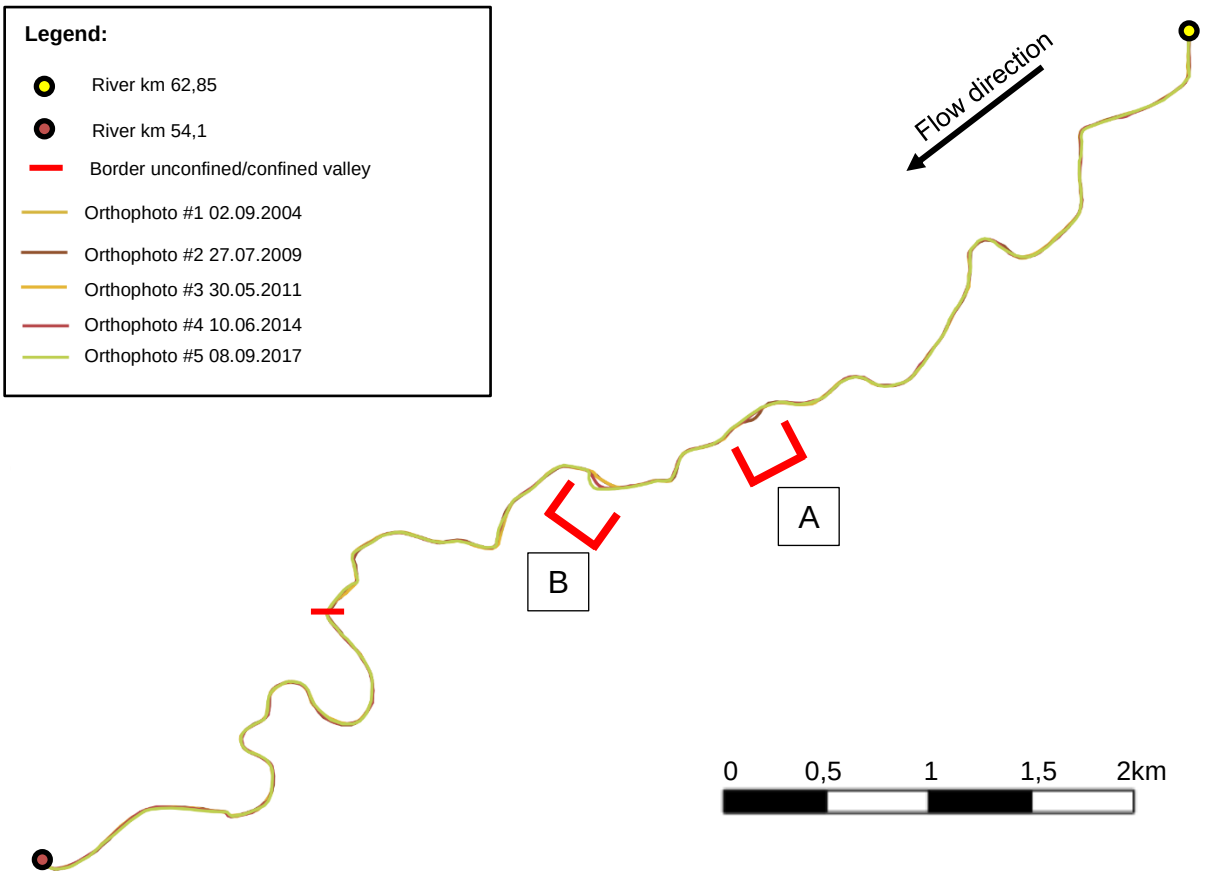


Figure 98: Overlapping the thalwegs of the orthophotos of the Salza River study area.

6.1.4 Hotspot Sinuosity index and cross section

Next the hotspot of the Salza River, lying between river km 58.7 and 58.8 as initially described in chapter *3.2 Hot spot between river km 58.7 - 58.8,* will be analysed by examining the available orthophotos. Besides the 5 orthophotos already analysed in chapter *6.1.2 orthophotos of the study area dating 2004 - 2017,* I could find a newer satellite image of only the hotspot on Google Earth with the recording date 07.09.2019 which will also be examined. The accompanying tables with the measured lengths, distances and indexes can be found in chapter *11. Appendix* and will only be addressed with the Table number. In order to evaluate the sinuosity index of the hotspot, as described in chapter *5.1.2 Methods,* first the distance had to be measured. The distance of the hotspot of the Salza River measured 305m. Since all orthophotos were georeferenced the value could be applied to all other sets, see Table 48.

Next the lengths of the Salza River between the river km 58.7 and 58.8 were measured for each scan flight date, resulting in the values in Table 49.

Using the distance from Table 48 and the measured lengths from Table 49 the sinuosity index was calculated. The results are in Table 50, additionally showing the numerical changes between each scan flight date. From 2004 to 2009 we do not really see a vast change in the index with only a minor increase of 0.0033. This can also be said for the timeframe from 2009 to 2011, where there was only a minor decrease with -0.0066. A significant change can be found from the measured indexes of 2011 and 2014, where the value increased by 0.0525. This change, which was visually described in Figure 84, resulted from a flooding event which occurred on the 01.05.2014 with a peak discharge of 179 m^3/s, being the 4^{th} largest peak ever recorded. From the year 2014 to 2017 the index did increase again substantially by 0.0984 due to widening of the hotspot. Lastly from 2017 to 2019 the sinuosity index seemed to have decreased again ever so slightly possibly halting the further ongoing bank erosion. Overall, from 2004 to 2019 the index increased from 1.0426, being more or less straight to 1.1803 turning into a beginning meander in a timeframe of 15 years.

In order to visualize the changes of the Table 50, all thalwegs of the six orthophotos were compiled and overlapped in Figure 99. What we see is, that the lengths of the Salza River measured for the orthophotos 2004, 2009 and 2011 did in fact not change. The large sinuosity index increases from 2011 to 2014 can be seen through the change in the river flow from the

violet line in Figure 99 to the jump in the blue line in Figure 99. Also, the increased widening from 2014 to 2017 is noticeable by the change from the blue line to the light green line in Figure 99, which also correlates with the sinuosity index increase. The index in Table 50 however states that there has been an ever so slight decrease in sinuosity from 2017 to 2019. However, looking at the Figure below we notice that that Salza River has in fact moved further downstream and the erosion bank increased in width.

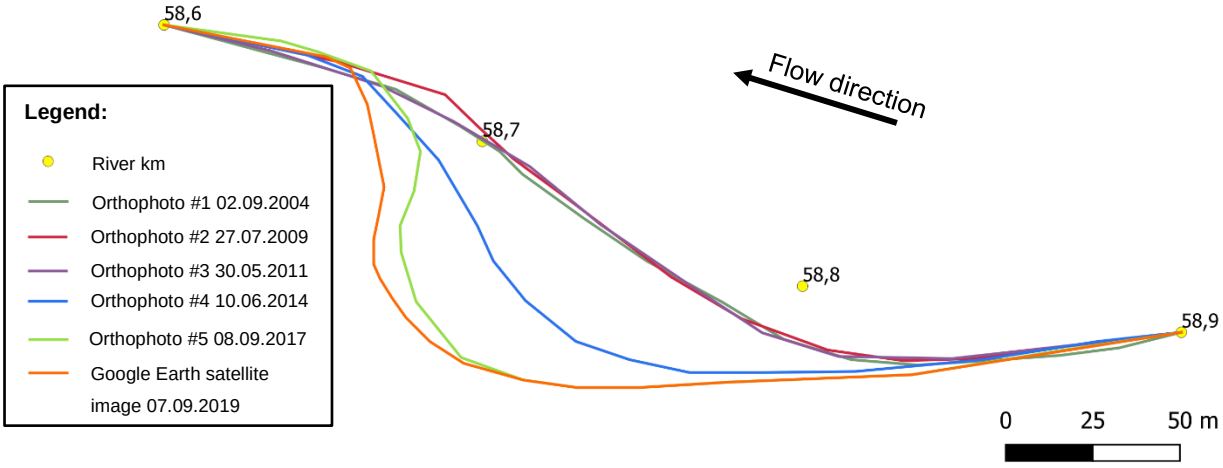


Figure 99: Overlapping the thalwegs of the orthophotos of the erosion hotspot in the Salza River study area.

The visual changes in the above overlapping thalwegs were also numerically measured in QGIS giving the change in riverbed displacement, see Table 14. Looking at the orographic left bank, there was no change in the bank location from 2004 through to 2011. From 2011 to 2014, following the flooding event there was a widening of 26.78m of the left bank. The left bank widened another 19.08m from 2014 to 2017 and 5.55m from 2017 to 2019. The total riverbed displacement from 2004 to 2019 amounted to 51.41m.

Table 14: Changes in Riverbed displacement at the erosion hotspot in the Salza River study area.

orthophoto	Scan flight date	Riverbed displacement of left bank (m)	Σ Riverbed displacement of left bank (m)
#1	02.09.2004	0	-
#2	27.07.2009	0	-
#3	30.05.2011	0	-
#4	10.06.2014	26.78	26.78
#5	08.09.2017	19.08	45.86
#6	07.09.2019	5.55	51.41

The changes in the riverbed displacement from Table 14 are also seen in Figure 100, where the hotspot of all 6 timeframes can be visually compared. In every image the red line represents the riverbed. As mentioned, no change could be noticed in the first three images from 2004 to 2011. A drastic increase could be seen in 2014 where the riparian vegetation was fully removed on the orographic left bank, and a compound bar formed on the orographic right bank. The erosion of the left bank further increased in the 2017 orthophoto without the riparian vegetation in place. The compound bar also increased in size. In 2019 the widening of the hotspot seemed to have slowed down, but the river moved slightly further downstream, removing more riparian vegetation. Additionally, the compound bar has undergone plant succession securing the bar from further erosion. The riverbed itself stayed more or less the same width over the 15-year timeframe, indicating a riverbed displacement rather than a riverbed widening.



Figure 100: Changes of the erosion hotspot in all orthophotos of the Salza River study area.

6.2 Mapping of in and out-of-channel geomorphic units

The on-site mapping of the study area, as described in chapter *5.2.2 Methods* is based on the framework provided by WHEATON et al. 2015. Following the framework, the three generated maps will be presented in the same order as described in the methods chapter. Additionally, any changes between the initial and follow up mapping will be addressed at the end of chapter 6.*2.3* and a comparison with the provided ÖBf mapping will be made in chapter 6.*2.4*.

The mapping of all the features within the study area was done via a rough draft in situ in May of 2017, see Table 15, based on established guidelines for river mapping as described in WHEATON et al. 2015. A second follow up mapping was done in June of 2018 to see if any major changes occurred. The mapping was later digitalized via QGIS.

Table 15: Number of mappings of the Salza River study area.

Mapping	Date
#1	05.2017
#2	06.2018

6.2.1 First map: Mapping of fluvial margins

In total, four different margins were mapped, namely: the channel margin, the valley margin, the valley bottom margin and any confining margins, as can be seen on the map on the following page in Figure 101. The valley margin which is the maximum width of the valley is mapped in red. It stretches over 18,463 m over the total Salza River study area, with 6,058 m lying within the confined Salza River and 12,405 m lying in the unconfined river, see Table 16. As a reminder, the changeover between the confined and unconfined Salza River lies at river km 57. The valley bottom margin which *"…comprises the active channel and contemporary floodplain"* (WHEATON et al. 2015: 277) is mapped in orange and spans 17,001 m for the total Salza River, 5,495 m for the confined Salza River and 11,506 m for the unconfined Salza River. The valley bottom margin overlaps with the valley margin for the total Salza River with 40.75%, the confined Salza River with 44.29% and the unconfined Salza River with 39.02%.

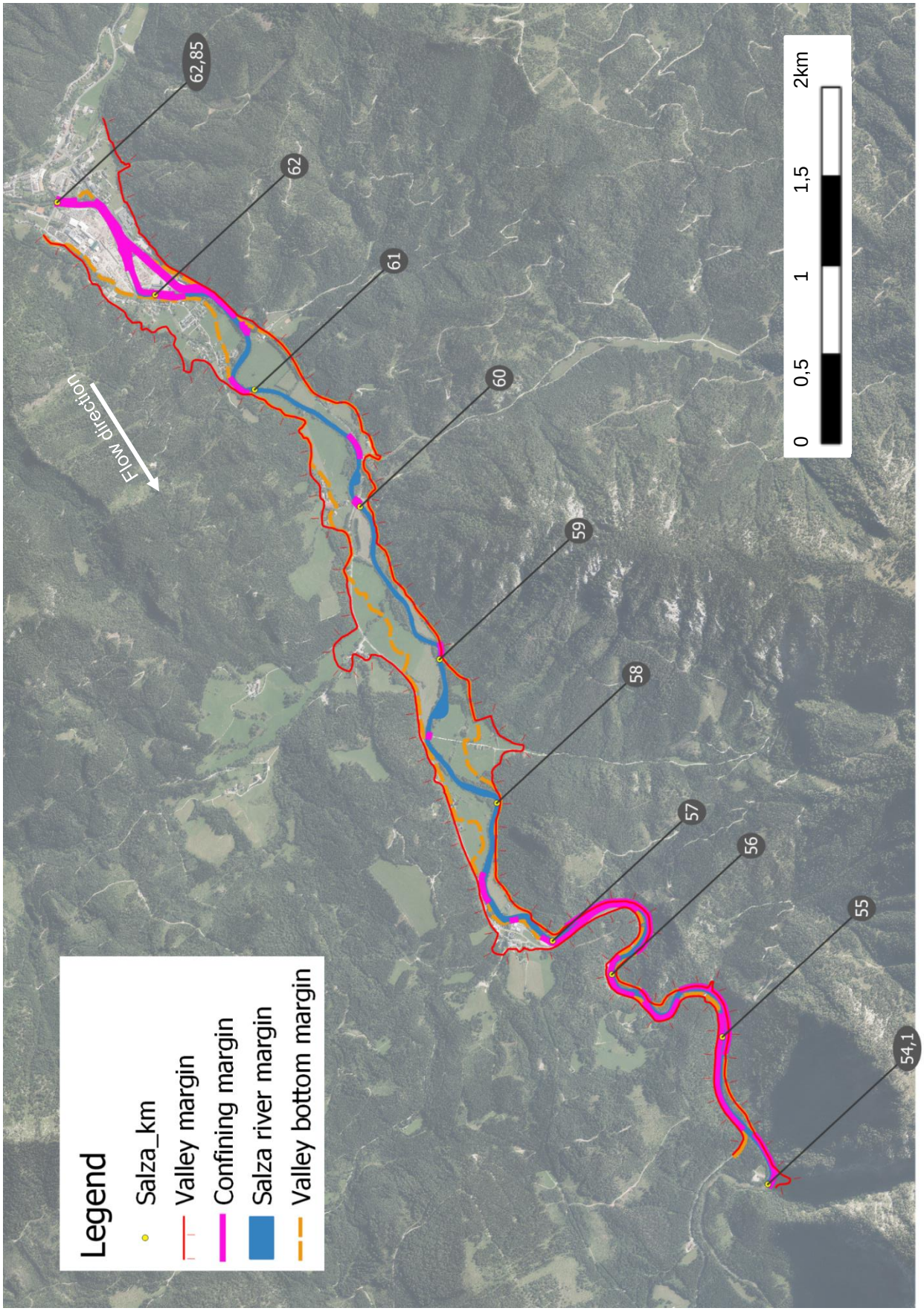


Figure 101: Mapped fluvial margins for the whole Salza River study area.

Table 16: Length of valley- and valley bottom margin and overlap in % of both of the Salza River study area.

	Total Salza River	Confined Salza River	Unconfined Salza River
Valley margin (m)	18,463	6,058	12,405
Valley bottom margin (m)	17,001	5,495	11,506
Overlap (%)	40.75	44.29	39.02

Next looking at the confining margin which *"…is defined as any section of channel bank that abuts against a valley margin, valley bottom margin, or anthropogenic margin."* (WHEATON et al. 2015: 277) and mapped in pink in Figure 101 we see a prominent difference in the confined and unconfined Salza River. Examining the values in Table 17 we can obtain the lengths for the river margin and the confining margin. For the total Salza River, the confining margin spans over 6,907 m or overlapping 38.58% of the river margin. However, while the confining margin abuts only 29.11% of the river margin in the unconfined Salza River, the confining margin for the confined Salza River abuts 57.79% of the river margin. The results from Table 30 are also compiled in the Figure 102 for better visualization of the difference between the river segments. The shapefile of the confining margins will also be used in the modelling later.

Table 17: Length of river margin and confining margin as well as overlap in % of both of the Salza River study area.

	Total Salza River	Confined Salza River	Unconfined Salza River
River margin (m)	17,901	5,913	11,988
Confining margin (m)	6,907	3,417	3,490
Overlap (%)	38.58	57.79	29.11

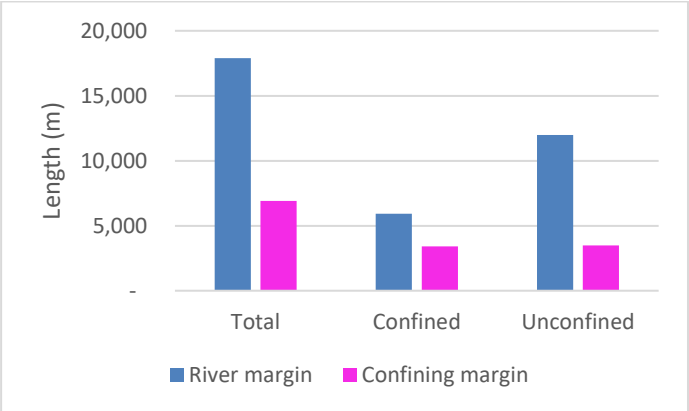


Figure 102: Bar chart visualizing the results from Table 17 of the length of river and confining margin of the Salza River study area.

Next looking at the zoomed in map exeprts on the following page, the confining margins in the upper unconfined Salza River are mostly anthropogenic where the river was straightened, like between river km 62 and 62.85, see top map in Figure 103, or the river bends which were reinforced via riprap or groynes. The lower unconfined Salza River, see middle map in Figure 103, barely exhibits confining margins. In this section the confinement is due to a bridge abutment, or the Salza River touches the valley bottom margin. The river in the confined Salza River on the other hand, see bottom map in Figure 103, is mostly confined either via the valley margin or the valley bottom margin and is thus restricted in lateral and longitudinal movement.

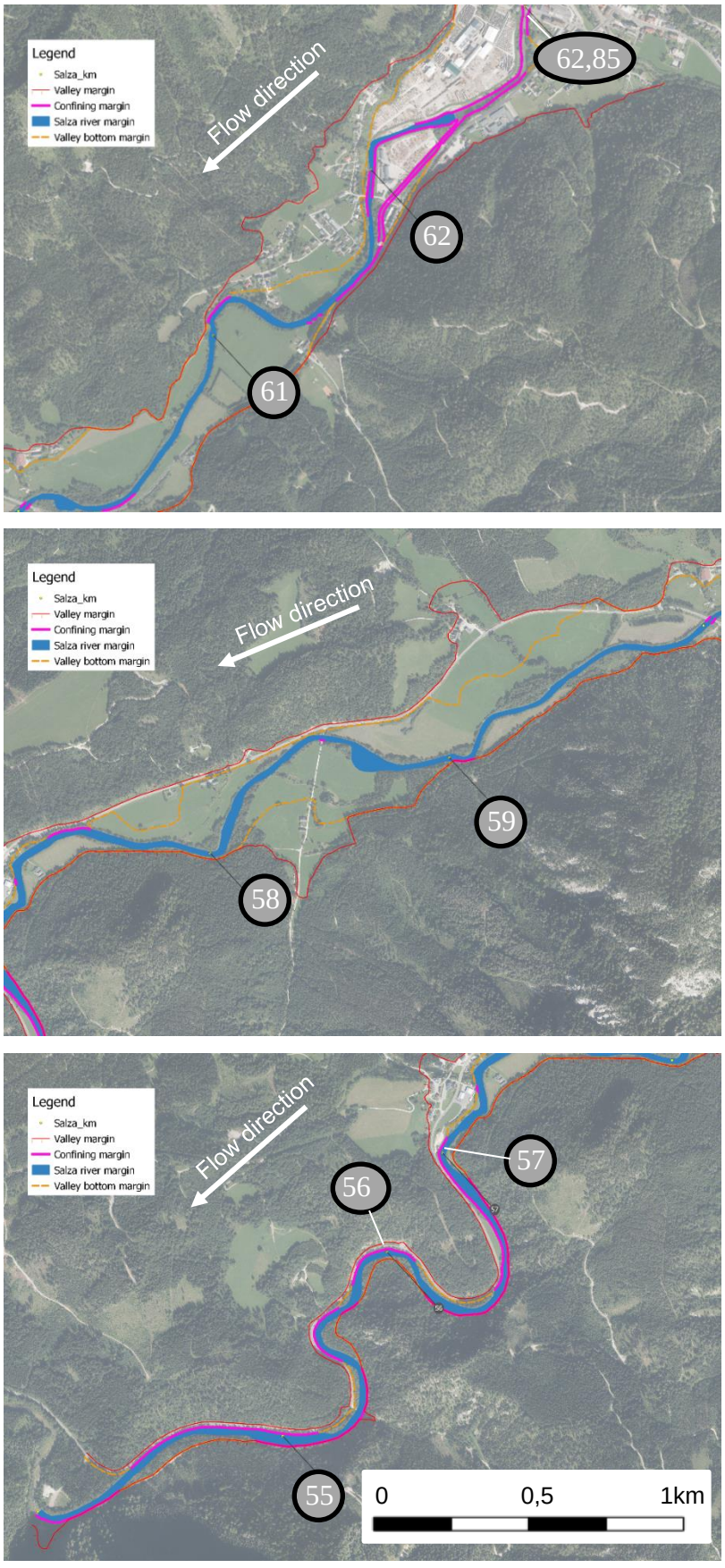


Figure 103: Top: Mapped fluvial margins of the upper unconfined Salza River, Middle: Mapped fluvial margins of the lower unconfined Salza River and Bottom: Mapped fluvial margins of the confined Salza River.

6.2.2 Second map: Mapping of Tier 2 geomorphic units

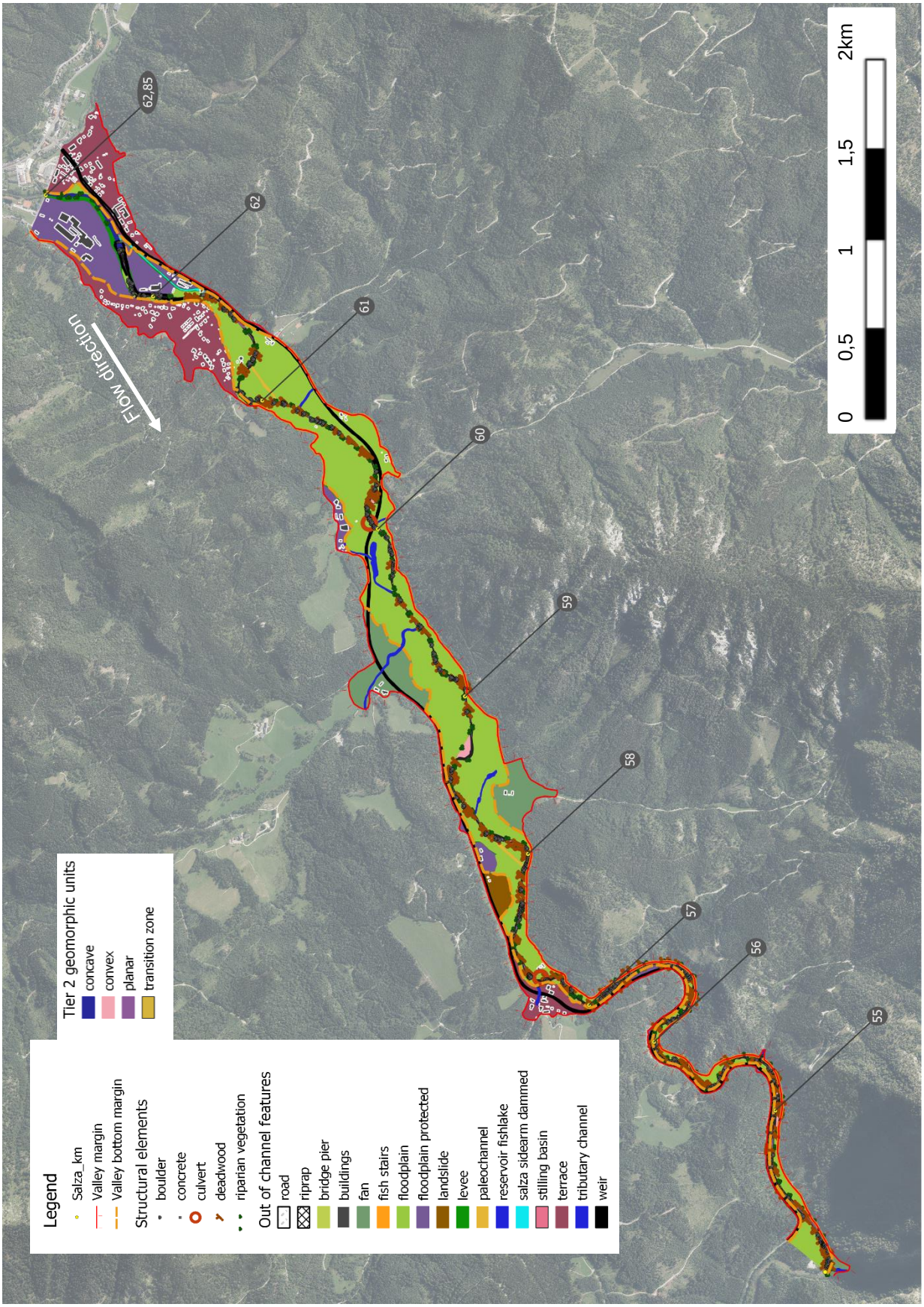


Figure 104: Mapped Tier 2 geomorphic units for the whole Salza River study area.

The second mapping consisted of mapping the structural in-channel elements, the Tier 2 in-channel geomorphic units as well as the out-of-channel features of the whole Salza River study area, see Figure 104. In addition to the on-site mapping, the road as well as buildings were mapped by remote sensing via the latest orthophoto. From a first glance at the large map in Figure 104, we can deduct that the town of Gusswerk is mostly flood protected through being built on a terrace. The largest part of the Salza River in the unconfined valley, runs through a large floodplain whilst the floodplain of the unconfined segment is of smaller size and width.

Next, the overview map from Figure 104 will be zoomed into in 15 small map excerpts on the following pages in Figure 105, Figure 106 and Figure 107. The maps are alphabetically ordered in the flow direction of the Salza River starting at river km 62.85 in map A. In map A we see the large blue concave area, which is the dammed area above the weir. The orographic left riverside is mostly protected by a terrace and the orographic right river side is protected via a levee as was previously described in Figure 87 and Figure 88. In map B, below the weir, we see a dominating deep channel before and after the first river bend, with alternating concave and convex features in the bend itself. Running parallel is a dammed sidearm channel of the Salza River in turquoise, which only touches the Main channel at its in and outflow.

The predominant concave, deep channel at the end of map B follows into map C and changes over from the mid channel to the orographic left riverside at the outflow point of the dammed sidearm channel. In map C there is a mostly planar section next, before forming another concave deep channel in the following bends, where there are convex features in the shallow areas of the channel. Also, we begin to see a number of structural features, notably boulders and deadwood in stream as well as on the riverside. Out-of-channel we notice a paleo channel in the transition from map C to map D. In map D we have a mostly alternating planar and transition area with scattered convex features. Coming to the next bend in map E, the Salza River deepens again forming dominant concave areas with planar and convex areas alongside. There is also a convex island which has a concave tributary channel flowing around it. Map F has mostly planar and transition areas with concave deeper channels in the river bends. The same can be said for map G, with the addition of the hotspot forming a concave channel with a convex bar in pink. Beginning in map G and flowing into map H we see another paleochannel, recorded via the DEM. The bends in map H have yet again, deep concave

channels with mostly planar and convex features in between. There is a third paleo channel beginning in map H which ends in map I. Map I has another large concave unit in the bend on the right as well as several units in the midchannel region further downstream where there is a myriad of in stream boulders. The several houses on the orographic right riverside are protected.

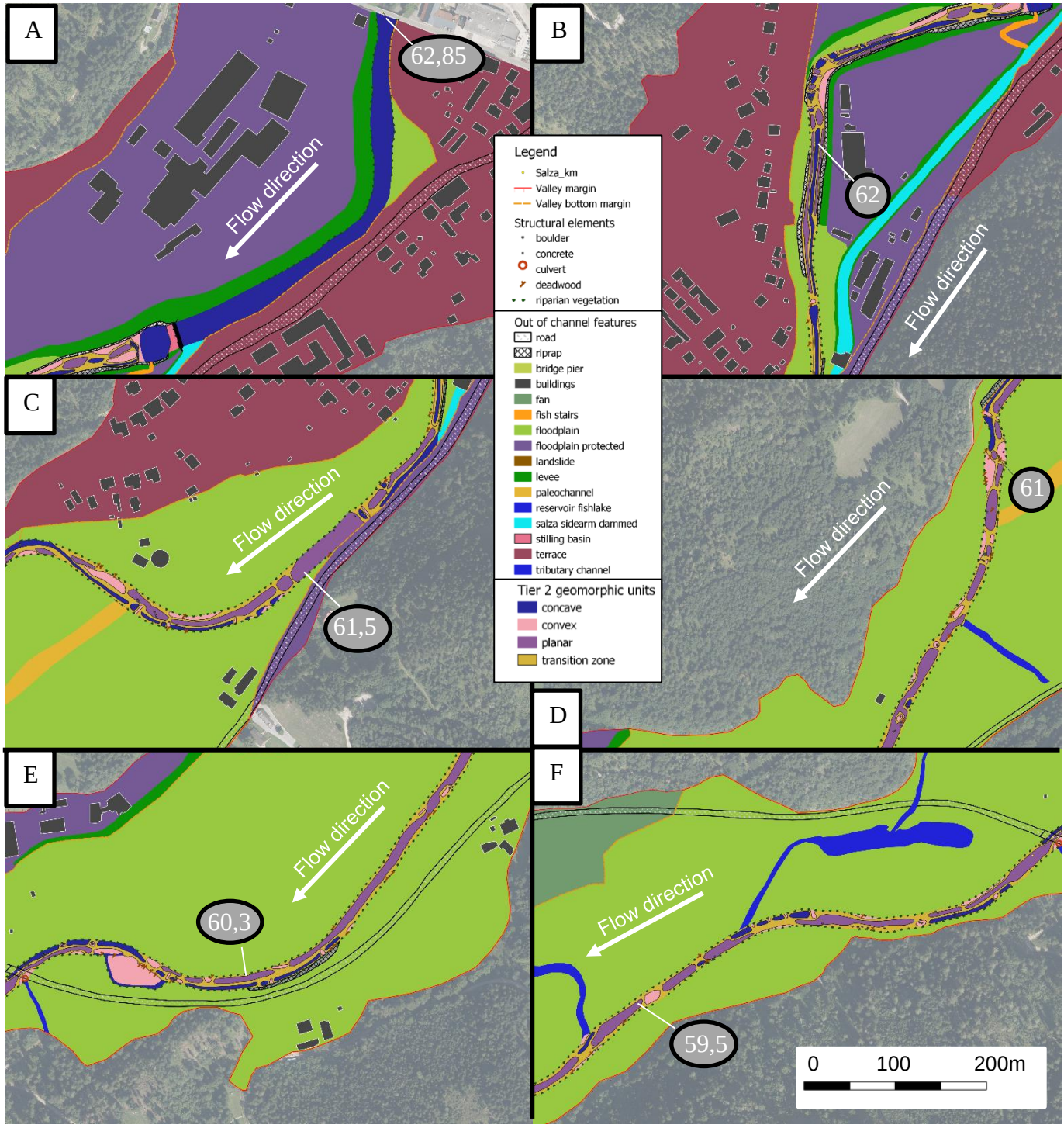


Figure 105: Mapped Tier 2 geomorphic units for the Salza River between river km 59.5 and 62.85.

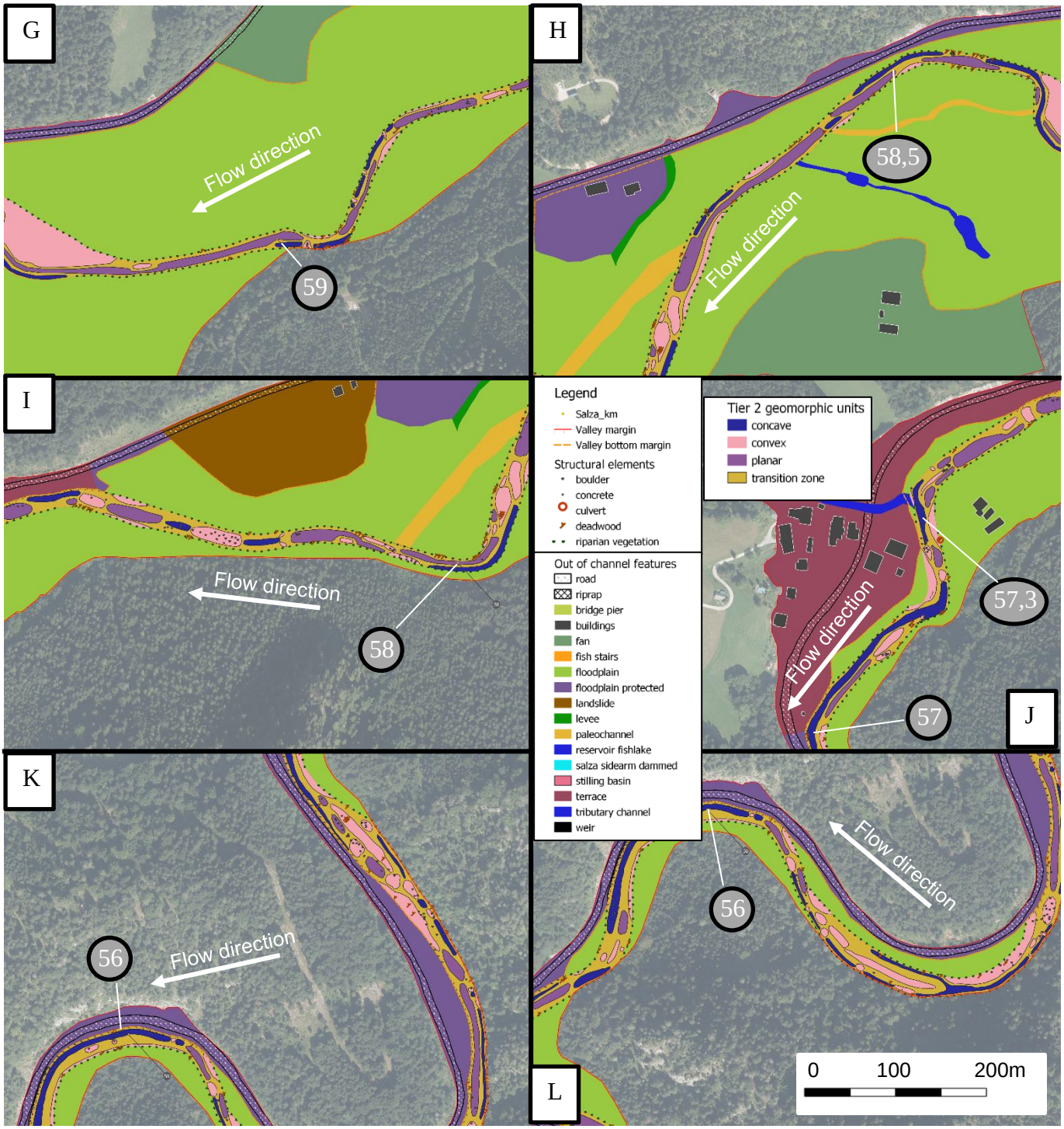


Figure 106: Mapped Tier 2 geomorphic units for the Salza River between river km 56 and 59.

Approaching the changeover from the unconfined and confined Salza River in map J, we notice a beginning narrowing of the floodplain. In channel there are concave areas in the river bends and varying planar, concave and transition areas in the residual riverbed. Also, several houses on the orographic right side are protected by a terrace. Looking at map K, the river flow is now very restricted in between an elevated terrace on the orographic right side and the valley margin on the orographic left side. In channel we see a complex arrangement of all tier

2 geomorphic units with boulders and deadwood scattered all around. Looking at map L, the river has another complex array of geomorphic units, and the channel is split in two parts by a concave unit.

Looking at map M, the Salza River once again has formed concave units in the bends, with an alternation of convex and concave features in the first bend. Map N has another complex array of geomorphic units near river km 55 and the Salza River is again split in two streams. Approaching the next bend in map N downstream, there is another prominent concave feature in the bend. In the last map O, approaching the end of the Salza River study area, there is a large planar feature and another complex array right before the bend with several boulders. In the final riverbend is another concave feature flowing around the outflow of a tributary.

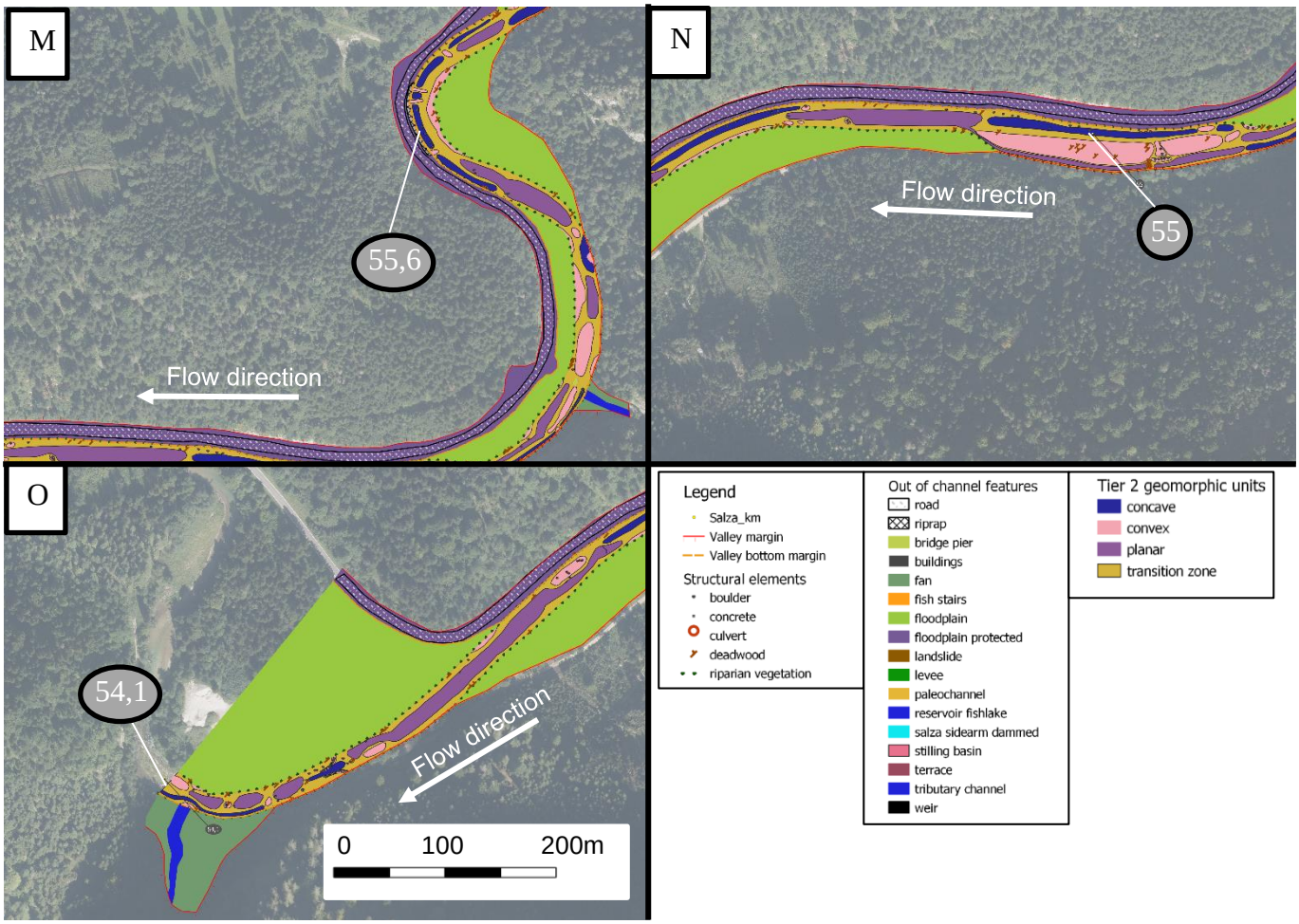


Figure 107: Mapped Tier 2 geomorphic units for the Salza River between river km 54.1 and 55.6.

Besides a mere written description, a numerical analysis of the Tier 2 in-channel features was also made by adding the area of all geomorphic units via the Field Calculator in QGIS. The absolute square meter values can be found in the Table 18 below and its accompanying relative values are depicted in Figure 108. In total the Salza River covers 190,182 m², with 70,631m² lying in the confined and 119,551 m² lying in the unconfined valley.

Table 18: Area coverage for the Tier 2 geomorphic units for the total, confined and unconfined Salza River study area.

	Total Salza River	Confined Salza River	Unconfined Salza River
Concave (m²)	39,986	9,971	30,015
Convex (m²)	33,718	15,130	18,588
Planar (m²)	42,311	13,257	29,054
Transition zone (m²)	74,167	32,273	41,894
Total (m²)	**190,182**	**70,631**	**119,551**

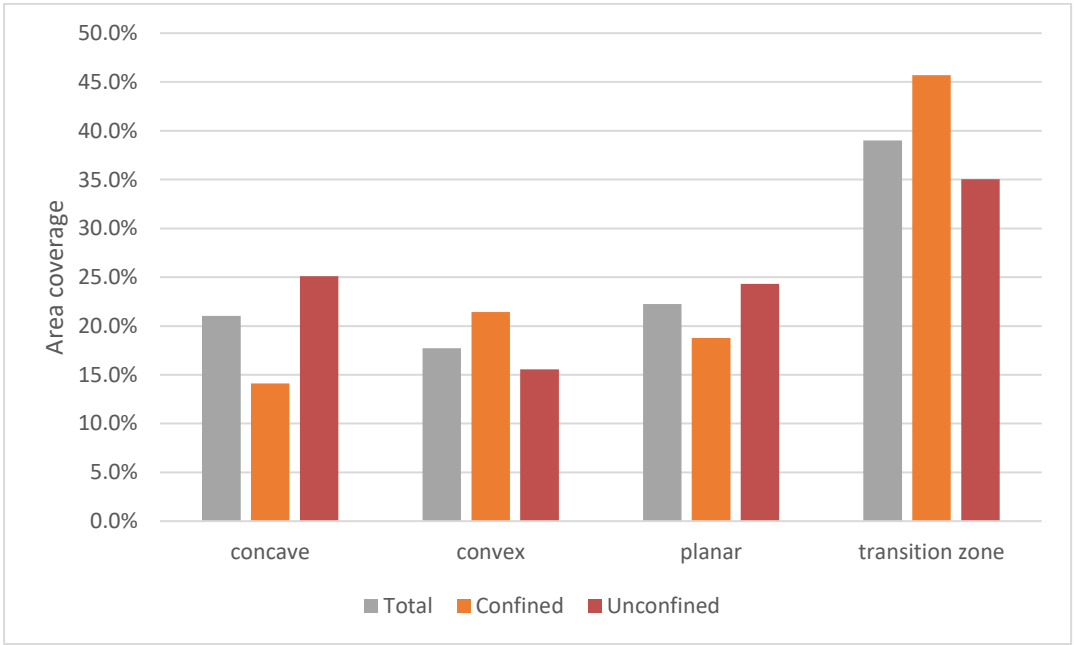


Figure 108: Area coverage of Tier 2 geomorphic units in the total, confined and unconfined Salza River study area.

Switching over to the diagram in Figure 108, looking at the Total Salza River in grey, we see that the transition zone is the most common unit with 39.0%. Second most common are planar geomorphic units with 22.2%. Moreover, concave and convex units for the total Salza River account for 21.0% and 17.7%. Noticeably however is how the confined Salza River differs from the unconfined Salza River. In relative values the transition zone amounts to a large 45.7% for the confined but only 35.0% for the unconfined Salza River. In addition, there were more convex units found in the confined Salza River, covering 21.4% vs covering 15.5% in

the unconfined Salza River. The unconfined Salza River however had more planar and distinctly more concave Tier 2 geomorphic units. The difference for the planar units is 24.3% vs 18.8% and for the concave units 25.1% vs 14.1% comparing the unconfined and confined Salza River.

Next, the riparian vegetation was analysed. Looking at Table 19, the whole Salza River margin had a length of 17,901 m, the confined Salza River 5,913 m and the unconfined Salza River 11,988 m. The riparian vegetation for the whole Salza River was present at 85.1% of the river margin. Examining the two Salza River segments we see that the confined Salza River had a riparian vegetation at 94.66% of the river margin and the unconfined at 80.38% of the river margin.

Table 19: Length of river margin and riparian vegetation as well as overlap in % of the total, confined and unconfined Salza River study area.

	Total Salza River	Confined Salza River	Unconfined Salza River
River margin (m)	17,901	5,913	11,988
Riparian vegetation (m)	15,233	5,597	9,636
Overlap (%)	**85.10**	**94.66**	**80.38**

Besides polygon features, structural elements within the river margin were mapped as point features. In total, see below in Table 20, 473 boulders, 2 concrete elements, 2 culverts and 240 deadwood elements were mapped. For the confined Salza River 204 boulders and 106 deadwood elements were mapped and for the unconfined 269 boulders, 2 concrete elements, 2 culverts and 134 deadwood elements were mapped. In comparison the unconfined Salza River had a lot more boulder and deadwood elements than the unconfined Salza River.

Table 20: Total recorded in-stream structural elements of the total, confined and unconfined Salza River study area.

	Total Salza River	Confined Salza River	Unconfined Salza River
Boulder count	473	204	269
Concrete count	2	0	2
Culvert count	2	0	2
Deadwood count	240	106	134

6.2.3 Third map: Mapping of Tier 3 geomorphic units

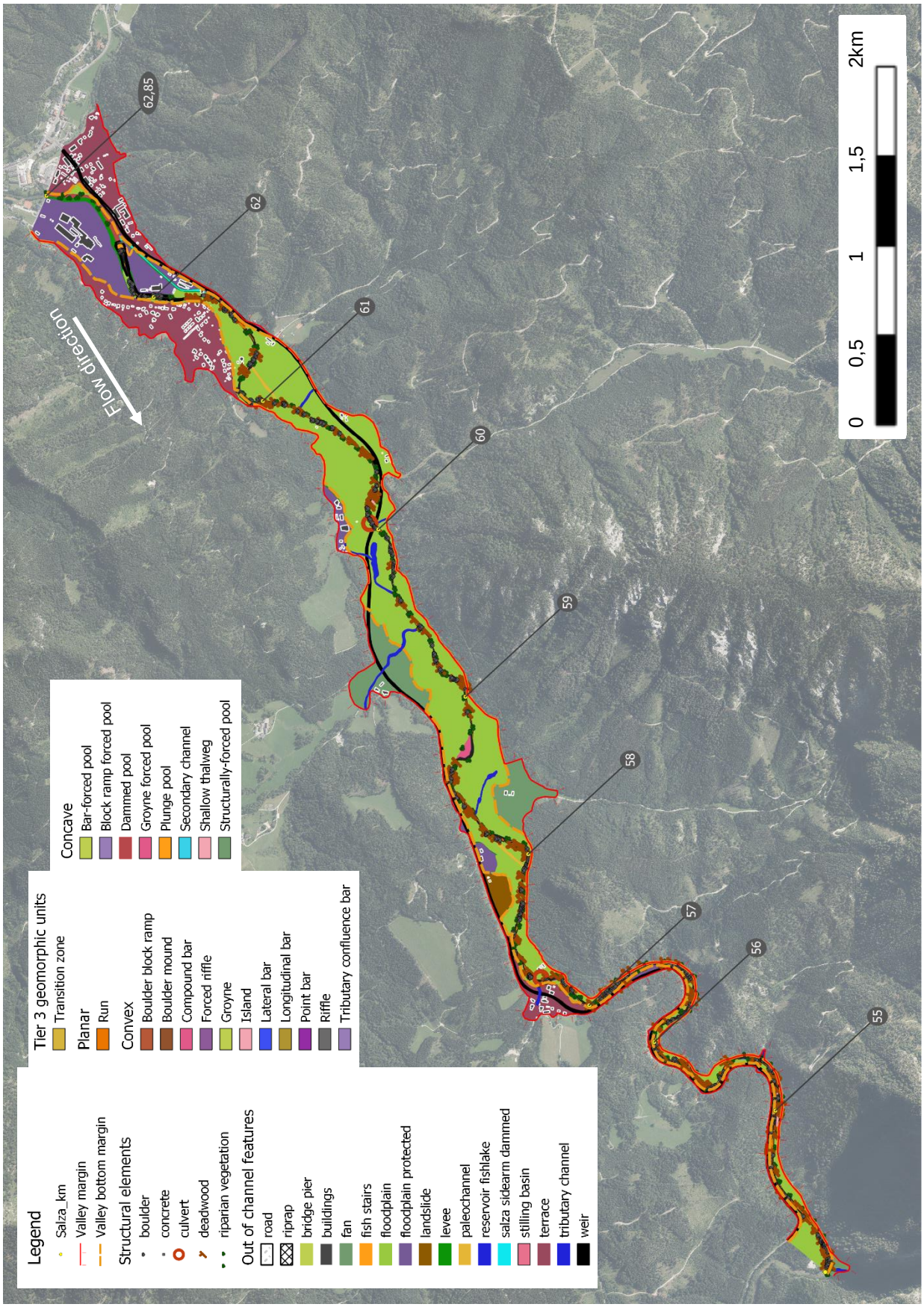


Figure 109: Mapped Tier 3 geomorphic units for the whole Salza River study area.

The third and final map consisted of specifying the previous mapped Tier 2 geomorphic units into Tier 3 geomorphic units as described in chapter *5.2.2 Methods*. The mapped Tier 3 geomorphic units for the whole Salza River study area can be found in Figure 109. The structural elements as well as out-of-channel features remain the same as in the second map, only the in-channel Tier 2 units have been supplemented with the in-channel Tier 3 units.

Next, the overview map from Figure 109 will be zoomed into in 15 small map excerpts on the following pages in Figure 110, Figure 111 and Figure 112. The maps are alphabetically ordered in the flow direction of the Salza River starting at river km 62.85 in map A. Looking at map A, the previous concave unit was defined as a dammed pool. Right after the weir, looking at map B, we see a plunge pool followed by several different convex and concave features such as a boulder block ramp, a block ramp forced pool and a longitudinal bar which led to a shallow thalweg, previously mentioned as a deep concave feature. In the first bend we have groynes with a groyne forced pool right behind. There is also a point bar in the inner bend. The shallow thalweg flows continuously with only block ramps in between around river km 61.8. Looking at map C we have a mostly planar section, which was identified to be a run, with block ramps in between and further groynes on the orographic left side before the bend. The shallow thalweg then flows again in the bends intersected by further block ramps and an island near the paleo channel. The Salza River in map D consists mostly of a run with an occasional riffle. Looking at map E, the Salza River has another shallow thalweg forming in the bend, where further block ramps are positioned, and reaches a complex riffle, pool, block ramp, pool with a large island on the orographic left side. Further lateral bars as well as a longitudinal bar follow before with bar forced pools on the outer bend of the curve before river km 60. Map F shows more run units with block ramps, block ramp forced pools and riffles found scattered in the river. Also, a tributary confluence bar formed in the lower tributary in map F.

Map G in Figure 111 has several riffle/structurally forced pool sequences and a point bar in the inner bend of the first river curve. At the confining margin above river km 59 there is a deep shallow thalweg with a large riffle right below. Approaching the hotspot, the Salza River has a mostly planar run unit before digging into the left erosion bank of the erosion hotspot via a shallow thalweg which mouths into a bar forced pool. The bar opposite the erosion

hotspot was mapped as a compound bar due to its variance in vegetated, non-vegetated, coarse and fine gravel areas with a residual water channel at the orographic right side.

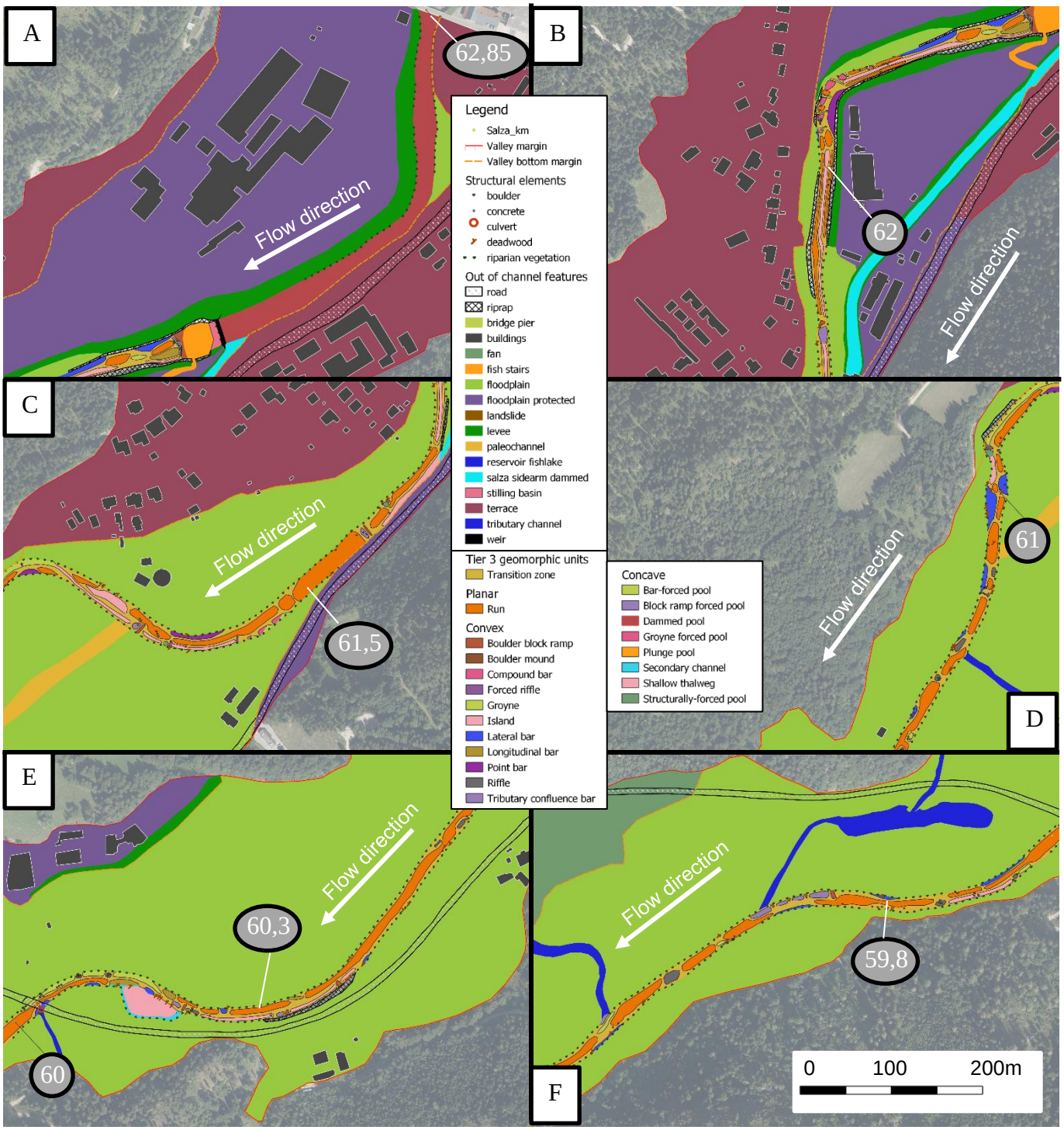


Figure 110: Mapped Tier 3 geomorphic units for the Salza River between river km 60 and 62.85.

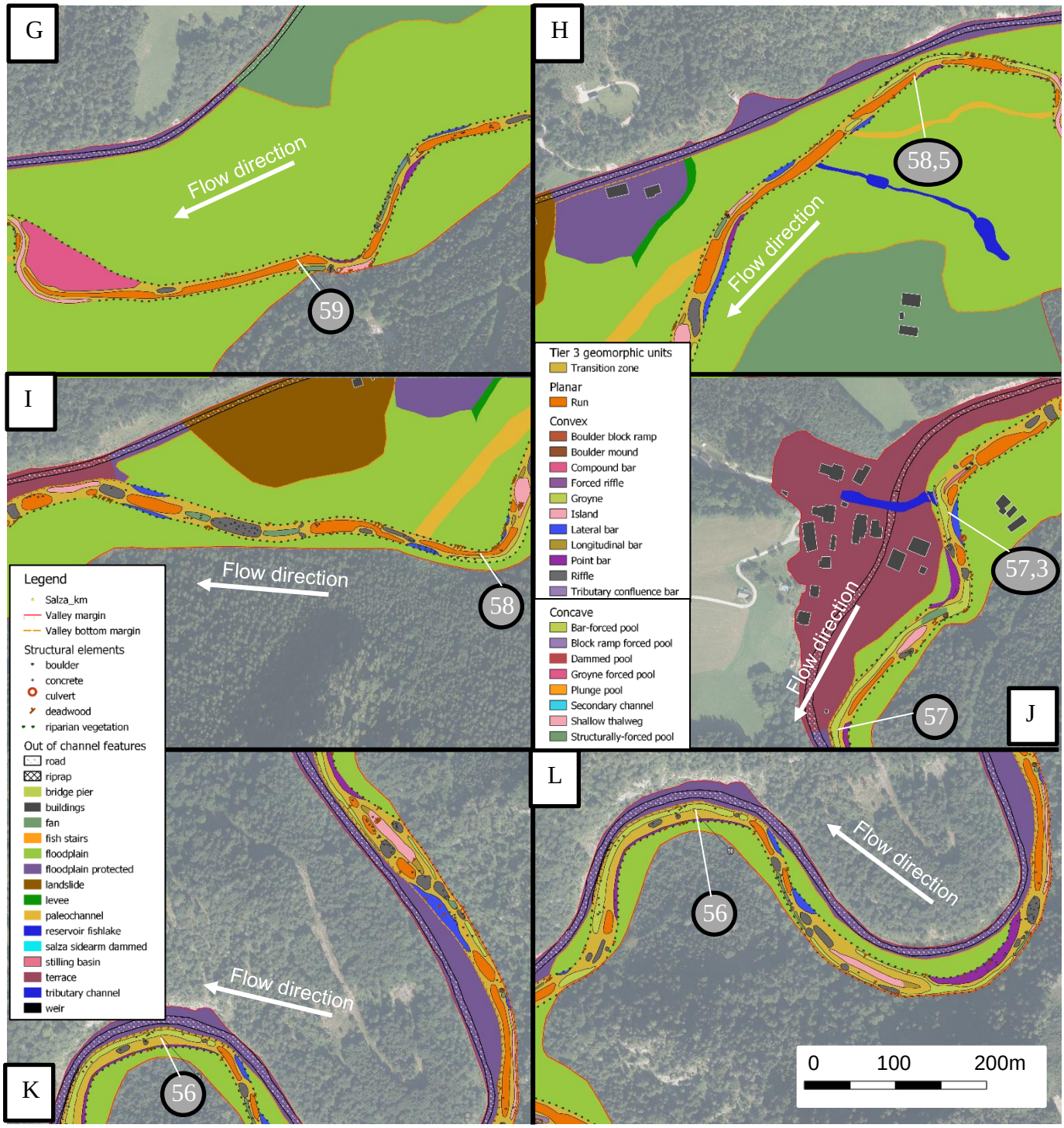


Figure 111: Mapped Tier 3 geomorphic units for the Salza River between river km 56 and 59.

Map H shows point bars in the inner bends of the river curves with mostly run units in the straight sections. Approaching river km 58 in map I, we have another complex array of units such as a riffle, longitudinal bar, island and lateral bars before flowing into a bar forced pool in the bend at river km 58. Several prominent riffle/pool sequences follow, with a very large riffle midway in map I, see grey oval, which in addition has a vast number of boulders. Further riffles are found next in the beginning of map J before we find a distinct forced bar

after a bridge pier. Another complex section is found next between river km 57 and 57.3 where bars, pools and riffles were mapped, leading into a very deep bar forced pool. A further island was located straight after, diverting the Salza River into a bar forced pool at river km 57 before flowing into the confined valley.

Map K shows a further complex set up of concave, convex and planar units with a large island in between splitting the Salza River in two. A lateral bar forces the river into a bar forced pool in map L and further into a shallow thalweg before approaching the first bend in the confined zone. Another point bar can be found in the inner bend with a further island splitting the Salza River once more into two streams. Several riffles and pools follow next, with another point bar in the inner bend and a bar forced pool in the outer bend at river km 56. More riffles and pools are right after, before looking at map M, flowing into several block ramps and block ramp forced pools at river km 55.6. A further variation of concave and convex units was mapped before reaching another island, in map N, at river km 55 and splitting the Salza River once again in two streams.

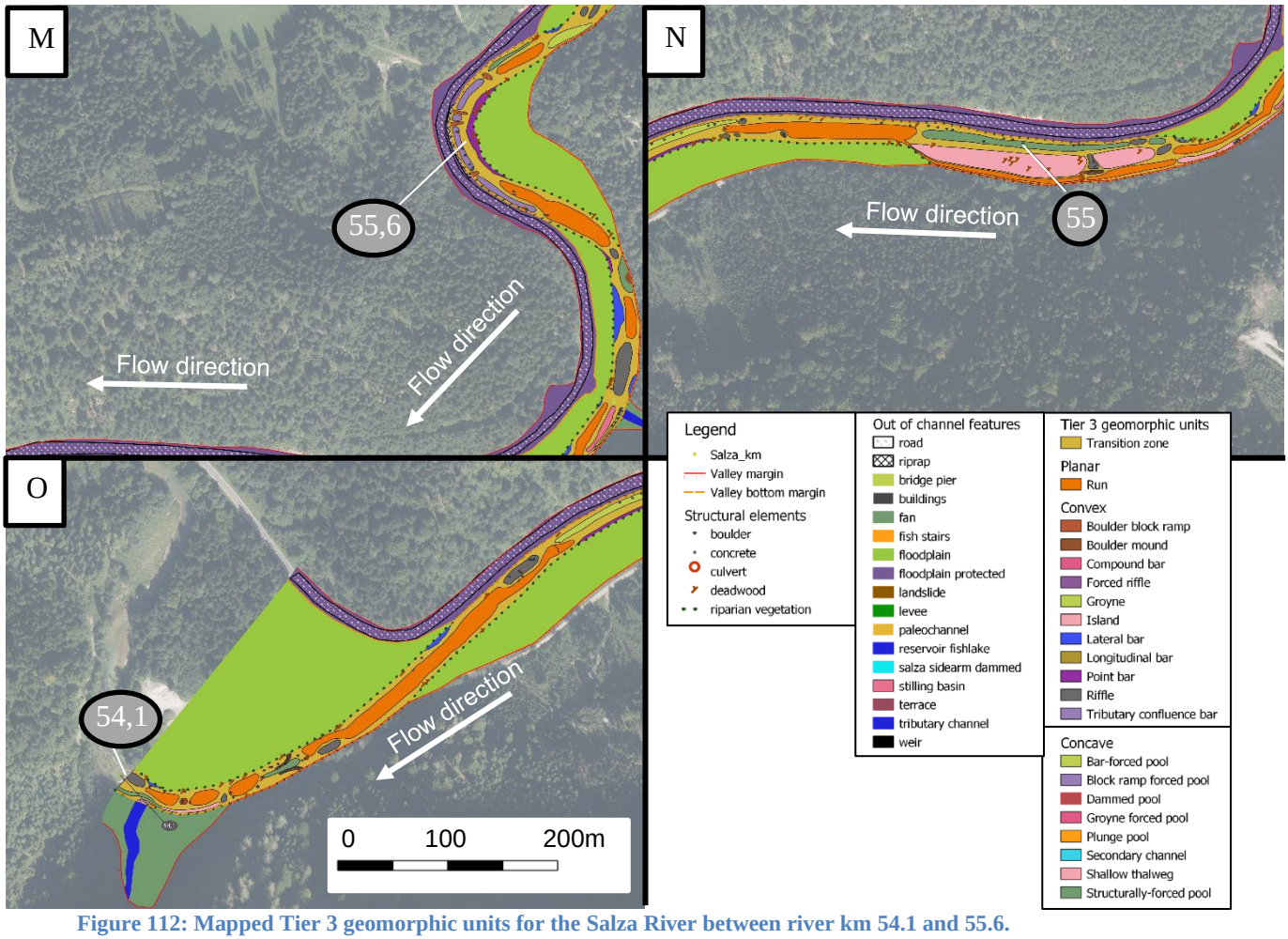


Figure 112: Mapped Tier 3 geomorphic units for the Salza River between river km 54.1 and 55.6.

In map O, the river has another point bar/bar forced pool combination in the penultimate curve with a riffle and large run right downstream. An interesting bottle neck formation was found before the last bend consisting of two boulder mounds with a structurally forced pool in between. Lastly the river has a riffle, run, riffle, run, riffle segment with a shallow thalweg forming in the outer bend and being formed into a structurally forced pool through a further tributary confluence bar.

Next the area coverage of the Tier 3 units was once again calculated for a numerical analysis. The absolute square meter values can be found in the below Table 21 and its accompanying relative values are depicted in Figure 113. Examining the table and the diagram on the following pages, we can see that the planar run feature as well as the transition zones are the largest occurring units in the whole study area as well in the confined and unconfined segments. More interesting however are the differences in the concave and convex units. The most common occurring concave geomorphic unit overall and in the unconfined segment is the dammed pool, whereas in the confined segment the bar forced pool occurs the most. Also, the shallow thalwegs and structurally forced pools were quite common. Least common was the groyne forced pool and a secondary channel. The largest area coverage of a convex feature was the island for the whole and confined Salza River, but the compound bar for the unconfined Salza River. Also, very prevalent for all segments were lateral and point bars as well as riffles. Least common was the structurally forced riffle and convex bar.

Regarding the location of possible fish spawn habitats, the fish occurrence in the Salza River are composed of Grayling, River- and Rainbow trout, according to the distributor of fish licenses in the study area [5]. Further the licensor states *"all tributary rivers are fish spawn and protection areas year-round"* (translated). The ÖBf wrote in a recent press release that *"Graylings but also trouts and rare Huchen or European bullhead spawn on gravel and depend on loose and well flushed Riverbed. To reproduce, the animals lay their eggs in the loose gravel bed where they grow up to larvae well protected from predators or the current."* (translated) [6].

Considering the first information, we can deduct that all mapped tributaries, pictured in dark blue in the Tier 3 maps, are possible fish spawn habitats. Further considering the ÖBf statement, all planar mapped runs, displayed in orange in the Tier 3 maps, are also possible

fish spawn habitats as well as transition zones under the right conditions. The area coverage for the potential fish spawn habitats in runs amounts to 22.25% for the total, 18.84% for the confined and 24.30% for the unconfined Salza River. The area coverage for the potential fish spawn habitats in transition zones amounts to 39.00% for the total, 45.69% for the confined and 35.04% for the unconfined Salza River. In total, therefore the potential area coverage for the fish spawn habitats in the whole Salza River study area amounts to 61.25% for the total, 64.53% for the confined and 59.34% for the unconfined Salza River.

Table 21: Area coverage for the Tier 3 geomorphic units for the total, confined and unconfined Salza River study area.

		Total Salza River (m^2)	Confined Salza River (m^2)	Unconfined Salza River (m^2)
Concave	bar forced pool	10,358	4,953	5,405
	blockramp forced pool	1,534	790	744
	dammed pool	16,786	0	16,786
	groyne forced pool	346	0	346
	plunge pool	1,150	1,150	0
	secondary channel	340	0	340
	shallow thalweg	5,955	861	5,094
	structurally forced pool	3,517	2,217	1,300
Convex	boulder block ramp	554	134	420
	boulder mound	289	265	24
	compound bar	4,915	0	4,915
	convex bar	49	49	0
	forced bar	342	224	118
	forced riffle	69	0	69
	groyne	206	0	206
	island	7,473	4,886	2,587
	lateral bar	6,138	2,080	4,058
	longitudinal bar	912	263	649
	point bar	5,428	3,344	2,084
	riffle	7,168	3,810	3,358
	structurally forced riffle	36	36	0
	tributary confluence bar	139	39	100
Planar	run	42,311	13,257	29,054
Transition zone		74,167	32,273	41,894
Total		**190,182**	**70,631**	**119,551**

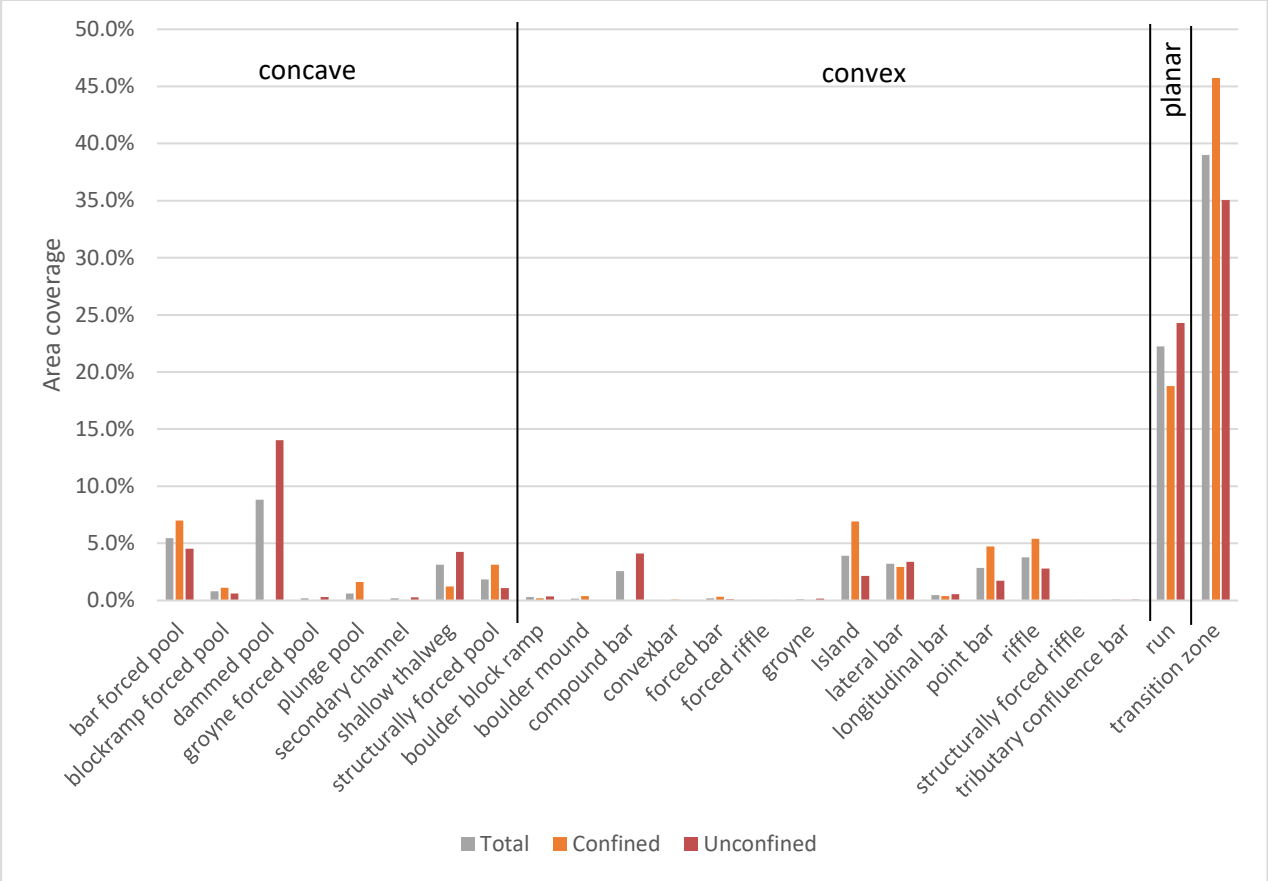


Figure 113: Area coverage of Tier 3 geomorphic units in the total, confined and unconfined Salza River study area.

After the initial mapping in May of 2017 a follow up in-field-mapping was done in June of 2018. However, no noteworthy changes happened in the 13-month period except for some relocation of deadwood and an increase in riparian vegetation. Thus, a follow up map was not created.

6.2.4 Comparison with ÖBf mapping

The entire extent of the ÖBf mapping of the Salza River provided to me, can be seen below in Figure 114. The river mapping of the blue line reaches from river km 55.3 to 60.7 and only includes two features each being a different fluvial rating of the Salza River. The green lines in the out-of-channel areas are differentiations between housing, agriculture, forestry, bank protection and fortified riverbed areas.

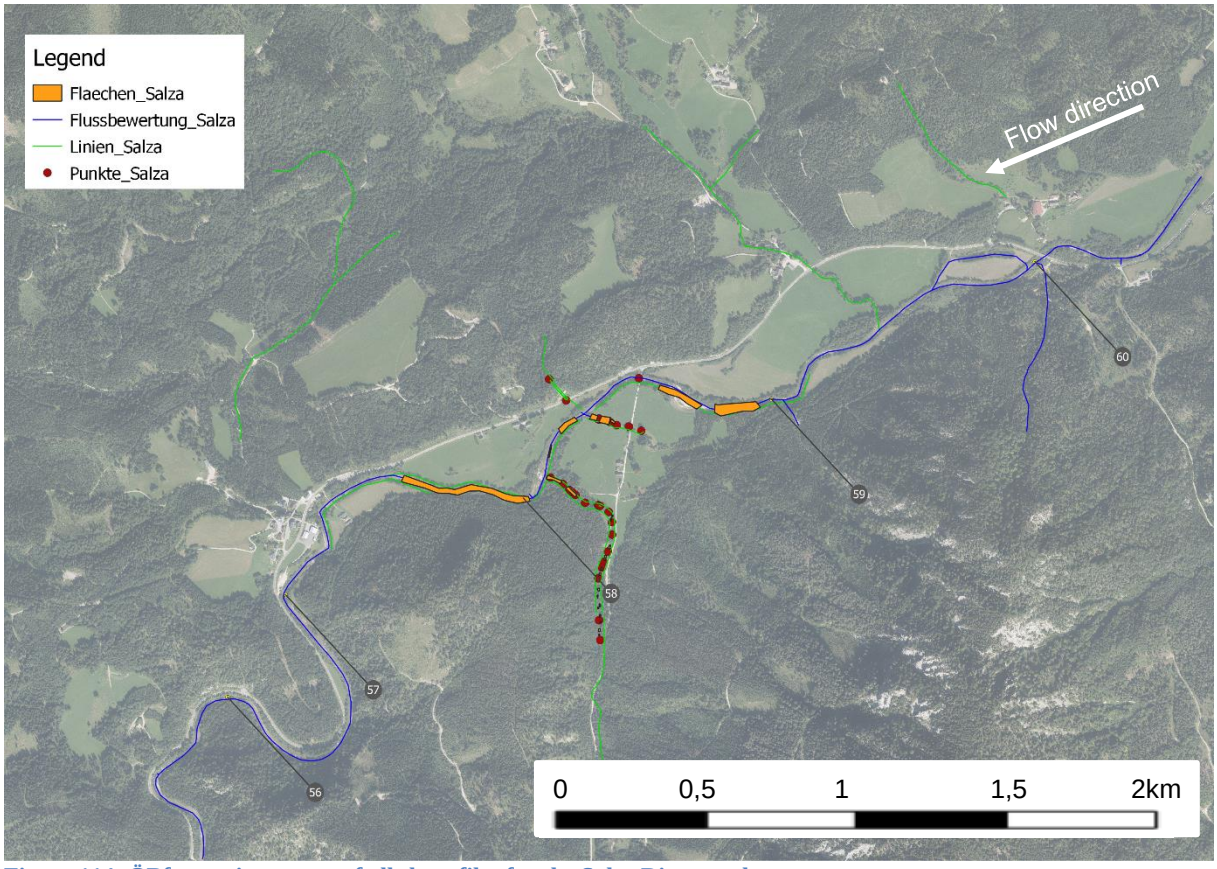


Figure 114: ÖBf mapping extent of all shapefiles for the Salza River study area.

Zooming into the map excerpt on the following page in Figure 115, which solely includes the polygon and point features, the mapping extent here lies between river km 57.6 and 59 of the Salza River. Noticeably are the two side channels of the Salza River which were mapped in greater detail than the main Salza River. Polygon features which were mapped are: gravel banks, neophyte occurrence, areas of riparian vegetation and the category other. Point features which were mapped are: deadwood, pipe, bridge, wooden rakes, check dam, waterfall and other.

There are five comparable polygon features in the main Salza River, 3 of which are mapped as riparian vegetation see red arrows in Figure 115 and 2 of which are gravel banks see light

blue arrows. The riparian vegetation can be confirmed from my mapping. The gravel banks however were not overlapping the mapped gravel banks in this thesis, partly since gravel banks occur and disappear quite frequently depending on the discharge rates. The only point feature mapped in stream of the Salza River is shown at the yellow arrow and is a bridge. The bridge pier was also marked in my mapping.

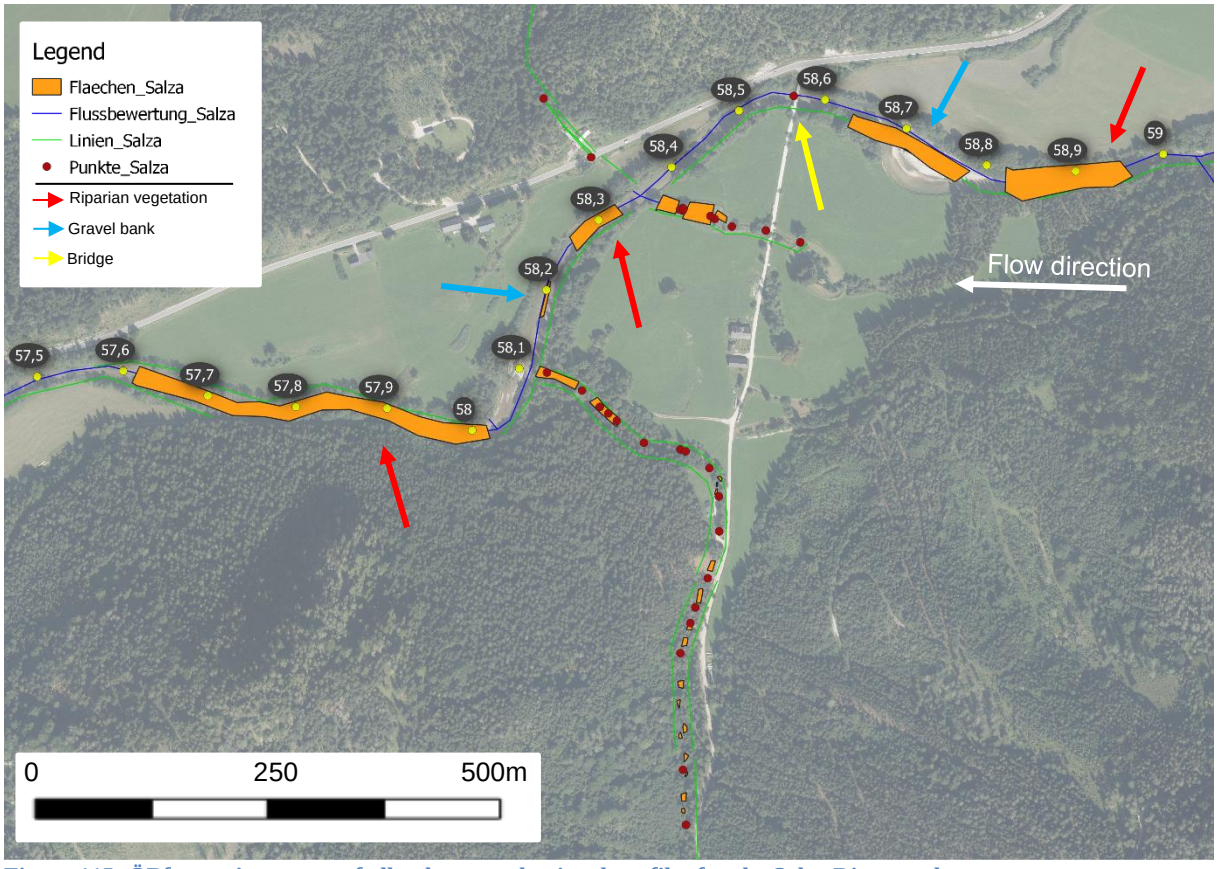


Figure 115: ÖBf mapping extent of all polygon and point shapefiles for the Salza River study area.

Overall, the ÖBf mapping of the main channel of the Salza River was coarsely mapped and in comparison, with the Tier 2 and Tier 3 mapping done in this thesis incomplete and therefore not particularly comparable.

6.3 Monitoring of the erosion hotspot

6.3.1 Erosion Pin Version 1

In order to measure any changes of the hotspot (seen in Figure 6) a monitoring was done over the period of roughly a year via two methods: via erosion pins and a photogrammetric analysis. An initial version of erosion pins was set up on 06.05.2017, followed by a second version on 15.06.2017, see Table 22. However, while no follow up measurement could be taken with the first method, only one follow up measurement of the second erosion pin method was obtainable due to unforeseen circumstances described below.

Table 22: Erosion pin versions used at the hotspot of the Salza River study area.

Measurement	Date	Version
#1	06.05.2017	1
#2	15.06.2017	2
#3	11.07.2017	2

The first erosion pin version used, was set up on the 06.05.2017 with the method described in chapter *5.3.2 Methods*. The result was a set of markers as seen in Figure 116. The setup was also communicated with the deputy manager of the ÖBf Gusswerk Stefan Friedl via Email on the 08.05.2017.



Figure 116: Set up of erosion pin method 1 at the erosion hotspot in the Salza River study area.

In Table 23, are the results for the initial erosion pin measurements. Pin 1 hereby is the closest pin visible from the perspective in Figure 116. However, upon arrival for a follow up

measurement of the erosion pins on the 15.06.2017, all pins were extracted from the erosion bank and placed nicely in two piles alongside the bank see Figure 117.



Figure 117: Extracted erosion pins at the erosion hotspot.

Table 23: Measurements for the first erosion pin method on the 06.05.2017.

Pin	Meter	Distance pin to bank edge (cm)
1	0	240.8
2	5	204.9
3	10	217.4
4	15	224.2
5	20	215.7
6	25	227.1
7	30	252.4
8	35	253.0
9	40	240.3
10	45	276.5
11	50	236.5
12	55	214.2
13	60	226.1
14	65	267.5
15	70	233.7
16	75	248.6
17	80	244.4
18	85	212.3
19	90	250.1
20	95	238.7
21	100	224.6
22	105	215.0
23	106.5	168.7

The view of the erosion hotspot after the pin extraction is seen below in Figure 118.



Figure 118: View of the erosion hotspot after the erosion pin extraction in the Salza River study area.

6.3.2 Erosion Pin Version 2

After the previous incident with the first erosion pin setup, a second erosion pin version was set up on the 15.06.2017 with the method described in chapter *5.3.2 Methods*. The final set up can be seen below in Figure 119. Pin 1 is the closest pin from the perspective.

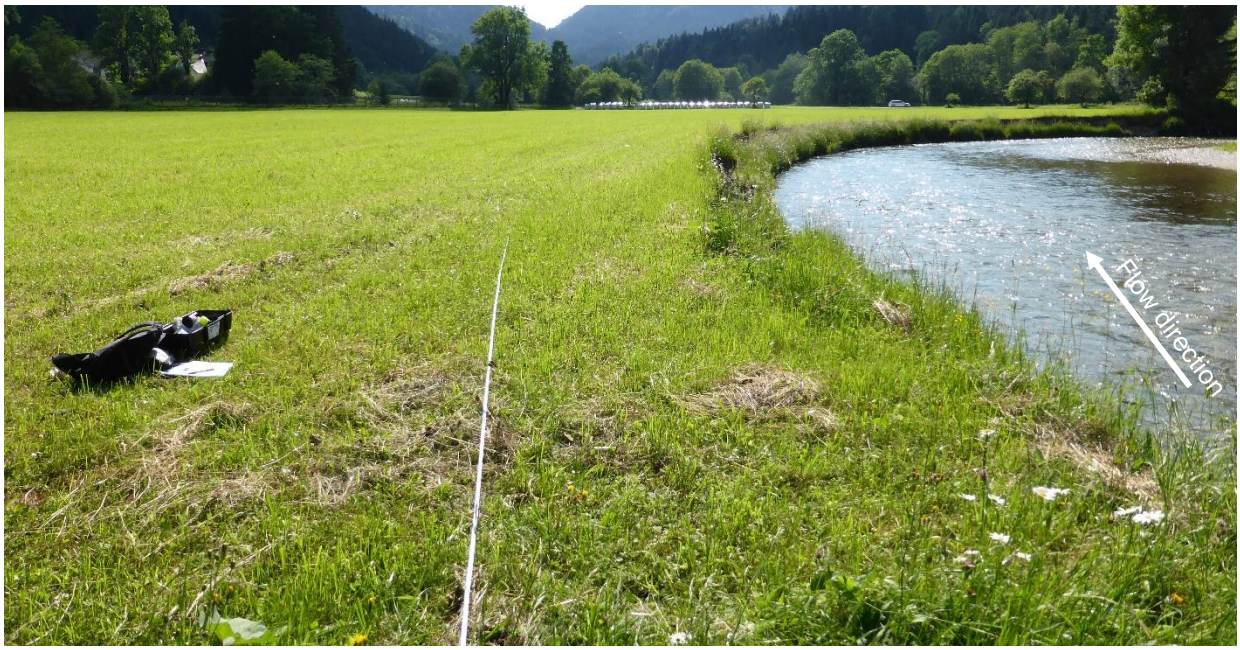


Figure 119: Set up of erosion pin method 2 at the erosion hotspot in the Salza River study area.

An initial and follow up measurement was done on the 15.06.2017 and the 11.07.2017. Following in Table 24, are the results for the version 2 erosion pin measurements.

Table 24: Measurements for the second erosion pin method.

Pin	Meter	Distance pin to bank edge (cm)		Difference #2 - #1 (cm)
		#1-15.06.2017	#2-11.07.2017	
1	0	284	281.5	-2.5
2	10	251.5	251.5	0
3	20	314.5	313.5	-1
4	30	332.5	320	-12.5
5	40	272	272	0
6	50	298.5	298	-0.5
7	60	337	337	0
8	70	272	271	-1
9	80	323	320.5	-2.5
10	90	328	327.5	-0.5
11	100	273	274	1
12	106.5	321	321	0

Examining the results from Table 24, we can deduct that overall, there was a clearly visible reduction in the measured distance from 15.06.2017 to 11.07.2017. There were three occasions where the distance did not change, and one instance where there was an increase by 1 cm. The largest decrease was measured with -12.5 cm and the smallest decrease with -0.5 cm. In total the mean change was -1.63 cm for the whole bank.

6.3.3 Photogrammetric analysis

In addition to the erosion pin methods 1 and 2, images for a photogrammetric analysis were taken on five separate occasions between 06.05.2017 and 11.06.2018, using the method described in chapter *5.3.2 Methods*. In total 5-point clouds were computed see below Table 25.

Table 25: Computed point clouds of the erosion hotspot in the Salza River study area.

Point Cloud	Image capture date
#1	06.05.2017
#2	15.06.2017
#3	11.07.2017
#4	06.10.2017
#5	11.06.2018

2D changes

In a prime step the computed point clouds were compared for any 2D changes along the whole erosion bank. The accompanying Gauss normal distributions can be found in chapter *11. Appendix* and will be mentioned below with the Figure number. Cloud #2 was first compared with cloud #1 see Figure 120. Any areas in light blue or green, are zones were the cloud #2 shows accumulation zones and any areas in orange or red are zones were the cloud #2 shows erosion zones compared to cloud #1. All measurements are in metres. We see a noticeable accumulation zone in the middle of the erosion hotspot and mostly erosion zones everywhere else. Looking at the Gauss normal distribution of the 2D changes from Figure 120 we see in Figure 158 the mean lying between -2.5 and -2 m showing there has been more erosion than accumulation zones from point cloud #1 to #2.

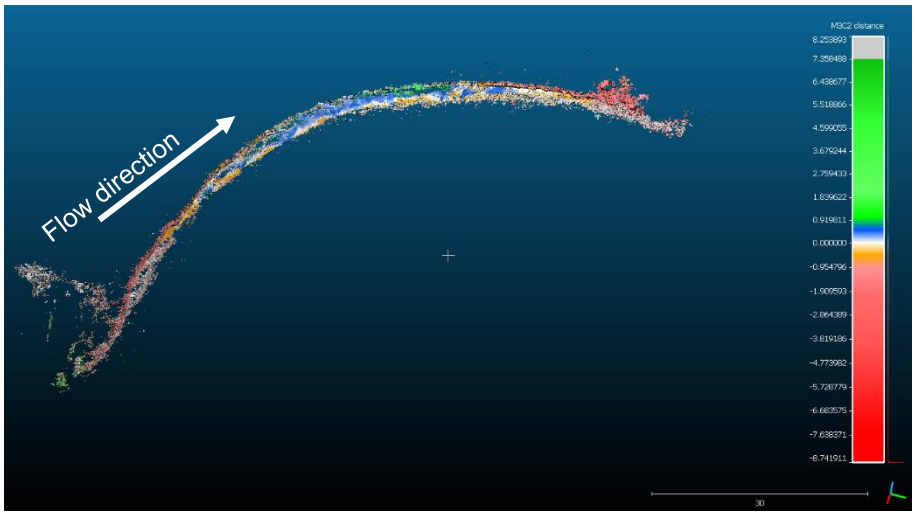


Figure 120: Comparison of any 2D changes (in metres) from cloud #1 to cloud #2.

Comparing point cloud #3 with point cloud #2 in Figure 121, we notice again considerable erosion within the bend of the erosion hotspot. Accumulation zones are only found on the edges. The mean of the Gauss normal distribution lies between -2 and -1.5 m, again showing more erosion than accumulation in that timeframe.

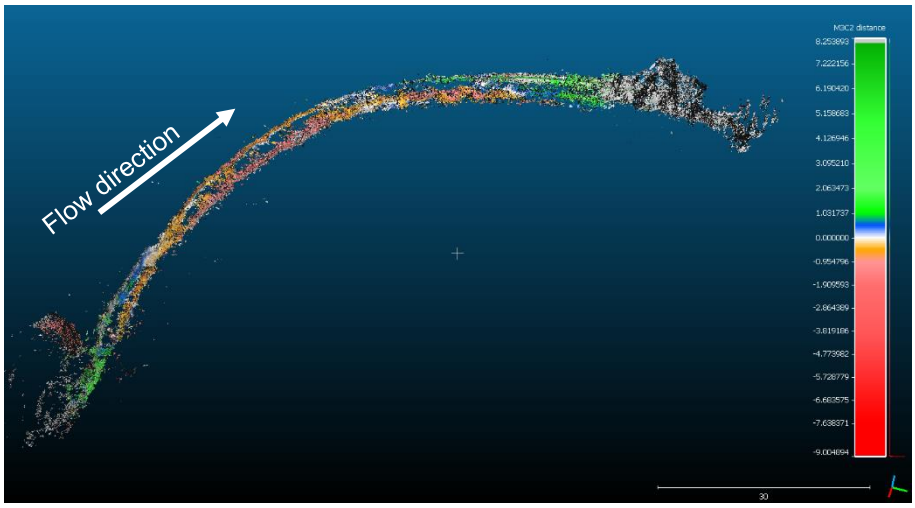


Figure 121: Comparison of any 2D changes (in metres) from cloud #2 to cloud #3.

Comparing cloud #4 with cloud #3 in Figure 122, we notice only little erosion and likewise only little accumulation. Examining the Gauss normal distribution in Figure 160 confirms this first glance with the mean lying between -1 and 0.5 m indicating a smaller rate of erosion than before.

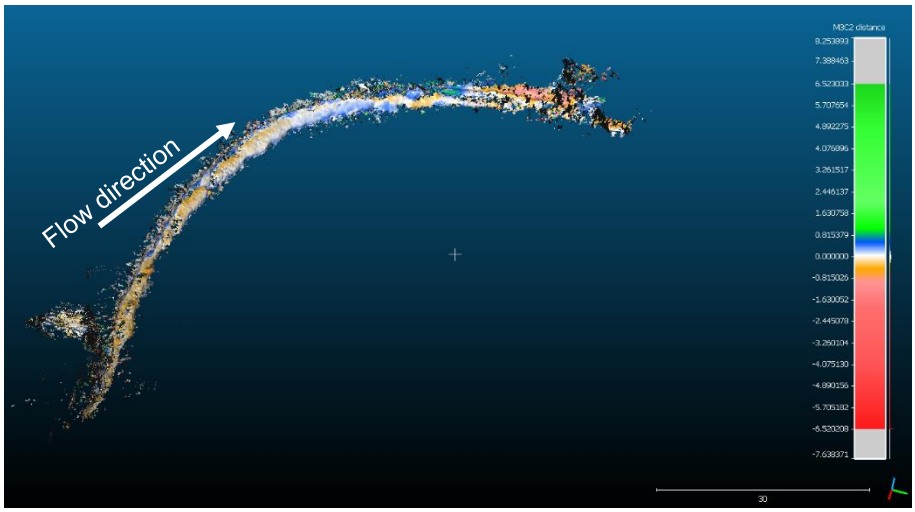


Figure 122: Comparison of any 2D changes (in metres) from cloud #3 to cloud #4.

Comparing the latest computed cloud #5 with cloud #4 in Figure 123 we can also deduct the rate of erosion and accumulation being similar to the previous comparison with only local erosion spots at the beginning and end of the bend and local accumulation in the middle of the bend. The Gauss normal distribution in Figure 161 indicated a mean value of roughly -2.5 m.

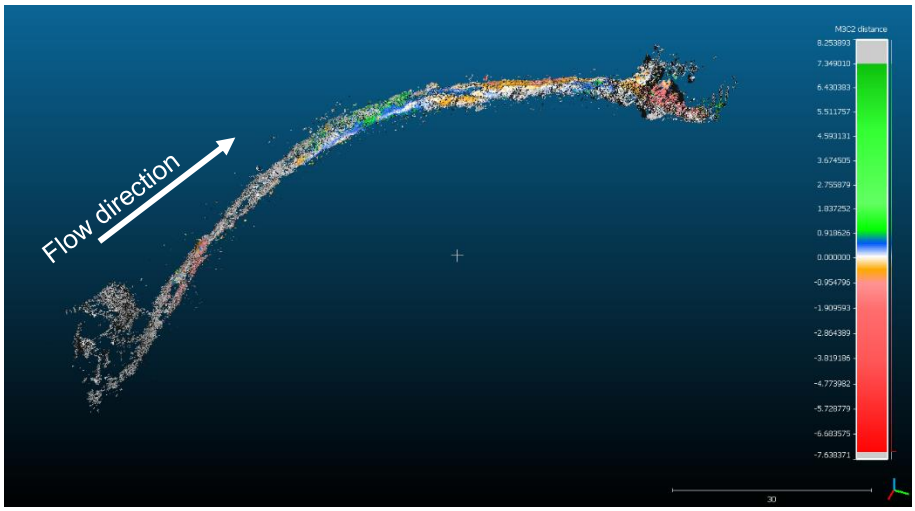


Figure 123: Comparison of any 2D changes (in metres) from cloud #4 to cloud #5.

Finally, the most recent cloud #5 from 11.06.2018 was compared with the initial cloud #1 from 06.05.2017, see Figure 124. We notice prominent erosion at the start and distinct erosion zones at the end of the bend. There seems to have been accumulation in the middle of the bend, see blue zone. The Gauss normal distribution gives a mean of roughly -2 m for the 13-month timeframe.

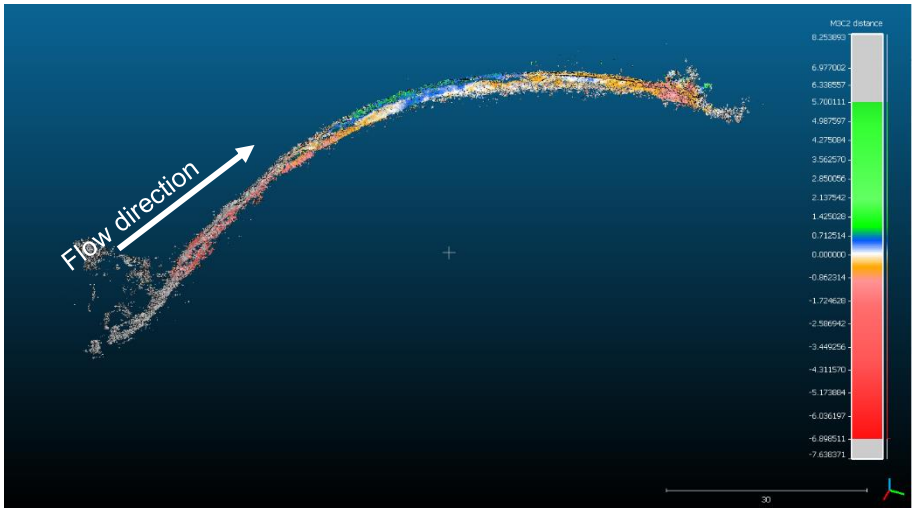


Figure 124: Comparison of any 2D changes (in metres) from cloud #1 to cloud #5.

2.5D changes

Next, a 2.5D volumetric analysis was done using the computed clouds from Table 25. In the below Figure 125, we see the changes in relative height of the 4 clouds viewed in the Z-axis projection. Areas in blue, as well as dark and neon green are cells which have decreased in relative height and areas in light green, yellow, orange and red cells which have increased in relative height. Additional all numerical volume changes can be found in Table 26.

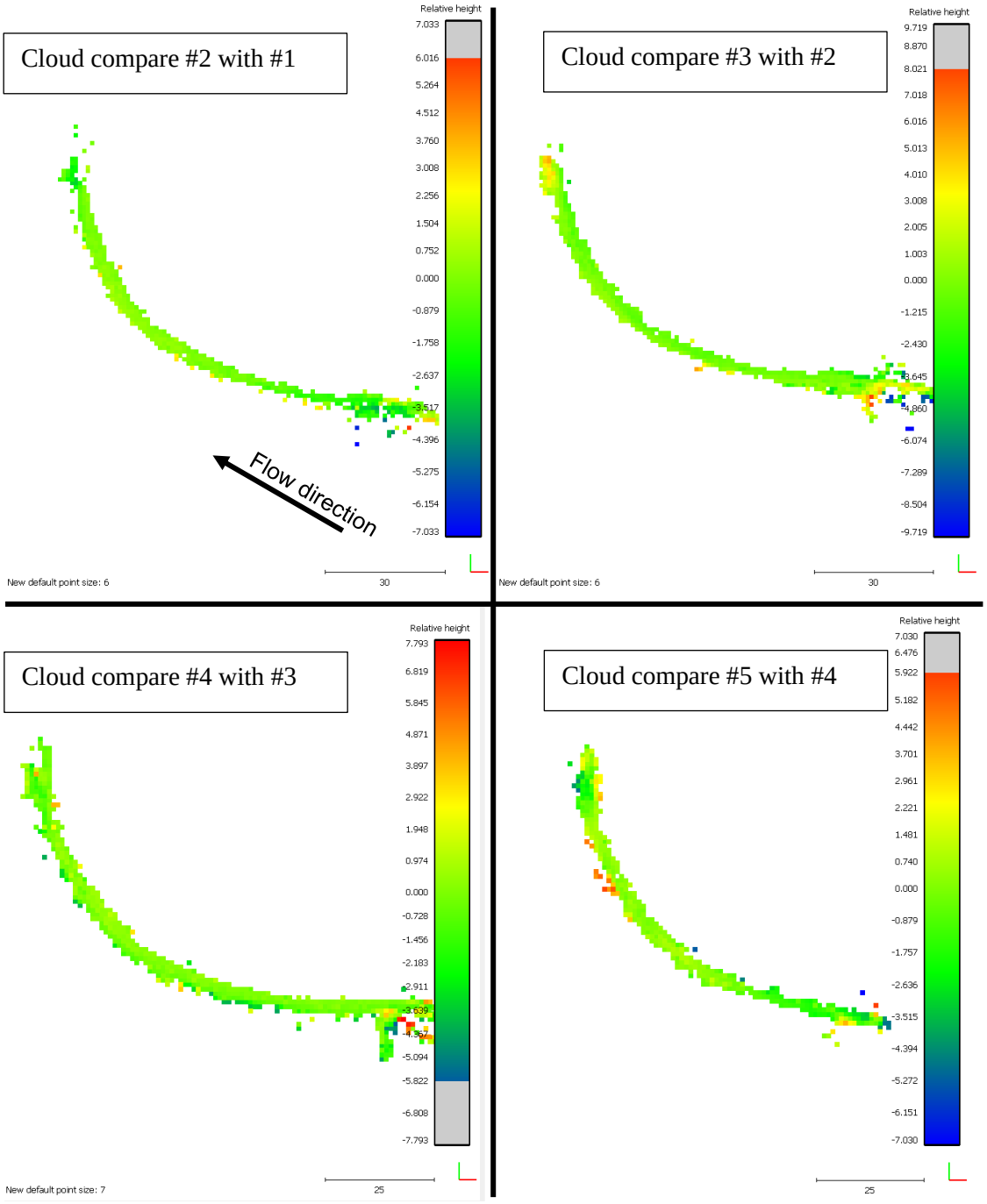


Figure 125: 2.5D cloud comparison of clouds #1, #2, #3, #4 and #5 of the erosion hotspot.

Further the most recent cloud #5 was compared with the initial cloud #1 and can be found in Figure 126 and its numerical volume changes in Table 26. Simply examining the colours in the five Figures, we would assume that overall, more cells have decreased in relative height.

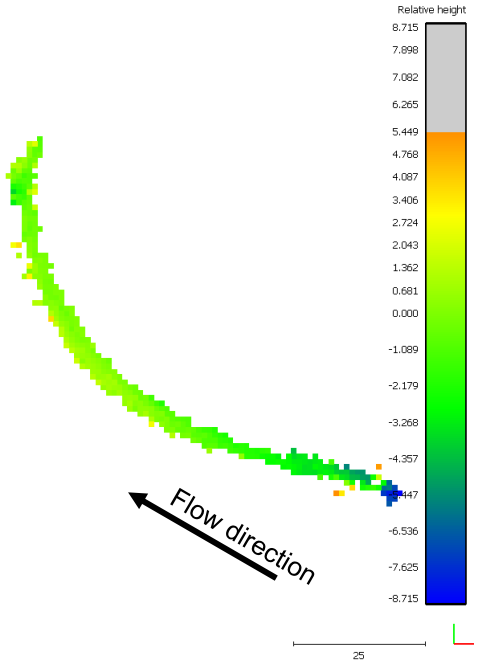


Figure 126: 2.5D cloud comparison of cloud #5 with #1 of the erosion hotspot.

This visual impression can also be validated by examining the values in the below Table 26. From cloud #1 to #2 there was an overall volume change of -177 m³, from cloud #2 to #3 of -17 m³, from cloud #3 to #4 of -94 m³ and from #4 to #5 of -52 m³. This totals to -340 m³ for all comparisons. Interesting is also that the volume change from cloud #1 to #5 accounts for -319 m³ which is nearly the same value as the sum and thus validates the results.

Table 26: 2.5D volume changes and additional metrics of the computed point clouds of the erosion hotspot in the Salza River study area.

Cloud	Added volume (m³)	Removed volume (m³)	Volume change (m³)	Matching cells (%)	Non-matching cells (%)		Average neighbour per cell
					Ground	Ceiling	
#2 with #1	+118	-295	-177	40.1	16.8	43.1	5,6/8
#3 with #2	+320	-337	-17	45.9	34.4	19.7	6/8
#4 with #3	+231	-325	-94	56	19.2	24.9	6/8
#5 with #4	+199	-250	-52	38.4	44.7	16.8	5,8/8
	Sum		-340				
#5 with #1	+115	-434	-319	47.3	33.0	19.7	5,9/8

6.4 Modelling of future hydro-geomorphic changes of the Salza River

The modelling results are split in two parts, first providing the results for the grain size approximations and then going into the results of the parametrization used for the modelling of the Salza River as well as the final modelling results for the timeframe 2019 - 2050 using the four discharge scenarios.

6.4.1 Granulometric analysis

Riverbed grain size approximation

In total, four line count analyses were carried out on two separate dates to approximate the riverbed grain size distribution using the method described in chapter *5.4.2 Methods*. The locations of the analyses are mapped as a green cross and can be seen in Figure 127. The line-count analyses #1 and #2 were carried out on the 07.05.2017 located between river km 58.7 and 58.8 and between river km 60.1 and 60.2 and the line-count analyses #3 and #4 were carried out during low water between river km 58.7 and 58.8 and roughly at river km 56.4.

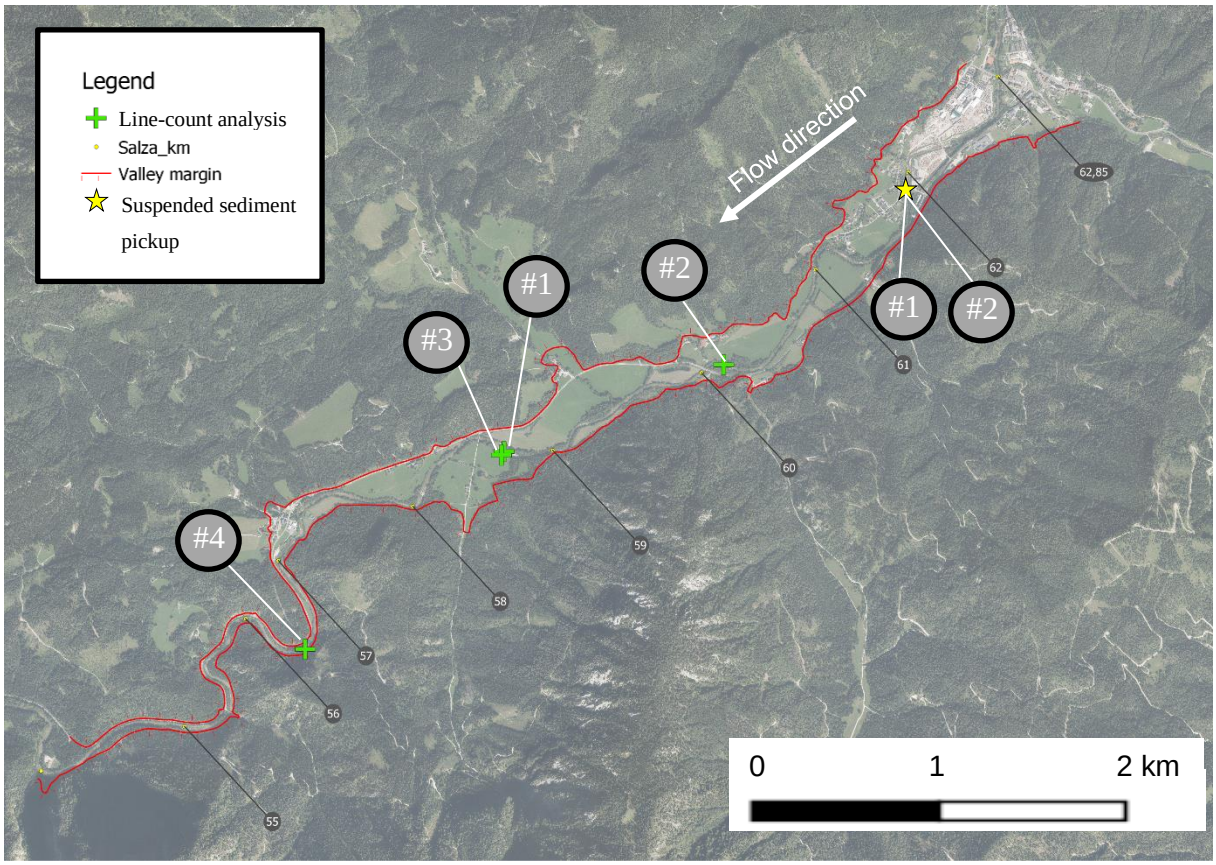


Figure 127: Location of line count analyses and suspended sediment pickup in the Salza River study area.

The locations of the line count analyses can be seen below in Figure 128. Analyses #1 and #2 were positioned more in the middle of a gravel bank with previous sedimented riverbed material, whereas during analyses #3 and #4 were positioned in more recent sedimented riverbed material and closer to the river.

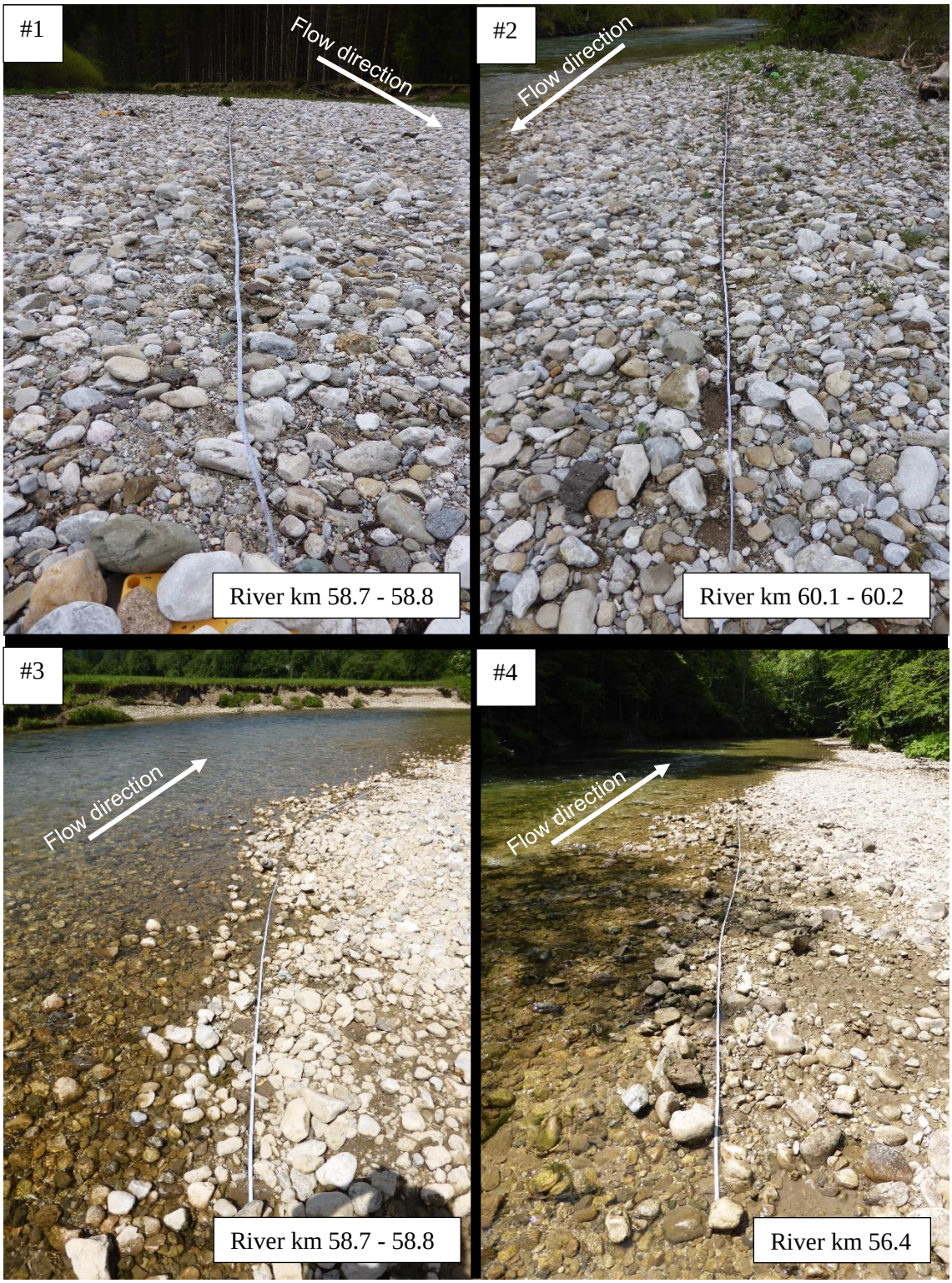


Figure 128: Close up of the four completed line-count analyses in the Salza River study area.

Before constructing the grain size distributions, the results of the line count analyses (LCA) had to fulfil two criteria to be counted as valid. FEHR stated that (translated from German) *"To ensure a representativity of the analysis, a minimum total of 150 rocks with a minimum of 30 rocks in the average grain size should be measured and counted."* (FEHR 1987: 1106). Below in Table 27 are the statistics for all four measurements. We can see that the total number of rocks measured were 241 for #1, 260 for #2, 180 for #3 and 171 for #4. All numbers are clearly over the minimum requirement of 150 *(Sum n)*. Also, the number of rocks in the average grain size *(Sum n mean)* were all clearly above the minimum requirement of 30 stated by Fehr.

Table 27: Rock statistics for the compiled digitalized line-count analyses (LCA) of the Salza River study area.

	LCA #1	LCA #2	LCA #3	LCA #4
Min (cm)	2	2	2	2
Max (cm)	11.6	17.2	15	20
Mean (cm)	4.1232	5.2988	5.4994	5.9883
Sum n	241	260	180	171
Sum n mean	41	71	59	41

The computed results of the four valid LCA can be found in Figure 129, where additionally a mean was calculated of all four to provide a fair representation for a grain size distribution for the whole study area, which was used for further calculations.

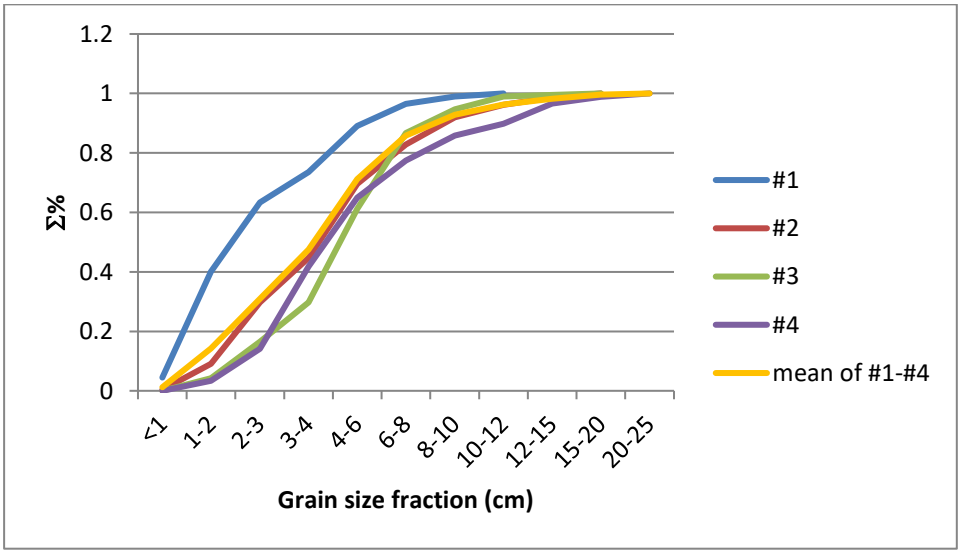


Figure 129: Computed results of the four line-count analyses of the Salza River study area with a mean of all four.

Taking the mean LCA and using the described method in chapter *5.4.2 Methods* the following Fuller curve was picked which best fit the distribution of the coarse grain sizes (FEHR 1987: 1109), see Figure 130.

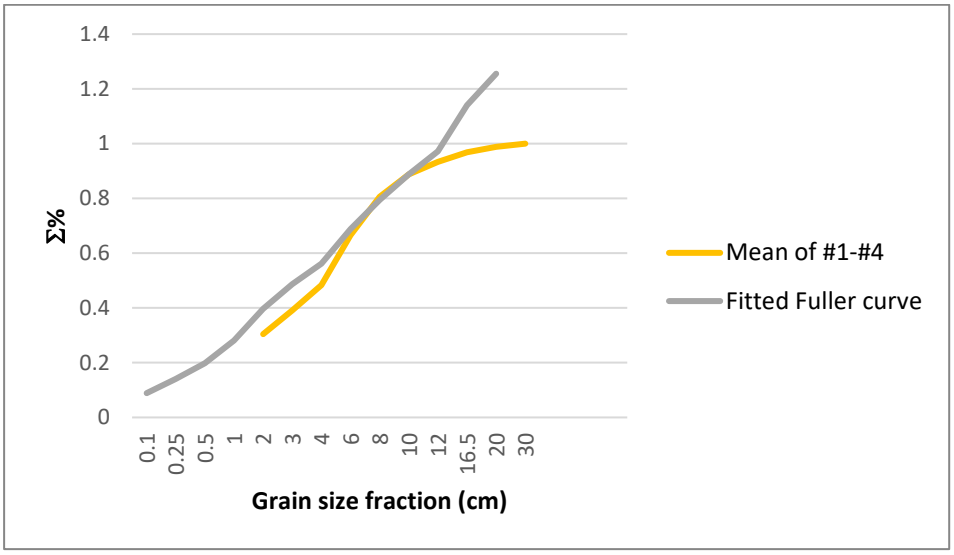


Figure 130: Mean line count analysis with the picked Fuller curve.

Next the two lines were merged into one, using the calculations described in chapter *5.4.2 Methods*. The result was a grain size distribution for a total of 14 grain size classes which can be found in Figure 131 and its accompanying values in Table 28.

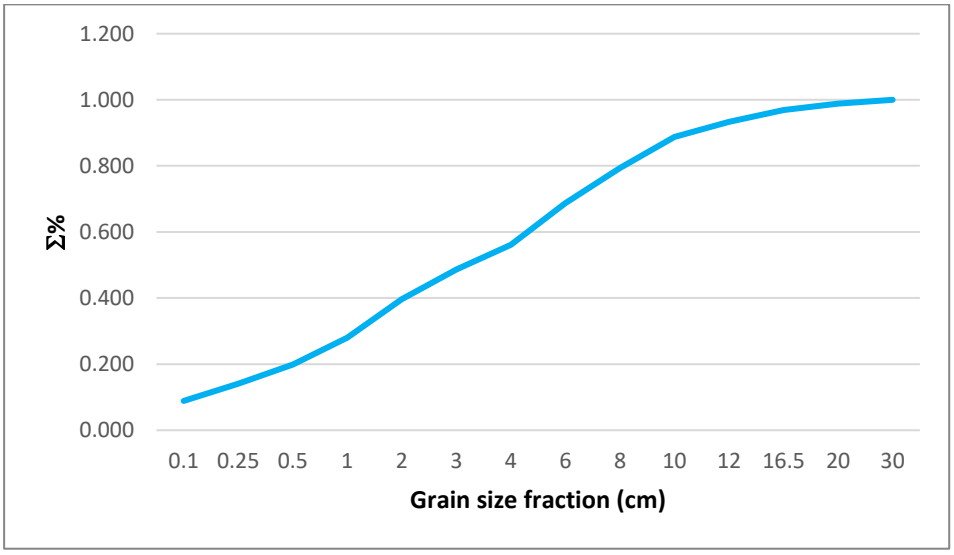


Figure 131: Approximated grain size distribution for the Salza River study area.

Table 28: Values for the approximated grain size distribution for the Salza River study area.

Grain size class	Grain size fraction (cm)	Σ%	Δ%
1	0.1	0.089	0.089
2	0.25	0.140	0.052
3	0.5	0.198	0.058
4	1	0.281	0.082
5	2	0.397	0.116
6	3	0.486	0.089
7	4	0.561	0.075
8	6	0.688	0.126
9	8	0.794	0.106
10	10	0.888	0.094
11	12	0.933	0.045
12	16.5	0.969	0.036
13	20	0.989	0.020
14	30	1.000	0.011

However, because the used modelling software CAESAR-Lisflood only uses a maximum of 9 grain size classes, the approximated grain size distribution had to be condensed into 9 grain size classes. Below is the final condensed grain size distribution in Figure 132 and its accompanying values are found in Table 29 which were used in the modelling of the Salza River study area.

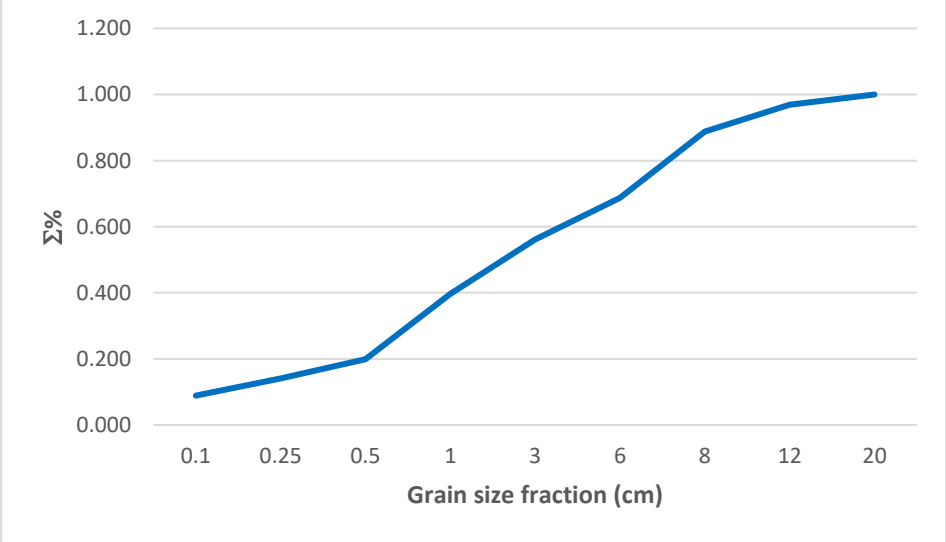


Figure 132: Condensed approximated grain size distribution for the Salza River study area.

Table 29: Values for the condensed approximated grain size distribution for the Salza River study area.

Grain size class	Grain size fraction (cm)	Σ%	Δ%
1	0.1	0.089	0.089
2	0.25	0.140	0.052
3	0.5	0.198	0.058
4	1+2	0.397	0.198
5	3+4	0.561	0.164
6	6	0.688	0.126
7	8+10	0.888	0.200
8	12+16.5	0.969	0.081
9	20+30	1.000	0.031

Suspended grain size approximation

In a second step the grain size distribution was approximated using a primitive collecting method during a flooding event described in chapter *Suspended grain size approximation*. In Figure 127 the pickup locations are marked with a yellow star. Both samples were obtained on the 12.08.2018 at the bridge lying between river km 61.9 and 62. Below in Table 30 are the results for each sample as well as a calculated mean for both. The mean weight of suspended solids collected for both 1.5l bottles was 0.4635g which amounted to a mean suspended concentration of 0.309g/l.

Table 30: Results for the approximated suspended grain size distribution for the Salza River study area.

Measurement	Weight Filter empty (g)	Weight Filter with suspended solids (g)	Weight suspended solids (g)	Suspended concentration (g/l)
1	1.799	2.254	0.455	0.30333˙
2	1.800	2.272	0.472	0.31466˙
Mean	**1.7995**	**2.263**	**0.4635**	**0.309**

6.4.2 Modelling

The modelling chapter is divided into two chapters, where the results for the parametrization are described and listed in the first chapter and the results for the actual modelling results follow afterwards.

Parametrization

The parametrization was the initial step, were the parameters in the different tabs in CAESAR-Lisflood were altered to see which combination of parameters most realistically depicts the actual rate of erosion and accumulation in the Salza River study area. The parametrization was done for the timeframe 2011 - 2018 as described in chapter *Parametrization (pre-modelling)*. Particular emphasis was on the parameters in the sediment tab, see Figure 133 on the right, because these parameters have the most influence on the rate of erosion and accumulation of a river.

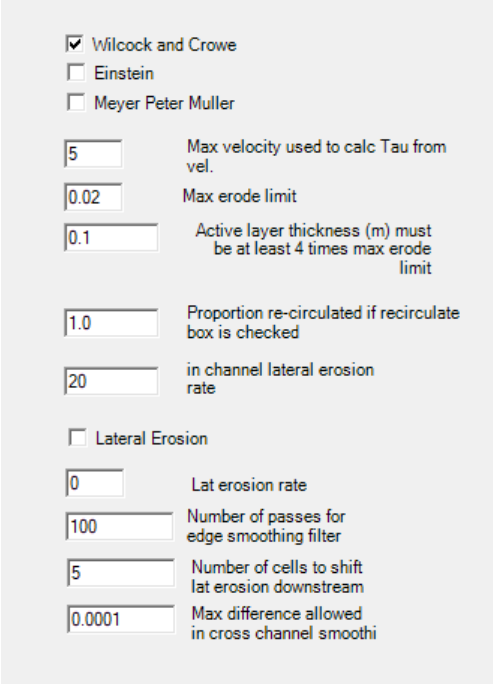


Figure 133: Sediment parameters in CAESA-Lisflood.

My approach was to alter the different sediment parameters and examine which impact they have on the model. For each parameter I started modelling for the year 2011 (the recording year for the available DEM) and if the initial modelling was decent and adequate, I modelled additional years with the same parameters until 2018 using the DEM from the previous model. My computed bedrock data file and grain size classes were used for all model runs as well as the original annual discharge data.

Before changing any parameters, I did a run-through with the default settings in CAESAR-Lisflood as seen in Figure 133 for the timeframe 2011 - 2018. The results of this run were used as a basis for comparison. My following parametrization results always relate to the changes compared to the model run with the default settings and will be addressed in the same order as in the tab, seen in Figure 133.

Using the tick box *Einstein* instead of *Wilcock Crowe* after modelling the years 2011 and 2012 the riverbanks were eroded at a very fast rate, especially at the erosion hotspot and was therefore not optimal. Using the tick box *Meyer Peter Müller* instead of *Wilcock Crowe* after modelling the years 2011 and 2012 the results showed notably higher lateral erosion and was therefore also not optimal.

The parameter *Max velocity used to calc Tau from vel.* remained unchanged since T. J. Coulthard notes *"This is rarely used, but sometimes needed in very steep slopes."* [9], and the Salza River study area does have steep slopes. Changing the parameter *Max erode limit* from 0.02 to 0.01 after modelling the years 2011 - 2018 the results looked good initially and the erosion hotspot looked more realistic, however overall, the Salza River started to meander more which did not depict reality and was thus not optimal. The parameter *active layer thickness* (height of erodible active sediments) remained unchanged since the value 0.1 m approximately matches the Salza River study area.

Increasing the parameter *proportion recirculated,* the results after modelling the years 2011 - 2016 show similar results as with the default settings, however the middle part of the Salza River started to meander more than in reality and was thus not optimal. Altering the parameter *in-channel lateral erosion rate* to 10 and in a subsequent run to 15 after modelling the years 2011 – 2015, the results show that using the rate 15, the erosion rate is less than with the default settings and using the rate 10, the erosion rate is even less and is thus not optimal. The default rate of 20 here seems more realistic.

Ticking the *lateral erosion rate* tick box and changing the value to 0,0001 after modelling the years 2011 - 2012 the results show a far too high erosion rate and was thus not optimal. And finally, the last three parameters remained unchanged, as the previous results have already provided a useable set of parameters which approximates reality.

Looking at the results for the overall Salza River study area, the default parameter settings are best suited since any changes of the parameters have an unwanted impact and are thus not optimal. All used parameters for the modelling with CAESAR-Lisflood Version 1.9j can be found in Table 31 and using these same exact parameters provides repeatability in my results.

Table 31: Final Parameters used in CAEASR-Lisflood for the modelling of the Salza River study area.

File tab	Reach Mode	✓			
	Dem data file	dem.txt			
	Bedrock data file	bedrock.txt			
Numerical tab	Min time step (s)	1			
	Max time step (secs)	3600			
	Run start time (h)	0			
	Max run duration (h)	10000			
	Memory limit	1			
Sediment tab	Size1	0.001	0.0888		
	Size2	0.0025	0.0516		
	Size3	0.005	0.0581		
	Size4	0.01	0.1985		
	Size5	0.03	0.1644		
	Size6	0.06	0.1262		
	Size7	0.08	0.2001		
	Size8	0.12	0.0813		
	Size9	0.2	0.0310		
	All 9 grainsizes?	✓			
	Suspended	✓	0.066		
	Wilcock and Crowe	✓			
	Max velocity used to calc Tau from vel.	5			
	Max erode limit	0.02			
	Active layer thickness (m)	0.1			
	Proportion recirculated	1.0			
	In-channel lateral erosion rate	20			
	Lateral erosion	✓			
	Lateral erosion rate	0			
	Number of passes for edge smoothing filter	100			
	Number of cells to shift lateral erosion	5			
	Max difference allowed in cross channel smoothing	0.0001			
Hydrology tab	Input 1	✓	543	28	Qyear.txt
	Input data time step (mins)	60			
	Divide inputs by	1			
Slope processes tab	Slope failure threshold	85			
Window after load data	Recirculate sediment	✓			

Modelling

The last part will dive into the computed results of the modelling of the Salza River study area using four different discharge scenarios for the timeframe 2019 - 2050, as described in chapter *5.4.2 Methods.* The results will be in the order of first examining changes in sinuosity of the modelled Salza River using the DEMs of the year 2050, then going into where and when significant changes happened comparing cross sections and altitude profiles, then assessing the volumetric changes in erosion and accumulation and lastly looking into how the D50 grain size changed throughout the modelling.

To assess the sinuosity, first the distances and lengths had to be assessed using the method described in chapter *5.1.2 Methods*. The accompanying tables with the measured lengths, distances and indices can be found in chapter *11. Appendix* and will only be addressed with the Table number. Besides the initial DEM from 2011, the 2018 DEM of the pre-modelling as well as the 2050 DEM of each of the four different discharge scenarios were analysed. To recollect, the four discharge scenarios are 1. Similar discharge(m^3/s) for 2019 - 2050, 2. More discharge (m^3/s) for 2019 - 2050, 3. A lot more discharge (m^3/s) for 2019 - 2050 and 4. Only the 2014 discharge (m^3/s) for 2019 - 2050 compared with discharge timeframe 1976 - 2018. The statistical data for the discharges are found in Table 12 and Table 13 and their accompanying discharge curves in Figure 52.

First the distances for all DEMs for the total, unconfined and confined Salza River were computed, see Table 51. Next the lengths for all DEMs for the total, unconfined and confined Salza River were computed, see Table 52.

Using the given distances and lengths, we can find the sinuosity index for the unconfined Salza River in Table 53. Compared with the initial 2011 DEM, the DEM for the pre modelled year 2018m increased in sinuosity by 0.0534. Comparing the modelled DEMs from 2050 with the 2018 DEM, all reduced in sinuosity between -0.0063 and -0.0487. Interestingly the sinuosity does not correlate directly with the increased discharge. The 2050 DEM from the model 4. decreased the most in the sinuosity index compared to 2018m, followed by model 1, model 3 and model 2.

Using the given distances and lengths we can find the sinuosity index for the confined Salza River in Table 54. Compared with the initial 2011 DEM, the DEM for the pre modelled year 2018m again increased in sinuosity by 0.0152. Comparing the modelled DEMs from 2050 with the 2018 DEM, all DEMs from all discharge scenarios decreased between -0.0045 to -0.0146 where model 4 had the largest decrease and model 3 the least decrease.

Same as before using the given distances and lengths we can find the sinuosity index for the total Salza River in Table 55. Compared with the initial 2011 DEM, the DEM for the pre modelled year 2018m again increased by 0.0433 reflecting the results for the two segments. Comparing the modelled DEMs from 2050 with the 2018 DEM, also all DEMs from all discharge scenarios decreased in sinuosity between -0.0066 for model 2 and -0.0397 for model 4. Further model 3 decreased by -0.0193 and model 2 by -0.0226.

To put the sinuosity changes of the Salza River study area in perspective, following in Figure 134 are the thalwegs of the Salza River for the initial 2011 DEM, in green, as well as the pre-modelled 2018 DEM, in purple. Looking at the changes in the 7-year modelling timeframe there are four main areas of change marked with letters from A to D. While section A, B and D somewhat depict reality, section C does highlight the erosion hotspot quite nicely.

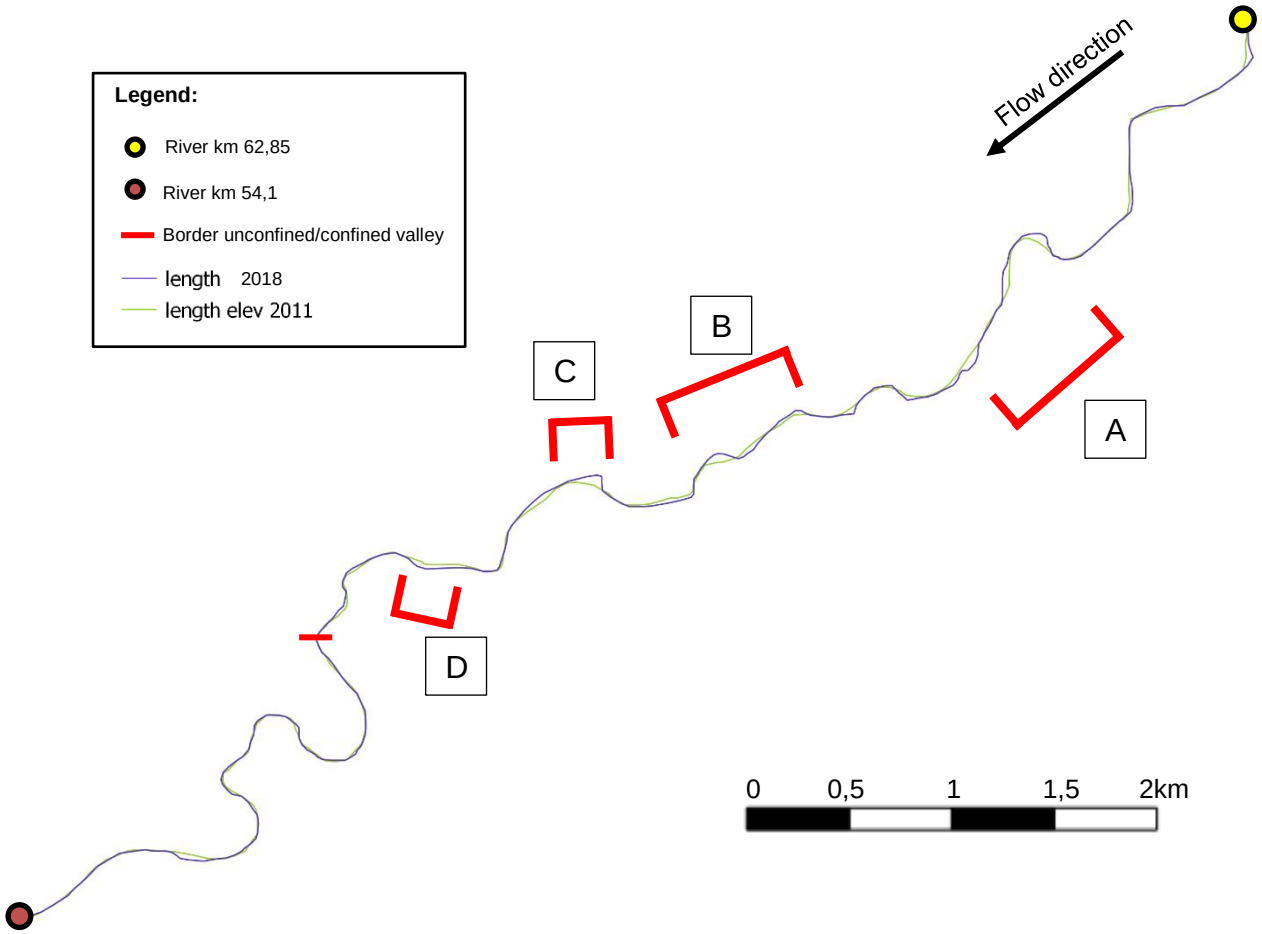


Figure 134: Overlapping the thalweg of the 2011 DEM and pre-modelled 2018 DEM of the Salza River study area.

In a second comparison the pre-modelled 2018 DEM was overlapped with the 2050 DEMs of the four discharge scenarios, see Figure 135. In it we see 4 main areas where a change has happened during modelling. Additionally, the year of each occurring change for each section can be found in Table 32. Section A, being the first bend after the weir, was incised in every modelled discharge scenario occurring between the years 2031 - 2034. Section B was an area where the Salza River was cut off in every discharge scenario. It occurred first in model 3 in 2031 and latest in model 4 in 2044. Interestingly, after the cut off, the Salza River flows in the exact mapped paleochannel as described in chapter *6.2.2 Second map: Mapping of Tier 2 geomorphic units* . Section C witnessed another cut-off of the river bend in the Figure, and it also occurred in all 4 models. First visible in model 1 in 2024 and the latest in model 2 in 2031. The final major area of change was a further river cut off into a historic paleo channel which was also mapped and described in chapter *6.2.2 Second map: Mapping of Tier 2*

geomorphic units . However, this cut off only happened in model 3 in the year 2041 and in model 4 in the year 2033.

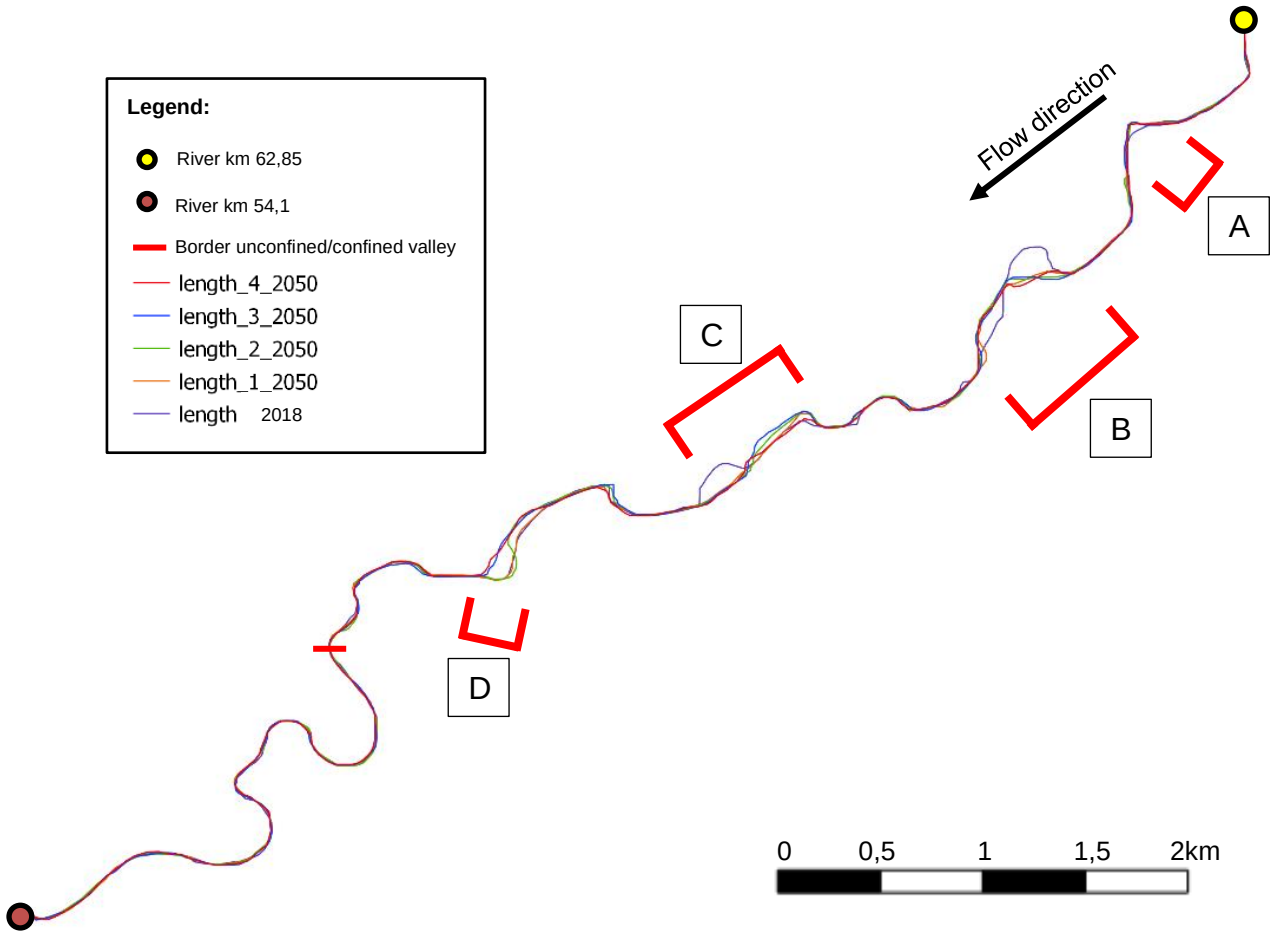


Figure 135: Overlapping the thalweg of the pre-modelled 2018 DEM as well as all four 2050 DEMs for the four different discharge scenarios of the Salza River study area.

Table 32: Year of change for the four main sections marked in Figure 135.

DEM	Year of change Section A	Year of change Section B	Year of change Section C	Year of change Section D
1_2050m	2034	2043	2024	-
2_2050m	2034	2041	2031	-
3_2050m	2031	2031	2029	2041
4_2050m	2032	2044	2028	2033

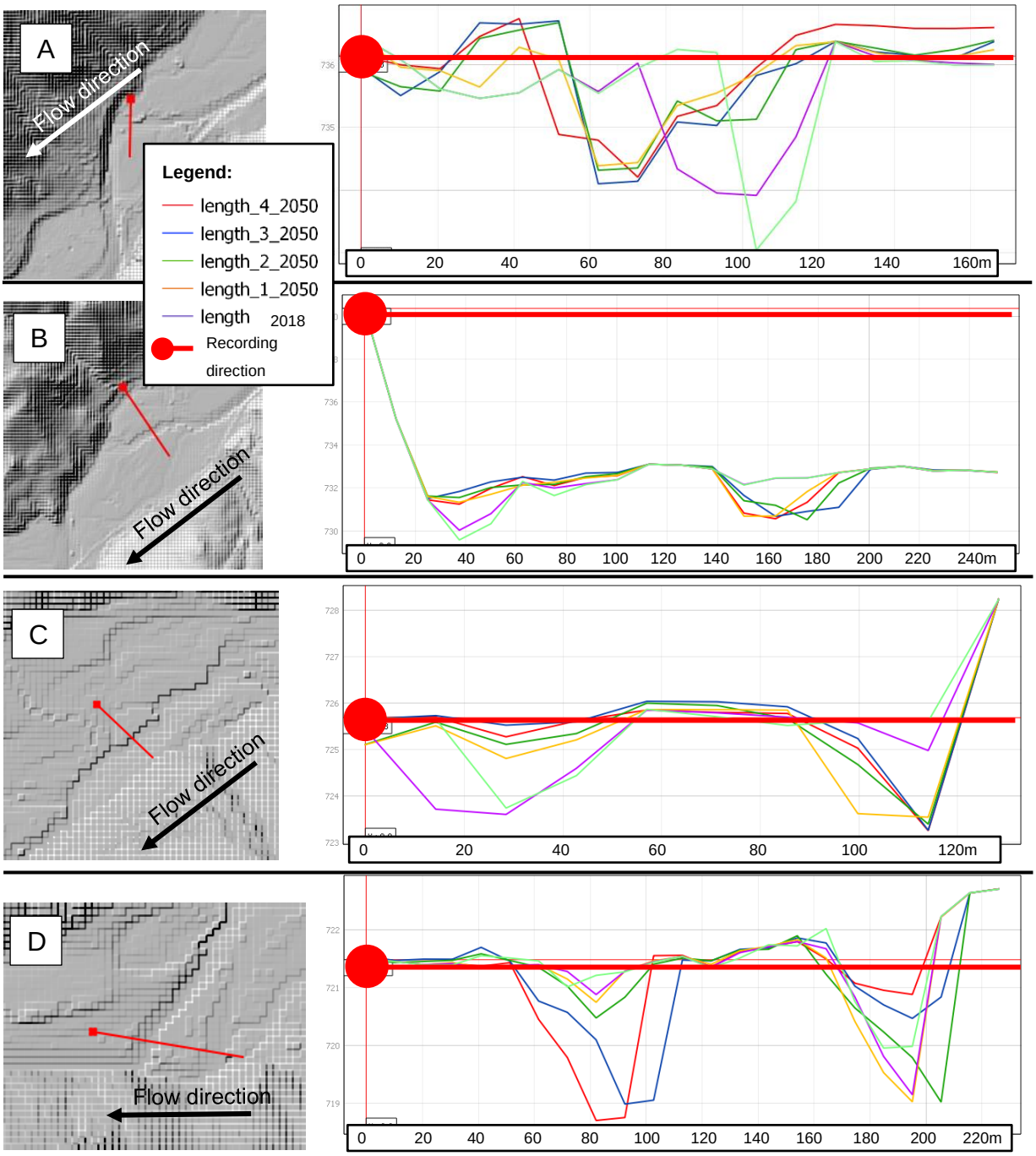


Figure 136: Change in the cross sections of the four detected potential changes in the four modelled 2050 DEMs compared to the pre modelled 2018 DEM.

The cross sections of the aforementioned four areas of change A to D from Figure 135 shed light on the potential lateral displacement of the riverbed see Figure 136. The shift in segment A is around 20 m to the orographic right side, the shift at segment B is around 130m to the orographic left side, the shift at segment C is around 80m to the orographic left side and the shift at segment D, which only occurred in scenario 3 and 4, is around 100m to the orographic right side.

Next the thalweg of the 2011 DEM from Figure 134 as well as all thalwegs displayed in Figure 135 were examined in their elevation profile of the Salza River. In the below Figure 137 we notice that all profiles have the same trajectory with very little differences. Something to point out though, between river km 59 and 62, the 2050 models have compared to the 2011 thalweg, accumulated material and slightly increased in riverbed height. On the other hand, between river km 54.1 and 59 and above river km 62 all thalwegs compared with 2011 have slightly incised into the riverbed.

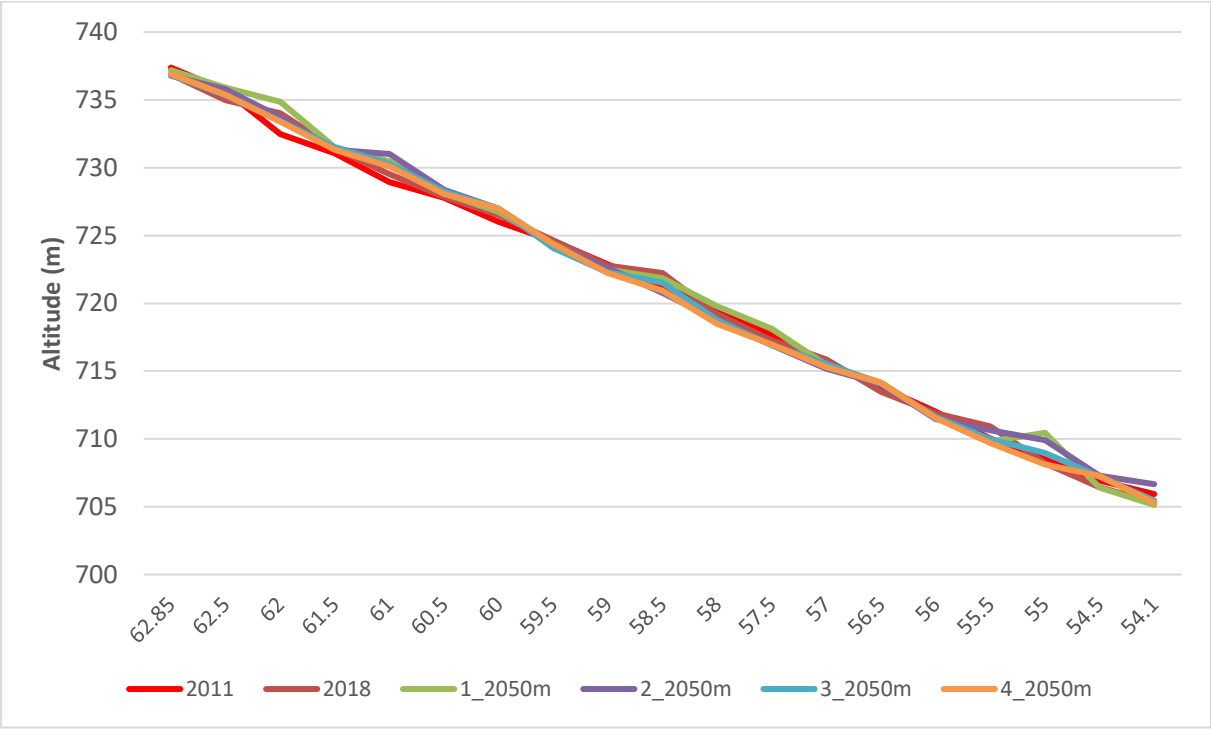


Figure 137: Elevation profile of thalwegs from the original 2011 DEM, the pre modelled 2018 DEM and the 2050 DEMs for all four discharge scenarios.

To assess the volumetric changes for each modelled year in CAESAR-Lisflood, the DEM output elevdiff.txt, which is a difference DEM of the input and output DEM, was analysed in Excel. For each model year the positive and negative values were added to obtain the volumetric sum of erosion and accumulation. This was done every year for all four discharge scenarios. For better reference the discharge scenarios used and already displayed in Figure 52 are pictured a second time below in Figure 138.

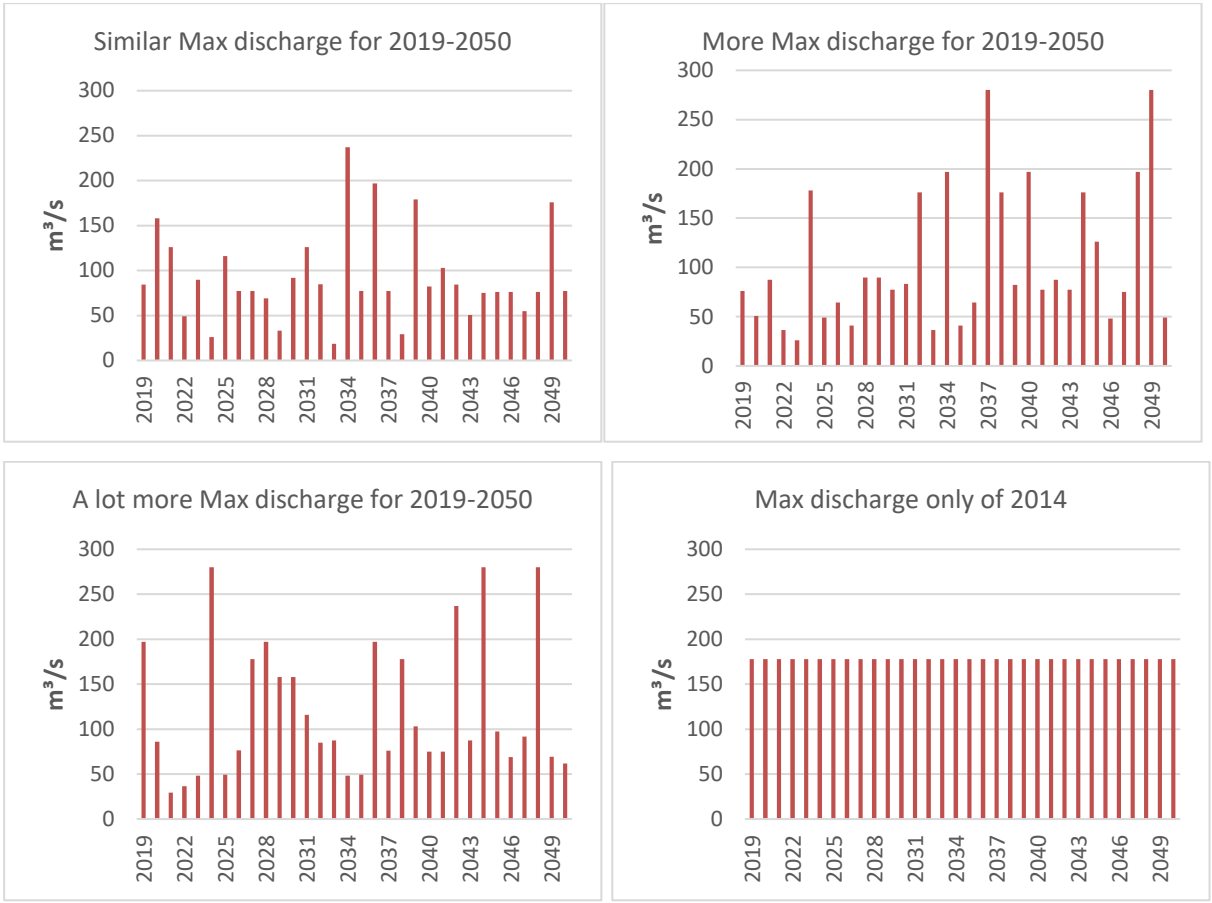


Figure 138: Max discharge scenarios used for the modelling of the Salza River study area.

First the erosion and accumulation rates for the scenario 1 will be analysed, being the scenario with similar discharge for the timeframe 2019 - 2050 as 1976 - 2018. In Figure 139 we see in green the accumulation volume in m³ and in red the erosion volume in m³ for every year. The largest erosion and accumulation (ero/acc) rates were in the year 2034 with -794.15 m³ and 796.75 m³ respectively which was also the year of highest discharge with a max of 237 m³/s see top left in Figure 138. The lowest volume change on the other hand was in year 2033 with -89.59 m³ and 89.95 m³. This also correlates with the lowest max discharge of 18.6 m³/s in 2033. The other four HQ10 flooding events in the years 2020, 2036, 2039 and 2049 are also somewhat visible in the volume change but are not as prominent. The mean erosion and accumulation rate for scenario 1 was calculated to be -241.74 m³ and 246.49 m³ see Table 33. The mean of the scenario 1 will also be used as a base for comparison for the other scenarios. In Table 34 the number of years with the same or higher ero/acc rate compared with the mean from scenario 1 are presented. In total for scenario 1, there were 13 years with the same or more volume than the scenario 1 ero/acc mean.

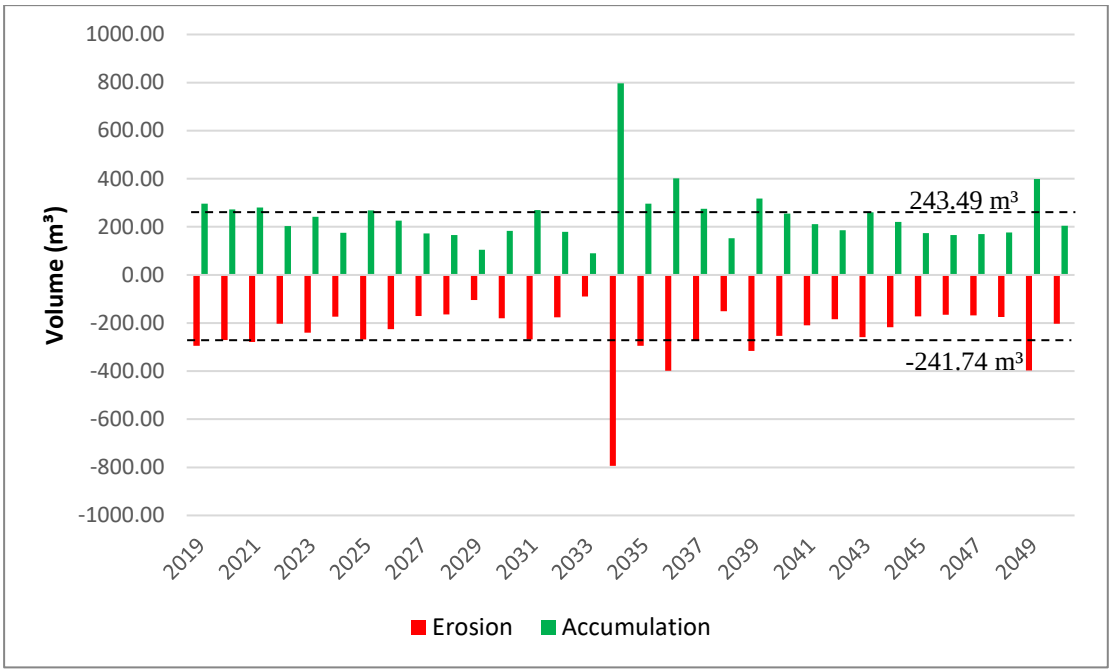


Figure 139: Erosion and accumulation volumes for the discharge scenario 1 for the timeframe 2019 - 2050.

Table 33: Mean erosion and accumulation rate for the time frame 2019 - 2050 for all four discharge scenarios.

DEM	Mean erosion rate 2019 - 2050	Mean accumulation rate 2019 - 2050
1_2050m	-241.74	243.49
2_2050m	-291.02	292.77
3_2050m	-307.20	309.07
4_2050m	-161.10	162.79

Table 34: Years with lower/higher erosion/accumulation rate than the 1_2050m mean erosion rate for all four discharge scenarios.

DEM	Years with lower erosion rate than the 1_2050m mean of -241.74 m³ 2019 - 2050	Years with higher accumulation rate than the 1_2050m mean of 243.49 m³ 2019 - 2050
1_2050m	13	13
2_2050m	14	14
3_2050m	17	17
4_2050m	1	1

The volume changes for the second scenario can be found in Figure 140, modelled with more discharge in 2019 - 2050 as 1976 - 2018. The highest rate of erosion and accumulation was found to be in year 2037 with -820.89 m³ and 823.87 m³. This correlates with the highest

recorded max discharge to be in 2037. However, the year 2049 which also had the same max discharge of 280m³/s only had a volumetric change of -601.49 m³ and 604.63 m³ or roughly 25% less change than in the year 2037. The least volumetric change was in 2023 with rates of -87.18 m³ and 88.21 m³ correlating with the smallest discharge. Overall, the mean erosion and accumulation rate for scenario 2 was calculated to be -291.02 m³ and 292.77 m³ see Table 33. In total for scenario 2, there were 14 years with the same or more volume than the scenario 1 ero/acc mean

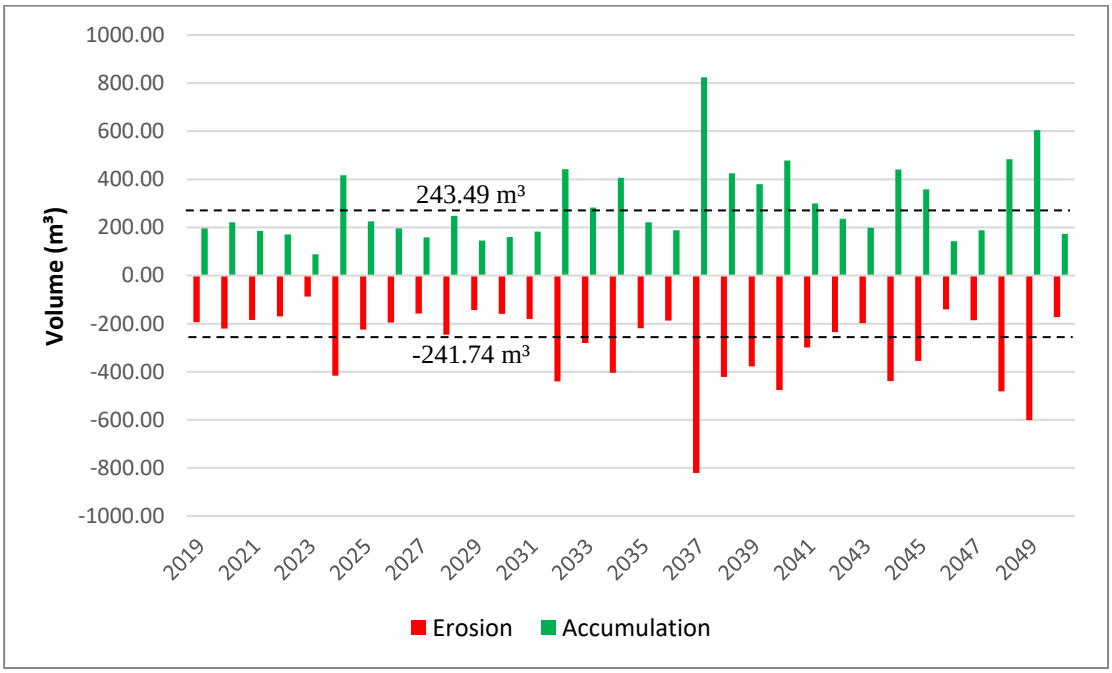


Figure 140: Erosion and accumulation volumes for the discharge scenario 2 for the timeframe 2019 - 2050.

Examining scenario 3 next, which was modelled with a lot more discharge see Figure 141, we see the largest rate of erosion and accumulation was in 2024 with -957.3 m³ and 960.04 m³. The year 2024 also had the max discharge of 280 m³/s. There were however two other years with same max discharge of 280 m³/s in 2044 and 2048 but the rates were -550.24 m³/553.7 m³ and -541.43 m³/544.87 m³ respectively, nearly half of the volume change from 2024 although having the same discharge. The least volumetric change was found in the year 2035 with -96 m³ and 96.68 m³. Interestingly the year 2035 only had the 4th smallest discharge in the whole-time frame. Overall, the mean erosion and accumulation rate for scenario 3 was calculated to be -307.20 m³ and 309.07 m³ see Table 33. In total for scenario 3, there were 17 years with the same or more volume than the scenario 1 ero/acc mean

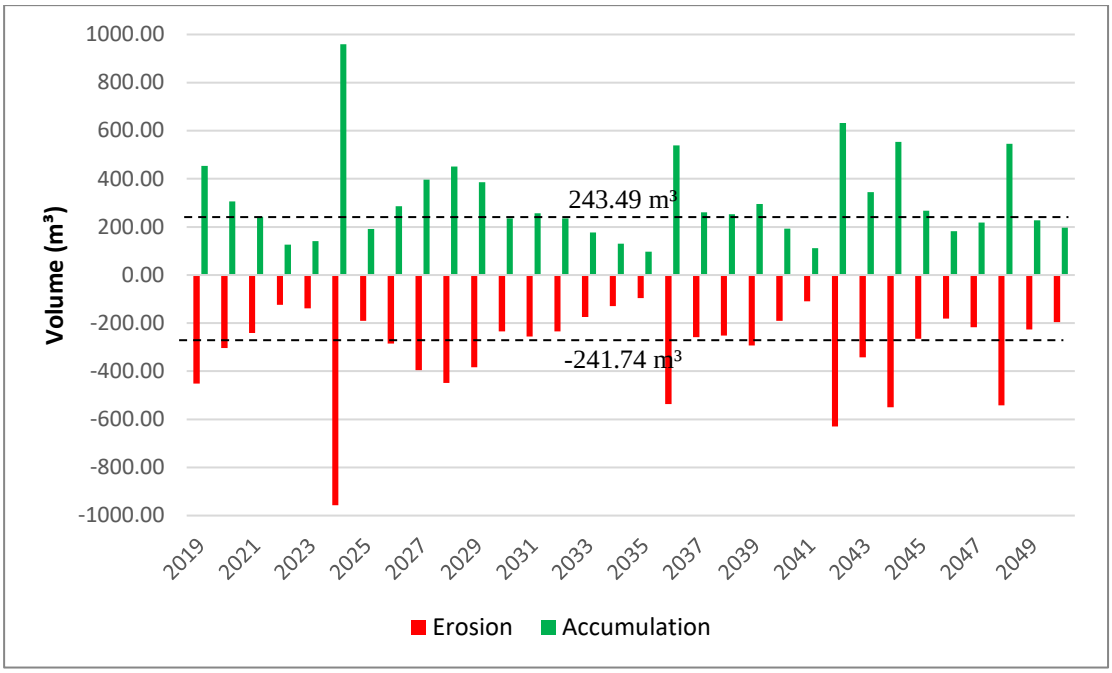


Figure 141: Erosion and accumulation volumes for the discharge scenario 3 for the timeframe 2019 - 2050.

Lastly, in Figure 142 are the erosion and accumulation rates for scenario 4 using only the discharge from year 2014. The largest volume change was found in the first modelled year of 2019 with -287.93 m³ and 289.63 m³. The year 2049 on the other hand had the least volume change of only -101.89 m³ and 103.72m³. Overall, the mean erosion and accumulation rate for scenario 4 was calculated to be -161.10 m³ and 162.79 m³ see Table 33. In total for scenario 4, there was only 1 year with the same or more volume than the scenario 1 ero/acc mean

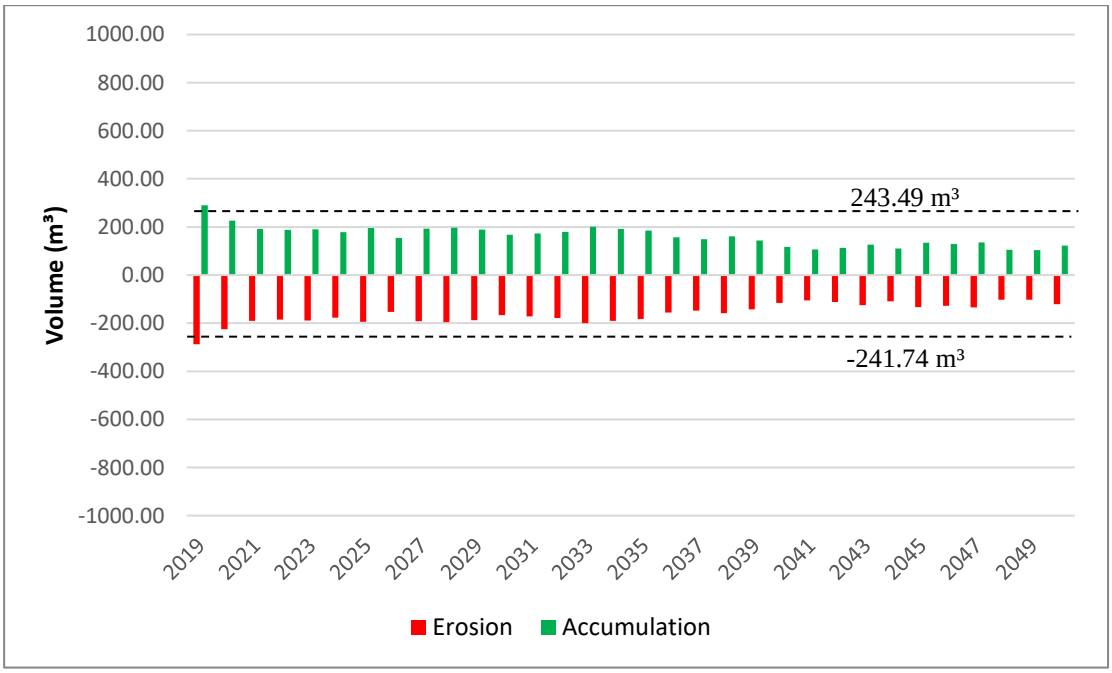


Figure 142: Erosion and accumulation volumes for the discharge scenario 4 for the timeframe 2019 - 2050.

Comparing the overall erosion and accumulation for the timeframe 2019 - 2050 for each scenario we can see a disparity in the results, see Figure 143. Scenario 1 had a total erosion and accumulation volume of -7,735.84 m³/7,791.54 m³, scenario 2 of -9,312.59 m³/9,368.7 m³ and scenario 3 of -9,830.53 m³/9,890.12 m³ correlating with an increase in discharge. Scenario 4 however, modelled only with the discharge of year 2014, had a total erosion and accumulation volume of -5,155.31 m³/5,209.21 m³, nearly half of scenario 3.

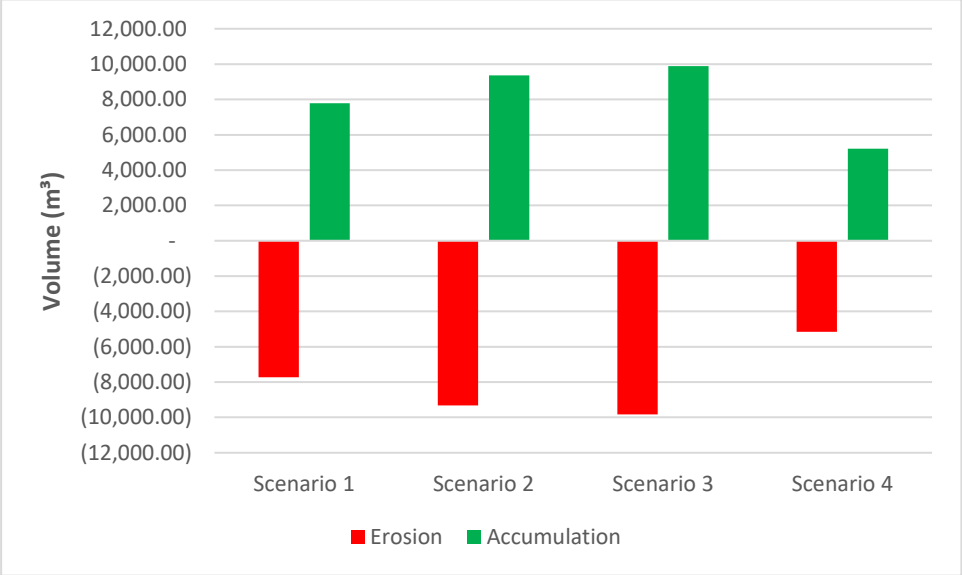


Figure 143: Total erosion and accumulation volumes for all four discharge scenarios for the timeframe 2019 - 2050.

The last unit which will be compared are the values for the D50 grainsizes. Hereby the DEM output d50top.txt in CAESAR-Lisflood, which is the D50 grain of the surface layer of sediment was analysed in Excel. The mean of all values for each year was calculated for all discharge scenarios. In Figure 144 are the curves for the mean D50 values for every year in the timeframe 2019 - 2050 for each scenario. We notice that the D50 for the scenarios 1, 2 and 3 are all fairly similar and are all lying roughly between 2.1 cm and 2.9 cm. Scenario 4 on other hand does not vary as much and only lies within 2.1 cm and 2.3 cm.

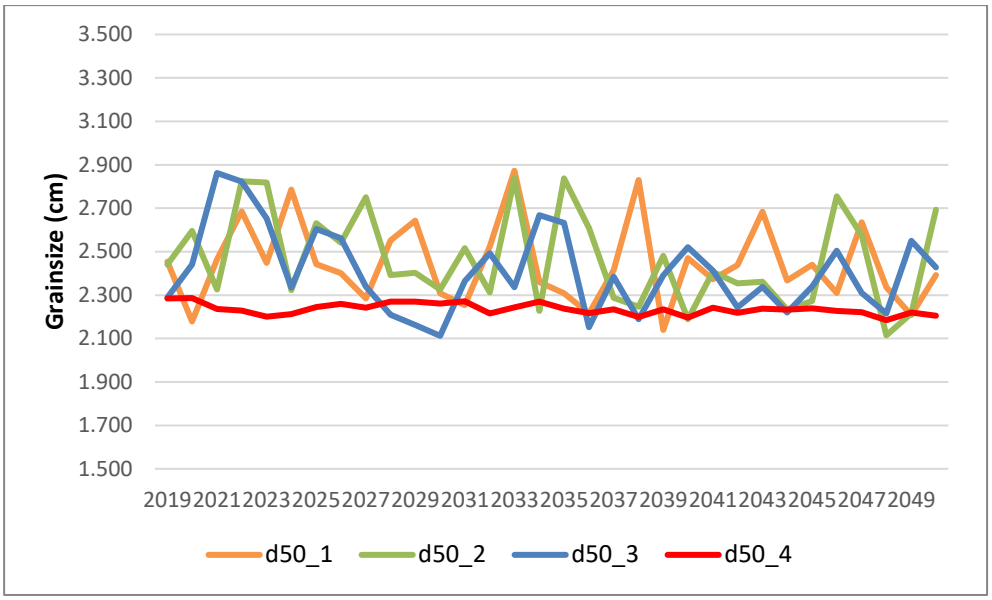


Figure 144: D50 grainsizes for the four different discharge scenarios for the timeframe 2019 - 2050.

In the last chart in Figure 145, are the linear trendlines from the D50 values for the four discharge scenarios. The same for all scenarios is the negative trend from 2019 to 2050 however at different rates. While the trendline for scenario 1 starts at 2.4998 cm in 2019 it is at 2.4027 cm in 2050 and higher than scenario 2 and 3 although being lower in 2019 than the two. Scenario 2 and 3 both follow a very similar trajectory with the difference that the values for scenario 2 are higher at the end of year 2019 and 2050 than scenario 3. The final trendline for scenario 4 has a very gradual decline but also has the lowest D50 values of all scenarios.

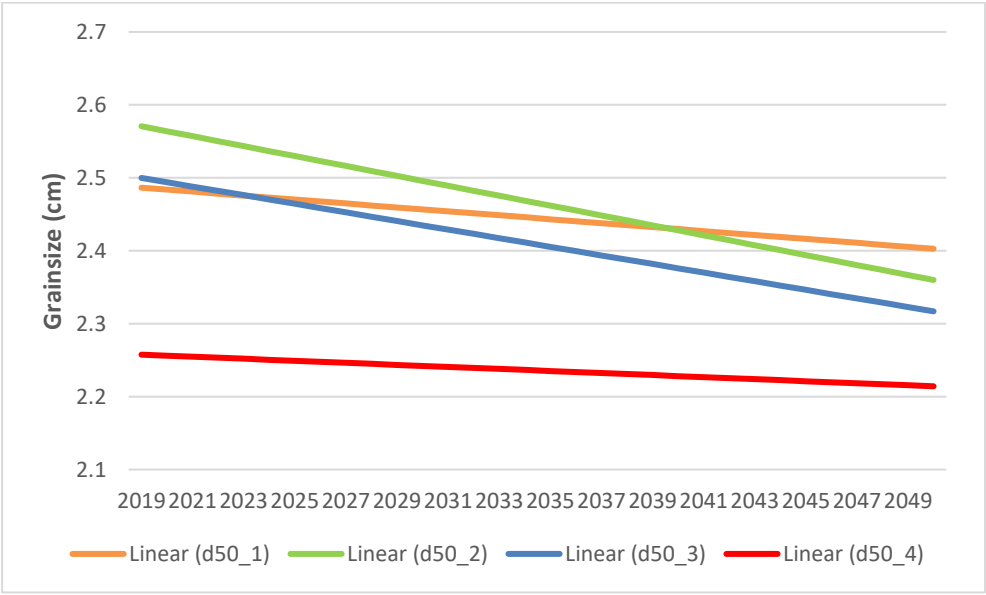


Figure 145: Linear trendlines for the D50 grainsizes for the four different discharge scenarios for the timeframe 2019 - 2050.

7. Discussion

In the final chapter of the thesis the applied methods and presented results will be put in context and compared for their validity with suitable results from findings in the scientific literature. The order of discussion will follow the order of presented results first discussing the reconstruction of past changes in the Salza River, then discussing the mapping, monitoring and modelling results. Finally, the research questions and hypotheses will be addressed closing the findings of this thesis.

7.1 Reconstruction of past hydro-geomorphic changes of the Salza River

In a first step, the historic changes of the Salza River were analysed descriptively in chapter *6.1.1 Historical maps of the study area dating 1678 - 1887* by evaluating the available historic maps from 1678 - 1887. All maps except for the oldest Vischer map from 1678 were georeferenced to enable a better comparison. Additionally, more recent changes were also analysed descriptively in chapter *6.1.2 orthophotos of the study area dating 2004 - 2017* by evaluating the available orthophotos from 2004 - 2017. All orthophotos were already georeferenced.

While the analysis of historic maps is nothing new and is the only possible option to evaluate historic land cover change, historic maps are prone to a few limitations which can affect results. *"This can be understood in terms of spatial position, timing of the situation represented in the survey, or correctness of the map content and its interpretation."* (ZLINSZKY et al. 2013: 4598). The older the map the more inaccurate it generally is, as seen in the oldest map of the Salza River study area, the Vischer map from 1678 in Figure 56. The lack in positional accuracy can also be seen in the first available reasonable maps of the Salza River study area, the Josephinische land survey recorded between 1784 - 1785 and the Franziszeische land survey recorded between 1809 - 1818 due to the state-of-the-art at that time. *"Hence, for a correct use of old maps for historical research, it is necessary the evaluation of accuracy and reliability of their information content after the georeferencing process."* (PINDOZZI et al. 2015: 1).

Compared with the two oldest maps, I noticed a very good positional mapping accuracy in the three more recent historical maps namely the Franziszeische cadastre recorded between 1817 and 1861, the Franziszeische land survey recorded between 1821 - 1836 and the Francisco-

Josephinische land survey recorded between 1869 - 1887. This increase in precision is accompanied with an improvement in mapping tools. *"During the nineteenth century the level of accuracy and reliability of maps, due to geodetic survey, was finally attained in many European countries as a consequence of the general achievements in cartographic techniques."* (PINDOZZI et al. 2015: 1). However, although the accuracy has improved drastically, the resolution in the most recent maps is still very low and thus does not enable a closer riverbed analysis (STATUTO et al. 2017: 10). Besides these limitations, historic maps, when mapped correctly, offer an advantage compared to newer aerial images. *"They do not suffer from atmospheric influences (e.g., cloud cover or haze) as is often the case in remote sensing images."* (FUCHS et al. 2015: 54)

The descriptive results of the three most recent historic maps can therefore be seen as valid while the results for the three oldest maps must be taken with caution due to their lack in mapping accuracy.

When visually evaluating more recent land cover changes, orthophotos are the state-of-the-art remote sensing image. orthophotos hereby are georeferenced images and *"are characterized by having a uniform scale and showing objects in their true geographical locations."* (HABIB 2007: 25). They are therefore true to position and are only limited by cloud cover or bad lighting conditions during the recording flight. Since all acquired orthophotos were recorded at optimal times, all described visual changes can be seen as accurate since orthophotos depict a true portrayal of reality. Nonetheless one minor limitation will be mentioned. Although orthophotos of the Salza River study area were available with intervals between 2 and 5 years, more intervals would yield more insight on when exactly the hydro-geomorphic changes occurred and developed, giving more insight on the rate of change.

Besides some natural alterations within the river course such as the erosion hotspot (still present), the local river widening (has transformed into its state before the widening) or the shift of local islands in the riverbed, overall, the past changes from natural causes in the historic maps as well as in the orthophotos were negligible. The most widespread changes occurred through man made interventions such as the construction of the dammed side arm channel, the weir, the levee or the fish ladder in the upper part of the Salza River study area.

In a second step, a sinuosity index was computed using the three most recent historic maps as well as all orthophotos to examine if and where the river has either straightened or has become more meandering/sinuous. *"The Sinuosity Index (SI) is one measurement used to understand shape distortions of rivers/streams, where it evaluates the effect of a river's paths over a particular region (and vice versa)"* (KALANTAR et al. 2020: 91) and was used to determine the change with a numerical value in addition to the previous descriptive analysis.

When assessing changes of a river, the use of a sinuosity index is commonly found in the scientific literature and was also applied in these exemplary selected articles: (KALANTAR et al. 2020), (GARCÍA et al. 2019), (KAR et al. 2020) and (MOMIN et al. 2020). Besides the sinuosity index, there are more parameters which can be analysed and used jointly such as the braiding index, hydraulic sinuosity index and topographic sinuosity index used by (MOMIN et al. 2020: 15) or Muller's Sinuosity Index which was used by (KAR et al. 2020: 38,39), however the sinuosity index alone sufficed in this thesis.

The main limitation of the used sinuosity index method mainly depends on the underlying quality of the map or orthophoto and the previous mentioned points also apply here. Further the digitalization of the lines is prone to human error when deciding where the thalweg flows. This can have a minor impact on the calculated index, however if all lines are digitalised by one person the impact can be reduced.

The poor mapping accuracy of the three most recent historic maps can be clearly seen by examining Figure 96 when overlapping the thalwegs of the three historic maps. Although the three thalwegs do overlap quite well, considering their mapping date, there is still a high mapping error. When overlapping the thalweg of the most recent historic map with the oldest orthophoto in Figure 97 we are comparing a perfectly georeferenced orthophoto with a historic map. Again, considering the maps recording year the thalwegs do flow very similar, but the mapping accuracy of the historic map is not true to position. Although when speculating, it could theoretically be possible that the thalweg in the historic map is in fact true to position and has only altered its riverbed since then. But that is more speculation and cannot be confirmed or disproven.

Comparing the orthophotos in Figure 98, when overlapping the thalwegs of the orthophotos we see how mapping accuracy has improved in a matter of 200 years. Except for two alterations in the river course the thalwegs of all orthophotos overlap perfectly. One of the two alterations was at the erosion hotspot between river km 58.7 - 58.8 where in addition to the orthophotos a satellite image from 2019 was available. In Figure 100 we saw the optical change which occurred at the erosion hotspot from 2011 to 2014, 2014 to 2017 and again from 2017 to 2019 and one would have assumed an incremental increase in sinuosity from 2011 to 2019, which was interestingly not the case. The riverbed displacement was the highest from 2011 to 2014 by 26.78 m and then from 2014 to 2017 by 19.08 m. However, the riverbed has not changed substantially from 2017 to 2019 (only 5.55 m) compared to the previous values and seems to have slowed down in the erosion rate. Also, the results found that the sinuosity index at the hotspot, see Figure 99, increased from 2004 to 2017 from 1.0426 to 1.1902, but has decreased by -0.0098 from 2017 to 2019. The used numerical parameters hereby gave more insight into the actual change which happened in the study area.

7.2 Mapping of in and out-of-channel geomorphic units

As mentioned earlier in the state-of-the-art chapter *4.2 Mapping*, the difficulty prior to mapping was to find a mapping framework which provides sufficient tools to map the in and out of stream hydro-geomorphic units. Most fluvial mapping methods found in the scientific literature today, revolve around assessing flood risks and mostly preoccupy around hydrological parameters i.e., water depth and lateral water expansion at altering discharge rates. WHEATON et al. 2015 provided a complete, usable and repeatable river mapping framework and the results in this thesis were presented like WHEATON'S results and thus can only be compared with it. However, limitations which also apply to other mapping frameworks will be discussed.

The first and main field work mapping of the study area was done in 2017 during optimal weather as well as during mean discharge conditions where the confining margins and tier 2 shapes were mapped. These were then digitalized off-site, and the tier 2 shapes were further broken down into tier 3 shapes in a separate map. Further, the available DEM was used to detect out-of-channel features as well as the valley and valley bottom margin which were not visible during the mapping. And orthophotos were applied to map the man-made structures such as the main road and buildings.

The first presented map shows the confining margins of the Salza River study area, see overview map in Figure 101 and zoomed in map excerpts in Figure 103 using the defined framework by WHEATON et al. *"Confining margins can then be added based on where the channel margin abuts other margins that constrain its ability to adjust laterally. These margins form the basis for identification and coding of the out-of-channel geomorphic units."* (WHEATON et al. 2015: 275). Furthermore, the article by O'BRIEN et al. in 2019 using the same mapping framework adds that *"The confining margin is the portion of the potential confining margin that actually abuts the active channel."* (O'BRIEN et al. 2019: 1833). Overall "*The margins help better explain the link between the valley setting and the assemblages of geomorphic units one is likely to find."* (WHEATON et al. 2015: 292).

The mapped confining margins hereby further give insight into where the river can move laterally which also ties into the previous findings when overlapping the thalwegs of the orthophotos. The lower segment of the study area hereby has not undergone significant river course changes since 57.79% of the confined Salza River has a confining margin and is naturally restricted through bedrock. The two river alterations visible, when overlapping the thalwegs were both located in the upper segment of the study area in the unconfined Salza River, were only 29.11% of the Salza River has a confining margin. O'BRIEN has further defined percentages of valley bottom confinement to label the valley setting where an 85% or higher is labelled as confined, 10-85% partly confined and below 10% unconfined. Using these increments, the throughout the thesis described lower confined channel would be declared as partly confined lying in the 50-85% bracket and the throughout the thesis described as upper unconfined channel would also be declared as partly confined lying in the 10-50% range (O'BRIEN et al. 2019: 1833). Noted at the bottom of the table is: *"Note: this does not cover all river types or all possible combinations within ranges"* (O'BRIEN et al. 2019: 1833). Labelling the lower Salza River segment as partly confined versus on my part confined does seem reasonable, as the river still has some possible minute lateral movement. Labelling the upper part however as also partly confined does not seem to fit the findings from the field work. I believe the top part of the Salza River right above and below the weir, affect this value and a possible sub segment could have solved this. A possible new segmentation could then be as follows: river km 61.8 - 62.85 anthropologically confined, river km 57 - 61.8 unconfined and river km 54.1 - 57 partly confined.

The only limitation of the confining margin mapping lies by the mapper himself. To the best of my ability, I mapped these confining margins in 2017 using WHEATON'S framework which also provided essential data for the modelling, described later. During the follow up mapping in 2018 no additional confining margins were found. However, there is a degree of marginal human error which must be considered. Further, another mapper might delineate the confining margins slightly different.

The second presented map shows the Tier 2 in and out-of-channel geomorphic units as well as in-channel structural elements, see overview map in Figure 104 and zoomed in map excerpts in Figure 105, Figure 106 and Figure 107. Citing Wheaton et al.: *"We define the shape of a geomorphic unit in terms of whether or not it exhibits topographic curvature (i.e., a departure from a plane). This is convenient, because curvature is a direct derivative of topography, such that it is the second derivative of elevation with respect to distance (slope is the first derivative). Using curvature, a geomorphic unit's shape can be defined as predominantly concave (curving inwards), convex (curving outwards), or planar (lacking curvature)."* (WHEATON et al. 2015: 284). Further *"In tier 2, we identify the broad type of structural element, and in the case of natural structural elements we further differentiate between inorganic (e.g., bedrock and boulders) and organic structural elements (e.g., large woody debris)."* (WHEATON et al. 2015: 278).

The importance in mapping structural elements preferably before mapping geomorphic units is that *"Structural elements have the potential to create hydraulic conditions that are conducive to scour where they accelerate flow around the obstructions they cause (e.g., carving a forced pool) and can create bar deposits (e.g., eddy bar) in their shear zones."* (WHEATON et al. 2015: 279).

Looking first at the out-of-channel geomorphic units, we get a deeper insight from the first map showing the margins. We see that fans, landslides or terraces form natural flood protected areas which also coincides with the number of houses positioned there. The largest landcover within the valley bottom margin of the previously newly defined medium segment as well as the lower segment are floodplains where few houses are positioned. Mapping the out-of-channel units was not so straight forward, as the features examined in field were not always obvious. Only by using the DEM as a cross reference in the field as well as during the

off-site digitalization, was it possible to name the features. A good example for this were the three mapped paleochannels, which at first while mapping in field where not clearly detectable. Only through cross referencing the DEM maps which I had in the field, did the features pop out and were possible to be mapped as paleo channels. However, it should be noted, that the feature definitions were solely done by me using Wheaton's framework. Some areas, such as the landslide, or floodplain protected features might be defined differently by another mapper.

The located and mapped in stream structural elements in ascending quantities were culverts, concrete boulders, deadwood and natural boulders with a total count of 2, 2, 240 and 473 for the whole study area. The boulders were the most present element also having the biggest effect on the geomorphic units causing forced riffles and forced pools. Deadwood elements which were also found quite often, had a distinct influence on the riverbed throughout the whole Salza River study area.

WHEATON et al. 2015 presented his mapped tier 2 and tier 3 channel geomorphic units across three different example sites in the Figure 11 of his article (WHEATON et al. 2015: 291), which can be seen in Figure 146 on the following page. *"These three reaches are representative of river types in confined (Wright Creek), partly confined (Bear Valley Creek), and laterally unconfined valley settings (Lemhi River), allowing us to test the framework across a range of river and valley types."* (WHEATON et al. 2015: 288) and will be used to compare the results found for the Salza River.

First examining WHEATON'S Tier 2 assemblages we see that in the confined Wright River the planar units outweigh the others with the transition zone having the second largest proportion. The Bear valley being a partly confined valley equally has concave and transition zones as the most predominant features. And lastly the Lemhi River being an unconfined river, consists mostly of transition zones. Comparing these tier 2 proportions with the tier 2 proportions of the mapped units for the Salza River area, see Figure 147, at first glance the results best compare with the unconfined Lemhi River as the transition zone is most common in the total, confined and unconfined Salza River. Looking closer at the total Salza River, the proportions are very similar to the Lemhi River except that there were more mapped planar features in the

Salza River, but we can safely say that every river is unique and that differences will emerge among the same river types.

Examining the proportions for the confined valley closer, we notice even more transition zones compared to the total Salza River and that the confined results also do not overlap very well with the results for the confined Wright River in WHEATON'S article, where planar features were most common. The other common features in the Salza River in descending order of the confined valley are convex, planar and concave. Interestingly there are more concave than convex features for the Wright River and exactly opposite more convex than concave features in the confined Salza River. Since the Salza River was mapped using the same framework, the differences must be either due to different river conditions or possibly mapping during different water levels and thus having a different result.

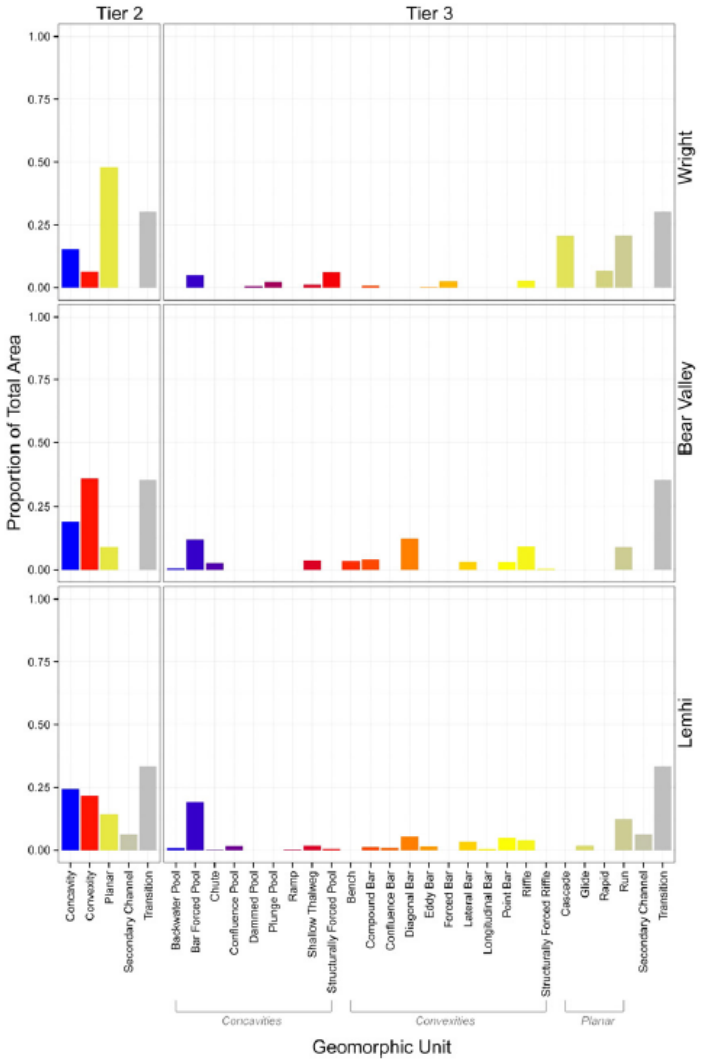


Figure 146: Contrasting assemblages of tiers 2 and 3 in-channel geomorphic units across the three example sites (WHEATON et al. 2015: 291).

Looking closer at the proportions of the unconfined Salza River, the transition zone is also the most common but not that dominant as with the confined and total Salza River. Here the concave features slightly outweigh the planar features with convex features being the least common. The results best compare with the unconfined Lemhi River where the order in descending order is transition, concave, convex and planar compared with the order in descending order of the unconfined Salza River being transition, concave, planar, convex. Only planar and convex features are different, which is probably due to a slightly different river setting.

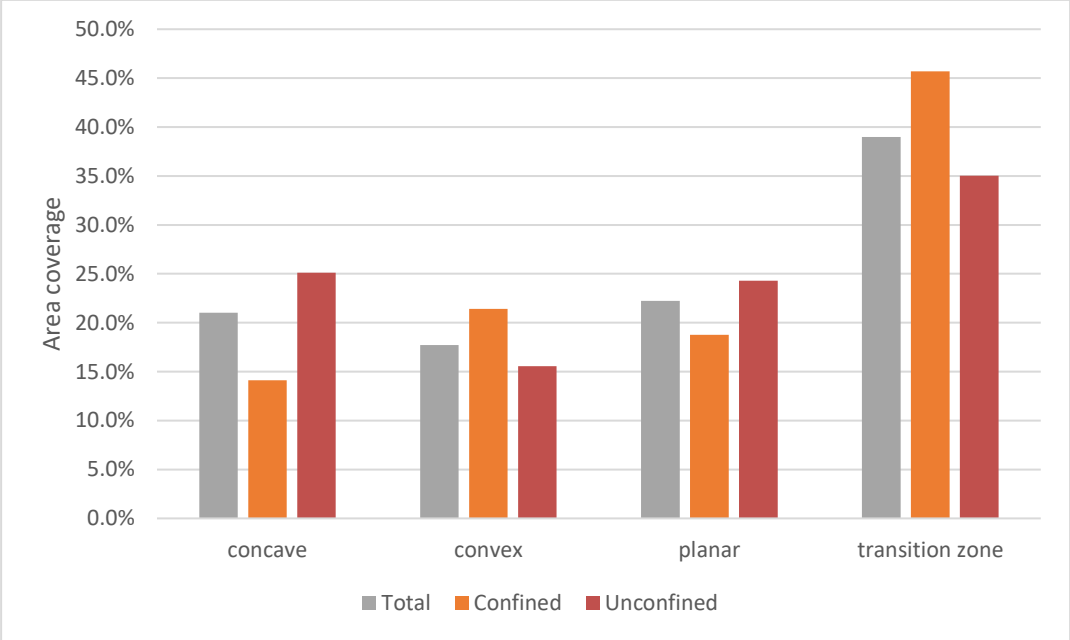


Figure 147: Area coverage of Tier 2 geomorphic units in the total, confined and unconfined Salza River study area.

The third and final presented map shows the Tier 3 in and out-of-channel geomorphic units as well as in-channel structural elements, see overview map in Figure 109 and zoomed in map excerpts in Figure 110, Figure 111 and Figure 112. The structural elements in stream as well as the out-of-channel units remained unaltered to the second map. Using WHEATON'S proportion bar chart template, the area coverage of Tier 3 geomorphic units was once more graphed in Figure 149 for better reference. The concave dammed pool had the largest proportion for both the total and unconfined Salza River and is mainly due to the fact the constructed weir between river km 62.3 and 62.4 dammed a roughly 500 m stretch of the Salza River, which influences the results. Coming back to the previously proposed alteration of segmenting the Salza River into three segments instead of two, might have resulted in more comparable results. Only the Wright River in WHEATON'S article had a dammed pool. The

most common concave feature in the confined Salza River was the bar forced pool. Only the unconfined Lemhi River had a bar forced pool as the predominant concave feature.
Looking at the convex features, the most common feature for the total and confined Salza River were islands followed by riffles. There were no islands mapped in WHEATON'S three rivers, however riffles were the most common unit in the partly confined Bear Valley River and were also common in the Lemhi River. The unique river setting of the Salza River hereby cannot exactly be compared with any of WHEATON'S rivers. The most common feature for the unconfined Salza River was a compound bar followed by lateral bars. Compound bars were common in the Bear valley setting and lateral bars in both the Bear valley and Lemhi setting.

The bar which was defined as a compound bar was the bar opposite of the erosion hotspot between river km 58.7 - 58.8, see left image in Figure 148. Originally a lateral bar after the initial erosion in 2014 it was mapped as a compound bar in 2017 because the bar contained several features such as described in the river styles framework (BRIERLEY et al. 2005: 97), see image on the right. The mapped bank contained a scour, chute channel, vegetated bar, unvegetated bar etc. see image on the left.

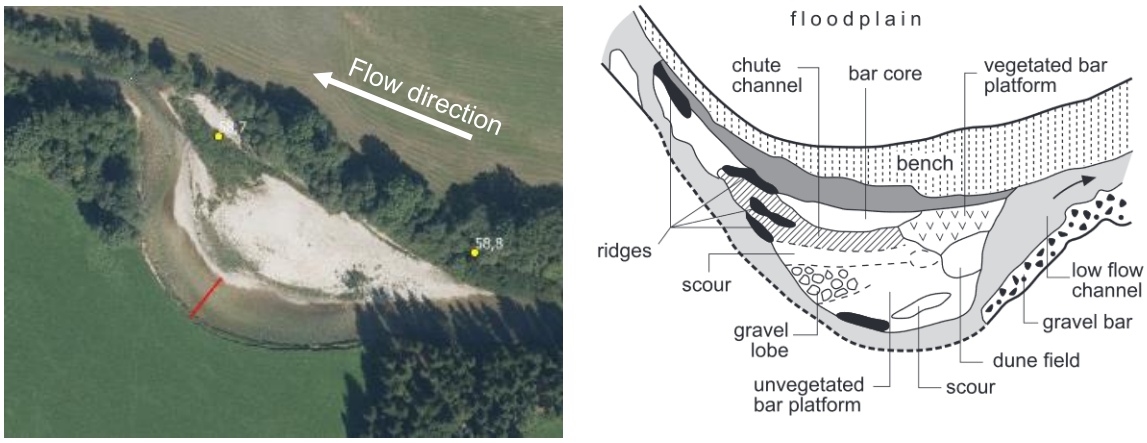


Figure 148: Left: 2017 orthophoto of compound bar between river 58.7 - 58.8, Right: Compound point bar with bar platform, ridges and chute channel (BRIERLEY et al. 2005: 97).

Lastly the planar features were the second most common feature in the total, confined and unconfined Salza River and only consisted of a run which are *"Stretches of uniform and relatively featureless bed, comprising bedrock or coarse clasts (cobble or gravel). These smooth flow zones are either free-flowing or imposed shallow channel-like features that connect pools. They may occur in either alluvial or bedrock-imposed situations. Individual boulders may protrude through otherwise uniform flow."* (BRIERLEY et al. 2005: 83). Runs were also the most common planar features for all three rivers in WHEATON'S findings.

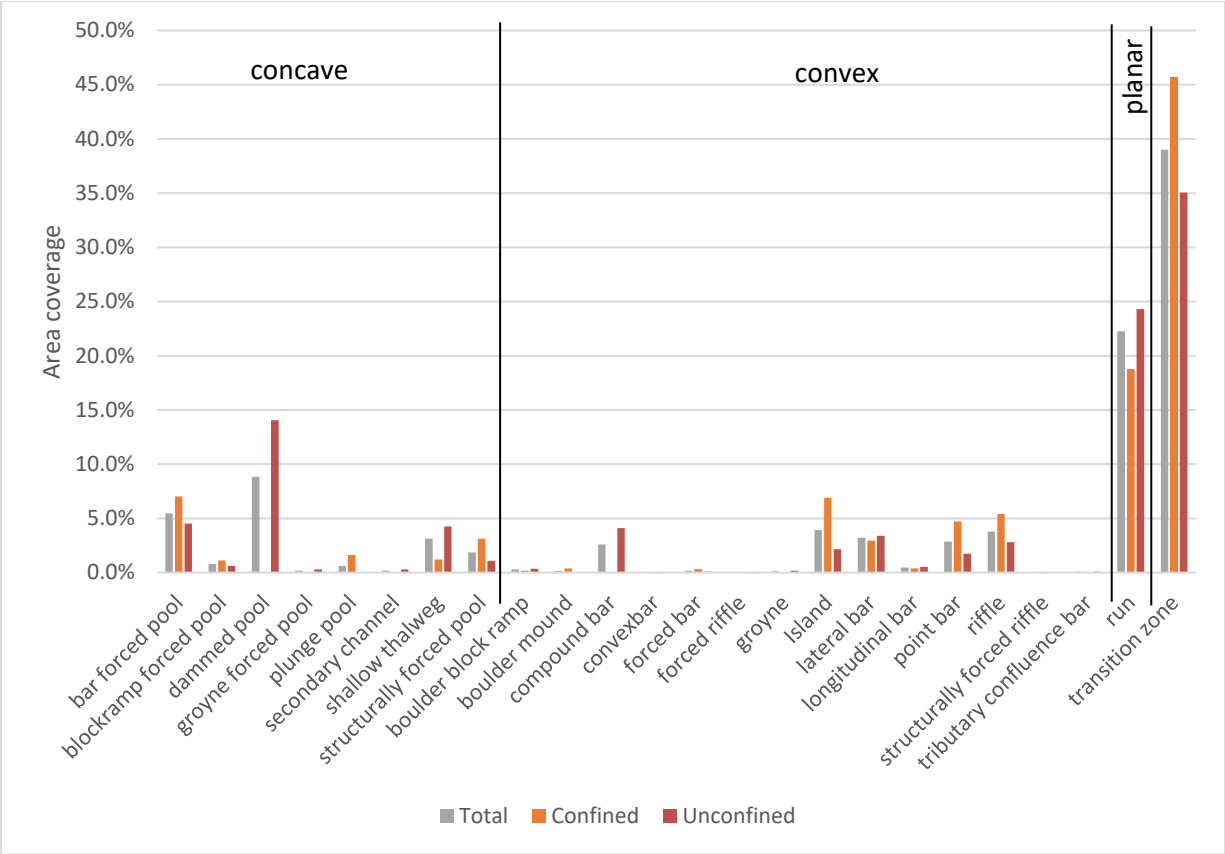


Figure 149: Area coverage of Tier 3 geomorphic units in the total, confined and unconfined Salza River study area.

Using the River Styles framework formulated in BRIERLEY et al. 2005 and applied by WHEATON et al. 2015, offered a complete method for mapping in and out of stream geomorphic units as well as structural elements and margins to portray the Salza River study area as detailed as possible. Mapping the margins (valley margin, valley bottom margin, river margin and confining margin) and structural elements (culverts, concrete boulders, deadwood and natural boulders) were very straightforward and simple. Same can be said of mapping the tier 2 geomorphic units. However, delineating the tier 3 geomorphic units was quite strenuous especially when more than one unit fit the current setting. Here I believe lies the greatest margin of error for mapping a new study area as well as mapping an already mapped area as more mappers have more opinions thus resulting in potentially slightly varied tier 3 mapping results. Also mapping the transition zones will depend on the mapper and differ from every mapper.

To put it in WYRICK'S words: *"Mapping errors arise from user subjectivity, varying surface water patterns when the same area is observed at different discharges and viewpoints, and difficulty in creating a complete map with no gaps or overlaps in delineated polygons."* (WYRICK et al. 2013a: 14). *"However, in coming years it is highly likely that as emerging*

technologies and data resolution improve, and processing speeds increase, much of the initial, baseline survey of rivers will become semiautomated or fully automated, and new plug-in tools will be available to undertake, at least, a first filter of the types, distribution and behavioural attributes of rivers we see in our landscapes" (FRYIRS et al. 2019: 13).

Nonetheless *"The taxonomy helps minimizes operator variance in the definition and mapping of geomorphic units. Resulting products readily facilitate quantification of features (and their patterns) along river systems, providing a coherent physical platform to assess the dynamic template of riverscapes."* (WHEATON et al. 2015: 293).

Closing the mapping discussion with a look back at the ÖBf mapping, in Figure 114 and zoomed in in Figure 115, one must conclude that the highly detailed mapping of the Salza River study area and the graphed proportional area coverage of the tier 2 and tier 3 mapping using the River styles framework and WHEATON'S approach unfortunately are not comparable with the ÖBf mapping.

7.3 Monitoring of the erosion hotspot

When monitoring the erosion hotspot between river km 58.7 - 58.8, the initial plan was to use erosion pins as described by (LAWLER 1992: 803) where some form of rod would have been horizontally placed into the bank at different heights and lengths along the bank erosion. However due to the local circumstance of the collapsed bank, the method had to be discarded on-site, as described at the beginning of chapter *5.3.2 Methods.* Interestingly the same bank condition and its accompanied difficulty was already described by Hooke, see image on the right. "*Bank hydraulic conditions are such that the main removal takes place by collapse or slumping of large blocks of material after the peak has passed….It has been suggested that this slumping may be related to the rate of fall of the hydrograph (Twidale, 1964) but this is difficult to observe or measure. The process of slumping involves large blocks which topple forward but usually remain intact with the grass continuing to grow on the side."* (HOOKE 1979: 54).

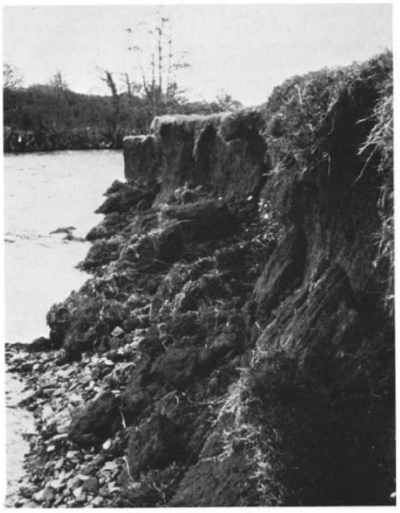


Figure 150: Slumped bank material (HOOKE 1979: 54).

The alternatively adapted version 1 method, described thoroughly in chapter *5.3.2 Methods* faced another issue and was also discarded on-site after only providing one set of measurements. The adapted version 2 method, described in chapter *5.3.2 Methods* yielded two sets of measurements but also had to be discarded, because the pins were unlocated.

When trying to compare the method and results of the adapted version 2 erosion pin method, one comes across difficulties in finding comparable sources. Most articles mentioning the use of erosion pins mostly apply the method as LAWLER intended it to be used as in these exemplary selected articles: (COUPER et al. 2002), (HARDEN et al. 2010), (HARDEN et al. 2013) and (LAWLER et al. 1999). Therefore, a comparison cannot be made. What can be said, is that the version 2 method was a simple workaround and only yielded one value for the entire height of the bank instead of several compared with the erosion pin method from LAWLER 1992. The limitations for the version 2 method are however the same as the mentioned erosion pin limitations by LAWLER. *"(a) Spatial sampling difficulties, (b)interpretation of readings, (c) movement of pins, (d) loss of pins and (e) effects of pins on bank conditions."* (LAWLER 1992: 798, 805). The mentioned movement of pins was the main limitation for the version 1 method and the loss of pins was the main limitation for the version 2 method. Further the readings from the version 2 method using the meter stick, has an estimated margin of error of +/- 0.5 cm which relativizes the results. The mean change was -1.63 cm across the whole bank, thus indicating a light erosion rate in the 1-month timeframe. When used over a longer timeframe the results would have yielded more convincing results.

Adjacent to the erosion pins, the erosion hotspot was photographed on 5 separate occasions between 05.2017 and 06.2018, see Table 5, to perform a photogrammetric analysis with the acquired images described in chapter *5.3.2 Methods*. The use of this additional method was a blessing in disguise as it yielded relevant results for all timeframes, compared with the adapted erosion pin methods.

The advantages of photogrammetry are manifold and already numerously mentioned when reading through the scientific literature. Following are a few selected citations mentioning the core advantages to which not much can be added.

"Photogrammetry reduces spatial sampling problems and enables bank erosion to be monitored with minimal contact on the bank face itself." **(**BARKER et al. 1996: 1).

"Photogrammetry represents an alternative, non-intrusive technique for monitoring landform evolution." **(**PYLE et al. 1997: 754).

"One of its main advantages is the minimization of field work. Photogrammetry has now become a widely used technique even for local scale mapping applications." **(**KOEHL et al. 2020: 63).

"For example, photogrammetry can serve complementarily to quantify volumetric changes from Overlapping photographs (Lane et al., 2010), or ALS to provide recent topographic elevations and reconstruct past morphologies (Rhoades et al., 2009)." **(**DURÓ et al. 2018: 935).

"Regarding the data collection through Photogrammetry "The research reviewed here evidences numerous advantages over traditional methods; namely the hyperspatial resolution, spatially explicit and spatially continuous data which can be obtained more quickly, more easily, more flexibly, and more frequently than using other approaches." **(**WOODGET et al. 2017: 14)

One addition I would like to add after my hands on experience, is that the method of photogrammetry is very cost-effective. Besides essentially a high-resolution digital camera with a GPS location function and optimally a camera tripod nothing more is needed for the acquisition of the images. MICHELETTI et al. 2014 have even gone so far in their article to *"…test the acquisition of high-resolution topographic and terrain data using hand-held smartphone technology…"* (MICHELETTI et al. 2014: 2) which would enable everyone with a smartphone to take images which can be used for photogrammetry. For the photogrammetric analysis and data processing there is freely available open-source software available. The advantages of this method are therefore very apparent and nowadays in my opinion the go to method when monitoring hydro-geomorphic changes such as bank erosion.

While using the method in the acquisition as well as data processing step, I came across several small limitations, briefly mentioned in chapter *5.3.2 Methods,* on which will be added. The camera positions were initially spray painted by me on the bar opposite the bank erosion to take all images from the same positions. However, the markings were washed away, and all further camera positions were only estimated. Since the photographed images were all GPS tagged by the camera, this initial worry dissolved after the data processing stage which showed that the exact camera position is only of secondary importance when using a GPS camera. More important is that there are several images taken from different locations of the same bank to later obtain a three-dimensional, stereoscopic image **(**BARKER et al. 1996: 1217). This so-called Structure from Motion (SfM) approach *"…differs by starting with the image matching process, of multiple images of unknown position, orientation and distortion, to produce many matched points. By doing this for multiple images of the same surface, it becomes possible through iteration to determine relative sensor position, orientation and distortion."* (MICHELETTI et al. 2014: 5).

Another mentioned limitation were the lightning conditions which in retrospect had a very large impact. For the photogrammetric software to compute a high-resolution 3D image, many matching points must be present (MICHELETTI et al. 2014: 5). The better the lightning condition during the recording, the more matching points during the processing. What was special at the erosion hotspot and was also mentioned prior, that up until the midday the sun shined onto the erosion hotspot at different locations creating inhomogeneous lightning conditions. Only after midday were the lightning conditions better as the erosion hotspot was illuminated by indirect light. This was the best workaround during the field work. However, during the photogrammetric processing, some areas of the erosion hotspot turned out to be too dark for the software to find enough matching points causing some gaps in the initial point cloud. These gaps were filled in by the software but nonetheless offer a margin of error when assessing changes during monitoring.

The blind zones caused by vegetation, also briefly mentioned in chapter *5.3.2 Methods,* were initially an issue which could be solved by cutting the gras and did not further affect the processing.

One limitation of the used method was the absence of Ground control points (GCP) during the image recording. Optimally when using a photogrammetric approach, one uses ground control points which are fixed points in the landscape and can be later used to align images. KOEHL et al. 2020 used GCPs during their UAV image recording and can be seen on the top of the riverbank in Figure 151.

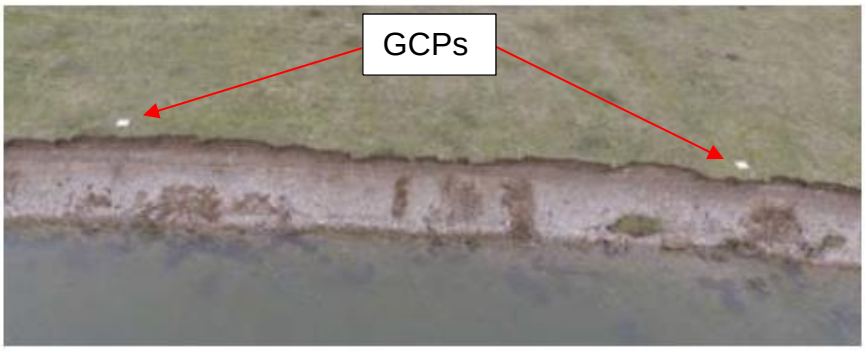


Figure 151: Bank morphology and coded targets as Ground Control Points (KOEHL et al. 2020: 65), edited.

Since I recorded images from the ground with my camera setup level to the erosion bank, using KOEHL'S method of GCPs was not feasible. The only possible location for GCPs in the study area would have been positioning them at the face of the bank. However, the face of the bank was in permanent transition as is common during bank erosions, shown schematically in DURÓ et al. in Figure 152. No GCPs were therefore used during the image recording which again compromises a margin of error.

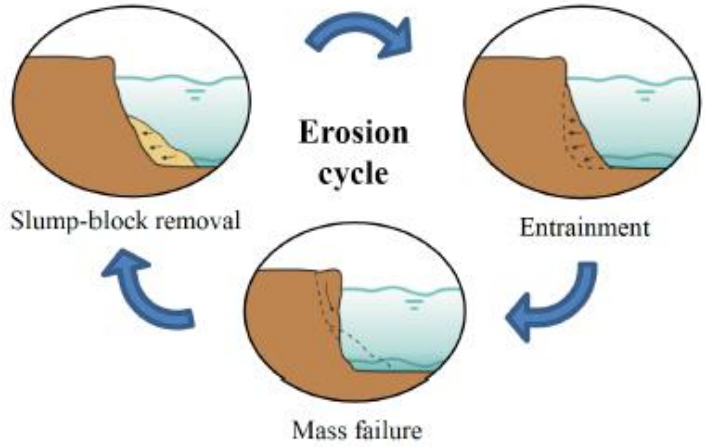


Figure 152: Schematic bank erosion phases (DURÓ et al. 2018: 935).

Bearing these limitations in mind, the results of the photogrammetric analysis will be shortly discussed. The 2D changes of the created point clouds were made using the M3C2 Distance algorithm developed by LAGUE et al. 2013 and available as a plugin in Cloud Compare.

"Currently, multiscale model-to-model cloud comparison (M3C2) is the most widely used

distance computation method used in the geosciences to evaluate 2.5D changing features, considering the time-sequential spatial information contained in point clouds." **(**DIFRANCESCO et al. 2020: 1). In my findings the 2D changes from the five different timeframes seem to not optimally represent the erosion rate. While the comparison images of any 2D changes visually seem decent, the normal distribution of the 2D changes show a different result. Since the mean normal distributions for the comparison 2D change for the cloud #1 to #2, #2 to #3, #3 to #4 and #4 to #5 read -2.5 cm to -2 cm, -2 cm to -1.5 cm, -1 cm to -0.5 cm and -2.5 cm, one would assume that the last comparison of the cloud #1 to cloud #5 has the sum of all with mean normal distribution lying somewhere in the -8 cm to -4 cm range. The real mean normal distribution for the cloud #1 to cloud #5 was however only at roughly -2 cm. Since the value deviates this greatly the margin of error for the results for the 2D change is perhaps larger than assumed and therefore the statement from **(**DIFRANCESCO et al. 2020: 1) cannot be approved in this thesis. However, the previous limitations might affect the results.

The 2.5D volumetric analysis, described in chapter *5.3.2 Methods*, seems to have yielded better results than the 2D analysis. The results found in Table 26 are once more presented in Table 35. The most promising factor of the 2.5D analysis, is that the volume change from cloud #5 to #1 is -319 m³ and the sum of the four comparisons is -340 m³. These values are nearly the same and only differ by 21 m³. Also, the calculated volume can be roughly confirmed through GIS measurements of the orthophotos. The weak spots of the results are, that the matching cells are all except 1 under 50% and the average neighbour per cell for all comparisons is below 6/8. Higher values for both would confirm that the results are more valid and herby are a margin of error. A comparison with other results however cannot be made, as no adequate study was found which used the 2.5D volume analysis for monitoring a bank erosion. To optimise this method in a further study, using ground control points as well as image capturing via a UAV or using a laser scanner would provide a higher accuracy in the results. The cost benefit as well as ease of use however speak for the applied method.

Table 35: Volume changes and additional metrics of the computed point clouds of the erosion hotspot in the Salza River study area.

Cloud	Added volume (m^3)	Removed volume (m^3)	Volume change (m^3)	Matching cells (%)	Non-matching cells (%)		Average neighbour per cell
					Ground	Ceiling	
#2 with #1	+118	-295	-177	40.1	16.8	43.1	5,6/8
#3 with #2	+320	-337	-17	45.9	34.4	19.7	6/8
#4 with #3	+231	-325	-94	56	19.2	24.9	6/8
#5 with #4	+199	-250	-52	38.4	44.7	16.8	5,8/8
	Sum		-340				
#5 with #1	+115	-434	-319	47.3	33.0	19.7	5,9/8

7.4 Modelling of future hydro-geomorphic changes of the Salza River

Prior to modelling, the riverbed grain size distribution, needed for the modelling, was approximated using a Line count analysis (Linienzahlanalyse by FEHR 1987) described in chapter *5.4.2 Methods.* In total, four-line count analyses (LCA) were conducted in the Salza River study area applying FEHR'S method yielding four grain size distributions. The results are shown in Figure 153, but also here once more for clarification. In retrospect the first LCA, seen on the top left in Figure 128, was measured too far from the river in the middle of the bank. The other three LCA were noticeably closer to the riverbed, see Figure 128, thus giving a better representation of the river grain size. This discrepancy can also be seen when comparing all LCA in Figure 153, where the first distinctly deviates from the other three. Nevertheless, all four were used to construct a mean grain size distribution which almost resembles the second line count analysis. If the first line count analysis would have been excluded from the mean, the mean would have not changed drastically, which was why it was left in.

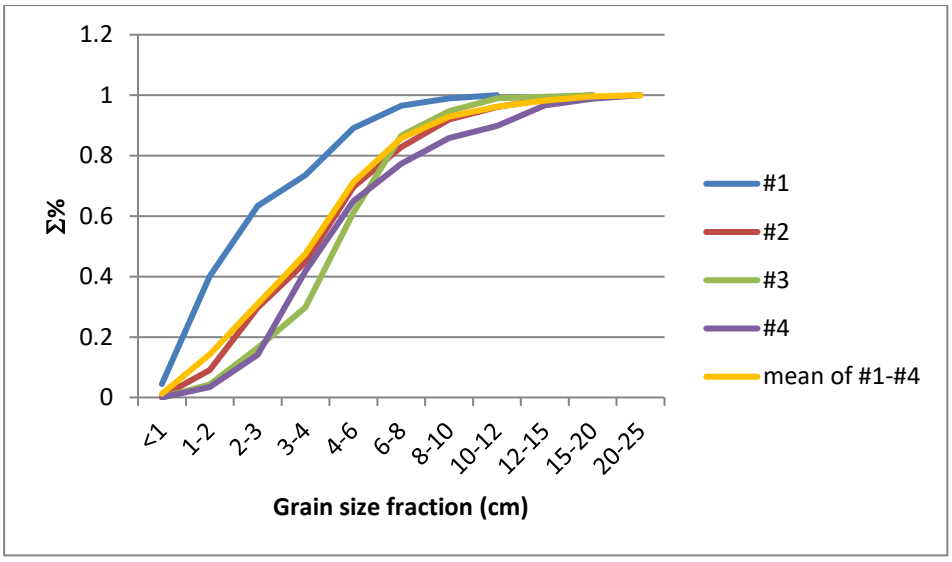


Figure 153: Computed results of the four line-count analyses of the Salza River study area with a mean of all four.

The limitations of the used LCA, mainly depend on adequate positioning of the LCA in the riverbed and that the b-axis of the stones are measured correctly. The results from the mean calculation in Figure 153 show that even if a suboptimal location is chosen, as long as there are more optimal locations from which to calculate a mean from, the results are still reasonable. Leading forward however excluding suboptimal locations is preferred. The second mentioned limitation is the measurement of the b-axis. This was done using a meter stick during the field work and after some practice there were no difficulties. Looking forward, using a calliper would facilitate the measurement, and was also recommended in (FEHR 1987: 1105). Both limitations however can easily be discarded when being meticulous during the measurement. Another aspect of the LCA which should be considered, is that it only represents a snapshot in time mirroring a short hydrological occurrence (STEPHAN et al. 2021).

One further limitation, which is a unique case in this thesis, is that the used results were inputted into the modelling software CAESAR-Lisflood. This software however only allows for 9 input values, while the line count analysis of the Salza River study area yielded 14 classes. Therefore 5 classes had to be deleted to fit the software while still ideally representing the grain size distribution for 14 classes. This is a margin of error and must be considered going forward.

The advantages of the method very much outweigh the limitations. The most advantage is the ease and speed of use. *"No other method in the field allows for such a speedily recording of a*

representable grain size distribution of the course material…The effort to conduct a line count analysis is meagre. 2 workers need around 15 minutes for one analysis which allows for repeatable application thus increasing the validity of the results." (translated) (FEHR 1987: 1105-1106). Another advantage is the cost benefit of the method, as not much except for a tape measure, calliper, pen and paper are needed for the recording.

An adapted primitive sampling method was also used to collect the suspended sediments during a small flooding event described in chapter *5.4.2 Methods.* In the end the results of the measured suspended concentration (g/l) had no use, as the modelling software CAESAR-Lisflood needs a fall velocity (m/s) of the suspended sediment as an input. In retrospect the fall velocity could have been determined using an adequate setup, however since the sampling method was very primitive and not planned beforehand, this was not carried out. The default values for the suspended sediments were therefore used during the modelling.

After all data was prepared to fit the requirements of CAESAR-Lisflood, the parametrization was performed using the method described in chapter *5.4.2 Methods* to yield the results found in Table 31 in chapter *6.4.2 Modelling.* The parametrization, with particular emphasis on the sediment tab, hereby was an *"…ensemble of runs, testing different combinations of values for parameters governing erosion rates and channel morphology, were tested to calibrate the model."* (FEENEY et al. 2020: 1274) and was an essential step prior to modelling. The obvious advantage of this model configuration is to obtain more realistic results as described by (COULTHARD et al 2017: 267-270). FEENEY et al. noted regarding this step: *"Calibrated parameters for some reaches are widely transferable, producing accurate geomorphic changes for some uncalibrated sites. However, large errors along some reaches indicate that reach-specific parameterization is recommended."* (FEENEY et al. 2020: 1273). Since the model calibration is a subjective process decided solely by the user, this can be seen as a limitation. Further, *"… factors such as the high number of parameters…can represent a limitation…" (*GIOIA et al. 2019: 2). Also, since particular emphasis was placed on the sediment tab, some parameters from other tabs which were not calibrated could possibly have a positive effect on the model calibration and future outcome, but this is more a speculative limitation.

The default sediment parameters in combination with the other parameters listed in Table 31, yielded the subjective best results for the model calibration. However, the limitations mentioned are a margin of error or better margin of opinion depending on who performs the model calibration and must be taken into consideration for the final step of the thesis, the modelling.

The modelling was carried out for four different discharge scenarios for the timeframe 2019 - 2050 using the calibrated parameters from Table 31 as described in chapter *5.4.2 Methods*. The computed results are presented in chapter *6.4.2 Modelling*. A sinuosity index calculation was first carried out for all scenarios for the final modelled year 2050, showing any lateral changes which occurred during the 31-year timeframe. For a comparison, the sinuosity index for the pre-modelled year 2019 and the original DEM recorded in 2011 was also added for reference. The pre-model results show four main areas of change in the Salza River study area see Figure 134. Although the segments A, B and D do not perfectly depict the actual river course change which happened during 2011 and 2018, the erosion hotspot using the configured parameters was best depicted, marked as segment C, as its possible future change is of importance. Hereby the limitation of using a model was already obvious as *"It is important to consider that these findings are based on numerical simulations that contain many simplifications and assumptions."* (COULTHARD et al. 2016: 769). A perfect representation of reality is rarely possible.

The potential future hydro-geomorphic changes are best seen in Figure 135 where the thalwegs of the 2018 DEM and all four 2050 DEMs are overlapped showing four areas of the Salza River which might be prone to hydro-geomorphic change, posted once again on the following page in Figure 154. No comparable results were hereby found in the scientific literature. However, the limitations are the same regarding the sinuosity index as described in chapter *7.1* . The change seen in segment A in the Figure 154 occurred for all four discharge scenarios between the years 2031 - 2034, see Table 36, altering the river bend into a nearly 90° angle and shifting the riverbed ca. 20m. Interestingly, although having largely different discharge rates the change occurred in all scenarios, indicating that not a large discharge rate is needed for the shift to happen. The levee positioned alongside the river at segment A was inputted through the bedrock.txt and respected by CAESAR-Lisflood. A further shift of the riverbed as shown in the model is not to be expected as the area is protected by the levee.

The second alteration which occurred during the modelling was at segment B in Figure 154 and occurred between 2031 - 2044 in all discharge scenarios, shifting the riverbed by 130m. As previously mentioned in the results, the potential new riverbed lies in a paleochannel, seen in the Tier 2 and Tier 3 maps. It seems obvious that the largest discharge scenario experienced the change first, however it seems illogical, that the change happened later in scenario 4 than in scenarios 1 and 2 as scenario 4 had more frequent high magnitude flooding events compared with scenarios 1 and 2.

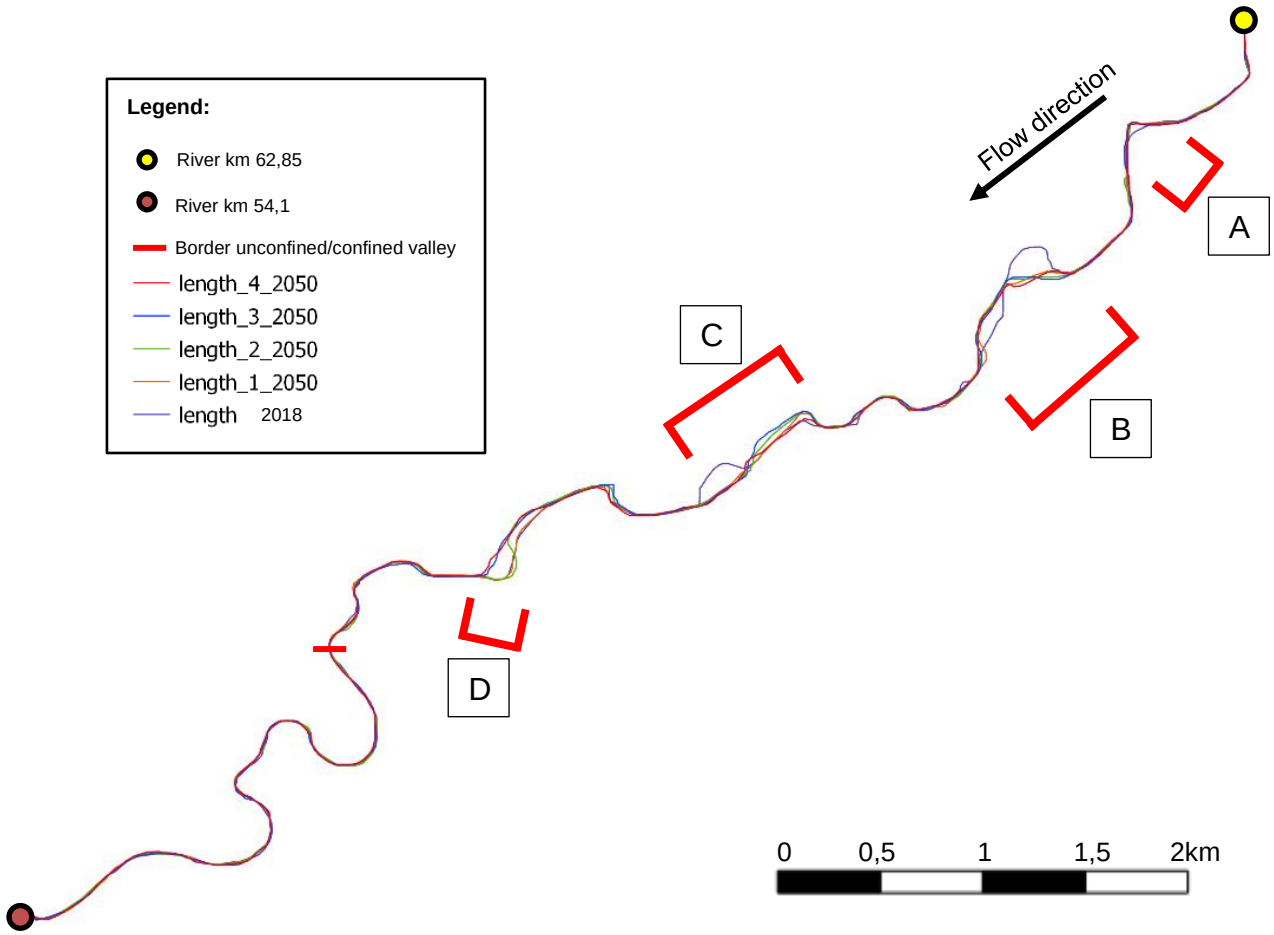


Figure 154: Overlapping the thalwegs of the pre-modelled 2018 DEM as well as all four 2050 DEMs for the four different discharge scenarios of the Salza River study area.

Table 36: Year of change for the four main sections marked in Figure 135.

DEM	Year of change Section A	Year of change Section B	Year of change Section C	Year of change Section D
1_2050m	2034	2043	2024	-
2_2050m	2034	2041	2031	-
3_2050m	2031	2031	2029	2041
4_2050m	2032	2044	2028	2033

The change at section C in Figure 154 occurred again for all discharge scenarios between the years 2024 - 2031 and is thus expected to potentially occur first in the Salza River study area shifting the riverbed by around 80m. Noteworthy, the change occurs first in scenario 1, although having the same discharge as in the timeframe 1976 - 2018. This segment does not seem to need a lot of discharge for hydro-geomorphic changes to happen and can thus be compared with segment A.

Segment D is unique as the change only occurred within scenarios 3 and 4 between the years 2041 and 2033 and not in the scenarios 1 and 2 with less discharge. Again, an interesting finding is that the change occurred 8 years earlier in scenario 4 than in scenario 3, although scenario 3 has distinctly higher mean discharge rates, shifting the riverbed by 100m.

The thalwegs seem to indicate, that a very high discharge rate as in scenario 3 does not result in more hydro-geomorphic changes as one would assume and that lower discharge rates as in scenarios 1 and 2 still cause 75% of all potential changes. Adding on to this thought, if there was potentially less discharge as in the timeframe 2019 - 2050 compared to 1976 - 2018, one can assume less hydro-geomorphic changes to occur. On the other hand, the erosion hotspot between river km 58.7 and 58.8 did not change drastically as presumed and seems to have stabilised. Overall, the sinuosity index of all four discharge scenarios for the year 2050 slightly decreased compared with the 2018 pre modelled sinuosity index as seen in Table 55.

The elevation profile using the results from the modelled year 2050 suggest a slight aggradation of the riverbed between river km 59.5 and 62, with the riverbed remaining constant or slightly incising the remaining river km compared to the original DEM recorded

in 2011. Hereby different discharge rates do not seem to have a drastic effect on the elevation profile.

Next, let us examine the modelling results for the total erosion and accumulation for the four discharge scenarios in Figure 143, additionally shown in Figure 155 for better reference. Since a model application is always a case-by-case study, the findings in this thesis do not compare with other findings in the scientific literature. However, analysing the sediment yield from CAESAR-Lisflood is commonly used and was applied in the selected articles by (COULTHARD et al. 2017), (HANCOCK et al. 2015) and (RAMIREZ et al. 2020). At first, the results show an obvious finding. The higher the discharge rates in a certain timeframe, in this case 2019 - 2050, the higher the total erosion and accumulation (ero/acc) volume. Scenario 3 with the highest discharge hereby also had the highest total ero/acc, while scenario 1 has a notably lesser ero/acc volume. Interestingly scenario 4 with the discharge from only the year 2014 has the lowest ero/acc volume of all, nearly half of scenario 3. However, scenario 4, despite these low volumes still caused the change at section D, while scenario 1 and 2 did not. Looking closer at the hydrological values from Table 12, which was posted once more for better reference in Table 37, we see that scenario 4, despite having a max discharge of 179 m³/s, the mean was only 6.05 m³/s. Scenarios 1, 2 and 3 in comparison have a mean discharge of 7.25 m³/s, 7.4 m³/s and 7.7 m³/s. One can deduct from these findings, that while a high max discharge causes more singular hydro-geomorphic changes, an overall higher mean discharge is responsible for a higher total ero/acc volume in the same timeframe.

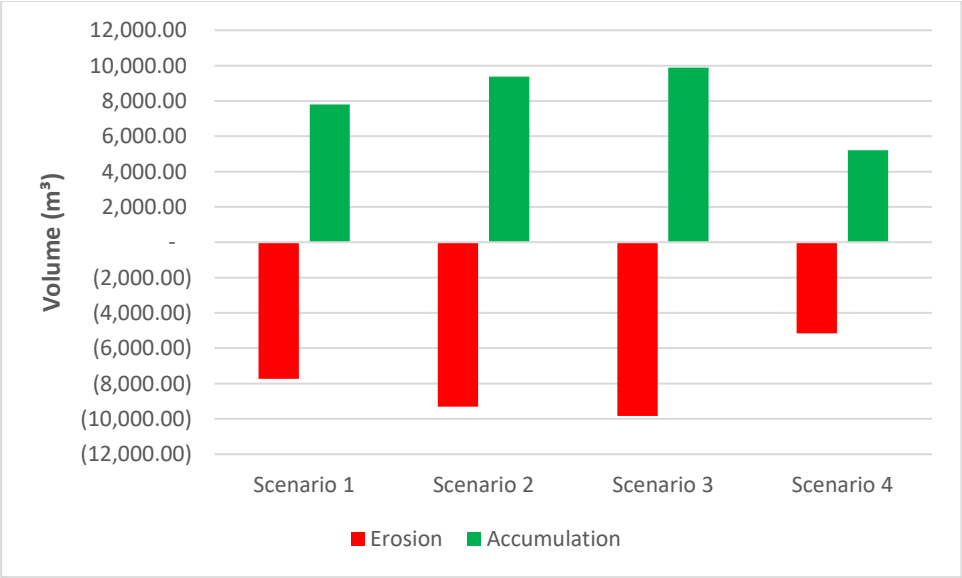


Figure 155: Total erosion and accumulation volumes for all four discharge scenarios for the timeframe 2019 - 2050.

Table 37: Statistical data for the four discharge scenarios for 2019 - 2050.

Statistics	Similar discharge(m^3/s) for 2019 - 2050	More discharge (m^3/s) for 2019 - 2050	A lot more discharge (m^3/s) for 2019 - 2050	2014 discharge (m^3/s) for 2019 - 2050
Mean	7.25	7.4	7.7	6.05
Min	1.63	1.38	1.35	2.57
Max	237	280	280	179

And lastly the D50 grain size results, for which there also are no comparable results in the scientific literature, provide a further insight into how different discharge scenarios affect the D50 grain of the surface layer of sediment. The D50 results were also discussed in the selected article by FEENEY et al. 2020. The linear trendlines of the D50 from Figure 145 are once more presented in Figure 156 for better reference. We see the D50 grain size after the first modelled year of 2019 is the highest in scenario 2, then scenario 3, then scenario 1 and finally scenario 4. Vice versa after the last modelled year of 2050, the D50 grain size is the highest in scenario 1, then scenario 2, then scenario 3 and finally scenario 4. The D50 Grain size decreased from 2019 to 2050 by 3.5% for scenario 1, 8.9% for scenario 2, 7.9% for scenario 3 and 2.0% for scenario 4, giving weight to the previously stated finding. When looking at the first three scenarios, a higher discharge causes a bigger decrease rate in the D50 grain size from 2019 to 2050. Further, higher discharge also results in an overall smaller D50 grain size. However, scenario 4 is an outlier when examining the results, as it has the lowest D50 grain size of all, after the modelled years 2019 and 2050. The reoccurring flooding event from year 2014 in scenario 4 most likely causes the outwash of smaller grainsizes from the study area.

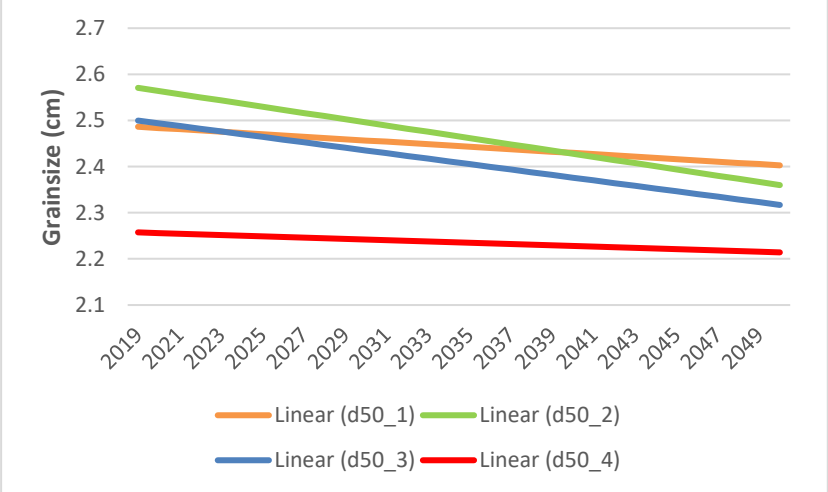


Figure 156: Linear trendlines for the D50 Grain size for the four different discharge scenarios for the timeframe 2019 - 2050.

The use of the 2D LEM modelling software CAESAR-Lisflood yielded relevant insight on both the potential hydro-geomorphic changes, ero/acc volume changes as well as changes in the D50 grain size and provided promising results. The encouraging results were also confirmed by (RAMIREZ et al. 2020: 11), (YU et al. 2019: 127), (FEENEY et al. 2020: 1290) as well as in the following statement by GIOIA et al.: *"The encouraging results presented here testify that a Caesar–Lisflood LEM can represent an effective approach to estimate the sediment yield in Mediterranean-type landscape and its application in unmonitored landscapes can help to unravel the short-term morpho-dynamics of mountain catchments and the role of fluvial and hillslope processes in geomorphological evolution."* (GIOIA et al. 2019: 14).

Bearing the limitations and the margin of error of CAESAR-Lisflood in mind, it forms a solid basis to locate areas of potential future hydro-geomorphic changes also noted in POEPPL et al.: *"The use of 2-D morphodynamic/landscape evolution models represents a step forward for studying and managing complex long-term geomorphic adjustments, sediment delivery, and related habitat issues following (multiple) dam construction and removal."* (POEPPL et al. 2019: 548)

7.5 Research questions and hypotheses

In the final discussion chapter, the research questions of this thesis will be answered and a response formulated regarding the formulated hypotheses. The order of discussion will follow the order of the formulated research questions from chapter *2. Research questions and hypotheses.*

Central research question:

> *"Which hotspots of hydro-geomorphic changes exist within the river course of the Salza River (between river km 54.1 - 62.85) in the area of Gusswerk, Styria and what is the expected future development of the river course?*

Central hypothesis:

> My hypothesis regarding the central research question reads as follows:
> I expect to find hotspots of hydro-geomorphic changes in the study area in the form of bank erosion in the river bends with more developed curvature especially in areas without riparian vegetation. Further I hypothesize, when modelling with a high

discharge scenario for the years 2019 - 2050 that the selected hotspots will cut-off the river and alter its existing riverbed by the year 2050.

Statement:
There have been several hydro-geomorphic changes during the past when examining the first comparable historical map, the Francisco-Josephinische land survey from 1869 - 1887 as well as the recent orthophotos from the years 2004 - 2017. The most prominent natural change was the river widening at river km 59.6 seen in the 2009 orthophoto and the bank erosion between river km 58.7 and 58.8 seen first in 2014. While the former has already morphed back into its pre 2009 state and is covered with primary plant succession, the latter has increased in size and shifted the river course however has stabilized in its 2019 extent. The most prominent anthropogenic change was the construction of the side channel and the weir in the upper part of the Salza River which occurred prior to the 2009 orthophoto as well as the fish ladder construction in 2006 at river km 62.3 and the levee construction in 2017 alongside river km 61.9 and 62.85. Further small bank and in-channel changes were noticeable, i.e. shifting of a bank, local bank erosion, removal of riparian vegetation, but did not alter the course of the Salza River. Going forward there are four main areas which could potentially change in the future course of the Salza River. The findings of modelling the timeframe 2019 - 2050 with four different discharge scenarios show that the first change could occur between 2024 - 2031 between river km 59.1 and 59.7 potentially straightening the course of the Salza River. The second change could occur between 2031 - 2034 potentially slightly eroding the river bend at river km 62.1 and potentially incising it. The third change could occur between 2031 - 2044 potentially shortcutting the existing river bend between river km 60.8 and 61.4 and reflowing in a historic paleo channel. And lastly, if there are very high future discharge rates in the timeframe 2019 - 2050 compared to 1976 - 2018, then between river km 57.8 and 58.3 the existing river could potentially reflow into an old paleo channel between 2033 and 2041.

Regarding the hypothesis it is true that all changes were found in river bends. However not all bends with a developed curvature were prone to changes as local factors determine where and when changes happen. Also, the confined Salza River below river km 57, though having the most developed curvatures did not experience any distinct changes, being that the river is confined in lateral expansion. Indeed however, in two of four cases the modelling results

show a potential existing riverbed cut-off. In addition, areas of removed riparian vegetation did seem to have more erosion at the spot but could recover with time and did not greatly affect the river course.

Question *a:*

"How fast is the rate of bank erosion at the hotspots?"

Hypothesis a:

The rate of bank erosion will mostly be affected by large flooding events which will heavily incise into the banks. With a high discharge scenario, I predict bank erosion rates of around 1 m per year. In addition, an absence of heavy floods will reduce and mitigate the bank erosion rate.

Statement:

Bearing the limitations of the applied methods in mind, the measured rate of bank erosion with the adapted erosion pin method version 2 was calculated to have a mean change of -1.63 cm across the whole bank from 15.06.2017 to 11.07.2017. The measured rate of 2D bank erosion via comparing the point clouds computed during the photogrammetric analysis showed a mean of roughly -2 m for the whole bank for the 13-month timeframe from 06.05.2017 to 11.06.2018. The measured rate of 2.5D volumetric bank erosion via comparing the point clouds computed during the photogrammetric analysis, showed a mean of roughly -319 m^3 for the whole bank for the timeframe from 06.05.2017 to 11.06.2018.

Regarding the predicted rate of bank erosion, the rate does approximate the actual results. Further since no large flooding events occurred during the study timeframe, no statement can be made to the effect of heavy floods on bank erosion rate.

Question *b:*

"Which changes of the riverbed are to be expected?"

Hypothesis b:

> The riverbed of the Salza River study area will alter laterally in areas with heavy bank erosion and possibly cut-off the existing river. Additionally, the riverbed will incise in areas of restricted lateral movement.

Statement:

Examining the modelled results, we can deduct that there are four potential areas of a lateral riverbed shift as well as a potential riverbed aggradation between river km 59.5 and 62 with the riverbed remaining constant or slightly incising in the remaining river km comparing the 2050 DEM for the modelled discharge scenarios to the original DEM recorded in 2011.

Regarding my hypothesis, the first proposition is correct when looking at the results from the modelling and interestingly the modelled results also show a potential incision below river km 59.5 which is where the Salza River is laterally confined.

Question *c:*

> *"How do cross sections of the riverbed alongside the hotspots change?"*

Hypothesis c:

> The cross sections of the majority of the riverbed will remain unchanged. However, in areas of increased bank erosion, the cross sections of the riverbed will widen.

Statement:

The prominent erosion hotspot which occurred after the flooding event in 2014, has greatly shifted the riverbed and displaced it by a total of 51.41 m from 02.09.2004 to 07.09.2019. Looking at the modelled results, we also see that the potential changes at segments A, B, C and D found at river km 62.1, 60.8 - 61.4, 59.1 - 59.7 and 57.8 - 58.3 shift the riverbed by roughly 20 m, 130 m, 80 m and 100 m.

Regarding my hypothesis, the results of the modelling show that the majority of the riverbed will in fact remain unchanged.

Question *d:*

"What impact do flood events have on the future river course development?"

Hypothesis d:

Flood events of a high magnitude alter the river. I think that the max discharge will have the highest effect based on the erosion hotspot which occurred after a flooding event in 2014. A discharge scenario with only the discharge from the year 2014 will most likely cause the most impact on the river course.

Statement:

From the past we have seen that a large flooding event with a discharge rate of 179 m^3/s caused a prominent bank erosion and thus one can assume that a similar large flooding event has a similar effect in the Salza River study area. Further, from the modelling results there is a correlation where larger volumes are eroded with a higher discharge mean, but more hydro-geomorphic changes occur with more frequent high magnitude flooding events. The modelling further showed that while a distinct hydro-geomorphic change does not always have to happen straight during the flooding event, it provides the trigger for the change to happen in the following years.

Regarding my hypothesis as just mentioned high magnitude flooding events do alter the river however not always immediately. As the modelling results showed, although high discharge events cause hydro-geomorphic changes, a higher annual mean discharge with lesser peak discharges creates more erosion than a lower annual mean discharge with more peak discharges.

Question *e:*

"Which role does the riparian vegetation have on the bank stability?"

Hypothesis e:

The riparian vegetation is natures natural bank protection. Where there is a removal of riparian vegetation, for example after a large flooding event, there will be an increased bank erosion rate as in the graphic below.

Statement:

The lack of riparian vegetation increases erosion at a present bank erosion as seen at the erosion hotspot between river km 58.7 and 58.8. A similar effect was noticed in the orthophotos from 2004 to 2009 at river km 58.2. However, the results also show that during straighter passages of the Salza River, a removal of riparian vegetation does not have as an extreme effect as in river bends. Nonetheless the results also show that banks with riparian vegetation are not as prone to erosion as they have a stabilizing effect also mentioned in the applied literature. *"Forested riparian zones significantly reduce sediment inputs and act as strong disconnectors between the agricultural source areas and the river channel."* (POEPPL et al 2012: 527). The importance of the riparian vegetation shows the mention in the oldest available Latin prose text available: *"Wherever there is a riverbank or wet ground, plant poplar cutting and reed thicket"* (CATO 150BC: 29).

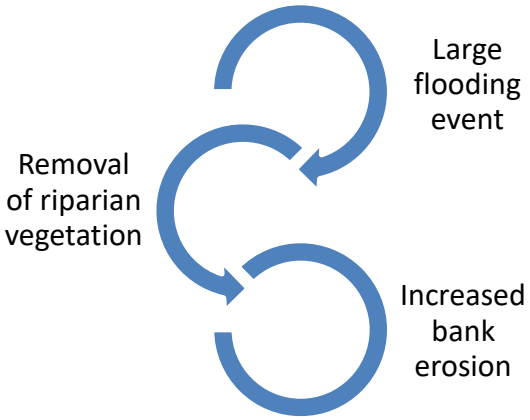


Figure 157: Cause and effect of the removal of riparian vegetation.

From the findings I can conclude that the hypothesis and the cause-and-effect diagram (Large flooding event→Removal of riparian vegetation→Increased bank erosion) is correct.

8. Conclusion

Examining the results from the past historical maps dating from 1678 - 1887 and more recent orthophotos dating from 2004 - 2017 (and 2019 solely for the erosion hotspot), the results show that the Salza River in the study area between river km 54.1 and 62.85 has underwent numerous hydro-geomorphic changes in the past with the erosion hotspot located between river km 58.7 and 58.8 being the most recent and largest natural change.

Mapping the study area during the field work has given insight onto the extent of the out-of-channel features building the extent for the lateral movement of the Salza River as well as in-channel structural elements (mostly natural boulders and deadwood) which affect the development of the in-channel Tier 2 and Tier 3 geomorphic units. The framework developed by WHEATON et al. 2015 was applied and proved to be of great utility. The Salza River study area in total, consists mainly of transition zones followed by planar, concave and convex features. The confined Salza River also mostly consists of transition zones followed by convex, planar and concave features while the unconfined Salza River also consisted mostly of transition zones followed by concave, planar and convex features.

Monitoring the erosion hotspot has provided a newly found awareness with issues, which arise when trying to observe natural changes and also with possible workarounds to nevertheless obtain useful data. The photogrammetric analysis hereby has proven to be an efficient and effective method. The results have shown a mean lateral change of -1.63 cm for the one-month timeframe between 15.06.2017 and 11.07.2017 using the adapted version 2 erosion pin method. The photogrammetric results show a mean 2D change in the Gauss normal distribution of roughly -2 cm using the M3C2 approach and a 2.5D volume change of -319 m^3 between 06.05.2017 and 11.06.2018.

Modelling the Salza River study area using the software CAESAR-Lisflood, has provided further insight into the potential future changes which the Salza River might undergo, depending on the future discharge rates. Four prone segments were highlighted and described. Using the approximated grain size distributions from the material of the Salza River give further weight to the results.

Looking back at the central research question, we can conclude that there were two main erosion hotspots, with the larger one having widened the Salza River drastically between river km 58.7 and 58.8 by 51.41 m from 2014 - 2019. The future development of the Salza River from 2019 - 2050 with the scenario of similar discharge and the scenario of more discharge than in the previous years, show that there are 3 areas of potential hydro-geomorphic change while the scenario with a lot more discharge and the scenario with only the discharge of year 2014 show 4 areas of potential hydro-geomorphic change.

The results gathered offer a very detailed insight into the past, present and future hydro-geomorphic changes and present a solid basis and reference point for further technical actions and/or measures and possibly deeper investigations of the study area.

9. Outlook and Perspectives

Based on the gathered and computed monitoring results one can assume that a similar rate of erosion is going to take place at the erosion hotspot between river km 58.7 and 58.8 in the future as in the timeframe 06.05.2017 to 11.06.2018 if the discharge rates remain similar. However, it is possible that a high magnitude flooding event could drastically alter the bank erosion even if the modelling results did not show this. The lack of riparian vegetation at the erosion hotspot and being in a river bend which has increased in curvature, make it more prone to future changes.

Regarding the outlook of the whole study area, the modelling results have shown that there are four potential areas of hydro-geomorphic change. CAESAR-Lisflood indicates that an increased discharge rate with more peaks causes the changes to happen earlier and in one segment between river km 57.8 - 58.3 to happen at all. Further, in total more erosion and accumulation will occur in the study area with a higher mean discharge. Vice versa the assertion can be made that if the discharge rates would in fact decrease in the future, that the erosion rates would also decrease and that some modelled changes might not occur at all. Bearing the limitations of the LEM in mind, the results are however only *"numerical simulations that contain many simplifications and assumptions."* (COULTHARD et al. 2016: 769). These offer a guidance for potential future countermeasures but cannot depict the reality as it is or will be.

Nonetheless, the results motivate to monitor the hotspot as well as the potential four areas of hydro-geomorphic change further into the future, in order to assess the potential hazards and if needed initiate counteractions.

10. Bibliography

AGISOFT METASHAPE User Manual Standard Edition, Version 1.6; available online under https://www.agisoft.com/pdf/metashape-pro_1_6_en.pdf.

BATES et al. (2010): A simple inertial formulation of the shallow water equations for efficient two-dimensional flood inundation modelling. – In: Journal of Hydrology Vol. 387 Issue 1-2 pp33-45; DOI: https://doi.org/10.1016/j.jhydrol.2010.03.027.

BARKER R., DIXON L. and HOOKE J. (1996): USE OF TERRESTRIAL PHOTOGRAMMETRY FOR MONITORING AND MEASURING BANK EROSION. – In: Earth Surface Processes and Landforms Vol. 22 Issue 13 pp 1217-1227; DOI: https://doi.org/10.1002/(SICI)1096-9837(199724)22:13<1217::AID-ESP819>3.0.CO;2-U.

BMLRT ABTEILUNG VII/3 - WASSERHAUSHALT (HYDROGRAPHISCHES ZENTRALBÜRO) (2011): Flächenverzeichnis der österreichischen Flussgebiete Ennsgebiet. – In: Beiträge zur Hydrographie Österreichs Heft Nr. 61. – Wien; available online under: https://info.bmlrt.gv.at/dam/jcr:b5013882-8535-4d2D-9113-e78477ae9536/FlVerz_Enns_2011.pdf.

BLÖSCHL G., HALL J., VIGLIONE A et al. (2019): Changing climate both increases and decreases European river floods. – In: Nature Vol. 573, pp 108–111, DOI: https://doi.org/10.1038/s41586-019-1495-6.

BRIERLEY G. J. and FRYIRS K. A. (2005): Geomorphology and River Management: Applications of the River Styles Framework. ISBN 1-4051-1516-5.

CATO M. P. (CATO the ELDER) (150BC): On farming.

COULTHARD T. J. (2001): Landscape evolution models: a software review. – In: HYDROLOGICAL PROCESSES Vol 15 pp 165-173; DOI: https://doi.org/10.1002/hyp.426.

COULTHARD T. J. and VAN DE WIEL M. J. (2012): Modelling river history and evolution. – In: Philosophical transactions of the royal society Vol. 370 pp 2123-2142 DOI: https://doi.org/10.1098/rsta.2011.0597.

COULTHARD T. J. and VAN DEWIEL M. J. (2017): Modelling long term basin scale sediment connectivity, driven by spatial land use changes. – In: Geomorphology 277, 265–281; DOI: https://doi.org/10.1016/j.geomorph.2016.05.027.

COULTHARD T. J., NEAL J. C., BATES P. D., RAMIREZ J., DE ALMEIDA G. A. M. and HANCOCK G. R. (2013): Integrating the LISFLOOD-FP 2D hydrodynamic model with the CAESAR model: implications for modelling landscape evolution. – In: Earth surface processes and landforms 38, 1897-1906; DOI: https://doi.org/10.1002/esp.3478.

COULTHARD T. J. and SKINNER C. J. (2016): The sensitivity of landscape evolution models to spatial and temporal rainfall resolution. – In: Earth system dynamics 4, 757-771; DOI: https://doi.org/10.5194/esurf-4-757-2016.

COUPER P., STOTT T. and MADDOCK I. (2002): INSIGHTS INTO RIVERBANK EROSION PROCESSES DERIVED FROM ANALYSIS OF NEGATIVE EROSION-PIN RECORDINGS: OBSERVATIONS FROM THREE RECENT UK STUDIES. – In: Earth Surface Processes and Landforms Vol. 27 pp 59-79; DOI: https://doi.org/10.1002/esp.285.

DIFRANCESCO P. M., BONNEAU D. and HUTCHINSON D. J. (2020): The Implications of M3C2 Projection Diameter on 2.5D Semi-Automated Rockfall Extraction from Sequential Terrestrial Laser Scanning Point Clouds. – In: Remote Sensing Vol. 12 Issue 11; DOI: https://doi.org/10.3390/rs12111885.

DURÓ G., CROSATO A., KLEINHANS M. G. and UIJTTEWAAL W. S. J. (2018): Bank erosion processes measured with UAV-SfM along complex bank lines of a straight mid-sized river reach. – In: Earth Surface Dynamics Vol. 6 pp 933-953; DOI: https://doi.org/10.5194/esurf-6-933-2018.

FEENEY C. J., CHIVERRELL R. C., SMITH H. G., HOOKE J. M. and COOPER J. R. (2020): Modelling the decadal dynamics of reach-scale river channel evolution and floodplain turnover in CAESAR-Lisflood. – In: EARTH SURFACE PROCESSES AND LANDFORMS Vol. 45 pp 1273-1291; DOI: https://doi.org/10.1002/esp.4804.

FEHR René (1987): Einfache Bestimmung der Korngrössenverteilung von Geschiebematerial mit Hilfe der Linienzahlanalyse. – In: Schweizer Ingenieur und Architekt Band 38, Heft 38 pp 1104-1109; DOI: https://doi.org/10.5169/seals-76710.

FLORSHEIM J. L., MOUNT J. F. and CHIN A. (2008): Bank Erosion as a Desirable Attribute of Rivers. – In: BioScience Vol 58 No 6 pp 519-529; DOI: https://doi.org/10.1641/B580608.

FRYIRS, K.A. and BRIERLEY, G.J. (2013): Geomorphic Analysis of River Systems: An approach to Reading the Landscape. John Wiley and Sons, Chichester, 345pp. ISBN 978-1-4051-9274-3.

FRYIRS K., WHEATON J. M., BIZZI S., WILLIAMS R. and BRIERLEY G. J. (2019): To plug-in or not to plug-in? Geomorphic analysis of rivers using the River Styles Framework in an era of big data acquisition and automation. – In: WIREs Water Vol. 6 Issue 5 pp; DOI: https://doi.org/10.1002/wat2.1372.

FUCHS R., VERBURG P. H., CLEVERS J. G. P. W. and HEROLD M. (2015): The potential of old maps and encyclopaedias for reconstructing historic European land cover/use change. – In: Applied Geography Vol. 59 pp 43-55; DOI: https://doi.org/10.1016/j.apgeog.2015.02.013.

GARCÍA J. H., DUNESME S. and PIÉGAY H. (2019): Can we characterize river corridor evolution at a continental scale from historical topographic maps? A first assessment from the comparison of

four countries. – In: Special Issue: Innovative Approaches in River Management and Restoration Vol. 36 Issue 6; DOI: https://doi.org/10.1002/rra.3582.

GIOIA D. and LAZZARI M. (2019): Testing the Prediction Ability of LEM-Derived Sedimentary Budget in an Upland Catchment of the Southern Apennines, Italy: A Source to Sink Approach. – In: Water Vol. 11; DOI: https://doi.org/10.3390/w11050911.

HABERSACK H. and KLÖSCH M. (2012): Monitoring und Modellierung von eigendynamischen Aufweitungen an Drau, Mur und Donau. – In: Österreichische Wasser- und Abfallwirtschaft Vol. 64 pp411-422; DOI: https://doi.org/10.1007/s00506-012-0007-9.

HABIB A. F., KIM E. M. and KIM C. J. (2007): New Methodologies for True orthophoto Generation. – In: Photogrammetric Engineering & Remote Sensing. Vol 73 No. 1 pp 025-036; DOI https://doi.org/10.14358/PERS.73.1.25.

HANCOCK G. R., COULTHARD T. J. and LOWRY J. B. C. (2016): Predicting uncertainty in sediment transport and landscape evolution – the influence of initial surface conditions. – In: Computers & Geosciences 90, 117-130; DOI: https://doi.org/10.1016/j.cageo.2015.08.014.

HARDEN C. P., CHARTRAND K. J. and HENRY E. (2010): Temporal Variability of Bank Erosion in East Tennessee Headwater Streams. – In: Southeastern Geographer 4 (50), 484-502; DOI: https://doi.org/10.1353/sgo.2010.0006.

HARDEN C. P., FOSTER W., MORRIS C., CHARTRAND K. J. and HENRY E. (2013): Rates and Processes of Streambank Erosion in Tributaries of the Little River, Tennessee. – In: Physical Geography Vol. 30 Issue 1 pp 1-16; DOI: https://doi.org/10.2747/0272-3646.30.1.1.

HARMAN W., STARR R., CARTER M., TWEEDY K., CLEMMONS M., SUGGS K. and MILLER C. (2012): A Function-Based Framework for Stream Assessment and Restoration Projects. US Environmental Protection Agency, Office of Wetlands, Oceans, and Watersheds, Washington, DC EPA 843-K-12-006; available online under: https://www.epa.gov/sites/default/files/2015-08/documents/a_function_based_framework_for_stream_assessment_3.pdf.

HAWKER L., BATES P., NEAL J. and ROUGIER J. (2018): Perspectives on Digital Elevation Model (DEM) Simulation for Flood Modelling in the Absence of a High-Accuracy Open Access Global DEM. – In: Frontiers in Earth Science Vol. 6 Article 233; DOI: https://doi.org/10.3389/feart.2018.00233.

HOOKE J. M. (1979): AN ANALYSIS OF THE PROCESSES OF RIVERBANK EROSION. – In: Journal of Hydrology Vol. 42 pp 39-62; DOI: https://doi.org/10.1016/0022-1694(79)90005-2.

KALANTAR B., AMEEN M. H., JUMAAH H. J., JUMAAH S. J. and HALIN A. A. (2020): ZAB RIVER (IRAQ) SINUOSITY AND MEANDERING ANALYSIS BASED ON THE REMOTE SENSING DATA. – In: The International Archives of the Photogrammetry, Remote Sensing

and Spatial Information Sciences Vol. XLIII-B3-2020 pp 91-95; DOI: https://doi.org/10.5194/isprs-archives-XLIII-B3-2020-91-2020.

KAR A. K., HEMBRAM R. and MOHANTY H (2020): Chapter 3. Study of Morphological Changes in Deltaic River of Odisha Using GIS. – In: Editor Water Management and Water Governance. Water Science and Technology Library Vol. 96. Springer, Cham; DOI: https://doi.org/10.1007/978-3-030-58051-3_3.

KOEHL M., PIASNY G., THOMINE V., GARAMBOIS P-A., FINAUD-GUYOT P., GUILLEMIN S. and SCHMITT L. (2020): 4D GIS FOR MONITORING RIVERBANK EROSION AT MEANDER BEND SCALE: CASE OF MOSELLE RIVER. – In: The International Archives of the Photogrammetry, Remote Sensing and Spatial Information Sciences Vol. XLIV-4/W1-2020 pp 63-70; DOI: https://doi.org/10.5194/isprs-archives-XLIV-4-W1-2020-63-2020.

LAGUE D., BRODU N. AND LEROUX J. (2013): Accurate 2.5D comparison of complex topography with terrestrial laser scanner: Application to the Rangitikei canyon (N-Z). – In: ISPRS Journal of Photogrammetry and Remote Sensing Vol. 82 pp 10-26; DOI: https://doi.org/10.1016/j.isprsjprs.2013.04.009.

LARONNE J. B, OUTHET D. N., CARLING P. A. and MCCABE T. J. (1994): Scour chain employment in gravel bed rivers. – In: CATENA Vol. 22 Issue 4 pp 299-306; DOI: https://doi.org/10.1016/0341-8162(94)90040-X.

LAWLER (1992): The measurement of riverbank erosion and lateral channel change: a review. – In: EARTH SURFACE PROCESSES AND LANDFORMS, VOL. 18, pp 777-821; DOI: https://doi.org/10.1002/esp.3290180905.

LAWLER D. M., GROVE J. R., COUPERTHWAITE J. S. and LEEKS G. J. L. (1999): Downstream change in riverbank erosion rates in the Swale-Ouse system, northern England. – In: HYDROLOGICAL PROCESSES Vol. 13 Issue 7 pp 977-992; DOI: https://doi.org/10.1002/(SICI)1099-1085(199905)13:7<977::AID-HYP785>3.0.CO;2-5.

MICHELETTI N., CHANDLER J. H. and LANE S. N. (2014): Investigating the geomorphological potential of freely available and accessible structure-from-motion photogrammetry using a smartphone. – In: Earth Surface Processes and Landforms Vol. 40 Issue 4 pp 473-486; DOI: https://doi.org/10.1002/esp.3648.

MOMIN H., BISWAS R. and TAMANG C. (2020): Morphological analysis and channel shifting of the Fulahar river in Malda district, West Bengal, India using remote sensing and GIS techniques. – In: GeoJournal; DOI: https://doi.org/10.1007/s10708-020-10248-7.

O'BRIEN G. R., WHEATON J. M., FRYIRS K., MACFARLANE W. W., BRIERLEY G., WHITEHEAD K., GILBERT J. and VOLK C. (2019): Mapping valley bottom confinement at the network scale. – In:

EARTH SURFACE PROCESSES AND LANDFORMS Vol. 44 pp 1825-1845; DOI: https://doi.org/10.1002/esp.4615.

PINDOZZI S., CERVALLI E., CAPOLUPO A., OKELLO C. and BOCCIA L. (2015): Using historical maps to analyse two hundred years of land cover changes: case study of Sorrento peninsula (south Italy). – In: Cartography and Geographic Information Science Vol. 43 Issue 3 pp 250-265; DOI: https://doi.org/10.1080/15230406.2015.1072736.

POEPPL R. E., KEILER M., ELVERFELDT K.V., ZWEIMÜLLER I. and GLADE T. (2012): The influence of riparian vegetation cover on diffuse lateral connectivity and bio geomorphic processes in a medium-sized agricultural catchment, Austria. – In: Geografiska Annaler: Series A, Physical Geography 94, 511–529; DOI: https://doi.org/10.1111/j.1468-0459.2012.00476.x.

POEPPL R. E., COULTHARD T., KEESTRA S. D. and KEILER M. (2019): Modelling the impact of dam removal on channel evolution and sediment delivery in a multiple dam setting. – In: International journal of sediment research Vol. 34 Issue 6 pp. 537-549; DOI: https://doi.org/10.1016/j.ijsrc.2019.06.001.

PYLE C. J., RICHARDS K. S. and CHANDLER J. H. (1997): Digital Photogrammetric Monitoring of Riverbank Erosion. – In: The photogrammetric record Vol. 15 Issue 89 pp 753-764; DOI: https://doi.org/10.1111/0031-868X.00083.

RAMIREZ J. A., ZISCHG A. P., SCHÜRMANN S., ZIMMERMANN M., WEINGARTNER R., COULTHARD T. and KEILER M. (2020): Modelling the geomorphic response to early river engineering works using CAESAR-Lisflood. – In: Anthropocene Vol. 32; DOI: https://doi.org/10.1016/j.ancene.2020.100266.

SCHUMM, S.A. (1963) Sinuosity of Alluvial Rivers in the Great Plains. Bulletin of the Geological Society of America, 74, 1089-1100. DOI: https://doi.org/10.1130/0016-7606(1963)74[1089:SOAROT]2.0.CO;2.

STATUTO D., CILLIS G. and PICUNO P. (2017): Using Historical Maps within a GIS to Analyse Two Centuries of Rural Landscape Changes in Southern Italy. – In: Land Vol. 6(3) Issue 65; DOI: https://doi.org/10.3390/land6030065.

STEPHAN U., KAINZ S., HENGL M, MOSER M. and BITTERLICH W. (2021): Wasserbauliche Modellversuche zu Buhnen in steilen Gewässern – Möglichkeiten und Grenzen. – In: Österreichische Wasser- und Abfallwirtschaft Vol. 73 pp 134-143; DOI: https://doi.org/10.1007/s00506-020-00735-z.

TUCKER G. E. (2010): A SHORT INTRODUCTION TO LANDSCAPE EVOLUTION MODELING. Slightly modified version of short course notes from Summer School on Surface Process Modelling, Davos, Switzerland; available online under https://csdms.colorado.edu/mediawiki/images/Exercises_from_davos.pdf.

WAKONIGG Herwig (2010): Kapitel 4 Niederschlag. – In: Klimaatlas Steiermark PRETTENTHALER Franz - PODESSER Alexander - PILGER Harald (Editor); ISBN: 978-3-7001-6754-9 (=Studien zum Klimawandel in Österreich 4).

WETHERALD R. T. and MANABE S. (2002): Simulation of hydrologic changes associated with global warming. – In: JOURNAL OF GEOPHYSICAL RESEARCH, VOL. 107, NO. D19, 4379, DOI: https://doi.org/10.1029/2001JD001195.

WHEATON J. M., FRYIRS K. A., BRIERLEY G. J., BANGEN S. G., BOUWES N. and O'BRIEN G. (2015): Geomorphic mapping and taxonomy of fluvial landforms. – In: Geomorphology (248), 273–295; DOI: https://doi.org/10.1016/j.geomorph.2015.07.010.

WOODGET A. S., AUSTRUMS R. MADDOCK I. P. and HABIT E. (2017): Drones and digital photogrammetry: from classifications to continuums for monitoring river habitat and hydro morphology. – In: Wires Water Vol. 4 Issue 4; DOI: https://doi.org/10.1002/wat2.1222.

WYRICK J. R., SENTER A. E. and PASTERNACK G. B. (2013a): Revealing the natural complexity of fluvial morphology through 2D hydrodynamic delineation of river landforms. – In: Geomorphology Vol. 210 pp 14-22; DOI: https://doi.org/10.1016/j.geomorph.2013.12.013.

WYRICK J. R. and PASTERNACK G. B. (2013b): Geospatial organization of fluvial landforms in a gravel–cobble river: Beyond the riffle–pool couplet. – In: Geomorphology Vol. 213 pp 48-65; DOI: https://doi.org/10.1016/j.geomorph.2013.12.040.

YU W., KIM Y., LEE D. and LEE G. (2019): Hydrological assessment of basin development scenarios: Impacts on the Tonle Sap Lake in Cambodia. – In: Quaternary International Vol. 503 pp 115-127; DOI: https://doi.org/10.1016/j.quaint.2018.09.023.

ZLINSZKY A. and TIMÁR G. (2013): Historic maps as a data source for socio-hydrology: a case study of the Lake Balaton wetland system, Hungary. – In: Hydrology and Earth System Sciences Vol 17 Issue 11 pp 4589-4606; DOI: https://doi.org/10.5194/hess-17-4589-2013.

Further:

[1]www.basemap.at (last opened: on 02.11.2021)

[2]https://www.freemaptools.com/elevation-finder.htm (last opened: on 02.11.2021)

[3]http://app.hydrographie.steiermark.at/bilder/Hochwasserzentrale/Source/SteiermarkOverview_Pub.htm?timestep=+Oct+01+2020+06%3A00#?13,7 (last opened: on 02.11.2021)

[4] https://gis.stmk.gv.at/wgportal/atlasmobile/map/Basiskarten/Basiskarte (last opened: on 02.11.2021)

[5] https://pijawetz.com/de/salza-gusswerk (last opened: on 02.11.2021)

[6] https://www.bundesforste.at/service-presse/presse/pressedetail/news/fruehlingsgefuehle-unter-wasser-bundesforste-errichten-liebesnest-fuer-fisch-des-jahres.html (last opened: on 02.11.2021)

[7] Mapire (https://mapire.eu/de/), (last opened: on 02.11.2021)

[8] Cloud compare wiki, https://www.cloudcompare.org/doc/wiki (last opened: on 02.11.2021)

[9] CAESAR-Lisflood wiki, https://sourceforge.net/p/caesar-lisflood/wiki/Home/ (last opened: on 02.11.2021)

11. Appendix

Table 38: Measured distances (unconfined, confined and total) of the Salza River study area of the historic maps.

Map	Survey date	Distance (m) unconfined valley	Distance (m) confined valley	Distance (m) total
Franziszeische cadastre	1817-1861	4,928	1,570	6,468
Franziszeische Land survey	1821-1836	4,982	1,621	6,593
Francisco-Josephinische Land survey	1869-1887	4,943	1,768	6,697

Table 39: Measured lengths (unconfined, confined and total) of the Salza River study area of the historic maps.

Map	Survey date	Length (m) unconfined valley	Length (m) confined valley	Length (m) total
Franziszeische cadastre	1817-1861	5,885	2,710	8,595
Franziszeische Land survey	1821-1836	5,978	2,781	8,759
Francisco-Josephinische Land survey	1869-1887	5,834	2,905	8,739

Table 40: Sinuosity index for the unconfined valley of the historic maps of the Salza River study area.

Map	Survey date	Sinuosity index unconfined valley	Sinuosity index Change unconfined valley
Franziszeische cadastre	1817-1861	1.1942	-
Franziszeische Land survey	1821-1836	1.1999	0.0057
Francisco-Josephinische Land survey	1869-1887	1.1803	-0.0197

Table 41: Sinuosity index for the confined valley of the historic maps of the Salza River study area.

Map	Survey date	Sinuosity index confined valley	Sinuosity index Change confined valley
Franziszeische cadastre	1817-1861	1.7261	-
Franziszeische Land survey	1821-1836	1.7156	-0.0105
Francisco-Josephinische Land survey	1869-1887	1.6431	-0.0725

Table 42: Sinuosity index for the whole Salza River study area of the historic maps.

Map	Survey date	Sinuosity index total	Sinuosity index Change total
Franziszeische cadastre	1817-1861	1.3288	-
Franziszeische Land survey	1821-1836	1.3285	-0.0003
Francisco-Josephinische Land survey	1869-1887	1.3049	-0.0236

Table 43: Measured distances (unconfined, confined and total) of the Salza River study area of the orthophotos.

orthophoto	Scan flight date	Distance (m) unconfined valley	Distance (m) confined valley	Distance (m) total
#1	02.09.2004	4,910	1,780	6,679
#2	27.07.2009	--"--	--"--	--"--
#3	30.05.2011	--"--	--"--	--"--
#4	10.06.2014	--"--	--"--	--"--
#5	08.09.2017	--"--	--"--	--"--

Table 44: Measured lengths (unconfined, confined and total) of the Salza River study area of the orthophotos.

orthophoto	Scan flight date	Length (m) unconfined valley	Length (m) confined valley	Length (m) total
#1	02.09.2004	5,979	2,980	8,958
#2	27.07.2009	5,963	2,982	8,944
#3	30.05.2011	5,971	2,955	8,926
#4	10.06.2014	5,977	2,975	8,952
#5	08.09.2017	6,006	2,975	8,981

Table 45: Sinuosity index for the unconfined valley of the orthophotos of the Salza River study area.

orthophoto	Scan flight date	Sinuosity index unconfined valley	Sinuosity index Change unconfined valley
#1	02.09.2004	1.2177	-
#2	27.07.2009	1.2145	-0.0033
#3	30.05.2011	1.2161	0.0016
#4	10.06.2014	1.2173	0.0012
#5	08.09.2017	1.2232	0.0059

Table 46: Sinuosity index for the confined valley of the orthophotos of the Salza River study area.

orthophoto	Scan flight date	Sinuosity index confined valley	Sinuosity index Change confined valley
#1	02.09.2004	1.6742	-
#2	27.07.2009	1.6753	0.0011
#3	30.05.2011	1.6601	-0.0152
#4	10.06.2014	1.6713	0.0112
#5	08.09.2017	1.6713	0.0000

Table 47: Sinuosity index for the whole Salza River study area of the orthophotos.

orthophoto	Scan flight date	Sinuosity index total	Sinuosity index Change total
#1	02.09.2004	1.3412	-
#2	27.07.2009	1.3391	-0.0021
#3	30.05.2011	1.3364	-0.0027
#4	10.06.2014	1.3403	0.0039
#5	08.09.2017	1.3447	0.0043

Table 48: Measured distance of the erosion hotspot of all orthophotos in the Salza River study area.

orthophoto	Scan flight date	Distance (m) total
#1	02.09.2004	305
#2	27.07.2009	--“--
#3	30.05.2011	--“--
#4	10.06.2014	--“--
#5	08.09.2017	--“--
#6	07.09.2019	--“--

Table 49: Measured lengths of the erosion hotspot of all orthophotos in the Salza River study area.

orthophoto	Scan flight date	Length (m) total
#1	02.09.2004	318
#2	27.07.2009	319
#3	30.05.2011	317
#4	10.06.2014	333
#5	08.09.2017	363
#6	07.09.2019	360

Table 50: Sinuosity index for the erosion hotspot of all orthophotos in the Salza River study area.

orthophoto	Scan flight date	Sinuosity index total	Sinuosity index Change
#1	02.09.2004	1.0426	-
#2	27.07.2009	1.0459	0.0033
#3	30.05.2011	1.0393	-0.0066
#4	10.06.2014	1.0918	0.0525
#5	08.09.2017	1.1902	0.0984
#6	07.09.2019	1.1803	-0.0098

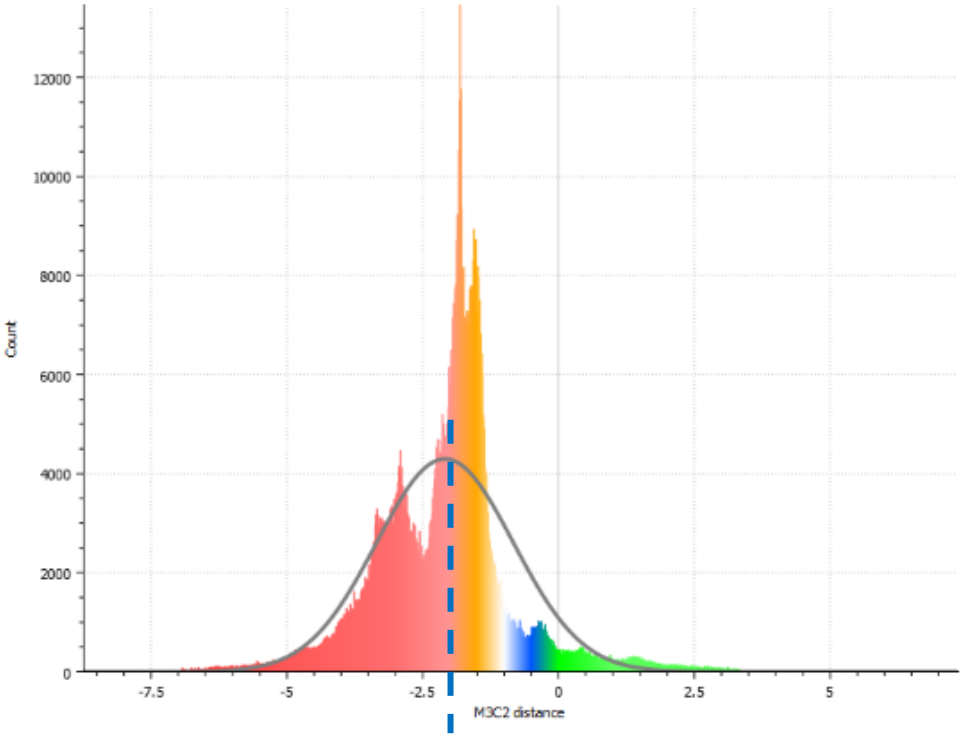


Figure 158: Normal distribution of the 2D changes (in metres) from cloud #1 to cloud #2.

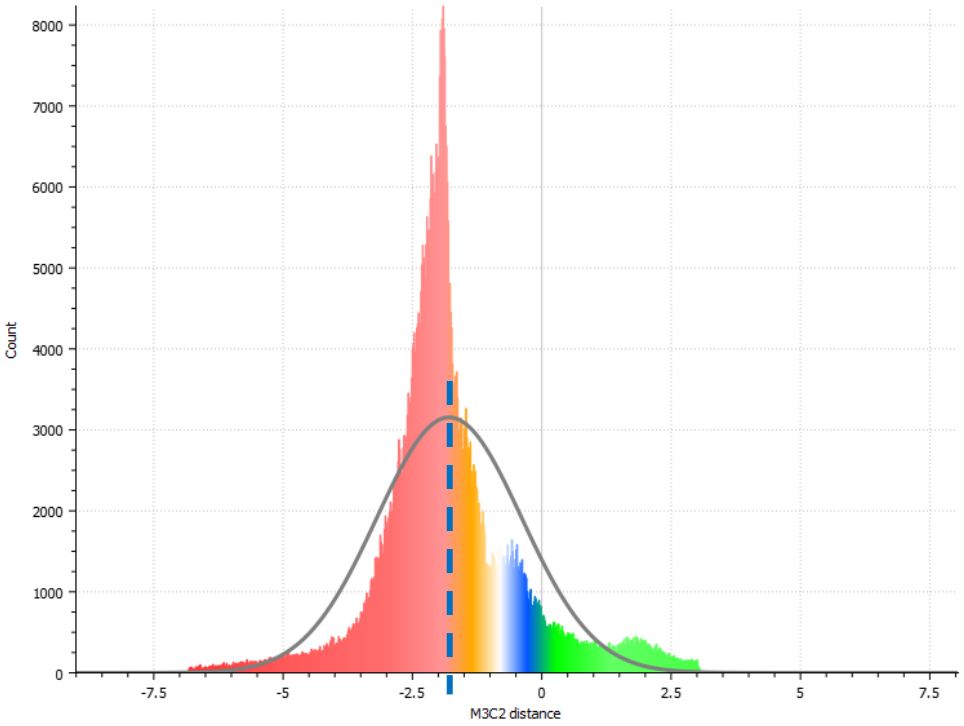


Figure 159: Normal distribution of the 2D changes (in metres) from cloud #2 to cloud #3.

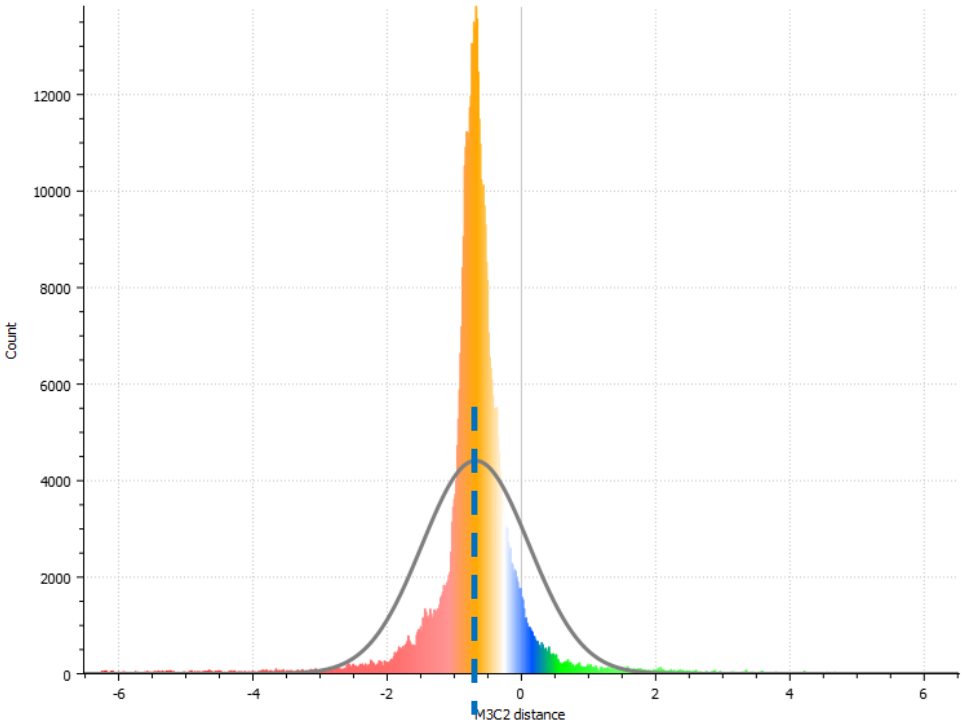


Figure 160: Normal distribution of the 2D changes (in metres) from cloud #3 to cloud #4.

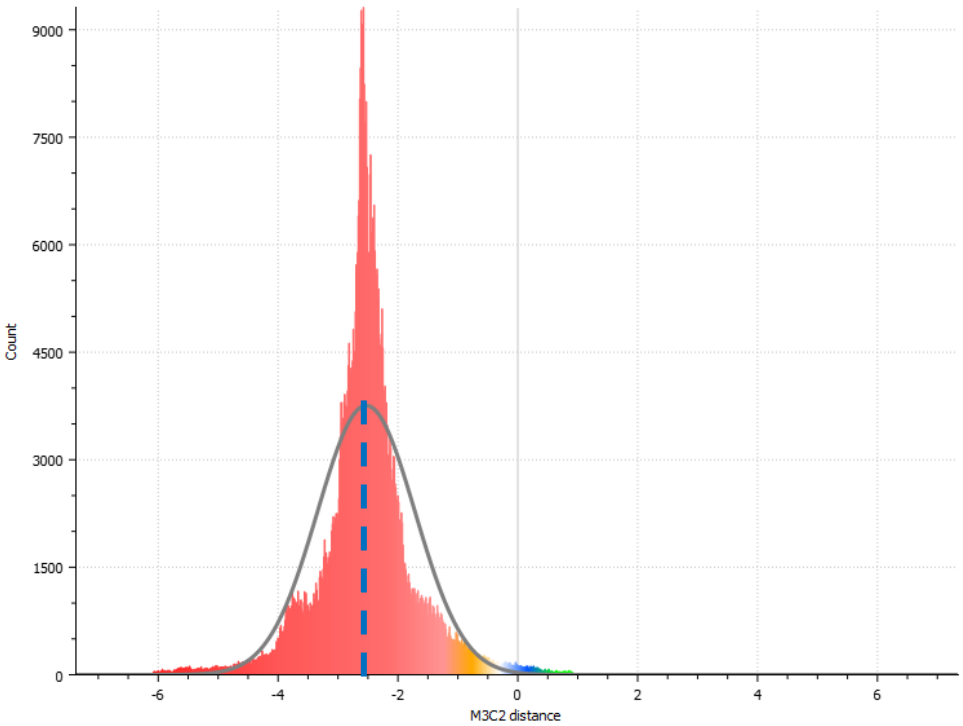


Figure 161: Normal distribution of the 2D changes (in metres) from cloud #4 to cloud #5.

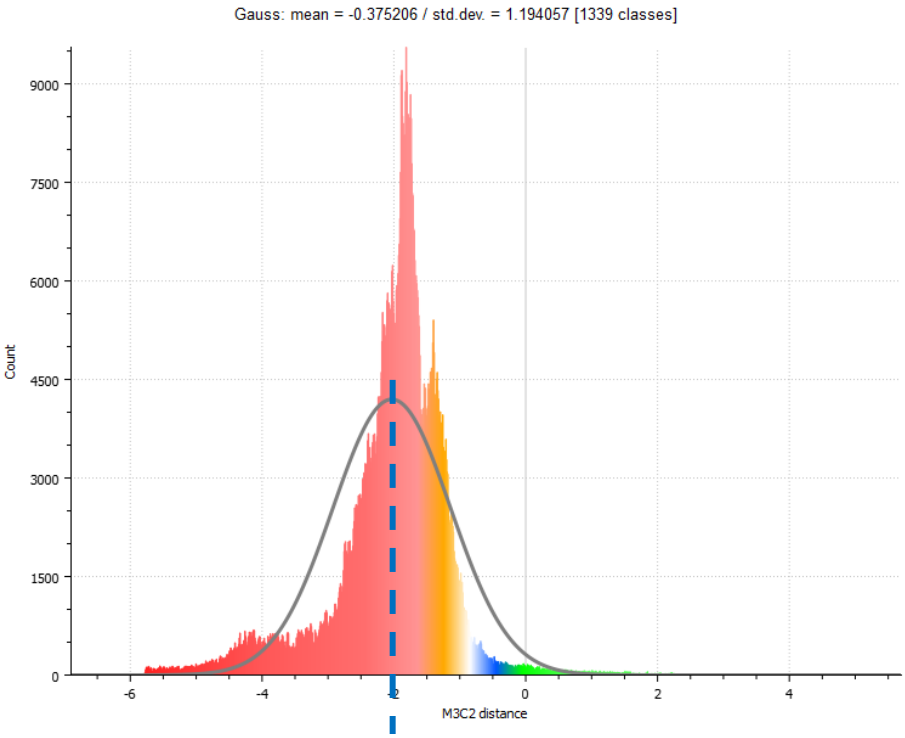


Figure 162: Normal distribution of the 2D changes (in metres) from cloud #1 to cloud #5.

Table 51: Measured distances (unconfined, confined and total) of the Salza River study area of initial DEM, pre-modelled year 2018 and modelled year 2050 for the five different discharge scenarios.

DEM	Distance (m) unconfined valley	Distance (m) confined valley	Distance (m) total
2011	4,909	1,779	6,676
2018m	--"--	--"--	--"--
1_2050m	--"--	--"--	--"--
2_2050m	--"--	--"--	--"--
3_2050m	--"--	--"--	--"--
4_2050m	--"--	--"--	--"--

Table 52: Measured lengths (unconfined, confined and total) of the Salza River study area of initial DEM, pre-modelled year 2018 and modelled year 2050 for the five different discharge scenarios.

DEM	Length (m) unconfined valley	Length (m) confined valley	Length (m) total
2011	5,990	2,951	8,941
2018m	6,252	2,978	9,230
1_2050m	6,116	2,963	9,079
2_2050m	6,221	2,965	9,186
3_2050m	6,131	2,970	9,101
4_2050m	6,013	2,952	8,965

Table 53: Sinuosity index for the unconfined valley of the Salza River study area of initial DEM, pre-modelled year 2018 and modelled year 2050 for the five different discharge scenarios.

DEM	Sinuosity index unconfined valley	Sinuosity index Change unconfined valley	
2011	1.2202	-	
2018m	1.2736	0.0534	With 2011
1_2050m	1.2459	-0.0277	With 2018m
2_2050m	1.2673	-0.0063	With 2018m
3_2050m	1.2489	-0.0246	With 2018m
4_2050m	1.2249	-0.0487	With 2018m

Table 54: Sinuosity index for the confined valley of the Salza River study area of initial DEM, pre-modelled year 2018 and modelled year 2050 for the five different discharge scenarios.

DEM	Sinuosity index confined valley	Sinuosity index Change confined valley	
2011	1.6588	-	
2018m	1.6740	0.0152	With 2011
1_2050m	1.6655	-0.0084	With 2018m
2_2050m	1.6667	-0.0073	With 2018m
3_2050m	1.6695	-0.0045	With 2018m
4_2050m	1.6594	-0.0146	With 2018m

Table 55: Sinuosity index for the whole Salza River study area of initial DEM, pre-modelled year 2018 and modelled year 2050 for the five different discharge scenarios.

DEM	Sinuosity index total	Sinuosity index Change total	
2011	1.3393	-	
2018m	1.3826	0.0433	With 2011
1_2050m	1.3599	-0.0226	With 2018m
2_2050m	1.3760	-0.0066	With 2018m
3_2050m	1.3632	-0.0193	With 2018m
4_2050m	1.3429	-0.0397	With 2018m